Overflow and wave overtopping induced failure processes on the land-side slope of a dike

MSc. Thesis

L.A. Ponsioen

Technische Universiteit Delft

TU Delft Delft University of Technology

Flanders Hydraulics Research

Flanders State of the Art

Challenge the future

DELFT UNIVERSITY OF TECHNOLOGY

MSC THESIS

Overflow and wave overtopping induced failure processes on the land-side slope of a dike

by

L.A. PONSIOEN

A thesis submitted in partial fulfilment of the requirements
for the degree of Master of Science

in the

Coastal Engineering
Department of Hydraulic Engineering

Supervisor:	*Institution:*
Prof.Dr.Ir. C. VAN RHEE	Delft University of Technology
Dr.Ir. M. VAN DAMME	Delft University of Technology
Dr.Ir. B. HOFLAND	Delft University of Technology
Ir. P. PEETERS	Flanders Hydraulics Research

May 2016

Preface

This MSc thesis is the result of the final project to fulfil the requirements for my Master degree in Hydraulic Engineering at Delft University of Technology. Through this way I would like to thank everybody who helped bringing this project to a good end. Many thanks to the members of my graduation committee: Prof.Dr.Ir. C. Van Rhee, Dr.Ir. M. Van Damme, Dr.Ir. B. Hofland and Ir. P. Peeters. Their varying fields of expertise has helped me in many ways during my thesis and have made research on this subject possible. Special thanks to Myron Van Damme, who has been an excellent daily supervisor for the past 8 months and was always ready to help when I was stuck during my research.

I would like to express sincere gratitude to Flanders Hydraulics Research, and especially to Patrik Peeters, for making me participate in a spectacular experiment. Subsequently I thank Gerben van der Meer, Frans Roorda and Jan Bakker for their great collaboration during the wave overtopping experiments at the Wijmeers-II polder. Furthermore I would like to thank Max Rademacher, Mark van Veenendaal and Marc van Reijen for their help during my Matlab struggles, my programming skills have improved significantly thanks to their help. During the overflow experiments at Wijmeers-II an overflow simulator was used which was built by the technical support staff of the Hydraulic laboratory at the Civil Engineering faculty of Delft University of Technology. Without their skills the construction of the simulator would have been a major difficulty, therefore I would like to thank the entire technical support staff of the Hydraulic laboratory for their help and input.

Last but definitely not least I would like to thank my parents for their loving support in every possible way during my study.

Luc Ponsioen
Delft, May 2016

Abstract

This thesis discusses the breach initiation processes at the land-side slope of a dike, due to overflow and wave overtopping. To date still little is known about the actual failure process of land-side slope covers. Therefore, starting in 2007, numerous wave overtopping experiments have been executed in The Netherlands and Belgium using a wave overtopping simulator. This simulator simulates different kinds of storm events by releasing volumes of water over the land-side slope according to a predetermined schedule. Flanders Hydraulics Research and Delft University of Technology performed another wave overtopping experiment in November 2015. The wave overtopping simulator as well as a new designed overflow simulator were used to test the breach initiation processes of the land-side slope of a river-dike adjacent to the river Scheldt, near the Wijmeers-II polder in Belgium. The data obtained from this experiment is presented in this thesis, and was used to evaluate current damage initiation theories.

Currently the most advanced approach for determining the amount of erosion, or 'damage', to the land-side slope is the 'Excess volume approach' by Hughes [17, 18] who based his model on earlier developed models by Van der Meer [36] and Dean et al. [10]. This approach determines damage on the land-side slope based on overflow theories and overflow experiments (CIRIA experiments [13]). An overtopping wave is thereby modelled as a very short overflow event in which damage is assumed to be bottom shear stress induced. The Excess volume approach has therefore been applied on the Wijmeers-II data in order to verify the predictive accuracy of this theory.

Contrary to the experimental outcome, the Excess volume approach predicted a heavier damage on the overflow test sections than on the wave overtopping test section. Due to these test results the correct representation of reality of the Excess volume approach is questioned in this thesis. Extensive investigation of video material obtained during the experiments showed that overtopping waves separate from the slope before reattaching with the slope. This separation time leads to a jet flow impacting the slope under an angle. Due to a decrease in discharge during a wave overtopping, the impact location moves towards the crest within the overtopping time of a wave. This discovery led to the development of a new modelling approach in which this phenomenon is considered.

In this new 'Wave impact approach', damage on the grass cover is assumed to be caused by wave overtopping induced jet pressures in cracks in the grass cover. These cracks are present due to weather conditions and temperature influences in the supporting clay layer. Wave overtopping induced jet pressure in the crack pushes the walls further aside leading to growth of the crack. This

crack growth continues until the pressure in the crack becomes too high and grass aggregates are lifted from the cover. This crack growth is assumed to only occur when the wave overtopping induced jet pressure in the crack exceeds a critical pressure threshold P_c. The location at which the highest cumulative excess impulse load occurs is the location at which the most damage is expected. Verification of the theory against other experiments confirms the theory.

A preview of the breach initiation process discovered in this thesis is given in Figure 1.

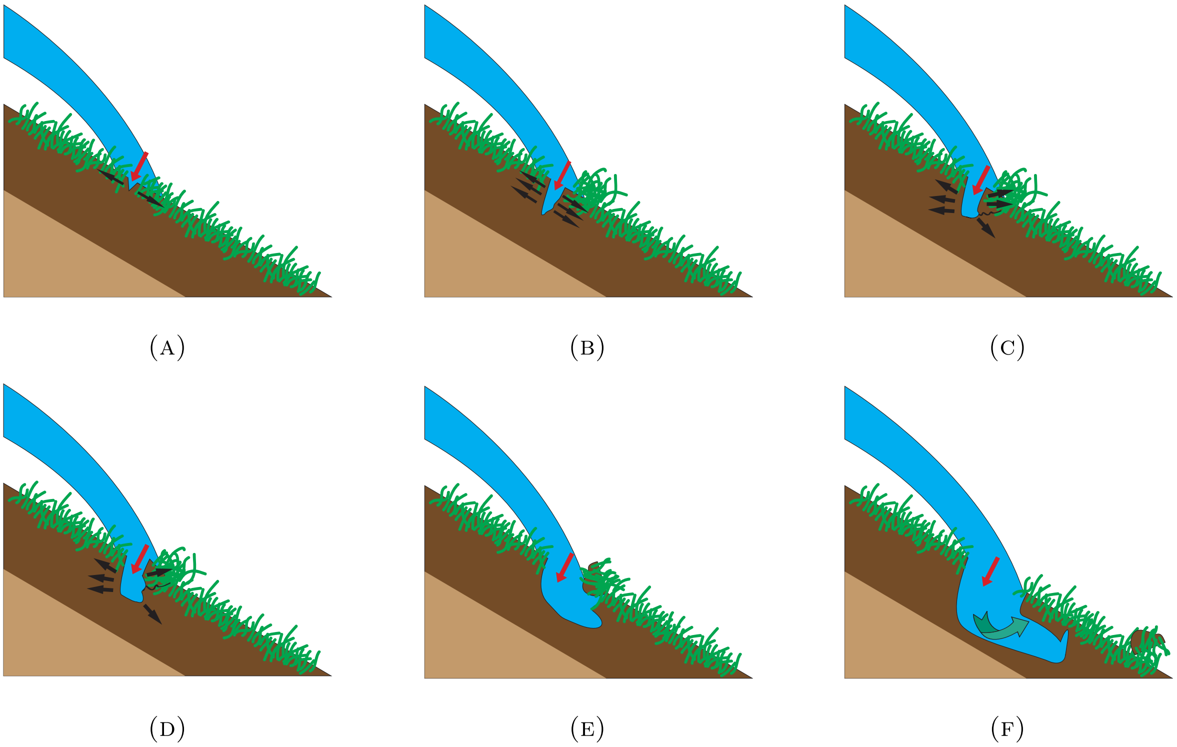
(A) (B) (C)

(D) (E) (F)

Figure 1: Wave overtopping induced failure process clarified in 6 steps.

Samenvatting

In dit afstudeerwerk wordt het bres initiatie proces op het binnentalud van een dijk als gevolg van golfoverslag en overstroming besproken. Vandaag de dag is er nog weinig bekend over het daadwerkelijke faalproces van de afdeklaag op binnentaluds. Met die gedachte zijn vanaf 2007 meerdere golfoverslag experimenten uitgevoerd in Nederland en België met behulp van een goloverslag simulator. Deze simulator is in staat om verschillende soorten stormen te simuleren door volumes water over de dijk heen te lozen volgens een vooraf bepaald schema. Het Waterbouwkundig laboratorium in Antwerpen en de TU Delft hebben in november 2015 wederom golfoverslag proeven uitgevoerd, ditmaal gecombineerd met overloopproeven. De golfoverslag simulator en een overloopsimulator, ontworpen door de TU Delft, zijn gebruikt om de erodeerbaarheid van het binnentalud van een dijk langs de Schelde rivier in de Wijmeers-II polder in België te testen.

Momenteel is de meest gavanceerde benadering voor het bepalen van de hoeveelheid erosie, of 'schade', op het binnentalud de Overtollige volume aanpak ontwikkeld door Hughes [17, 18] welke zijn aanpak baseerde op eerdere publicaties van Van der Meer [36] en Dean et al. [10]. Deze benadering bepaalt schade op het binnentalud door middel van overloop theorieën uit overloop experimenten verkregen data (CIRIA experimenten [13]). Een overslaande golf wordt daarbij benaderd als een zeer korte versie van een overstroming waarin aangenomen wordt dat de schade wordt veroorzaakt door bodem schuifspanning. De Overtollige volume aanpak is daarom toegepast op de verkregen data uit de Wijmeers-II experimenten, om te testen of de voorspellingen van de theori kunnen worden geverifieerd.

Tegenstrijdig tot the experimentele uitkomst, voorspelde de Overtollige volume aanpak een zwaarder schadebeeld bij de overloop proeven dan bij de golfoverslag proeven. De uitkomst van de Wijmeers-II experimenten geeft hierdoor reden tot het bekritiseren van de Overtollige volume aanpak. Uitgebreid onderzoek van beeldmateriaal van de Wijmeers-II proeven leidde uiteindelijk tot de conclusie dat overslaande golven voor significante afstand gescheiden blijven van het talud voordat deze inslaan op het binnentalud. Hierdoor veroorzaakt de overslaande golf een waterstraal die onder een hoek op het binnentalud spuit. Doordat het debiet tijdens een overslaande golf afneemt, verschuift de locatie waar de straal contact maakt met het binnentalud richting de kruin. Deze ontdekking heeft geleid tot de ontwikkeling van een nieuwe modelaanpak waarin dit fenomeen wel is opgenomen.

In deze nieuwe 'Golf inslag benadering', wordt aangenomen dat schade op de afdeklaag van het binnentalud wordt veroorzaakt door de druk van de eerder beschreven waterstraal in reeds aanwezige

scheuren in de afdeklaag. Deze scheuren zijn veroorzaakt door weer- en temperatuurinvloeden op de onderliggende kleilaag. De druk in een scheur, veroorzaakt door de overslaande waterstraal, leidt tot het uit elkaar duwen van de scheur-zijden waardoor deze groter en dieper wordt. Er wordt aangenomen dat het proces van vergroten van scheuren alleen gebeurt wanneer de druk van een door golfoverslag gevormde waterstraal hoger is dan een bepaalde drempel waarde P_c. Aangezien gedurende een storm meerdere golven over de dijk heen zullen slaan, is de locatie op het binnentalud waar de hoogste cumulatieve impuls belasting voorkomt ook de locatie waar de meeste schade is te verwachten. Verificatie van de theorie bevestigd deze hypothese.

Een voorbeeld van het in dit afstudeerwerk ontdekte bres initiatie proces is geschematiseerd weergeven in figuur 2.

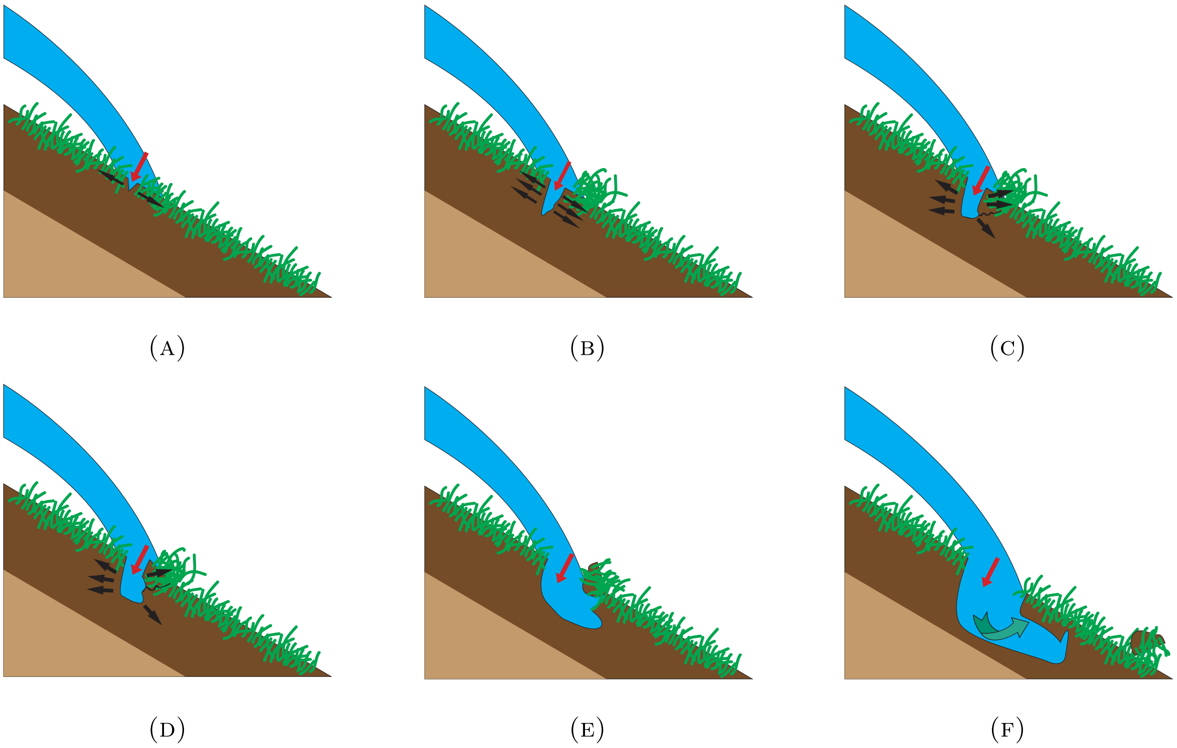

(A) (B) (C)

(D) (E) (F)

FIGURE 2: Door golfoverslag geïnitieerde erosie prosessen van de afdeklaag van het binnentalud, verduidelijkt in 6 stappen.

Contents

Preface ii

Abstract iv

Samenvatting vi

Contents ix

1 Introduction 1
- 1.1 Problem definition 2
- 1.2 Research objective 3
- 1.3 Research questions 3
- 1.4 Report structure 5

2 Theoretical background 7
- 2.1 Breaching processes of dikes 7
  - 2.1.1 6 phases in dike breaching 7
  - 2.1.2 Phase 1: Initial failure of grass sod 9
  - 2.1.3 Phase 2: Clay cover failure 13
- 2.2 Wave overtopping on a dike 13
  - 2.2.1 Wave run-up height 13
  - 2.2.2 Wave run-up velocity 14
  - 2.2.3 Wave run-up depth 14
  - 2.2.4 Wave Run-up discharge 15
- 2.3 Overtopping shear stress 16
  - 2.3.1 Dike crest 17
  - 2.3.2 Landward side 18
  - 2.3.3 Levee side velocity 19
- 2.4 Excess volume approximation 19
  - 2.4.1 Excess volume approximation on wave overtopping 20
  - 2.4.2 Excess volume approximation on steady overflow 22

3 Experimental set-up 25
- 3.1 Overtopping simulator 25
- 3.2 Overflow simulator 25
- 3.3 Test sections 27
- 3.4 Description of experiments 29
  - 3.4.1 Overtopping 29

3.4.2 Overflow . . . 29
3.4.3 Calibration of simulators . . . 30

4 Overflow experiment results 33
4.1 Damage description overflow tests . . . 33
4.2 Water depth . . . 36
4.3 Flow velocities during overflow tests . . . 36
4.3.1 Infra-red camera . . . 38

5 Overtopping experiment results 41
5.1 Paddle wheels and surfboards . . . 41
5.2 Water depth . . . 44
5.3 Flow velocity . . . 45
5.4 Peak discharge . . . 47
5.5 Calculated wave volumes . . . 48

6 Existing theory applied on Wijmeers-II data 49
6.1 Overflow induced land-side slope velocity . . . 49
6.2 Basis for overtopping theories . . . 51
6.2.1 Velocity-, Shear stress- or Work-basis? . . . 51
6.3 Excess volume approach . . . 52
6.3.1 Verification of overtopping theory . . . 53
6.4 Application of Excess volume approximation . . . 55
6.4.1 Result . . . 57
6.5 Conclusion and discussion . . . 58

7 Wave impact approach 59
7.1 Failure mechanism . . . 59
7.1.1 Phase 1: Initial failure of grass sod . . . 59
7.1.2 Grass cover failure process described from Wijmeers-II observations . . . 61
7.1.3 Phase 2: Clay cover failure . . . 61
7.2 Wave impact effect . . . 64
7.2.1 Separation time . . . 65
7.2.2 Wave impact location . . . 65
7.2.3 Wave impact stress . . . 67
7.2.4 Wave impact angle . . . 69
7.3 Damage on land-side slope . . . 71
7.3.1 Individual wave overtopping load . . . 71
7.3.2 Total load on land-side slope . . . 73
7.3.3 Damage threshold . . . 73
7.3.4 Maximum damage indication . . . 74
7.3.5 Residual strength land-side slope . . . 76
7.4 Quantification of damage threshold . . . 76
7.5 Analytical approach for including crest water depth . . . 79
7.6 Numerical solution . . . 80
7.6.1 Simplified approach . . . 80
7.6.2 Including crest water depth in numerical approach . . . 82
7.7 Sensitivity analysis . . . 84

7.8 Summary and discussion 85

8 Verification of Wave impact approach 89
8.1 Wijmeers-II experiments 89
8.2 Tielrodebroek experiments 92
8.3 Afsluitdijk experiments 94
8.4 Zeeuwse zeedijken experiments 96
8.5 Results 98
8.6 Conclusion and discussion 100

9 Conclusions and Recommendations 103
9.1 Conclusions existing land side slope erosion models 103
9.2 Conclusions new developed land side slope erosion model 104
9.3 Answering research questions 104
9.4 Recommendations 107

Bibliography 109

List of Figures 112

List of Tables 119

Symbols 121

A Overtopping probability 123
A.1 Overtopping probability parameters 123
A.2 Overtopping variables expressed in each other 125
A.3 Probability of exceedance 126
A.4 Conclusion 129

B Overtopping terms expressed in each other 131

C Breaching process of a dike 135
C.1 Breaching processes of dikes 135
C.1.1 6 phases in dike breaching 135
C.1.2 Phase 1: Initial failure of grass sod 136
C.1.3 Phase 2: Clay cover failure 140
C.1.4 Phase 3: Scour development in sand core 142
C.1.5 Phase 4: Headcut erosion 144
C.1.6 Phase 5 and 6: Development into full breach 145

D Residual strength land-side slope 147

E Analytical approach for Wave impact model 149

F Verification of Wave impact approach 155
F.1 Wijmeers-II experiments 155
F.2 Afsluitdijk experiments 157
F.3 Friese Waddenzeedijk experiments 158
F.4 Zeeuwse zeedijken experiments 160

F.5 Tholen experiments 163

G Tracking plots Infrared camera **165**

G.1 Track and velocity components of the floater 165

H Peddle wheel and surf board data **179**

I Description of damage during overflow tests **195**

1 | Introduction

In the Netherlands and Belgium a significant part of the dikes have been rejected by inspection committees as they do not meet today's safety standards. Improving the dikes to let them meet these standards requires large investments. With this in mind the question recently arose if it is actually the case that the dikes are too weak or could it be that the design criteria for dikes are too high? Born in mind that for instance residual strength in dikes is not included in the determination of the strength of a dike, this could actually be a reasonable scenario. Including these aspects could change the design criteria for a dike and get numerous dikes of the list of rejected dikes and thereby saving the national governments money. This research is set up to determine more accurately what the risks of overflow and overtopping on a dike are. Important aspects of the research is getting better insight into the initial failure processes in a dike breach.

Despite the fact that the Dutch history of water defence with dike systems goes back many centuries, we know surprisingly little about certain failure mechanisms of dikes. The most important reason for this is the simple fact that it is really hard to find a place where you can experimentally create a dike breach. Governments almost never allow experiments on existing dikes. The risk of demolishing a dike and therefore creating a temporary weak spot in the national primary water defence system is simply too high. Therefore, when an opportunity presents itself to allow dike breaching experiments on an actual dike, one should take this opportunity with both hands. That is exactly what happened at the dikes surrounding the Wijmeers-II polder close to Schellebelle, Belgium. According to the Belgian 'Sigma-plan' pieces of land are being given back to the river by using them as flood plains. This leads to more room for the river when an extremely high river discharge event occurs and therefore leads to less floods. The creation of flood plains means new dikes have to be made and pieces of existing dike need to be demolished. This creates a window of opportunity for scientist to perform as many experiments on the piece of to be demolished dike as possible. It was therefore that Patrik Peeters of Flanders Hydraulics Research and Myron van Damme of Delft University of Technology came up with a plan to perform three different kinds of experiments on the Wijmeers-II polder dike: wave overtopping, steady overflow and finally a breach experiment.

Wave overtopping experiments have been executed several times in the past 7 years. In order to execute these experiments, in 2006 a wave overtopping simulator was designed and build by Infram B.V. and Royal Haskoning DHV. The wave overtopping simulator was tested extensively on different locations before it was used in practice. When the testing was finished the simulator was used in practise for the first time during wave overtopping experiments at Delfzijl, in the North of

The Netherlands. The overtopping experiments at Delfzijl appeared to be a success, therefore in the 5 years after the Delfzijl experiment, wave overtopping experiments have been executed at 5 more locations in The Netherlands. A wave overtopping experiment combined with a complete dike breach experiment has been executed in Tielrode, Belgium in 2013. The success of this experiment has led to the wish for another breach experiment, this time combined with both overflow and wave overtopping experiments, in Belgium. Experiments have been executed near the town of Schellebelle in the Wijmeers-II polder in Belgium. The wave overtopping simulator developed by Infram B.V was used again as well as an overflow simulator, designed by Luc Ponsioen and Myron van Damme for the purpose of this experiment. The data obtained from the Wijmeers-II experiments is primarily used in this MSc. thesis.

1.1 Problem definition

The design criteria for dikes in The Netherlands and Belgium are nowadays primarily based on initial failure of a dike. In the current failure criteria it is assumed that a dike will fail as soon as the grass cover layer of the dike has failed. However, in these criteria, the so called residual strength of the supporting clay layer in the dike is not been taken into account. It is therefore desirable to get better insight into the initial failure processes of a dike. The residual strength in the supporting top layers of a dike could reset the criteria for dike design.

Current dike breaching models are mainly based on constant overflow processes. Although a start has been made for breaching models based on wave overtopping of the dike, the development of these models is rather slowly. This is mainly caused by the lack of knowledge about wave overtopping induced initial failure processes. Recent experimental research has increased the knowledge about the overtopping processes of waves. The impact however of wave overtopping on the process behind breach initiation of the grass- and clay layers and how this relates to overflow failure remains quite unknown. Because this wave impact process is not included in dike failure models a potential under-estimation of the strength of the land side slope of a dike may occur.

Existing wave overtopping induced erosion modelling approaches are mostly empirical based. The modelling approach assume an overtopping wave to be a short overflow event with decreasing flow velocity and water depth in time. Therefore the leading stress for erosion processes on the land side slope is assumed to be bed shear stress. These empirical erosion models are based on overflow induced failure mechanisms, however an experiment that compares both overflow and wave overtopping on the same dike section have until thus far never been executed. Therefore the theory behind these erosion models has never been proven to be valid.

In order to test the empirical erosion models full scale overtopping and overflow experiments have been performed on a river dike near Schellebelle in Belgium. Subsequently a unique opportunity to validate land side slope erosion models was created.

1.2 Research objective

The main objective of this research is to expand the knowledge about initial failure processes and dike breaching processes. The research will focus on the failure process of the grass cover layer and supporting clay layer of a dike. Therefore failure processes of these layers are investigated and the impact of different kind of loads on the land side slope are considered. Existing wave overtopping induced erosion models are believed to be based on too many invalid assumptions. Therefore the ultimate goal of this research is to develop a new model or method to describe the wave overtopping induced failure process of the land side slope of a dike.

Experimental based validation of existing erosion models

Since some assumptions in existing land side slope erosion models, like the modelling of overtopping waves using overflow theories, are believed to be invalid, experiments are initiated with the objective to gather data to prove these beliefs. The data from these experiments should give new insights in the leading failure processes caused by wave overtopping. Generally this means the assumption of modelling overtopping waves as a short overflow event with decreasing flow velocity and water depth is essayed experimentally. Whether this assumption is right or not cannot be determined directly from the data, therefore a computer model is built based on the existing erosion model theory and the experimental data. If the outcome of the model does not match the outcome of the experiments, this supports the the hypothesis that waves cannot be modelled purely based on overflow theories.

Develop new land side slope failure model

Empirically based models are often hard to apply in situations deviating from the set up from which the empirical relation is derived. In order to develop a more general method to describe initial failure mechanisms on a land side slope an attempt is made to develop a purely process based model. A second objective of this model is to include failure probability. Existing erosion models are primarily based on mean wave overtopping discharges, but do not describe what the actual probability of exceedance of such overtopping wave discharges are.

1.3 Research questions

Prior to this thesis, the objective was to use an existing erosion model approach as developed by e.g. Hughes [17, 18] and attempt to extend this model with wave impact effects and the cascade effect of the land side slope on overflow. However, as the outcome of this thesis demonstrates, this model was basically rejected by the data obtained from the Wijmeers-II experiments, see Chapter 6. Therefore the choice is made to develop an entirely new method for the determination of damage on the land side slope. The research is based on several research questions, of which the main research question is:

Main research question

What is the influence of wave impact on the initial failure process of the land side slope of a dike? And what is a physical based method to include this effect in a breach initiation model?

The sub-questions corresponding to this main research question are:

Sub-questions

- Can existing breach initiation theories of land-side slope based failure of a dike be verified with experimental data?
- What is the leading stress in wave overtopping induced failure?
- What is the wave overtopping induced failure mechanism of the grass and clay cover of a land side slope?
- How can the impact of overtopping waves be included in a wave overtopping induced land side slope erosion model?

1.4 Report structure

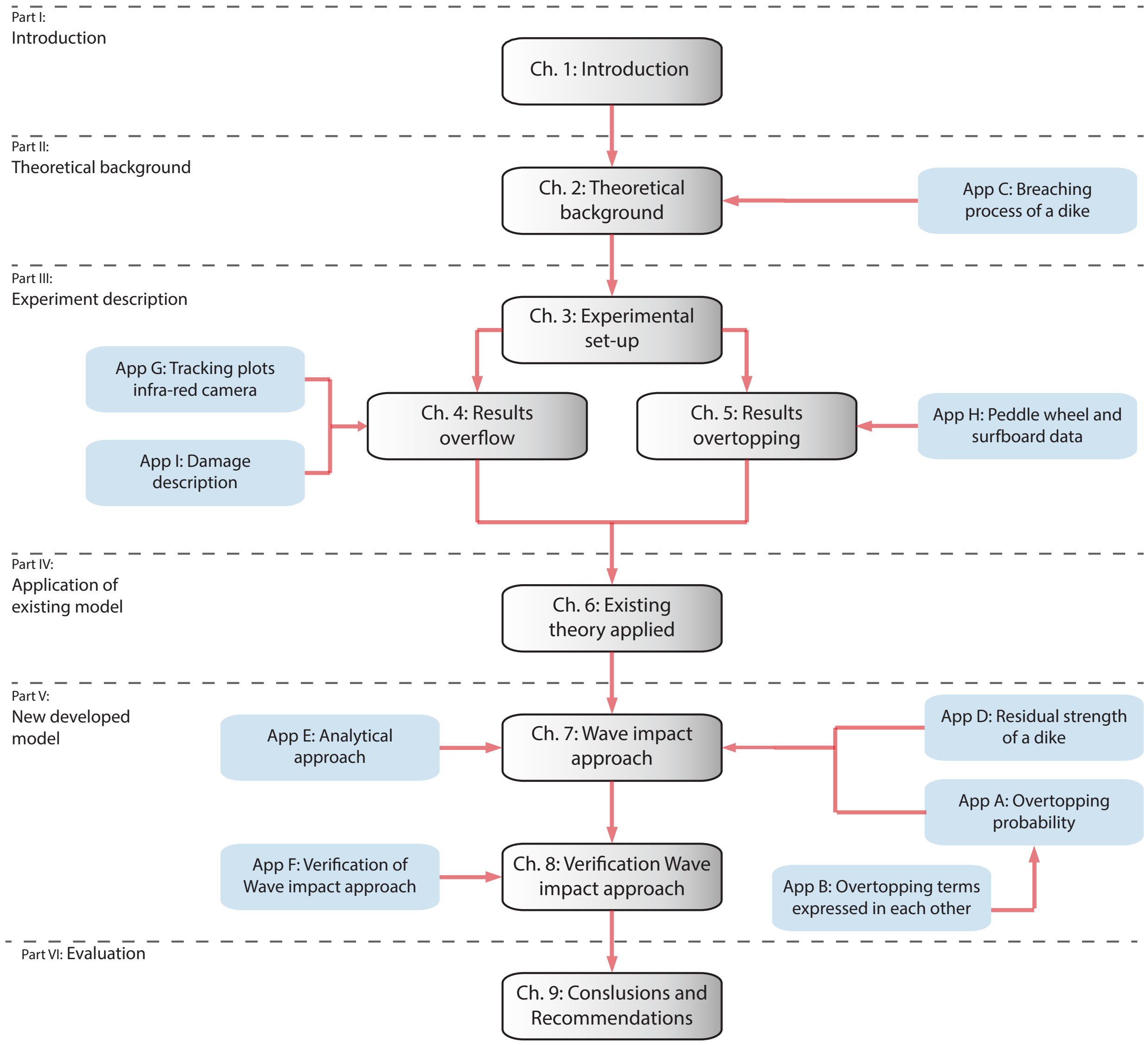
Part I:
Introduction
Ch. 1: Introduction
Part II:
Theoretical background
Ch. 2: Theoretical background
App C: Breaching process of a dike
Part III:
Experiment description
Ch. 3: Experimental set-up
App G: Tracking plots infra-red camera
App I: Damage description
Ch. 4: Results overflow
Ch. 5: Results overtopping
App H: Peddle wheel and surfboard data
Part IV:
Application of existing model
Ch. 6: Existing theory applied
Part V:
New developed model
App E: Analytical approach
Ch. 7: Wave impact approach
App D: Residual strength of a dike
App A: Overtopping probability
App F: Verification of Wave impact approach
Ch. 8: Verification Wave impact approach
App B: Overtopping terms expressed in each other
Part VI: Evaluation
Ch. 9: Conslusions and Recommendations

FIGURE 1.1: Thesis structure

2 | Theoretical background

Background information about the breaching process of grass covered dikes with a sand core is given in this chapter. The breaching process itself is described briefly, followed by a more elaborate description of the calculation of overtopping waves during a storm event.

2.1 Breaching processes of dikes

The breaching process of dike is elaborately described in the Phd. thesis of D'Eliso [11]. D'Eliso primarily based his research on the 5 phases in breaching described by P. Visser [41] who based his 5 phases theory on experimental research. D'Eliso increased the number of phases in dike breaching by describing it in 6 phases, which are described in section C.1.1. The scope of this thesis is on the initial failure processes of the land-side slope of a dike. Therefore not all phases as described by D'Eliso or Visser are relevant. An elaborate description of all the phases described by D'Eliso is given in Appendix C. In this section only brief description of the relevant phases is given.

2.1.1 6 phases in dike breaching

D'Eliso [11] described in his Phd. thesis the process of dike breaching in six phases. His model reproduces the whole breaching process in the following six phases:

1. Failure of the grass due to gradual erosion.
2. Local erosion of the clay cover.
3.
    - 3a. Scour erosion and headcut advance in the clay cover up to sand core exposure to flow action
    - 3b. Instantaneous sliding of the clay cover, initial breaching channel at the inner slope with bed of sand and slopes of clay.
4. Dike crest shortening due to scour erosion in sand, progressive failure of the clay cover at the crest.
5.
    - 5a. Dike crest lowering and breach widening due to scour erosion in sand and breach slopes instability, progressive failure of clay cover at the outer slope, driven by wave overtopping.

- 5b. Dike crest lowering and breach widening due to scour erosion in sand and breach slopes instability, progressive failure of clay cover at the outer slope, driven by combined flow

6.
- 6a. Full breach, breach widening due to scour erosion in sand and breach slopes instability driven by super-critical flow in the breach (transitional flow)
- 6b. Breach widening due to scour erosion in sand and breach slopes instability up to equilibrium final breach driven by sub-critical flow in the breach (non-transitional flow)

The six phases as described by D'Eliso are demonstrated in figure C.1 and C.2.

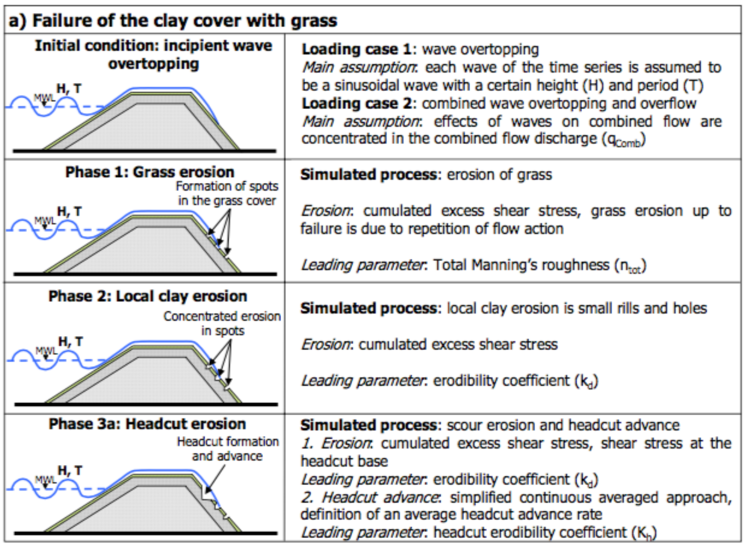

a) Failure of the clay cover with grass	
Initial condition: incipient wave overtopping	**Loading case 1**: wave overtopping *Main assumption*: each wave of the time series is assumed to be a sinusoidal wave with a certain height (H) and period (T) **Loading case 2**: combined wave overtopping and overflow *Main assumption*: effects of waves on combined flow are concentrated in the combined flow discharge (q_{Comb})
Phase 1: Grass erosion	**Simulated process**: erosion of grass *Erosion*: cumulated excess shear stress, grass erosion up to failure is due to repetition of flow action *Leading parameter*: Total Manning's roughness (n_{tot})
Phase 2: Local clay erosion	**Simulated process**: local clay erosion is small rills and holes *Erosion*: cumulated excess shear stress *Leading parameter*: erodibility coefficient (k_d)
Phase 3a: Headcut erosion	**Simulated process**: scour erosion and headcut advance *1. Erosion*: cumulated excess shear stress, shear stress at the headcut base *Leading parameter*: erodibility coefficient (k_d) *2. Headcut advance*: simplified continuous averaged approach, definition of an average headcut advance rate *Leading parameter*: headcut erodibility coefficient (K_h)

H, T
MWL
Formation of spots in the grass cover
Concentrated erosion in spots
Headcut formation and advance

FIGURE 2.1: Breaching of sea dikes initiated by wave overtopping: modelling phases and simulated processes as indicated by D'Eliso [11]

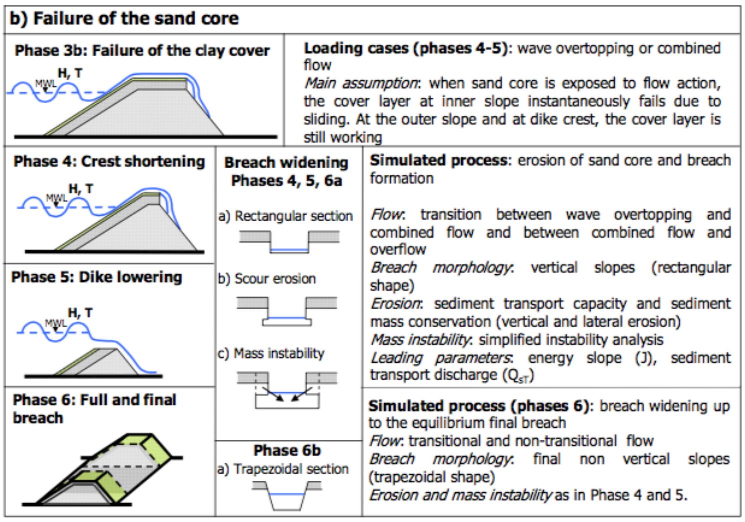

b) Failure of the sand core		
Phase 3b: Failure of the clay cover	**Loading cases (phases 4-5)**: wave overtopping or combined flow *Main assumption*: when sand core is exposed to flow action, the cover layer at inner slope instantaneously fails due to sliding. At the outer slope and at dike crest, the cover layer is still working	
Phase 4: Crest shortening	**Breach widening Phases 4, 5, 6a** a) Rectangular section b) Scour erosion c) Mass instability	**Simulated process**: erosion of sand core and breach formation *Flow*: transition between wave overtopping and combined flow and between combined flow and overflow *Breach morphology*: vertical slopes (rectangular shape) *Erosion*: sediment transport capacity and sediment mass conservation (vertical and lateral erosion) *Mass instability*: simplified instability analysis *Leading parameters*: energy slope (J), sediment transport discharge (Q_{ST})
Phase 5: Dike lowering		
Phase 6: Full and final breach	**Phase 6b** a) Trapezoidal section	**Simulated process (phases 6)**: breach widening up to the equilibrium final breach *Flow*: transitional and non-transitional flow *Breach morphology*: final non vertical slopes (trapezoidal shape) *Erosion and mass instability* as in Phase 4 and 5.

FIGURE 2.2: Breaching of sea dikes initiated by wave overtopping: modelling phases and simulated processes as indicated by D'Eliso [11]

2.1.2 Phase 1: Initial failure of grass sod

The initial failure process of the grass cover layer on a land-side slope is described in many researched. Almost every research on initial grass cover failure describes the process slightly different. Roughly four different failure mechanisms are distinguished from the literature which are described by D'Eliso [11], Stanczak [12, 28, 29], Hoffmans [14, 15] and Trung & Verhagen [31].

Wave impact on the land-side slope forces any present cracks in the sod to enlarge, which leads to the failure process as illustrated later on in this thesis, in Figures 7.3a to 7.3f. Figure 2.3, from a report written by the Technical Advisory Committee on Water Retaining Structures in The Netherlands [30], shows the presence of the cracks in clay and grass cover layers. The picture shows a cross-section of a typical sea-dike cover made of clay with vegetation. Crack formation in the soil creates aggregates of various dimensions. The composition of the cracks and aggregates, together with pores and aggregates made by burrowing animals, is called the 'soil structure' [30]. The formation of soil structure depends both on properties of the clay, as well as on the external factors that determine changes in suction pressure. Burrowing animals such as mice and moles, and grass roots cause the dynamic of soil structure - new aggregates are being formed and then collapse again continuously. The strongly developed soil structure occurs when soil is subjected to continuous expanding and shrinkage of the clay due to natural processes. This kind of development is characterized by the aggregates that are clearly individually recognizable and that show few connections with each other. An other type (i.e. fine structure) occurs due to rapid changes in water content, e.g., due to rainfall. According to information given by TAW (1996) [30], in the uppermost decimeters under the grass cover the soil structure is usually strongly developed and consists of relatively small (i.e. millimetres to centimetres) aggregates that are often linked to each other by roots [29].

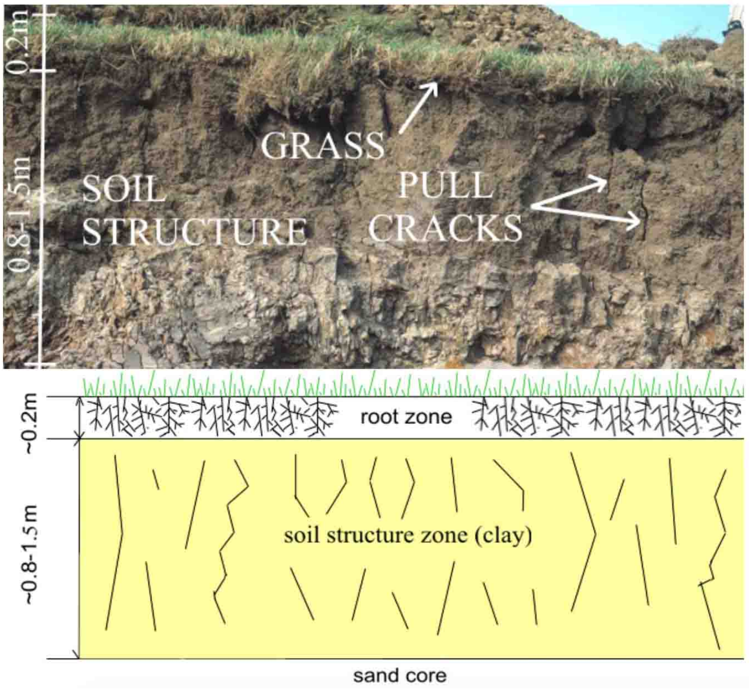

FIGURE 2.3: Cracks in grass and clay cover layer, picture from TAW 1996 report [30]

A. Valk describes in her MSc. thesis further how cracks in the grass and clay cover develop under influence of multiple impact events as follows:

> After several impacts, the entrance wall of the crack starts to erode. At the same time, the crack width is getting wider and the block walls of the clay in both side of the crack are lifted (Figure 2.4a) After being hit several times by the impacts, cracks were observed inside the water-filled crack walls. At the same time, at the surface, next to the water-filled crack, horizontal cracks are also observed as the reaction against the repeatedly impact pressures (Figure 2.4b). Furthermore, the cracks formation along the crack wall and at the surface becomes the weak points where the blocks of soil are finally removed (Figure 2.4c).

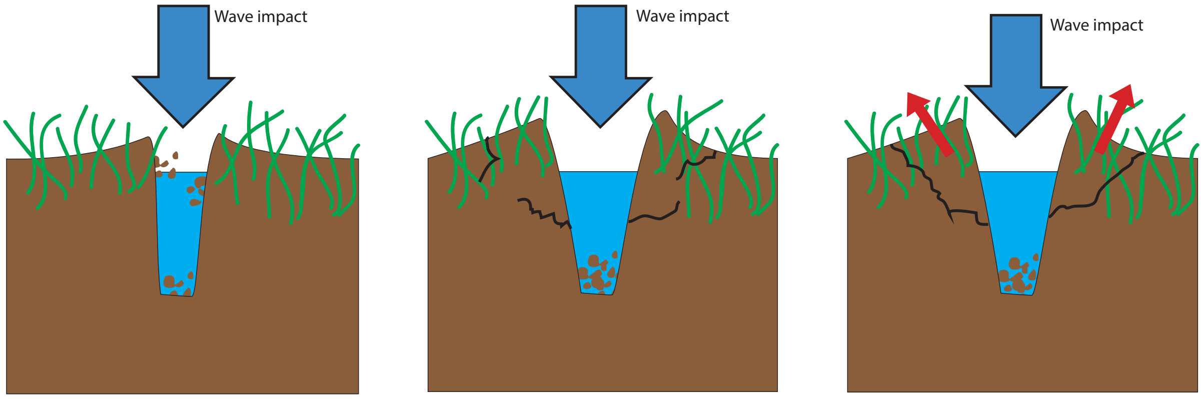

(A) (B) (C)

FIGURE 2.4: Erosion of grass or clay cover described by A. Valk [32].

D'Eliso theory

According to D'Eliso [11] the grass cover layer fails due to gradual erosion, mostly as a particle detachment due to flow-induced shear stress on clay soil. This is described in Phase 1 in section C.1.1. In his models D'Eliso assumed that breach initiation is detected along the land-side slope assuming weak sections. Failure starts at a randomly located section at the inner slope. Field tests have shown that the erosion at the dike crest is much lower than at the inner slope and therefore assumed negligible [11]. D'Eliso recommends to use a permissible tractive force based model for the effective shear stress on the grass cover layer since this is the only approach that directly includes the effects of wave overtopping flow.

Stanczak and Führbötter theory

Stanczak [28, 29] did experimental research on the impact required for the development of cracks in clay and grass cover layers. Stanczak based his research on Führbötter [12] who stated in 1966:

> If a water-filled crack of depth a and length L (the width of the crack is not involved in the calculation) is subject to an impact pressure pmax then the pressure is instantly

> (speed of sound in water C = 1485 m/s = speed of pressure propagation) transferred in the full magnitude to the two side walls of the crack.

Using this principle, and the assumption the weight of the soil is negligibly small, the forces on the walls of the crack are determined. These forces are absorbed by the compression and the shear strength of the soil behind the walls of the crack. This leads to $p_{\max} = 2c$ as the critical impact pressure, i.e. the shear failure occurs for impact pressures $p_{\max}$ greater or equal to the double of cohesion $2c$.

The critical impact pressure $P_{\max} = 2c$ as found by Führbötter has never been proven experimentally by Stanczak. However, this was due to limitations of the formation of the experiments. Therefore the theory has never been rejected as well. The calculations done by Führbötter are purely physical based. Although the theory includes some assumptions that to thus far have never been proven to be valid, Führbötter's critical impact pressure of $P_{\max} = 2c$ is proposed as a possible explanation for the critical pressure required to cause aggregate movement.

Hoffmans theory

Hoffmans at al. [15] researched the required pressure to lift a grass-clay aggregate from the cover layer. Hoffmans et al. developed a formula to describe the required pressure according to the turf-element model. An overtopping wave develops both an impact force induced compressive stress as well as a shear stress on the grass sod causing clumps of grass sod to be pulled out of the cover layer. Interesting to notice is that the stems of the grass were all more or less intact when a clump was pulled out. This indicates a failure process due to failure of clusters of roots pulled out of the clay cover and not failure of individual stems of grass. Hoffmans et al. [15] extensively researched this failure process and defined the failure of a grass-clay aggregate as:

$$F_p \geqslant F_w + \Sigma F_s + \Sigma F_c + F_g \tag{2.1}$$

In which F_p is the load of an overtopping wave, F_w the weight of the overflowing water, ΣF_s the sum of the shear forces, ΣF_c the sum of cohesion forces and F_g the grass force. The acting forces on a clay aggregate are demonstrated in Figure 2.5.

A relation for the minimum required pressure for soil failure is derived from Equation 2.1:

$$p \geqslant (1 + 2f)(\rho_s - \rho)gd + 5c_s + \sigma_g \tag{2.2}$$

If the shear and cohesion forces on the clay aggregate do not act on the four sidewalls, so if the clay aggregate is only fixed at the bottom, there is only cohesion at the bottom. The shear stresses on the walls reduce to zero and the cohesion decreases therefore decreases:

$$p \geqslant (\rho_s - \rho)gd + c_s + \sigma_g \tag{2.3}$$

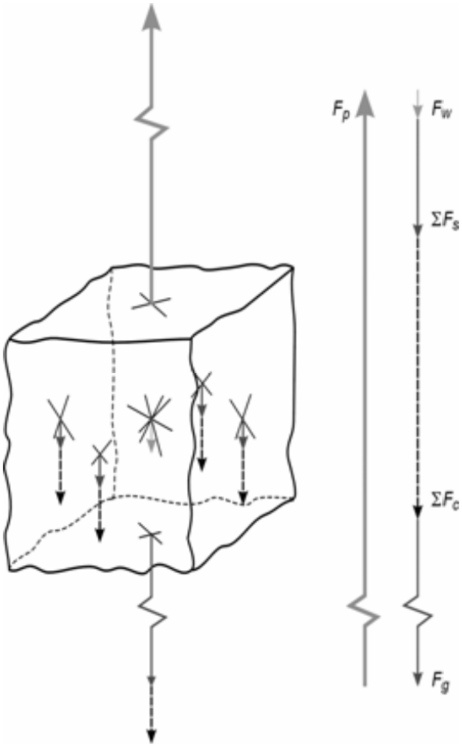

FIGURE 2.5: Forces acting on a clay aggregate, picture from a paper by Hoffmans et al. [15]

.

Here p is the pressure fluctuation caused by an overtopping wave or overflow, f a friction factor, ρ_s the density of soil, ρ the density of overtopping water, d the representative aggregate diameter, c_s the cohesion of soil and σ_g is the normal grass strength, given as:

$$\sigma_g = t_r \frac{A_r}{A} cos\ \theta_s \tag{2.4}$$

Here t_r is the root tensile stress, A_r/A the root area ratio (RAR) and θ_s is defined as the angle of shear deformation. The critical condition for lifting the grass-clay aggregate is reached if $p = P_{\max}$ and if the mean bed shear stress τ_0 equals the critical bed shear stress τ_c. Since pressure peaks can reach up to $p_{\max} = 18\tau_0$, this leads to:

$$\tau_c = \alpha_\tau((\rho_s - \rho)gd + c_s + \sigma_g) \qquad \alpha_\tau = \frac{1}{18} \tag{2.5}$$

Trung and Verhagen theory

Le Hai Trung [31] described in a paper about the failure processes of grass covered slopes due to overtopping the process of 'roll up' damage. Trung describes the findings of similar overtopping experiments as Wijmeers-II, only this time in Friesland in The Netherlands. This roll up process, in which the grass cover basically rolls up like a carpet, is a failure process that has been documented multiple times during the Wijmeers-II experiments.

2.1.3 Phase 2: Clay cover failure

Erosion of the clay layer occurs as soon as the grass layer has failed. Clay cover erosion can roughly be divided into two phases [11]

- a. *Local clay erosion*, phase 2 of figure C.1 and C.2. Key parameters of the selected model to calculate the vertical erosion depth (dz) are the erodibility coefficient (k_d) and the critical shear stress ($\tau_{0,cr}$).
- b1. *Headcut erosion*, for extended explanation see Appendix C, phase 3a of figure C.1 and C.2. Calculation of the vertical depth (dz) and the headcut advance (dZ). Important parameters are the initial headcut height ($H_{H,0}$) and the erodibility coefficient (K_h).
- b2. *Clay cover failure*, phase 3b of figure C.1 and C.2, initial breach channel height ($H_{b,0}$) and width ($B_{b,0}$)

Phases 3, 4, 5 and 6 in the breaching process are out of the scope of this research subsequently they are not further described in this chapter. For a brief description of the breaching process after initial failure occurred, reference is made to Appendix C.

2.2 Wave overtopping on a dike

The flow velocity, water depth, discharge and volume of overtopping waves over a dike are determined from the wave run-up height on the water side slope. In the next sections the calculation of these parameters is further explained.

2.2.1 Wave run-up height

Wave overtopping on a dike is amongst others determined by the wave run-up height, which is an important boundary condition in wave overtopping. Lots of research on wave run-up height and wave overtopping is done by Schüttrumpf and Van Gent [26]. The wave run-up height is described by $R_{u,2\%}$ for design purposes. $R_{u,2\%}$ is exceeded by 2% of the incoming waves. In the Dutch and European standards, respectively the TAW2002 [34] and EurOtop manual [23] the 2% wave run-up is defined as:

$$\frac{R_{2\%}}{H_s} = \min\left(1.65\gamma_b\gamma_f\gamma_\beta\xi_0\left(4.0 - \frac{1.5}{\sqrt{\xi_0}}\right)\right) \tag{2.6}$$

Battjes [7] showed that for deep fore-shores the wave run-up for relatively smooth slopes is Rayleigh distributed. Van Damme [33] fitted the Rayleigh distribution against wave run-up for several exceedance probabilities to determine how scale parameters change for different exceedance probabilities. This led to an arbitrary description of wave run-up [33].

For $\xi_0 \leq 1.8$:

$$R_{n\%} = \gamma_b \gamma_f \gamma_\beta \xi_0 H_s 0.93(-ln(P))^{1/2} \tag{2.7}$$

For $\xi_0 > 1.8$:

$$R_{n\%} = \gamma_f \gamma \beta \frac{H_s}{1.65}\left(4.0 - \frac{1.5}{\sqrt{\xi_0}}\right) 0.93(-ln(P))^{1/2} \tag{2.8}$$

in which: $R_{2\%}$ = Run-up height $[m]$
$\gamma_b, \gamma_f, \gamma_\beta$ = Factors for respectively: the effect of the berm, roughness on the slope and angle of incipient wave attack
H_s = Significant wave height $[m]$
ξ_0 = Breaker parameter
P = Probability of exceedance

2.2.2 Wave run-up velocity

Since kinetic energy is transferred into potential energy during a wave run-up, the wave run-up distance depends on the wave run-up velocity of the front of the wave. This is also described as the peak velocity of the wave during a run-up event [25]. In the EurOtop manual [23] the relation for wave run-up velocity is described as follows.

$$\frac{u_{n\%}}{c_{u,n\%}\sqrt{gH_s}} = \sqrt{\frac{R_{n\%} - z}{H_s}} \tag{2.9}$$

in which: z = An arbitrary height above the slope below $R_{n\%}$ $[m]$
$c_{u,n\%}$ = Parameter indicating the loss in energy.

The decrease in velocity during a wave was described by Hughes [18]. In this equation T_0 is the total overtopping time per wave, t is a time step between $[0, T_0]$ and a is a calibration parameter.

$$u(t) = u_{\max}\left(1 - \frac{t}{T_0}\right)^a \tag{2.10}$$

2.2.3 Wave run-up depth

In the EurOtop manual the normalized maximum wave run-up depth is described by

$$\frac{d_{n\%}(x_*)}{H_s}\frac{\tan\alpha}{c_{d,n\%}} = \frac{R_{n\%} - z}{H_s} \tag{2.11}$$

Here $d_{n\%}(x_*)$ is defined as the normalized maximum wave run-up depth. $c_{d,n\%}$ was found to vary according to the overtopping probabilities. Hughes [18] discovered that the depth decreases linearly over time per wave cycle and described this with equation 2.12. Hughes found that for $b = 1$ a reasonable approximation could be obtained.

$$d(t) = d_{\max}\left(1 - \frac{t}{T_0}\right)^b \tag{2.12}$$

2.2.4 Wave Run-up discharge

The 2% wave run-up discharge is described by Van Gent [38] and included in Van Damme's report [33].

$$\frac{q_{p,n\%}}{c_{q,n\%}\sqrt{gH_s^3}} = \left(\frac{R_{n\%} - z}{H_s}\right)^{1.5} \tag{2.13}$$

For $n = 2$ Van Gent found $c_{q,n\%} = 0.2$ which is apparently a close approximation of $c_{d,2\%} \cdot c_{u,2\%}$. Therefore it is assumed that $q_n\% = c_{d,2\%} \cdot c_{u,2\%}$. This relation indicates the strong relation between overtopping velocity and overtopping depth, with the side note that $q_{n\%}$ is the maximum discharge of the wave front. This led to the following equation:

$$q(t) = q_p\left(1 - \frac{t}{T_0}\right)^{a+b} \tag{2.14}$$

The volume of water per wave follows from the integration of 2.14 with respect to time from $t = 0$ to $t = T_0$ [18], leading to:

$$V^{1.16} = 0.43 q_p T_0 \tag{2.15}$$

The normalized relation for wave overtopping volumes was also given by Van Gent [38].

$$\frac{V_{n\%}}{H_s^2} = \left(\frac{R_{n\%} - z}{H_s}\right)^2 \tag{2.16}$$

Combining relation 2.15 and 2.16 leads to an expression for the factors a and b:

$$a + b = 2.33V^{0.16} - 1 \tag{2.17}$$

For an assumed linear decrease in water depth, $b = 1$, this leads to:

$$a = 2.33V^{0.16} - 2 \tag{2.18}$$

2.3 Overtopping shear stress

The peak overtopping shear stress can be determined based on the peak overtopping velocity. Therefore it is assumed that the main velocity component is parallel to the embankment surface and that the impact of other mean velocity components are negligible small in comparison [33]. Firstly the bed shear stress is defined as:

$$\tau = \frac{\rho_w v^2 n^2}{d^{1/3}} \tag{2.19}$$

in which: ρ_w = Density of the water
v = Mean veocity component parallel to the embankment surface
n = Manning coefficient $[s/m^{1/3}]$
d = Hydraulic radius

Then the peak shear can be expressed as follows:

$$\frac{\tau_{n\%}}{\rho_w n^2 H_s^{2/3} (\tan\alpha)^{1/3} c_{\tau,n\%}} = \left(\frac{R_{n\%} - z}{H_s}\right)^{2/3} \tag{2.20}$$

In this relation $c_{\tau,n\%} \approx \frac{c_{u,n\%}^2}{c_{d,n\%}^{1/3}}$

In order to find an expression for the surplus shear stress it is necessary to express the bed shear stress as a function of time [33]:

$$\tau(t) = \tau_p \left(1 - \frac{1}{T_o}\right)^s \tag{2.21}$$

Where the power s is given by:

$$s = \min\left(\max\left((4.66V^{1.16} - 4.33), \frac{5}{3}\right), \frac{10}{3}\right) \tag{2.22}$$

When all the expressions for the normalized run-up are combined, T_0 can be expressed in terms of the peak shear stress, leading to [33]

$$T_0 = \frac{\tau_p^{1.23} (\tan\alpha)^{0.59}}{\rho_w^{1.23} n^{2.46} g^{2.96} 0.43 c_{\tau,n\%}^{1.23} c_q} \tag{2.23}$$

In this relation τ_p is defined as the shear stress at the intersection of the waterside slope.

The change in shear stress due to an overtopping wave is expressed in the following relation of τ with respect to time:

$$\tau(\hat{x},t) = \tau_p(\hat{x})\left(1-\frac{t}{T_0}\right)^m \tag{2.24}$$

For the purpose of failure analysis it is important to determine when the shear stress exceeds the critical shear stress. This is expressed in the following relation:

$$t_1(\hat{x}) = -T_0\left(\frac{\tau_c}{\tau_p}\right)^{1/m} + T_0 \tag{2.25}$$

Here the power m is a function of the location along the embankment parameter, therefore also t_1 is a function of time. The amount of eroded material follows from integrating the shear stress from $t=0$ to $t=t_1$:

$$\int_{t=0}^{t=t_1} \tau(\hat{x},t)dt = -\frac{T_0}{m+1}\tau_p(\hat{x})\left(\frac{\tau_c}{\tau_p(\hat{x})}\right)^{1+1/m} + \tau_c T_0\left(\frac{\tau_c}{\tau_p(\hat{x})}\right)^{1/m} - \tau_c T_0 + \frac{T_0}{m+1}\tau_p(\hat{x}) \tag{2.26}$$

For the expressions for $a+b$ and m see Van Damme's report page 12.

Shear stress as a function of location is determined by Van Damme [33]. As the depth increases along the landslide slope the maximum values for the shear stress increase according to:

$$\tau(\hat{x}) = \left(\frac{\tilde{d}_{ot}}{d(\hat{x})}\right)^{7/3}\tau_p \tag{2.27}$$

$$d_{ot} = \frac{\tau_p}{\rho_w^{1.5} n^3 g^3 (\tan\alpha)^{1.5} c_{\tau,n\%}^{1.5}} \tag{2.28}$$

2.3.1 Dike crest

The overtopping flow on a dike crest is described by two parameters: overtopping velocity and layer thickness. The equation for the overtopping velocities was determined analytically by Schüttrumpf and Van Gent [26].

$$\frac{u_{c,2\%}}{u_{A,2\%}(R_C)} = \exp\left(-c_{c,u}^{*}\frac{x_c * f}{h_{c,2\%}}\right) \tag{2.29}$$

The equation for layer thickness was determined empirically.

$$\frac{h_{c,2\%}}{u_{A,2\%}(R_C)} = \exp\left(-c_{c,h}^{*}\frac{x_c}{B}\right) \tag{2.30}$$

in which: $u_{c,2\%}$ = Run-up velocity on the crest, exceeded by 2% of the waves $[m/s]$
$u_{A,2\%}$ = Run-up velocity on the sea-side, exceeded by 2% of the waves $[m/s]$
R_C = Freeboard $[m]$
$c^*_{c,u}$ = Empirical coefficient
x_c = Position on the dike crest with respect to the beginning of the dike crest $[m]$
f = Friction coefficient
$h_{c,2\%}$ = Layer thickness on the crest, exceeded by 2% of the waves $[m]$
$c^*_{c,h}$ = Empirical coefficient
B = Crest width $[m]$

In Table 2.1 the different empirical coefficients as determined by Schüttrumpf and Van Gent in 2002 are presented.

TABLE 2.1: Empirical coefficients as determined by Schüttrumpf and Van Gent.

	Schüttrumpf (2002)	Van Gent (2002)
Wave overtopping velocity $c^*_{c,h}$	0,5	0,5
Layer thickness $c^*_{c,u}$	0,89	0,4

2.3.2 Landward side

Overtopping flow on the landward side of the dike depends on the layer thickness and overtopping velocity at the end of the dike crest, the gradient of the landward side and the roughness of the surface [26]. Both Schüttrumpf and Van Gent derived a formula to determine the flow velocity and layer thickness at the inner slope of the dike. The Van Gent formula is:

$$u_{B,2\%} = \frac{k_2}{k_3} + k_4 \cdot \exp(-3k_2k_3^2 s_B) \tag{2.31}$$

With:

$$k_2 = \sqrt[3]{g \sin\theta} \tag{2.32}$$

$$k_3 = \sqrt[3]{\frac{1}{2}\frac{f}{h_{0,2\%}u_{0,2\%}}} \tag{2.33}$$

$$k_4 = u_{0,2\%} - \frac{k_2}{k_3} \tag{2.34}$$

in which: θ = Angle of the landward slope
$h_{0,2\%}$ = Layer thickness at the land-side end of the crest $[m]$
$u_{0,2\%}$ = Flow velocity at the land-side end of the crest $[m/s]$
s_B = Landward slope distance from the end of the crest $(\rightarrow \infty)$ $[m]$

2.3.3 Levee side velocity

In the article by Dean et al. [10] the land-side velocity of dikes is also investigated. The article is written in response to hurricane Cathrina in New Orleans.

A backwater curve as used in hydraulics is used to determine whether or not water velocities will approximately reach their terminal velocity while on the levee slope. The terminal velocity is given by

$$u_\infty = \sqrt{\frac{8gh\sin(\alpha)}{f}} \tag{2.35}$$

or

$$u_\infty = \left(\frac{8gq\sin(\alpha)}{f}\right)^{1/3} \tag{2.36}$$

The critical velocity on a levee depend on the critical slope α_c. This critical slope is determined by

$$\alpha_c = \sin^{-1}\left(\frac{f}{8}\right) \tag{2.37}$$

With f the Weisbach-Darcy coefficient. For $f = 0,08$ the critical slope $\tan\alpha_c = 0,01$. Since most levees have a slope between 0,1 and 0,2 all terminal velocities down the land-side slope will be supercritical although it is possible that the overtopping velocities at the levee crest will exceed terminal velocities in which case the velocities will decrease with distance down the landside slope.

According to Dean et al. it is suitable to base erosion on the terminal velocity although this is somewhat conservative.

2.4 Excess volume approximation

In order to compare the impact of wave overtopping and overflow on the land-side slope of a dike, a model is developed by Hughes [17] which is based on models developed by Dean et al. [10]. The model as developed by Dean et al. describes the damage on the land-side slope based on the time a certain threshold flow velocity is exceeded times the amount of exceedance. Hughes extended this model by eliminating some conservative assumptions and eventually described the acceptable amount of erosion as the summation of the excess wave volume above a certain threshold of each individual wave. The excess volume is described as the integral of the overtopping discharge above a certain threshold.

2.4.1 Excess volume approximation on wave overtopping

Dean, et al. (2010) assumed that the land-side slope of a dike should be resistant against stream power above the threshold limit done by an overtopping for a certain time. Acceptable erosion occurs on the land-side slope until such time the cumulative excess work exceeds the grass-damage threshold. Thus, for every overtopping wave in which the flow velocity is greater than the critical velocity, there will be a contribution to the accumulated total stream power. Dean, et al. proposed the following equation for assessing the tolerable limit of cumulative excess stream power for overtopping waves.

$$\sum_{n=1}^{N}(u^3 - u_{c,W}^3)\Delta t_n \leqslant \frac{E_W}{K_W \cdot \beta_W} \tag{2.38}$$

Where the right-hand side of the equation is a measure for acceptable erosion on the land-side slope. N is the amount of overtopping events and Δt_n the overtopping wave duration. Equation 2.38 can be rewritten to an equation where overtopping discharge and a discharge threshold determine the excess volume of water. This can only be done under the (conservative) assumption that the overtopping flow reaches its terminal velocity.

$$\sum_{n=1}^{N}\left(\left(\frac{2g \cdot \sin\theta}{f_F}\right) q_n - u_{c,W}^3\right)\Delta t_n \leqslant \frac{E_W}{K_W \cdot \beta_W} \qquad \text{for } q_n < \left(\frac{f_F u_c^3}{2g \cdot \sin\theta}\right) \tag{2.39}$$

Or

$$V_{ET}(t) = \sum_{n=1}^{N}(q_n - q_c)\Delta t_n \leqslant \frac{E_W}{K_W \cdot \beta_W}\left(\frac{f_F}{2g \cdot \sin\theta}\right) \qquad \text{for } q_n < q_c \tag{2.40}$$

Where:

$$q_c = \left(\frac{f_f u_c^3}{2g \cdot \sin\theta}\right) \tag{2.41}$$

θ is in this case the slope angle of the land-side slope and f_F is the Fanning friction coefficient. For grass covered slopes the Fanning coefficient lies somewhere between $f_F = 0.01$ and 0.10. Multiple studies have been done on the correct value for the Fanning coefficient which all recommend different values. Hewlett et al. [13] studied the friction coefficient on slopes steeper than 1:3. This study recommended the use of a Manning coefficient $n_m = 0.02$, which can be related to the Chézy coefficient C_z using the hydraulic radius R. The Chézy coefficient can be related to the Fanning coefficient, as demonstrated in equation 2.42.

$$C_z = \frac{R^{1/6}}{n_m} \qquad\qquad C_z = \sqrt{\frac{2g}{f_F}} \tag{2.42}$$

leading to

$$f_F = \frac{2g \cdot n_m^2}{h^{1/3}} \tag{2.43}$$

Where h is the water depth of the overtopping wave. flow thicknesses over the land-side slope of 0.05 m, 0.15 m, 0.3 m, and 0.6 m have friction factors of $f_F = 0.021$, 0.015, 0.012, and 0.009, respectively. In the Wijmeers II experiments water depths between 0.05 and 0.3 m have been measured. Therefore, it seems reasonable as an initial assumption to use a friction factor in the range of f_F = 0.01 - 0.02 as a representative average for overtopped grass-covered land-side slopes. The above estimates assume the Manning coefficient n remains constant for different flow thickness, this is a somewhat conservative assumption since it might not be true in some cases.

Hughes [17, 18] described the excess volume of an individual wave by integrating the left-hand side of Equation 2.40 in time. Therefore the peak discharge q_p and overtopping time T_o of each individual overtopping wave are considered. These parameters are calculated from the wave volume V:

$$q_p = 0.184\ \sqrt{g}\ V^{3/4} \tag{2.44}$$

$$T_o = \frac{V^{1.16}}{0.43\ q_p} \tag{2.45}$$

With q_p the peak discharge. The change in discharge with time $q(t)$ is a combination of the relations that describe the change in flow velocity $u(t)$ and water depth $d(t)$ with time.

$$u(t) = u_p(1 - \frac{t}{T_o})^a \tag{2.46}$$

$$d(t) = d_p(1 - \frac{t}{T_o})^b \tag{2.47}$$

In which u_p is the peak velocity and d_p the peak water depth. When exponents a and b are unity, the decreases in flow thickness and velocity are linear (which turns out to be a reasonable assumption) [17]. A combination of Equation 2.46 and 2.47 leads to an expression for $q(t)$, where the power m is described by: $m\ =\ a + b$.

$$q(t) = q_p(1 - \frac{t}{T_o})^m \tag{2.48}$$

Which eventually leads to an expression for the excess wave volume V_E:

$$V_E = V_W \left[1 - (m+1)\left(\frac{q_c}{q_p}\right) + m\left(\frac{q_c}{q_p}\right)^{\frac{m+1}{m}}\right] \qquad for\ q_p > q_c \tag{2.49}$$

With q_p the peak discharge, q_c the critical discharge and V_W the overtopping wave volume. When the overtopping velocity and water depth are assumed to decrease linearly both factors a and b in Equation 2.46 and 2.47 would be 1, since $m = a + b$, this automatically means $m = 2$. Assuming both parameters decrease quadratically ($a = 2$ and $b = 2$) results in $m = 4$. Varying exponent m between 2 and 4 has only a minor effect, as demonstrated by Hughes [17]. Therefore, it would be reasonable and practical to set the exponent to m = 2 to simplify the application of Dean, et al.'s methodology to the HSDRRS levees [10]. This gives a slightly larger estimate of excess wave volume, so it would be a bit conservative. Setting m = 2 leads to:

$$V_E = V_W \left[1 - 3\left(\frac{q_c}{q_p}\right) + 2\left(\frac{q_c}{q_p}\right)^{\frac{3}{2}}\right] \qquad for\ q_p > q_c \tag{2.50}$$

Integrating Equation 2.48 in time gives an expression for overtopping wave volume related to q_p, T_o and m. This relation can be implemented in Equation 2.50.

$$V_W = \frac{q_p \cdot T_o}{m+1} \ \Rightarrow\ q_p = \frac{V_W \cdot (m+1)}{T_o} \tag{2.51}$$

Implementing in Equation 2.50:

$$V_{ET}(t) = \sum_{n=1}^{N} V_{W,n} \left[1 - \left(\frac{q_c T_{o,n}}{V_{W,n}}\right) + \frac{2}{3^{3/2}}\left(\frac{q_c T_{o,n}}{V_{W,n}}\right)^{3/2}\right] \leqslant \frac{E_W}{K_W \cdot \beta_W}\left(\frac{f_F}{2g \cdot \sin\theta}\right) \tag{2.52}$$

Where

$$q_c = \frac{f_F \cdot u_c^3}{2g \cdot \sin\theta} \tag{2.53}$$

$V_{W,n}$ and $T_{o,n}$ are, respectively, the total volume and overtopping time of the nth individual overtopping wave. The parameters u_c and $E_W/(K_W \beta_W)$ are constants related to the specific land-side slope dike cover.

2.4.2 Excess volume approximation on steady overflow

In his report Hughes [17] states:

"*A necessary assumption for equating steady overflow work to intermittent wave overtopping work is that erosion and subsequent slope damage is due to accumulated excess flow work on the slope. Furthermore, it must be assumed that the excess flow work is driving essentially the same erosion mechanism for the two cases. If, however, slope damage from overtopping waves is the result of strong impacts and perhaps high turbulence caused by the larger waves, the equivalence becomes more uncertain.*"

Due to lack of data Hughes was not able to verify his Excess volume approximation for steady overflow. While for wave overtopping approximation, as described in Section 2.4.1, there was some data on overtopping waves available is the steady overflow approximation purely theoretical.

Since we are dealing with a constant overflow discharge the excess volume in this case can quite easily be described by:

$$V_{ET}(t) = (q - q_c)t \ \leqslant \ \frac{E_W}{K_W \cdot \beta_W}\left(\frac{f_F}{2g \cdot \sin\theta}\right) \qquad \text{with } q > q_c \tag{2.54}$$

Where

$$q_c = \frac{f_F \cdot u_c^3}{2g \cdot \sin\theta} \tag{2.55}$$

And

$$q = \frac{f_F \cdot u^3}{2g \cdot \sin\theta} \qquad\qquad u = \left[\left(\frac{2g \cdot \sin\theta}{f_F}\right) q\right]^{1/3} \tag{2.56}$$

3 | Experimental set-up

This chapter gives an overview of the breach initiation experiments as performed by Infram, Flanders Hydraulics Research and Delft University of Technology at the Wijmeers-II polder in Belgium. The experiments consisted of a study to failure initiation due to overflow and wave overtopping on the inner slope of a dike, between the 2nd and the 18th of November 2015. These studies compared the outcomes of multiple wave overtopping and overflow tests.

The aim of the experiment was to gain insight in the processes leading to failure initiation of a dike with a grass and clay cover under wave overtopping and overflow conditions. The flow velocity, water depth and saturation of the top layer were monitored during the overtopping and overflow experiments. This experiment is unique as it facilitates the comparison of the effect of the peak load from overtopping waves with the constant load during overflow.

3.1 Overtopping simulator

The overtopping experiments were executed with the wave overtopping simulator as designed by Van der Meer Consulting and Van der Meer Innovation [34]. Overtopping waves are simulated by the controlled release of volumes of water from the simulator. The release of water is controlled by valves at the bottom of the reservoir of the simulator. The simulator was placed on a frame on the river side slope of the dike. A pump was placed in the river and connected to the simulator through multiple pipelines, which supplied water to the simulator. Both the simulator and the pump are presented in Figure 3.1.

3.2 Overflow simulator

In collaboration with the technical support staff at the hydraulic laboratory of the faculty of civil engineering at Delft University of Technology, the overflow simulator was designed to simulate flood levels in the river Scheldt corresponding with the overtopping discharges tested. Water was pumped from the river Scheldt and led through an overflow simulator, which distributes the water equally over a 2 meter wide dike section. The amount of overflow was controlled using a frequencially adjustable pump. The pump frequency was constantly adjusted to compensate the change in pump head due to tidal changes in the river Scheldt. At the inner slope water levels and flow velocities were measured. Water flowed over the dike until severe damage of the top layer occurs.

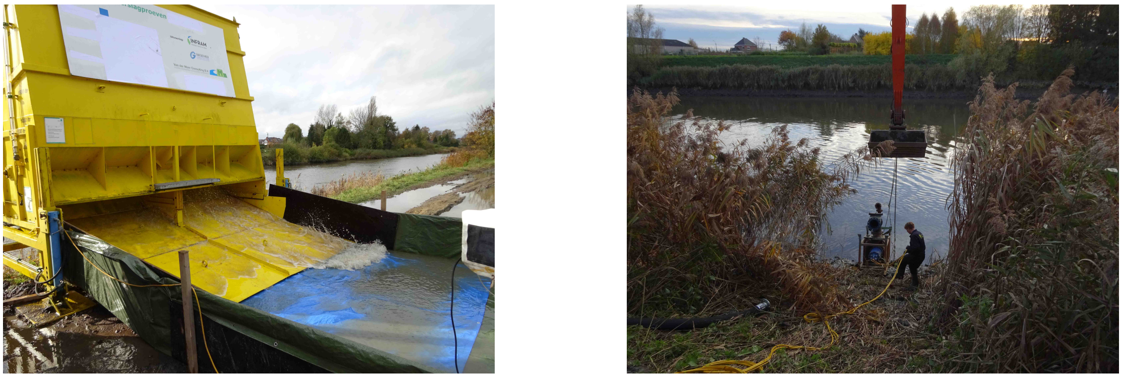

(A) Overtopping simulator (B) Pump placed deep into the river water during low tide

FIGURE 3.1: A pump was connected to the overtopping simulator through multiple pipelines. The pump was placed deep into the river water.

The simulator consists of a water tank with one lowered side (see Figure 3.2). The water tank is placed on the river side slope of the dike. Water flows over the edge of the lowered side and is guided through an open duct towards the crest of the dike. The water tank was designed to fit in the supporting frame of the overtopping simulator. The highly turbulent inflowing water was converted into a smooth flow in the overflow simulator. This was achieved by guiding water through a compartment with holes in the walls and ceiling which served as a energy dissipation chamber, see Figure 3.3. The hose of the pump was mounted as low as possible at the back of the reservoir. The outflow is relatively smooth and simulates extreme water levels in the river Scheldt well. The outflow of the simulator is demonstrated in Figure 3.4.

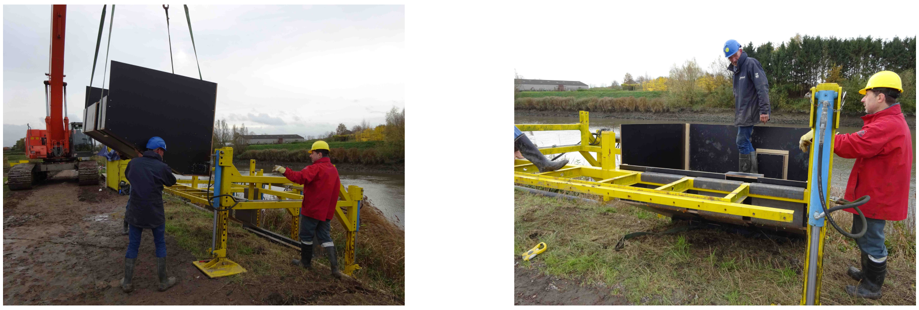

(A) Simulator reservoir (B) Mounted in frame

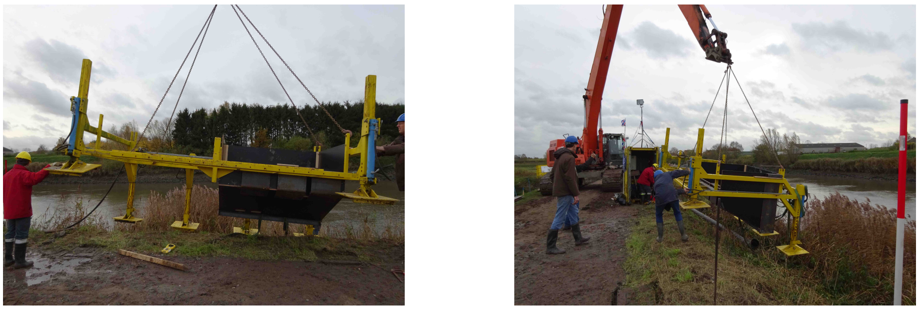

(C) Reservoir is supported by a steel frame (D) Simulator fits perfectly in frame

FIGURE 3.2: Overflow simulator

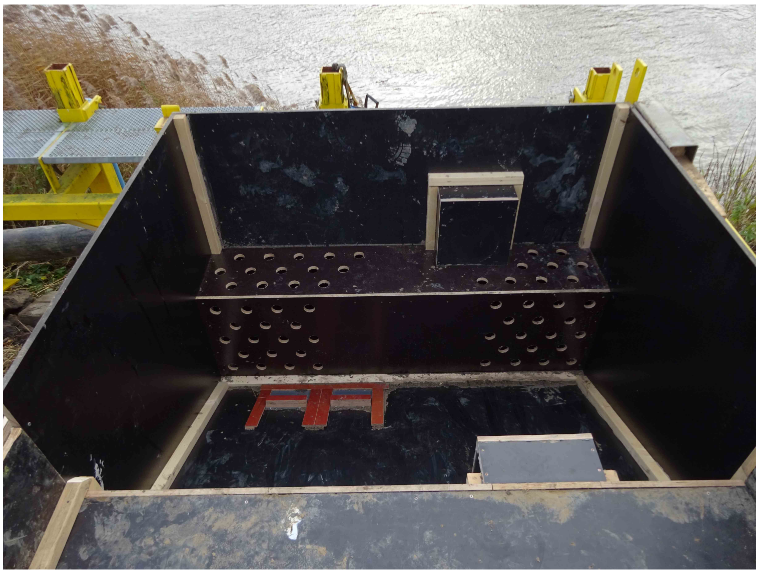

Figure 3.3: Interior of the overflow simulator

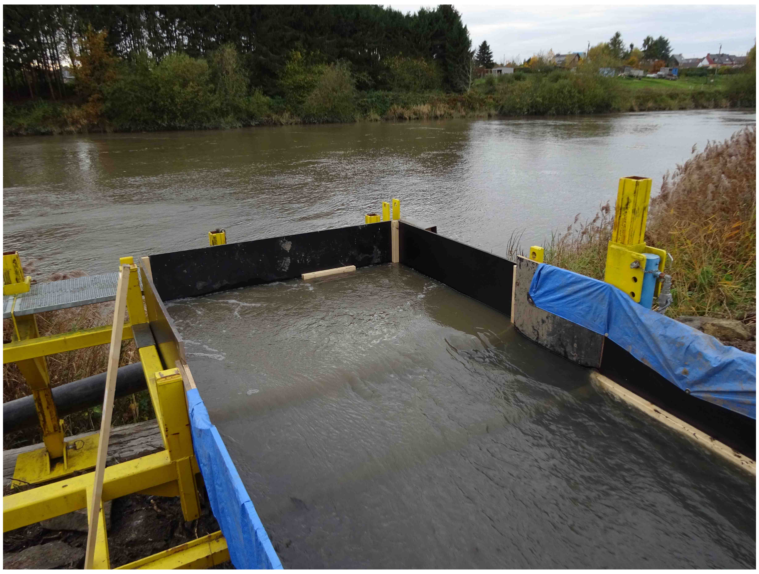

Figure 3.4: Outflow of the overflow simulator

3.3 Test sections

In total approximately 100 m of dike was available for testing. The dike section was divided into four sections of which two sections were reserved for overtopping experiments and two sections for overflow experiments. In Figure 3.5 the division of the test sections over the dike is illustrated. The test sections for the wave overtopping experiments were 4 m wide and the test sections for the overflow experiments were 2 m wide. On each test section a grid was printed of 1x1 m in order to indicate in which part of the test section damage would occur. The 0-line of the grid coincided with the end of the overflow/overtopping simulator. This is indicated in Figure 3.6.

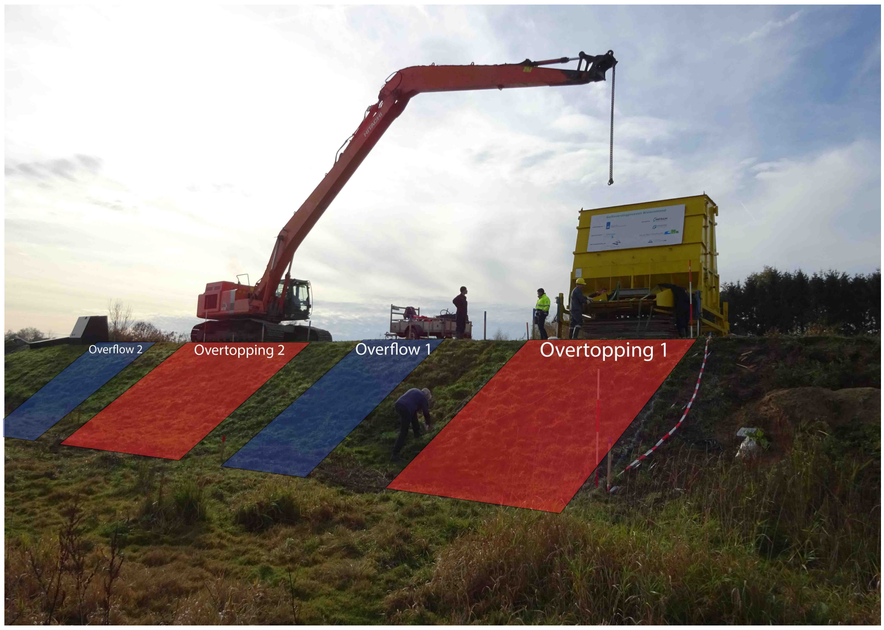
Overflow 2
Overtopping 2
Overflow 1
Overtopping 1

FIGURE 3.5: Division of the test sections over the dike

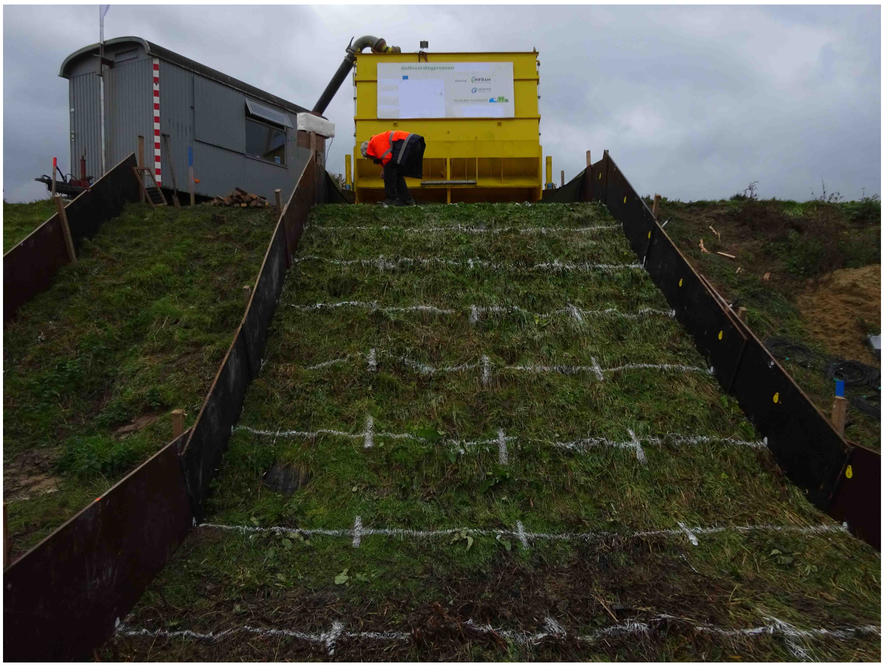

FIGURE 3.6: Test section for the first overtopping experiment.

3.4 Description of experiments

The experiments were executed by running both simulators for two hours at a specified discharge. After two hours the damage on the dike was analyzed. If no significant damage had occurred to the dike, another test was performed for 2 hours at a higher flow rate. Since the overtopping experiments were executed at an average wave overtopping volume of 1, 5, 10 and 25 $\mathrm{lm^{-1}s^{-1}}$ this was also the base for the overtopping experiments.

3.4.1 Overtopping

The overtopping experiments were executed of two different test sections. At the first test section four tests were done at average overtopping discharges of respectively 1, 5, 10 and 25 $\mathrm{lm^{-1}s^{-1}}$. Every test ran for two hours. On the second test section first hydraulic measurements were taken to determine the velocity and water depth of the overtopping waves. After the hydraulic measurements were completed another 25 $\mathrm{lm^{-1}s^{-1}}$ test was performed on the same test section.

The valves in the simulator were opened and closed according to a steering file. The flow into the simulator was constant, hence the time the valves were opened corresponded to the release of a wave with a certain water volume. The overtopping volume of a wave is related to the wave run-up height which in its turn is related to wave height and wave period. In order to simulate the overtopping volumes of a wave spectrum, a Weibull distribution was used to determine the overtopping volume of waves with an average wave height of 0.4, 0.6, 0.8 and 1.2 m. This information was used as input for the steering file of the overtopping simulator. Eventually the distribution of the overtopping wave volumes led to 4 different experiments with average overtopping volumes related to respectively 1, 5, 10 and 25 $\mathrm{lm^{-1}s^{-1}}$.

3.4.2 Overflow

The 1 and 5 $\mathrm{lm^{-1}s^{-1}}$ test was not executed at the overflow test section because at such a small flow water hardly made its way to the toe of the inner slope. Therefore it was decided to skip this tests. After executing the 5, 10 and 25 $\mathrm{lm^{-1}s^{-1}}$ overflow experiments for two hours each, hardly any damage visible. Therefore it was decided to further increase the discharge over the dike to 50, 75 and 85 $\mathrm{lm^{-1}s^{-1}}$. When eventually the discharge had been increased to 85 $\mathrm{lm^{-1}s^{-1}}$, the maximum capacity of the pump, still no significant damage was visible. Since the objective was to reach a discharge at which damage to the grass layer occurs the width of the test section was decreased to 1 m. This facilitated a maximum discharge of 170 $\mathrm{lm^{-1}s^{-1}}$. This increase in discharge eventually led to initial damage to the dike. However, due to the time schedule the simulator had to be moved to the final test section. Making it not possible to cause more damage to the first test section.

With the experience of the first test section in mind it was decided to split the second test section into 2 1 m wide parts. One part was left untouched, on the other part the grass layer was removed, see Figure 3.7. This gave the opportunity to run an overflow experiment on both the grass layer and directly on the clay layer. The grass section was tested for two hours at full capacity of the simulator. This caused negligible initial damage to the grass layer. It was decided to stop testing on the grass covered section and to test the exposed clay section. Running the simulator at 30 $\mathrm{lm}^{-1}\mathrm{s}^{-1}$ already led to damage after 15 minutes, after 45 minutes significant damage had occurred and the experiment was stopped. We then moved back to the grass covered part to try to cause more damage. After 9 minutes the entire test section collapsed due to the damage caused by the exposed clay part. Since there was some time left the wooden partitions that split the entire test section in half were removed. In order to look at the horizontal headcut development the simulator ran again at 30 $\mathrm{lm}^{-1}\mathrm{s}^{-1}$. This test ran for 19 minutes after which the crest of the dike became unstable and the test was stopped.

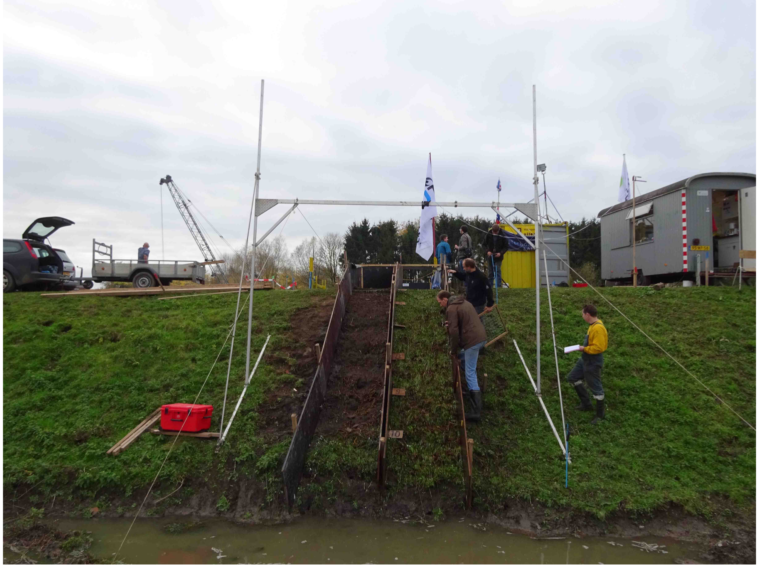

FIGURE 3.7: Second overflow test section. The section was split in half to create two parts: one to test on the grass layer and one to test directly on the clay layer.

3.4.3 Calibration of simulators

In order to regulate the discharge through the simulators a frequencially adjustable pump was used. With a tidal range of about 3 metres the pump head changed constantly. The outflowing discharges were therefore constantly monitored during the tests and the frequency at which the pump ran was adjusted when required. The inflow into the overtopping simulator was monitored using a riser tube which was mounted on one of the sides of the simulator. This riser tube was calibrated in order to indicate the amount of water inside the simulator. On the steering file of the overtopping simulator the volume of the wave that was released was indicated. When the level on the riser tube deviated significantly from the volume indicated on the steering file the pump frequency was adjusted.

The flow into the overflow simulator was measured using two different instruments. The first one was an acoustic discharge meter which was mounted on the supply pipe about 10 metres upstream of the simulator. The discharge meter is illustrated in figure 3.8a and 3.8b. The second instrument was an overflow weir which was placed just downstream of the overflow simulator at the overflow duct.

(A) Discharge meter

(B) Sensors of the discharge meter

In a uniform flow at low flow velocity, the water level at a certain distance upstream of a sharp weir is related to the overflow discharge according to:

$$Q = \frac{2}{3} \cdot m \cdot h_e \cdot \sqrt{\frac{2}{3} \cdot g \cdot h_e} \tag{3.1}$$

With:

$$m = 1,045 + 0,141 \cdot \left(\frac{h_e}{h_0} \right) \qquad h_e = h - h_0 + 0,0011 \tag{3.2}$$

in which: h_0 = Height of the weir $[m]$
h = Water depth upstream of the weir $[m]$

This relation was used to determine the discharge through the duct that led the water from the simulator to the dike crest. A sharp weir was placed in the duct and the water level upstream of the weir was measured, at constant discharge. Based on this water level the discharge was qualified. Field estimations of the flow velocity upstream of the weir indicated flow velocity in the order of 0,2-0,4 m/s, the influence of the velocity head over these ignored. The weir discharge meter is visualized in figure 3.9a to 3.9d. Since the discharge was defined rather quickly, the measurements were done at approximately 10 minute intervals.

The acoustic discharge meter and the weir showed similar results although the acoustic discharge meter consistently gave a higher value than the weir discharge meter. This difference can partly be explained by leakage of the simulator and because of inaccuracy in measuring the water depth upstream of the weir. The difference however was small enough to fit within the margin of error of both instruments.

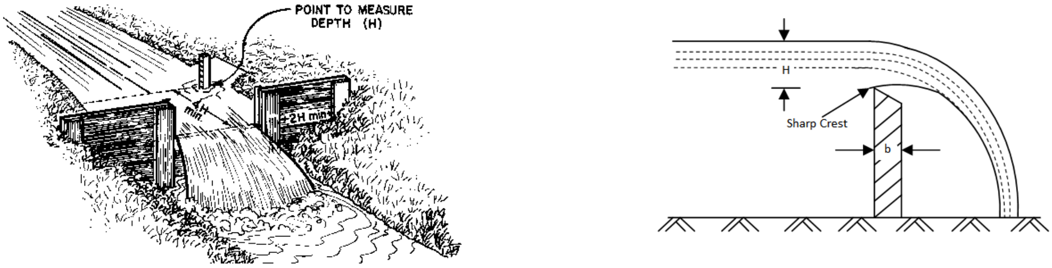
POINT TO MEASURE
DEPTH (H)
4H
min.
2H min.
H
Sharp Crest
b

(A) Weir discharge meter as applied in a small stream (B) Cross section of a weir discharge meter

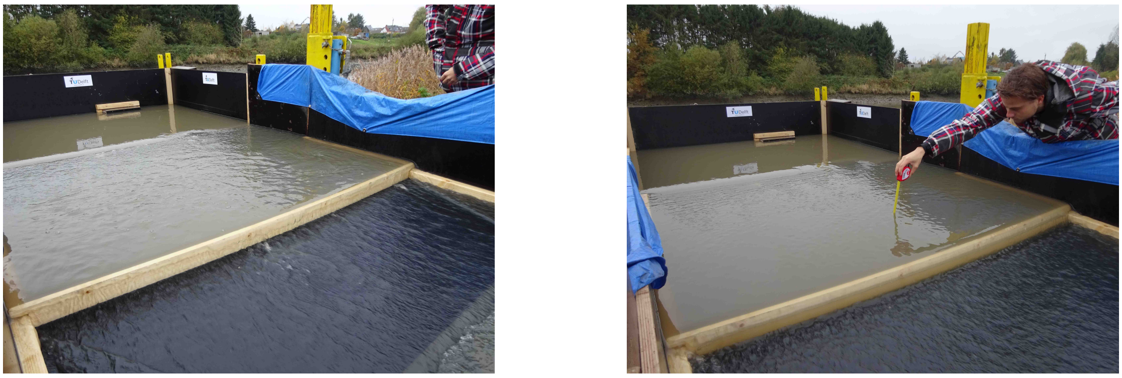

(C) Weir, immediately after placement (D) Manually measuring the water depth

Figure 3.9: Determination of the discharge of the outflow happened with a weir placed in the current. The water level upstream of the weir is related to the discharge according to equation 3.1

4 Overflow experiment results

During the breach initiation experiment four different parameters were measured: flow velocity, water depth, erosion development and saturation of the clay and grass layer. In this chapter the measurements of these parameters are evaluated.

4.1 Damage description overflow tests

Description of the damage after every hour of testing during the overflow test is given in Appendix I. In every cell of the 1x1 m grid as printed on the dike section the damage was indicated on a data sheet. Rocks and stones that appeared on the surface are indicated in red and actual damage to the grass layer is indicated in blue. The damage indication sheets are purely based on visual observation, size and depth of the damage spots was visually estimated. The plots are there to support the photographs.

The crest of the dike was not covered with a grass layer. Since the experiments were set up to test the erodability of grass layers the crest of the dike was covered with a plastic sheet. Therefore the first 3,5 m of the test section was covered in plastic. The grass cover was exposed about 1 m in front of the land side slope.

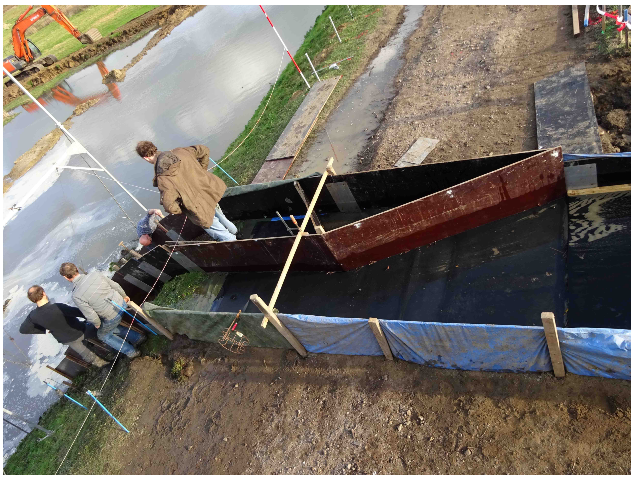

FIGURE 4.1: The first 3,5 m of the test section was covered with a plastic sheet to prevent erosion on the crest. Therefore the grass cover was exposed only just in front of the land side slope.

Exposed rocks and holes on the test section were noted before the tests started. A few rocks and spots with some minor damage were visible. The location of these spots are indicated in Figure I.1. After 1 hour of 10 $\mathrm{lm^{-1}s^{-1}}$ more spots of minor damage were found and when this test was finished after 2 hours the amount of exposed damage spots remained the same. During the 25 $\mathrm{lm^{-1}s^{-1}}$ test no notes of damage were taken after 1 hour. The damage pattern after 2 hours of 25 $\mathrm{lm^{-1}s^{-1}}$ did not significantly differ from the damage pattern after the 10 $\mathrm{lm^{-1}s^{-1}}$ test. At several spots the damage had become a bit worse and at one spot the roots of the grass were exposed. The total damage however was still little.

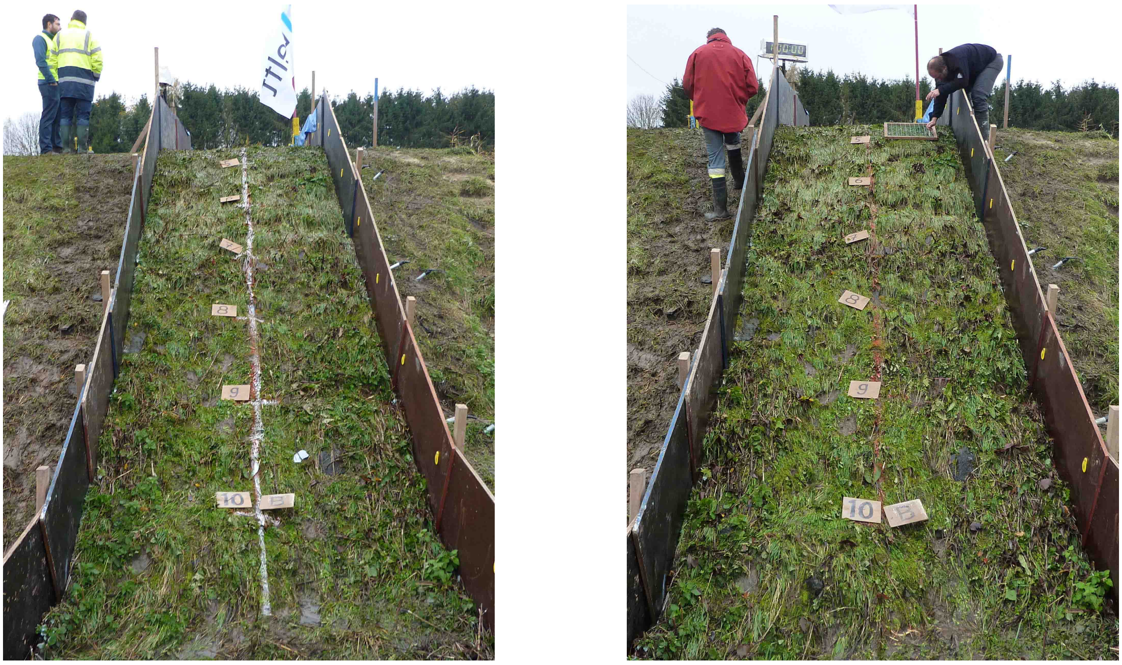

(A) Overview after 10 $\mathrm{lm^{-1}s^{-1}}$ test.

(B) Overview after 25 $\mathrm{lm^{-1}s^{-1}}$ test.

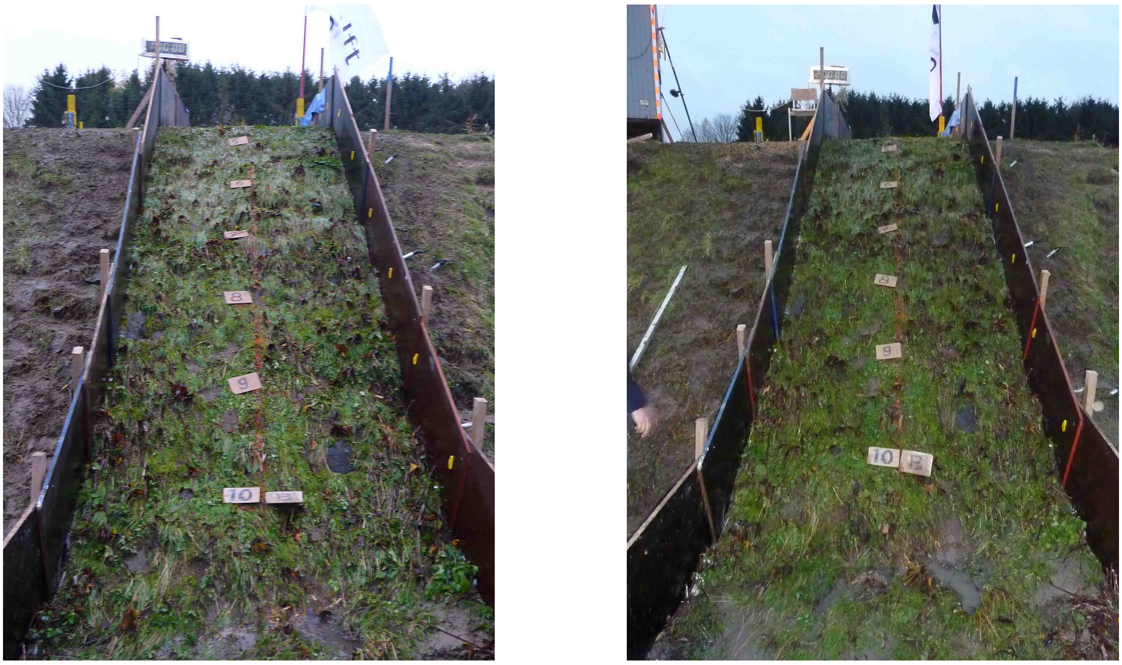

(C) Overview after 50 $\mathrm{lm^{-1}s^{-1}}$ test.

(D) Overview after 85 $\mathrm{lm^{-1}s^{-1}}$ test.

FIGURE 4.2: Overview of the damage pattern after the 10, 25, 50 and 85 $\mathrm{lm^{-1}s^{-1}}$ tests.

An overview picture of the damage after the 10, 25, 50 and 85 $\mathrm{lm^{-1}s^{-1}}$ tests is given in Figure 4.2 The damage pattern as visible after the 25 $\mathrm{lm^{-1}s^{-1}}$ test did not significantly change after the 50 and 85 $\mathrm{lm^{-1}s^{-1}}$ test. Therefore it was decided to reduce the width of the test section yielding a higher discharge per meter. At the 1 m wide test section 2 hour tests were performed at 125 and 170 $\mathrm{lm^{-1}s^{-1}}$. The findings of these tests, taken after 2 hours of testing, are presented in Figure I.8 and I.9. An overview picture of the test section after 2 hours testing at 125 and 170 $\mathrm{lm^{-1}s^{-1}}$ is given in Figure 4.3. In Figure 4.3b the first signs of significant damage are visible at the top of the test section. Whether this would rapidly develop in large damage spots or not is hard to say since we were not able to test this due to time.

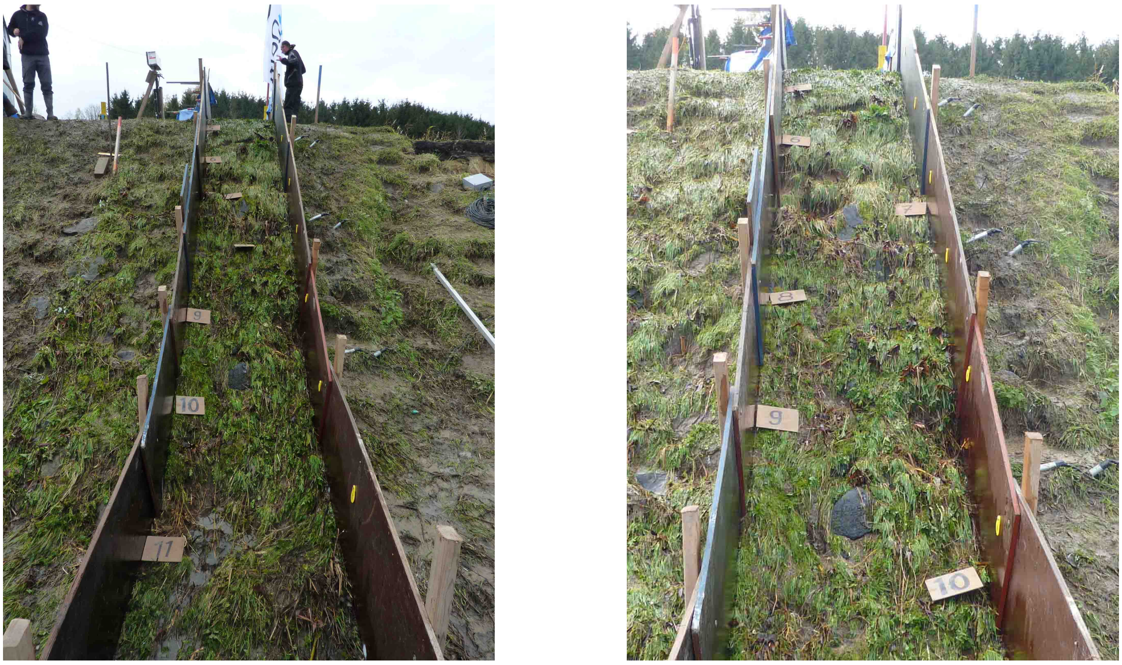

(A) Overview after 125 $\mathrm{lm^{-1}s^{-1}}$ test.

(B) Overview after 170 $\mathrm{lm^{-1}s^{-1}}$ test.

FIGURE 4.3: Overview of the damage pattern after the 125 and 170 $\mathrm{lm^{-1}s^{-1}}$ tests.

4.2 Water depth

During the overflow experiments an indication of the water depth was obtained using a ruler. Due to fluctuations in the water depth it was hard to determine the depth with an accuracy higher than 5 mm. This made the ruler accurate enough and besides that by far the most practical instrument.

The water depth was measured perpendicular to the embankment surface at 6 different points in the test section. Since the water depth varied over the width of the test section, the breadth averaged depth was used. The reference point was at the outflow point of the overflow simulator. From that point on the water depth was measured every meter until the water did no longer form a smooth flow any more. The points at which the water depths were measured are indicated in Figure 4.5. The results of the measurements are presented in Figure 4.4. Noticeable is that the length of the test section is 11 metres and the graph only shows data until 5 metres. This is because the water flow became aerated between point 5 and 6, making it nearly impossible to determine the water depth. The fluctuation in water depth in this aerated flow were determined to be of the order of 10 cm.

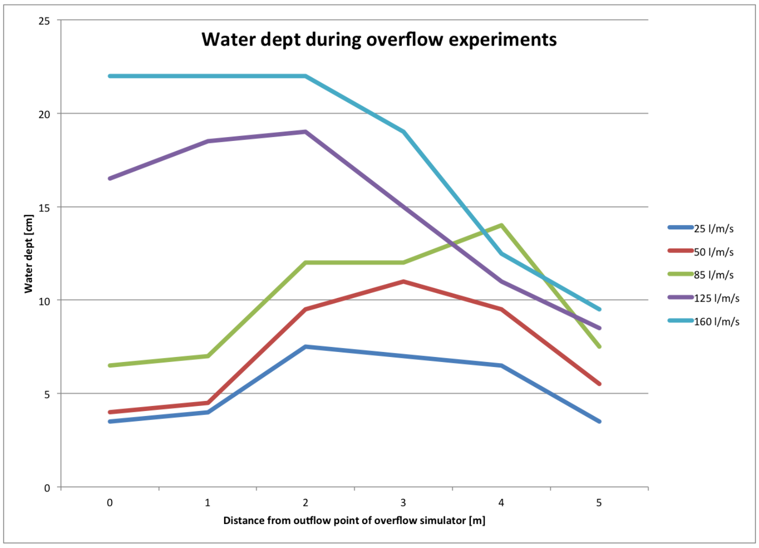

FIGURE 4.4: Overflow depth during different overflow discharges

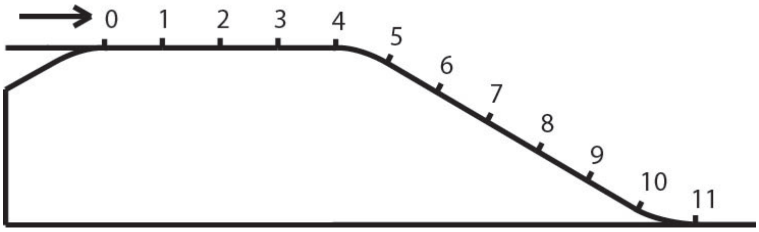

FIGURE 4.5: Measuring points during overflow simulation

4.3 Flow velocities during overflow tests

During the overflow test on the first test section some improvized velocity measurements were done to estimate the flow velocity of the aerated flow during 85, 125 and 160 $\mathrm{lm^{-1}s^{-1}}$ tests. The measurements were done by releasing a styrofoam ball in the current and measure the time it took for the ball to cover a distance of 6 m on the inner slope. For the 85 $\mathrm{lm^{-1}s^{-1}}$ test only two measurements were taken. The flow velocities over this two metre wide section differed over the width of the section. Figure 4.6 shows this, the flow is more aerated at the right part than at the left part. This made quite a difference in average flow velocity. Releasing the ball at the left part yielded 3.24 m/s while releasing the ball at the right section yielded 2.62 m/s. These measurements however are only snapshots during the test and therefore not representative for the entire test.

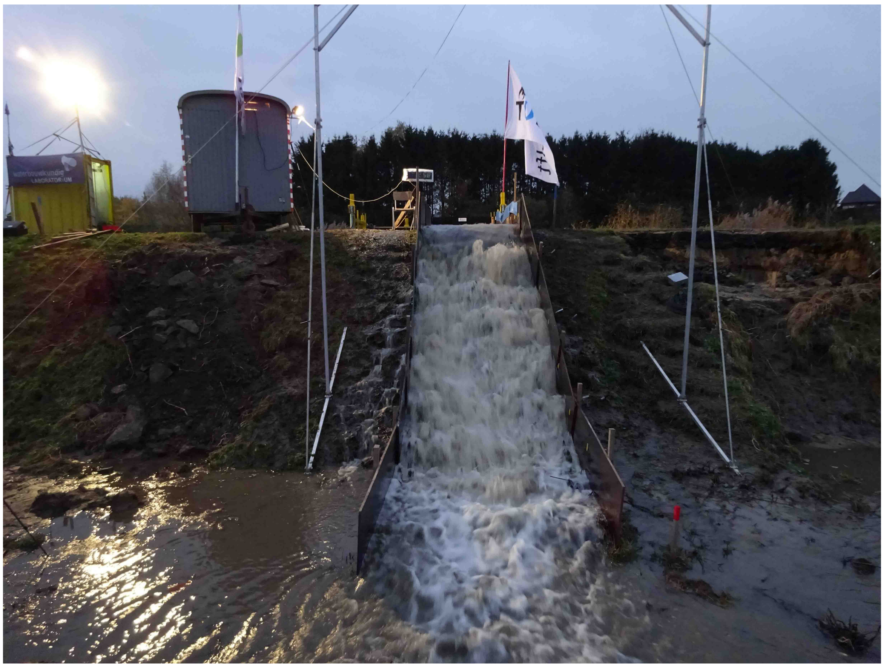

FIGURE 4.6: Overflow test at 85 $\mathrm{lm^{-1}s^{-1}}$. Although not clearly visible on the picture, the right part of the test section appeared to be more aerated than the left part.

For the 125 and 160 $\mathrm{lm^{-1}s^{-1}}$ each test was repeated three times. For every test two people (Luc and Patrik) used a stop-watch to measure the time. By taking the average of these 6 measurements a reasonable estimations could be made of the flow velocity. The results of these measurements are presented in Table 4.1.

TABLE 4.1: Estimations of the flow velocity at 125 and 160 $\mathrm{lm^{-1}s^{-1}}$. Table shows the stop-watch measurements of the time a floating ball lasted to cover a distance of 6 metres.

Test	125 $\mathrm{lm^{-1}s^{-1}}$		160 $\mathrm{lm^{-1}s^{-1}}$	
Measured by:	Luc	Patrik	Luc	Patrik
	2.0	2.0	1.9	2.0
	1.9	2.1	1.8	1.9
	2.1	2.4	1.8	2.0
Average	2.08 s		1.88 s	
Flow velocity	2.9 m/s		3.2 m/s	

During the overflow tests on the second overflow test section velocity measurements were done using the same paddle wheels as used during the hydraulic calibration of the overtopping test sections, see chapter 5.1. The result of these measurements are presented in figure 4.7. The flow velocity was measured at the crest, just after the crest line and 1.5 m below the crest line. At the measurement point at the crest also water depth measurements were done in order to determine the discharge of the flow. This was necessary because unfortunately the discharge meter that was installed at the hose did not work at the time.

Note: The velocity data as provided from the paddle wheels during the overflow tests still has an unclear outcome which is currently under investigation.

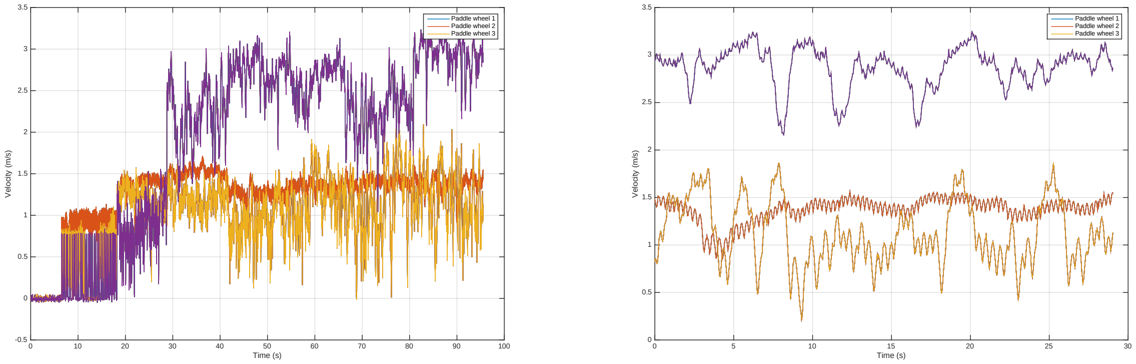

Figure 4.7: Velocity measurements as done by the paddle wheels during both the overflow tests

4.3.1 Infra-red camera

During the experiments velocities were determined from tracking particles using a FLIR A35 infra-red camera pointed at the flow over the inner slope of the dike. At the crest of the dike a hot drifter was released into the current. The drifter was advected by the current. The track followed by the drifter was recorded by the infra-red camera. Since the camera measured temperature contrasts, the track of the drifter was clearly visible on camera recordings. A screen-shot of one of the camera recordings is visible in Figure 4.8.

The infra-red camera recordings are processed using Matlab. It has been assumed that the drifter is the hottest object in the flow and therefore the most white object in a frame. Since the resolution of the infra-red camera is 320x256 pixels every frame is considered a 320x256 matrix of which every digit represents a single pixel. The value of each digit represents the white of the pixel. Starting when a small cluster of significant white is detected at the y=0 coordinate, a contour line is created around this cluster and the center of the contour line is plotted in a figure. This is done for every frame, creating a path line of the drifter through the current. If the position of each next point in time does not lie within a distance of the same order of magnitude as the distance to its previous point it is not plotted. In-stead, an-other cluster of high white-rates is found that does lie within the same order of distance.

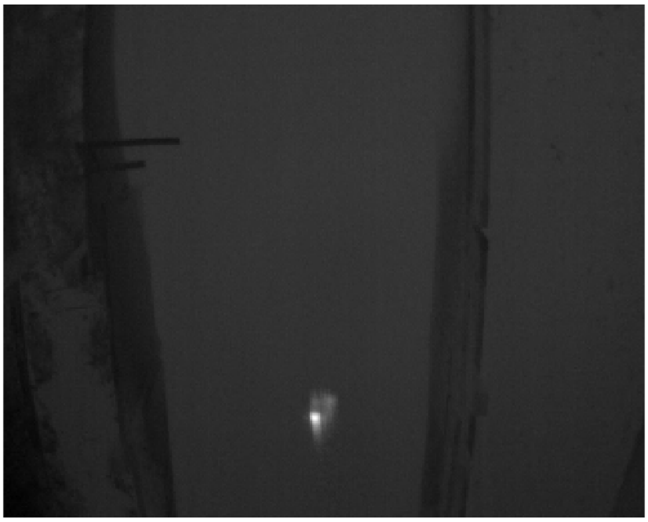

Figure 4.8: The warm floater as recorded by the infra-red camera.

The change in x- and y-coordinates of each point in the figure with time is used to determine the velocity of the drifter. The actual velocity of the drifter is determined by applying Pythagoras' law for the difference in x- and y-coordinates and dividing this value with the frame-rate of the camera. Since the frame-rate of the camera is 60 frames/s this leads to the following equation for the velocity of the drifter:

$$v = \frac{\sqrt{(x^{n+1} - x^n)^2 + (y^{n+1} - y^n)^2}}{1/60} \tag{4.1}$$

An other interesting parameter obtained from infra-red recordings is the velocity component in the length direction of the test section. Other velocity measurement methods applied only provide velocity data in the length direction of the test section. In order to compare the results from different measurement methods it is therefore important to also determine this velocity component. This is achieved by dividing the difference in y-coordinate between each frame plot by the frame rate:

$$v_y = \frac{y^{n+1} - y^n}{1/60} \tag{4.2}$$

Plots of the track of the drifter, its velocity and its length directed velocity component are presented in Appendix G. One can clearly see that the velocity components seem to have large scatter in its data. This scatter can be explained by two factors:

- The highly turbulent aerated flow is characterized by fluctuating velocities. Horizontal and vertical vortices cause the drifter to accelerate and decelerate in the current. This explains high peaks and low troughs in the graph.
- The drifter is not always clearly visible on the infra-red recording making it hard to track. Because the drifter disappears beneath the surface due to the aerated flow every now and then it also disappears of the screen of the recording. Since Matlab is unable to track the drifter at

that moment it basically guesses its location. This is not really a problem when the drifter is gone for a few frames, but when it has disappeared for a severe amount of frames the scatter in the data increases.

Mean flow velocities over the inner slope as obtained from the infra-red camera are presented in Table 4.2. The mean flow velocities are determined from the recordings by counting the amount of frames it takes the drifter to go from the top to the bottom of the recorded area. The length of the recorded area was measured using a ruler, the total length was 2.11 m. Like mentioned the frame-rate of the camera was 60 frames/s. The mean flow velocity is then calculated by:

$$v_m = \frac{\text{Section length}}{(Amount\ of\ frames)/60} \tag{4.3}$$

TABLE 4.2: Average flow velocities as obtained from the infra-red camera recordings

Pump freq.	1st test m/s	2nd test m/s
20	2.15	1.46
25	2.39	2.30
30	2.69	2.81
35	2.94	2.39
40	3.62	
45		3.62
50	3.62	3.96

5 | Overtopping experiment results

5.1 Paddle wheels and surfboards

Description of the damage on the grass cover as caused by the overtopping waves is described in the report *'Factual report overslagproef Wijmeers 2'* by Infram B.V. (only in Dutch) [2]. The water depth and flow velocity data as obtained from the overtopping experiments is processed in the next section.

During the overtopping and overflow tests velocity measurements were done using a paddle wheel. A paddle wheel is a basic velocity meter that measures flow velocities with a small wheel attached to a recording device. The rotating velocity of the wheel is measured by the recording device from which the flow velocity of the water can be determined. The paddle wheels were used during the hydraulic calibration. Before the second overtopping experiment started the paddle wheels were placed in the grass cover of the dike in order to measure flow velocity close to the bottom. Other paddle wheels were mounted on surf board like devices which float on water. By doing so the flow velocity at the water surface could be measured as well. The surfboards were also equipped with devices to measure the water depth. This is presented in Figure 5.1. The flow velocities during the overflow tests were only measured at the surface. This was done by holding the paddle wheel in the water flow manually. Velocities and water depths were measured at 4 spots. The location of the paddle wheels and surf boards are indicated in Figure 5.2. Unfortunately surf board 4 did not work properly causing the signal of the height meter to be unclear. Therefore water depth data from this surf board is not available.

During the hydraulic calibration of the overtopping tests the flow velocity and water depth of a wave with a predetermined discharge were measured. For each calibration value 3 waves were released from the simulator. The discharge of the waves was increased until the maximum capacity of the simulator was reached or until damage occurred. From the measurements a peak velocity and peak water depth were determined from which a peak discharge can be calculated. Since the flow velocity was measured at two points, at the water surface and at the bottom, two peak discharges are calculated per surf board. Peak discharges of each tested wave are presented in Table 5.2. The paddle wheel in surfboard II did not work, therefore only bottom velocity was measured at position II. The water depth and flow velocity data as obtained from the paddle wheels and the water depth meters is presented in Appendix H.

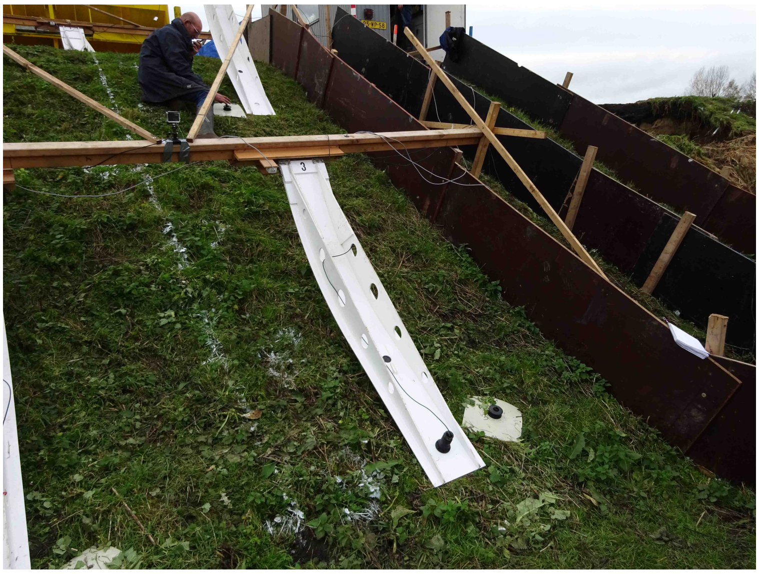

Figure 5.1: Both at the water surface and at the bottom the flow velocity was measured using a paddle wheel.

The position of the paddle wheels and surfboards on the test section is demonstrated in Figure 5.2 and described in Table 5.1. The position is described by the distance from the heart line (x-coordinate) and distance from the outflow point of the overtopping simulator (y-coordinate). A positive x-coordinate means the surfboard of paddle wheel is placed right from the heart line and a negative number means it is placed left from the heart line.

The numbering of the surfboards will be used to describe the position of the measurement devices in the next sections. So when 'position I' is mentioned, it is referred to the data as provided from the measurement instruments at the position of surfboard I, in this case surfboard I and paddle wheels 1 and 2. 'Position II' is surfboard II and paddle wheel 3 and 'Position III' is surfboard III and paddle wheels 4 and 5.

Table 5.1: Position of the surfboards and paddle wheels on the test section during the hydraulic measurements

Type	Number	Location (x; y)
Surfboard	I	0.00; 2.70
	II	1.35; 5.00
	III	0.85; 9.15
	IV	-1.10; 9.10
Paddle wheel	1	0.00; 2.70
	2	-0.35; 2.55
	3	1.00; 4.95
	4	0.85; 9.15
	5	1.20; 8.90
	6	-1.10; 9.20
	7	0.75; 9.10

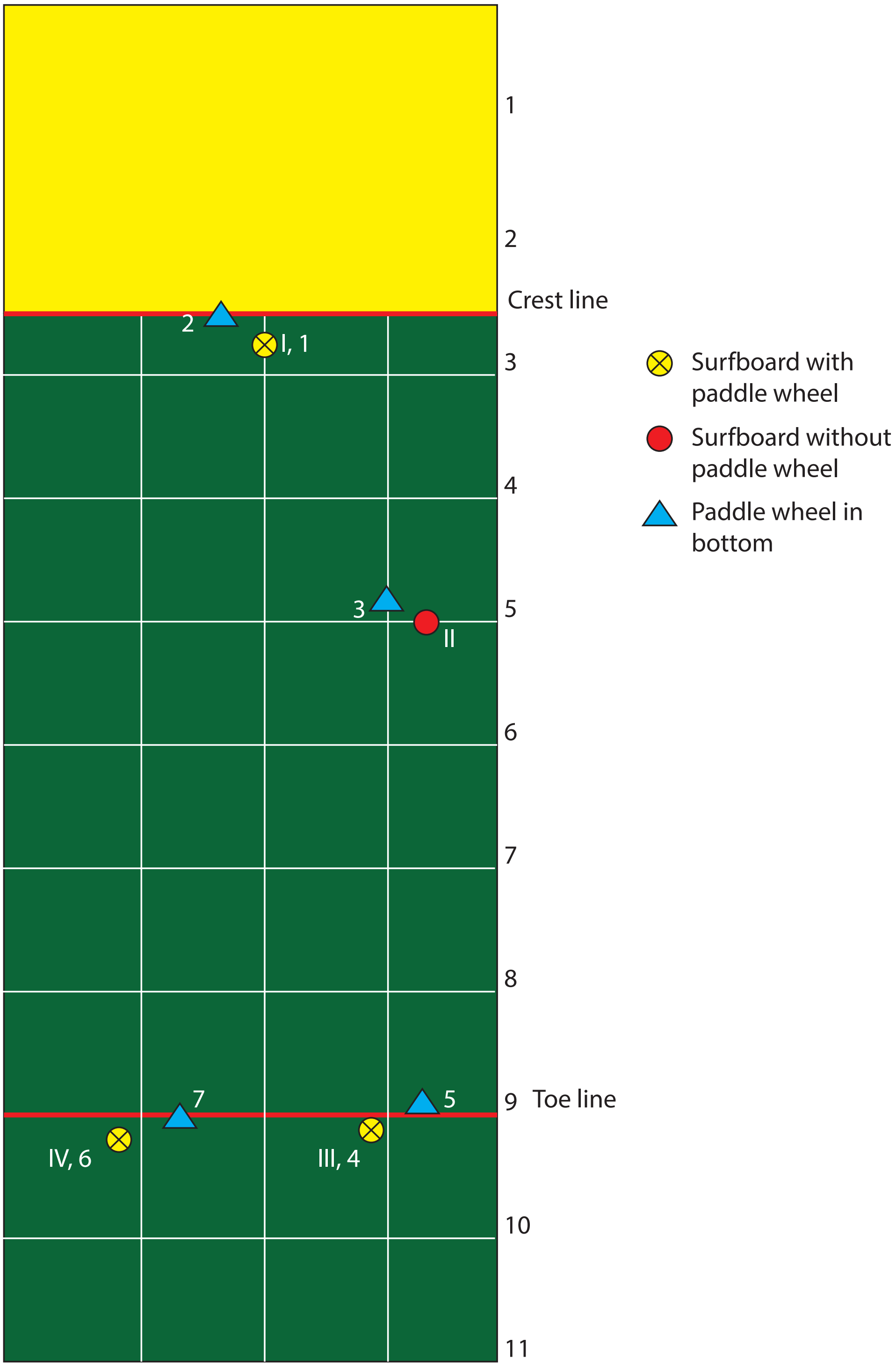
1
2
Crest line
2
I, 1
3
Surfboard with paddle wheel
Surfboard without paddle wheel
Paddle wheel in bottom
4
3
5
II
6
7
8
7
5
9 Toe line
IV, 6
III, 4
10
11

FIGURE 5.2: Positions of the surf boards and paddle wheels on the land side slope of the dike.

5.2 Water depth

In Figures 5.3 and 5.4 plots of the water depth of each overtopping wave as tested during the hydraulic measurement are presented. Each plot shows the water depth of overtopping waves at position I (at the crest), position II (halfway on the slope) and position III (at the toe). These figures show the development of the waterdepth of the overtopping waves along the slope. Like mentioned before the 500, 1000, 1500 and 2000 l/m wave tests were repeated 3 times, so per wave volume 3 peaks are visible in each plot in Figure 5.3. After executing these 12 tests the hydraulic measurement was stopped for a few minutes to check for any damage on the grass cover. After the break the 2500, 3000 and 3500 l/m waves were tested. Initially each wave was tested once, but after execution of these tests it was decided to repeat the 2500 l/m test another two times. The 3000 and 3500 l/m wave tests were not repeated because a single wave of this volume already caused damage to the dike. Since the grass cover was not allowed to be damaged severely during the hydraulic measurements it was decided not to repeat these tests.

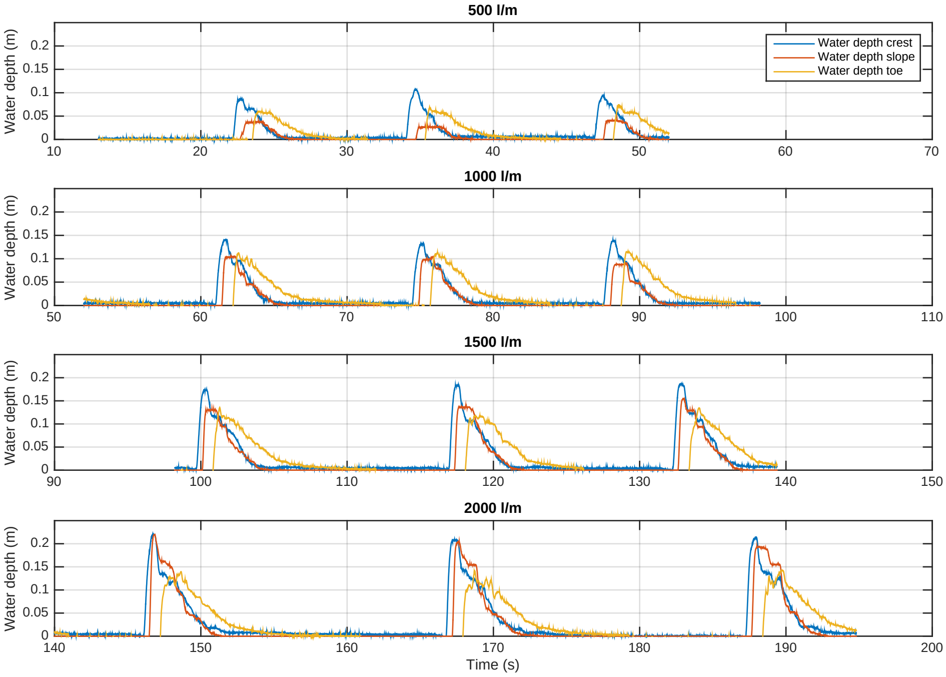

Figure 5.3: Wave height for overtopping waves of 500, 1000, 1500 and 2000 l/m. Each wave volume test was repeated 3 times.

In Figure 5.4 it is visible that the surfboard at position 3 was not working properly during the 3000 and 3500 l/m tests. Plots of the data as provided from these tests are too leading to an unrealistic depth pattern.

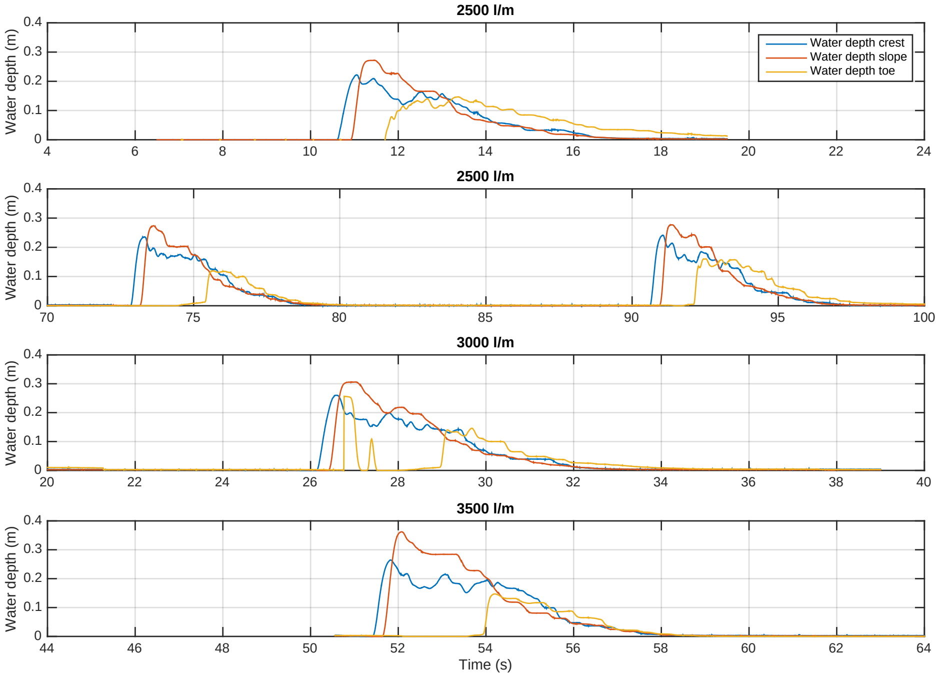

FIGURE 5.4: Wave height for overtopping waves of 2500, 3000 and 3500 l/m. Each wave volume test was executed once, after executing all three tests the 2500 l/m test was repeated another 2 times.

5.3 Flow velocity

Figures 5.5 and 5.6 show the development of the flow velocity of an overtopping wave. Like with Figures 5.3 and 5.4 the measurements are plotted for position I, II and III along the land side slope. Position I and III contained a velocity measurement device for bottom- and surface velocity while at position II only a bottom velocity measurement device was mounted. The paddle wheels mounted at position IV did give a clear velocity signal, however since the surfboard measuring the water depth was not functioning properly a clear discharge signal from these measurement instruments cannot be given. Therefore plots of these data are not included in this report.

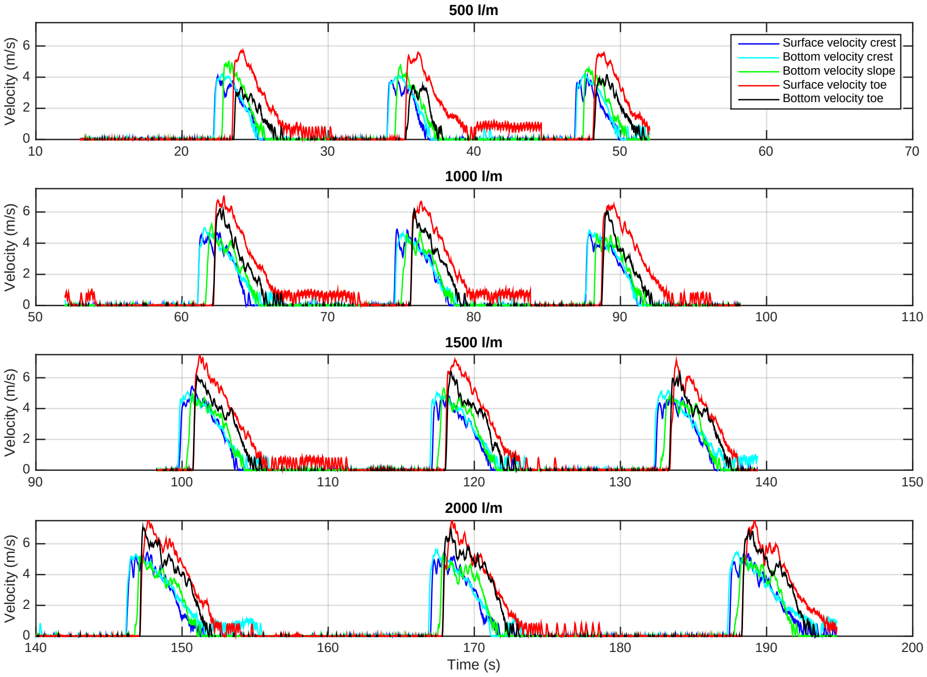

FIGURE 5.5: Surface- and bottom flow velocity for overtopping waves of 500, 1000, 1500 and 2000 l/m. Each wave volume test was repeated 3 times.

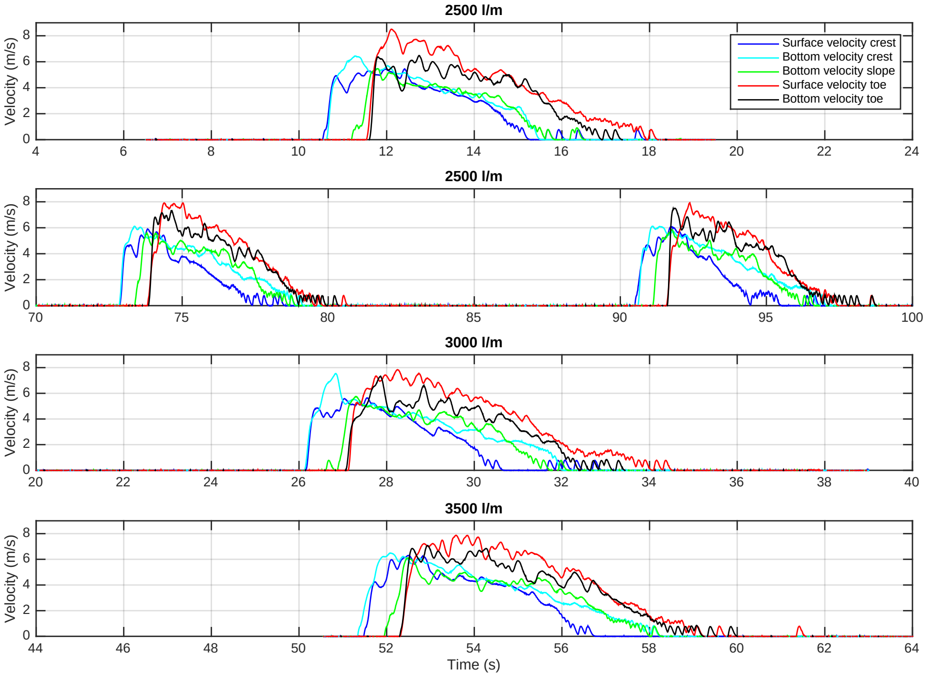

FIGURE 5.6: Surface- and bottom flow velocity for overtopping waves of 2500, 3000 and 3500 l/m. Each wave volume test was executed once, after executing all three tests the 2500 l/m test was repeated another 2 times.

5.4 Peak discharge

The hydraulic measurement was split up into two sessions. During the first session the 500, 1000, 1500 and 2000 l waves were tested and during the second session the 2500, 3000 and 3500 l waves. The peak discharge of each wave is determined using the data from these tests. These peak discharges are presented in Table 5.2 in order of appearance during the test. The peak discharge data from Table 5.2 is plotted and demonstrated in Figure 5.7.

TABLE 5.2: Peak discharges as determined from the data provided by the paddle wheels.

		Peak discharge				
Wave	Test	1-surface	1-bottom	2-bottom	3-surface	3-bottom
	(m^3)	(m^3/s)	(m^3/s)	(m^3/s)	(m^3/s)	(m^3/s)
First session						
1	0.500	0.32	0.36	0.19	0.35	0.20
2	0.500	0.39	0.43	0.13	0.34	0.21
3	0.500	0.34	0.39	0.18	0.40	0.29
4	1.000	0.63	0.69	0.54	0.73	0.70
5	1.000	0.54	0.60	0.45	0.70	0.61
6	1.000	0.55	0.63	0.40	0.74	0.69
7	1.500	0.78	0.88	0.65	0.97	0.78
8	1.500	0.81	0.91	0.73	0.83	0.72
9	1.500	0.80	0.95	0.62	0.84	0.85
10	2.000	1.13	1.17	0.92	0.93	0.83
11	2.000	1.03	1.17	0.92	0.99	0.85
12	2.000	1.01	1.16	0.99	0.90	0.85
Second session						
1	2.500	1.04	1.30	1.24	1.08	0.84
2	3.000	1.16	1.73	1.52	0.94	0.73
3	3.500	1.26	1.57	1.83	1.06	0.99
4	2.500	1.09	1.42	1.44	0.82	0.74
5	2.500	1.12	1.46	1.42	1.20	1.02

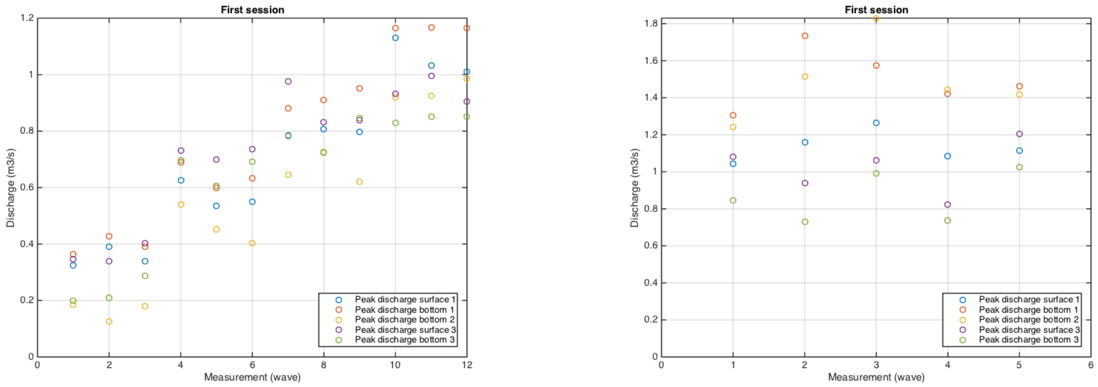

(A) First hydraulic measurement session.

(B) Second hydraulic measurement session.

FIGURE 5.7: Peak discharges as obtained from the data from the hydraulic measurements

5.5 Calculated wave volumes

The integral of the discharge of each tested wave gives the total volume of the wave. The volume of each tested wave as calculated from these integrals is indicated in Table 5.3. The table shows that the calculated wave volumes are more or less equal to the released volumes of the waves. The wave volumes calculated from the bottom velocity are somewhat lower than expected, the wave volumes calculated from the surface velocity are somewhat higher than expected. This is logical since in a flow on a slope velocity is in general lower at the bottom than at the surface. Due to the fact that the flowing water experiences more friction at the bottom than at the surface, water is more slowed down at the bottom. Flow velocity however is not linear divided over the water depth. A velocity profile over water depth looks more logarithmic than linear. Simply taking the mean value of the volume calculated from surface velocity and the volume calculated from bottom velocity is therefore not valid.

Table 5.3: Volume of each tested wave according to the data obtained from the surfboards and paddle wheels.

	Calculated volume of released wave				
Tested wave (m^3)	Surface-1 (m^3)	Bottom-1 (m^3)	Bottom-2 (m^3)	Surface-3 (m^3)	Bottom-3 (m^3)
0.500	0.44	0.48	0.26	0.50	0.27
0.500	0.45	0.52	0.18	0.61	0.30
0.500	0.42	0.50	0.25	0.62	0.40
1.000	0.94	0.99	0.67	1.18	0.91
1.000	0.90	0.92	0.65	1.21	0.90
1.000	0.88	0.96	0.58	1.25	0.88
1.500	1.37	1.41	0.93	1.77	1.32
1.500	1.24	1.40	1.07	1.80	1.36
1.500	1.36	1.52	0.99	1.43	1.25
2.000	1.85	1.98	1.38	2.25	1.88
2.000	1.79	1.96	1.37	2.01	1.83
2.000	1.79	1.95	1.63	2.07	1.77
2.500	2.27	2.56	1.96	2.73	2.20
2.500	2.28	2.77	2.38	1.23	1.07
2.500	2.28	2.86	2.53	2.51	2.22
3.000	2.55	3.05	2.51	1.45	1.15
3.500	3.29	3.76	3.40	1.79	1.52

6 | Existing theory applied on Wijmeers-II data

As shown in Chapter 4 and 5, during the overflow experiments at Wijmeers II the grass cover of the dike withstood the overflow much longer than predicted. According to the theory of Hughes [16] the grass cover should have failed somewhere around the 10 l/m/s test. However after several tests at much higher discharge, up to 170 l/m/s, the grass cover still had not failed. This gives room for thought since theory does not seem to meet reality. Therefore an extended analysis will be done on the obtained data to find an explanation for these differences.

6.1 Overflow induced land-side slope velocity

According to the theory developed by Van Gent [38] the land-side slope velocity u_B depends on the crest flow velocity u_{crest}, crest flow depth d_{crest} at the land-side end of the crest and the slope angle of the land-side slope θ. The Van Gent theory is explained in Section 2.3.2. Some basic crest flow depth measurements were done during different overflow tests. These measurements are presented in Section 4.3, a selection the flow depths at the end of the crest obtained from these measurements are presented in Table 6.1. Since the discharge during these tests was known, the flow velocity at the end of the crest could easily be determined ($u_{\text{crest}} = q/d_{\text{crest}}$).

TABLE 6.1: The flow depth measurements executed during the overflow tests are used to determine the crest flow velocity.

q $(m^3m^{-1}s^{-1}$	Measured d_{crest} (m)	Calculated u_{crest} (ms^{-1})
0.025	0.07	0.35
0.05	0.11	0.45
0.125	0.15	0.83
0.160	0.19	0.84

The parameters presented in Table 6.1 are used to determine the theoretical land-side slope flow velocity during the overflow tests according to the Van Gent theory. These theoretical values are compared to the land-side slope velocity measurements executed using and Infra-red camera and drifter. The drifter was warmed up and released in the flow close to the outflow of the overflow simulator, see Section 4.3. The infra-red camera, aimed at the land-side slope filmed the warmed drifter as it followed the current and flowed over the land-side slope. The velocity of the warmed drifter was determined later on using a tracking programme in Matlab. The average velocities determined from these measurements are presented in Table 4.2, detailed results from the tracking programme are presented in Appendix G. The theoretical flow velocities according to the Van Gent theory are presented in Figure 6.1.

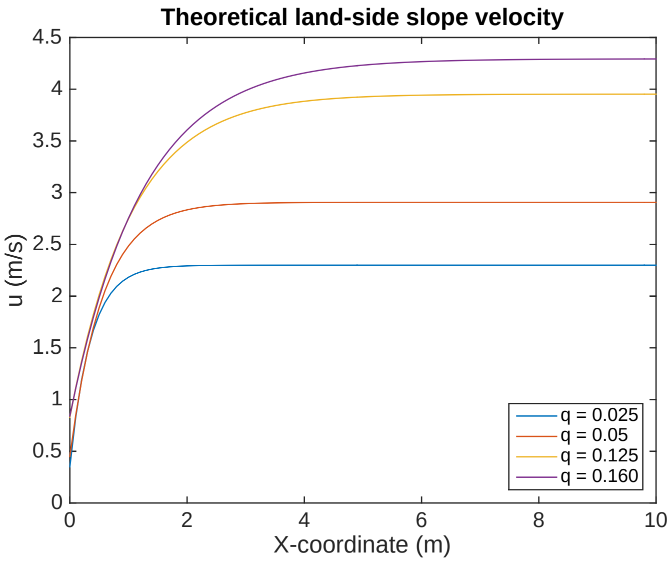

FIGURE 6.1: Theoretical crest flow velocity according to the Van Gent theory [38]. $X = 0$ marks the end of the crest i.e. the start of the land-side slope.

The Infra-red camera measured the velocity of the drifter on a track corresponding to $X = 2.5$ to $X = 4.6$ m in Figure 6.1. So the average velocity between $X = 2.5$ and $X = 4.6$ should be compared to the average velocities obtained from the Infra-red measurements. The average velocities obtained from the Infra-red camera measurements corresponding to respectively 0.025, 0.050, 0.125, 0.160 $m^3m^{-1}s^{-1}$ are presented in Table 6.2.

TABLE 6.2: Average flow velocities as obtained from the infra-red camera recordings

Discharge $m^3m^{-1}s^{-1}$	1st measurement ms^{-1}	2nd measurement ms^{-1}	Theoretical value ms^{-1}
0.025	2.15	1.46	2.3
0.050	2.39	2.30	2.9
0.125	-	3.62	3.8
0.160	3.62	3.96	4.0

Table 6.2 clearly shows that the theoretical value for the land-side slope velocity is slightly higher than the measured land-side slope velocity. This is probably caused by the cascade effect of land-side slope leading to decrease of the flow velocity.

6.2 Basis for overtopping theories

During the CIRIA overflow experiments, executed in 1987 by Hewlett et al. [13], the resistance of certain types of grass cover against overflow have been tested. This resulted in the standard numbers for acceptable erosion as demonstrated in Table 6.3 and Figure 6.2. Theories describing wave overtopping induced damage to the land-side slope are mostly based on the results from the CIRIA experiments.

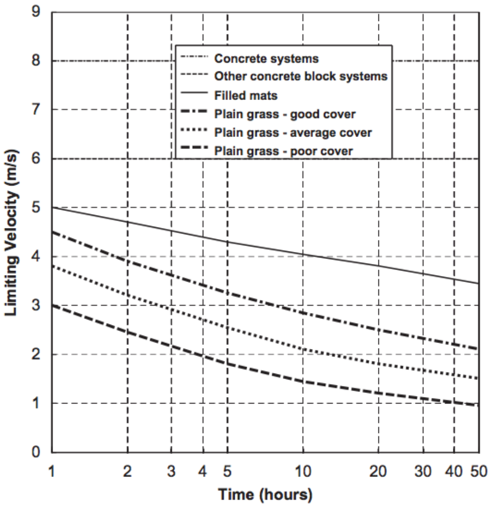

FIGURE 6.2: Combinations of (velocities, durations) for acceptable erosion of various coverings due to steady overtopping by Hewlett et al. [13] as reported in Hughes [16]

TABLE 6.3: Velocities and durations as obtained from the experiments executed by Hewlett et al. [13] (see also Figure 6.2)

Velocity (m/s)	Duration (h)		
	Good grass cover	Average grass cover	Poor grass cover
4.5	1	NA	NA
4.0	1.8	NA	NA
3.5	4	1.5	NA
3.0	8.5	2.5	1
2.5	20	5	1.9
2.0	50	14	3.8
1.5	NA	50	10
1.0	NA	NA	40

6.2.1 Velocity-, Shear stress- or Work-basis?

Based on the CIRIA experiments and the resulting standards for acceptable erosion on the land-side slope, different theories have been developed. According to the Dutch standards, wave load on the land-side slope is determined based on bottom shear stress, which is equivalent to the flow velocity squared, u^2 [15, 36]. Further research on wave load on the land-side slope is done by Dean et al. [10] who developed three different methods that were tested using measurements done by Hewlett et al. [13]. The methods were based on respectively velocity (u), shear stress (u^2) and work (u^3). The standard errors in velocity in each method was tested for three types of grass covers, from which the work based method consistently provided the lowest standard error by a significant amount.

The utility of the method developed by Dean et al. is that it provides a basis for accounting for the cumulative effects of variable erosion events. Based on their finding that the cumulative work is more appropriate than flow velocity or shear stress, it appears (perhaps somewhat intuitively), that the cumulative work within acceptable limits can be accomplished by any velocity above the critical value for the particular grass cover [10]. Based on the findings by Dean et al., a work based approach is chosen to be superior to a shear stress based approach. Since the method developed by Hughes et al. [17, 18] is the state of the art work based land-side slope erosion theory, this method is considered to be the best method to be applied on the Wijmeers-II data for erosion calculations.

6.3 Excess volume approach

In order to compare the impact of wave overtopping and overflow on the land-side slope of a dike, a modelling approach is developed by Hughes [17, 18] which is based on models developed by Dean et al. [10]. The model as developed by Dean et al. describes the damage on the land-side slope based on the time a certain threshold flow velocity is exceeded times the amount of exceedance. Hughes extended this model by eliminating some conservative assumptions and eventually described the acceptable amount of erosion as the summation of the excess wave volume above a certain threshold of each individual wave. The excess volume is described as the integral of the overtopping discharge above a certain threshold. This 'Excess volume approach' is verified with data from the Wijmeers-II experiments in this chapter. In the Excess volume approach the load of overtopping waves on the land-side slope are based on overflow theory, however experiments that confirm this assumption have never been executed until Wijmeers-II. Subsequently this provides a unique opportunity to either confirm or question the validity of the Excess volume approach.

The equation describing the wave overtopping load on the land-side slope according to the Excess volume approach is given in Equation 6.1. The overflow load on the land-side slope is described in Equation 6.3. For a full explanation of the Excess volume approach of respectively wave overtopping and overflow as developed by Hughes, reference is made to Sections 2.4.1 and 2.4.2.

$$V_{ET}(t) = \sum_{n=1}^{N} V_{Wn} \left[1 - \left(\frac{q_c T_{on}}{V_{Wn}} \right) + \frac{2}{3^{3/2}} \left(\frac{q_c T_{on}}{V_{Wn}} \right)^{3/2} \right] \leqslant \frac{E_W}{K_W \cdot \beta_W} \left(\frac{f_F}{2g \cdot \sin\theta} \right) \tag{6.1}$$

Where

$$q_c = \frac{f_F \cdot u_c^3}{2g \cdot \sin\theta} \tag{6.2}$$

V_{Wn} and T_{on} are, respectively, the total volume and overtopping time of the nth individual overtopping wave, u_c the critical flow velocity, f_F is a friction factor and θ is the slope angle. The parameters u_c and $E_W/(K_W \beta_W)$ are constants related to the specific land-side slope dike cover.

Excess volume approach on steady overflow

The Excess volume approach developed by Hughes is easily applicable on steady overflow, which is logical since the whole theory is actually based on overflow experiments [10, 17]. The excess volume approach equation of steady overflow becomes:

$$V_{ET}(t) = (q - q_c)t \;\leqslant\; \frac{E_W}{K_W \cdot \beta_W}\left(\frac{f_F}{2g \cdot \sin\theta}\right) \qquad \qquad \textit{with } q > q_c \tag{6.3}$$

6.3.1 Verification of overtopping theory

In order to check whether the Excess volume approach would be valid for the outcomes of the Wijmeers II experiments, the calculated peak discharges are compared to peak discharges obtained from the hydraulic measurements as demonstrated in Table 6.4. The table shows that the measured peak discharges approach the calculated peak discharges rather well. There is quite a difference between the peak discharges as determined from the bottom paddle wheels and the peak discharges as determined from the surface paddle wheels. This is due to the fact that bottom velocity in a flow is lower than surface velocity. Since we're dealing with highly turbulent flows the flow velocity is logarithmically divided over the water depth. Therefore a normalized flow velocity will be closer to surface velocity than to bottom velocity. This taken into account leads to the statement that the measured peak discharges approach the calculated peak discharges well enough to validate the usage of Equation 2.44.

Table 6.4: Calculated peak discharges compared to measured peak discharges.

			Peak discharge q_p per position				
Wave	Test (l)	q_p (calculated)	1-surface	1-bottom	2-bottom	3-surface	3-bottom
First session							
1	0.5	0.34	0.32	0.36	0.19	0.35	0.2
2	0.5	0.34	0.39	0.43	0.13	0.34	0.21
3	0.5	0.34	0.34	0.39	0.18	0.4	0.29
4	1	0.58	0.63	0.69	0.54	0.73	0.7
5	1	0.58	0.54	0.6	0.45	0.7	0.61
6	1	0.58	0.55	0.63	0.4	0.74	0.69
7	1.5	0.78	0.78	0.88	0.65	0.97	0.78
8	1.5	0.78	0.81	0.91	0.73	0.83	0.72
9	1.5	0.78	0.8	0.95	0.62	0.84	0.85
10	2	0.97	1.13	1.17	0.92	0.93	0.83
11	2	0.97	1.03	1.17	0.92	0.99	0.85
12	2	0.97	1.01	1.16	0.99	0.9	0.85
Second session							
1	2.5	1.15	1.04	1.3	1.24	1.08	0.84
2	3	1.31	1.16	1.73	1.52	0.94	0.73
3	3.5	1.47	1.26	1.57	1.83	1.06	0.99
4	2.5	1.15	1.09	1.42	1.44	0.82	0.74
5	2.5	1.15	1.12	1.46	1.42	1.2	1.02

The assumption that wave overtopping induced flow velocity and water depth both decrease linearly in time during an overtopping event is also validated. This is done by plotting lines of Equation

2.46 and 2.47 over the measured data and check for similarities. Three examples are demonstrated in Figures 6.3 to 6.5. The plots show that Equation 2.48 approaches the data points rather well as it comes to the shape of the line. The data however shows a slightly higher peak discharge compared to the calculated peak discharge. As mentioned before, this is partially due to the points at where velocities were measured, namely at the surface and at the bottom, while Equation 2.48 calculates the normalized discharge. However, Equation 2.48 somewhat under-estimates the overtopping wave discharge compared to the data. Therefore the Excess volume approach for wave overtopping provides an overly positive image of the acceptable erosion on the land-side slope.

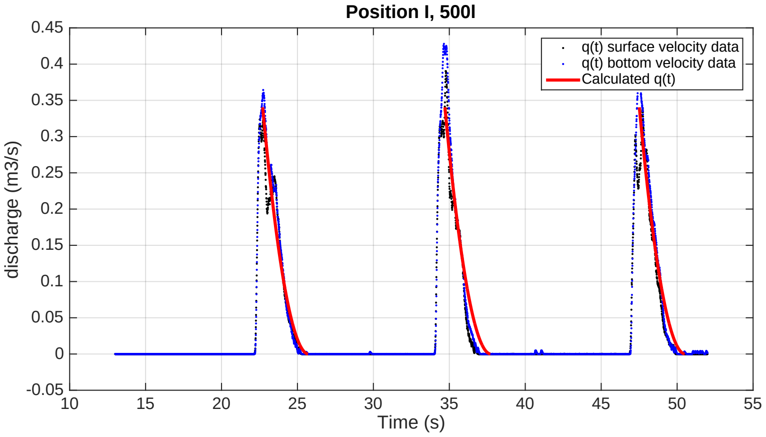

FIGURE 6.3: Discharges as calculated using Equation 2.48 plotted over the measured discharge data at the crest (position I) for a 0.5 m^3 wave

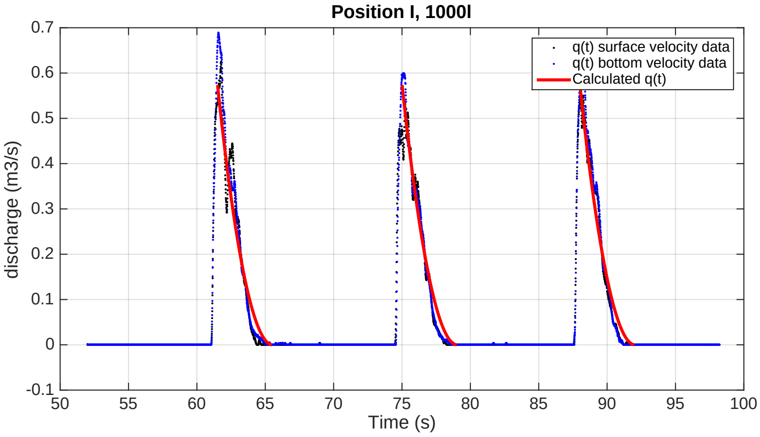

FIGURE 6.4: Discharges as calculated using Equation 2.48 plotted over the measured discharge data at the crest (position I) for a 1.0 m^3 wave

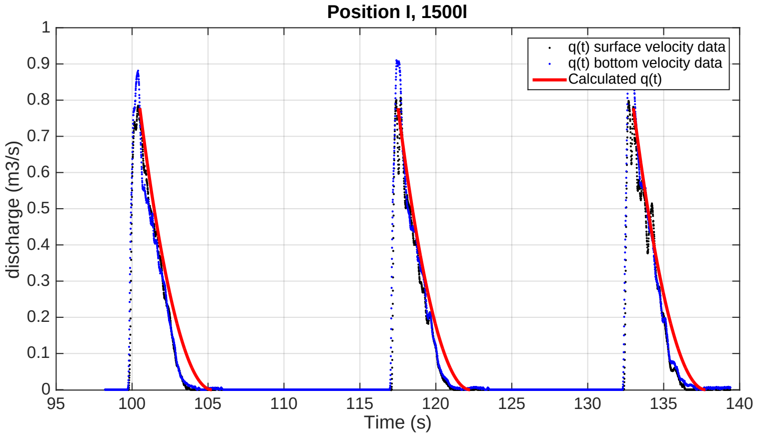

FIGURE 6.5: Discharges as calculated using Equation 2.48 plotted over the measured discharge data at the crest (position I) for a 1.5 m^3 wave

6.4 Application of Excess volume approximation

The right-hand side of Equation 2.52 and 2.54 basically describes the amount of damage on a dike. As described below, this is a factor that should be the constant for both the overtopping and overflow tests. Therefore this entire part has been replaced by the single damage factor D_E:

$$\frac{E_W}{K_W \cdot \beta_W}\left(\frac{f_F}{2g \cdot \sin\theta}\right) = D_E \tag{6.4}$$

Equation 6.1 is applied on the overtopping volumes released during the overtopping experiments at the Wijmeers-II polder in order to calculate the theoretical damage on the land-side slope. The volumes are calculated J.W. Van der Meer using the theory as described by Schüttrumpf and Van Gent [25]. The calculated volumes were documented in a so called steering file, which were used as input values for the wave overtopping simulator. Due to constant calibration of the simulator we can assume that the wave volumes as described in the steering files have actually overtopped the dike during the experiments. Therefore these files are used for calculating the damage factor D_E caused by the overtopping waves, using the theory as described in Section 2.4.1. This value is compared to the same damage factor as calculated by the Excess volume approximation for steady overflow in Section 2.4.2.

A scatter plot of the steering files is given in Figure 6.6. This figure shows the volume of every wave released by the wave overtopping simulator during the test. For each wave volume the corresponding discharge in time $q(t)$ is calculated from which the excess volume is determined. The summation of these excess volumes provides the damage factor D_E. In total two overtopping experiments have been executed on two different test sections during the Wijmeers-II experiments. During the first experiment all waves as described in the steering file, and demonstrated in Figure 6.6, have been released by the simulator. During the second overtopping experiment only the waves for the hydraulic measurement (the second column in Table 5.2) and the 25 l/m/s tests have been executed. This means after the hydraulic measurement the wave volumes as presented in the lowest scatter plot in Figure 6.6 have been released over the land-side slope. The input values for the excess volume approximation on steady overflow are given in Table 6.5.

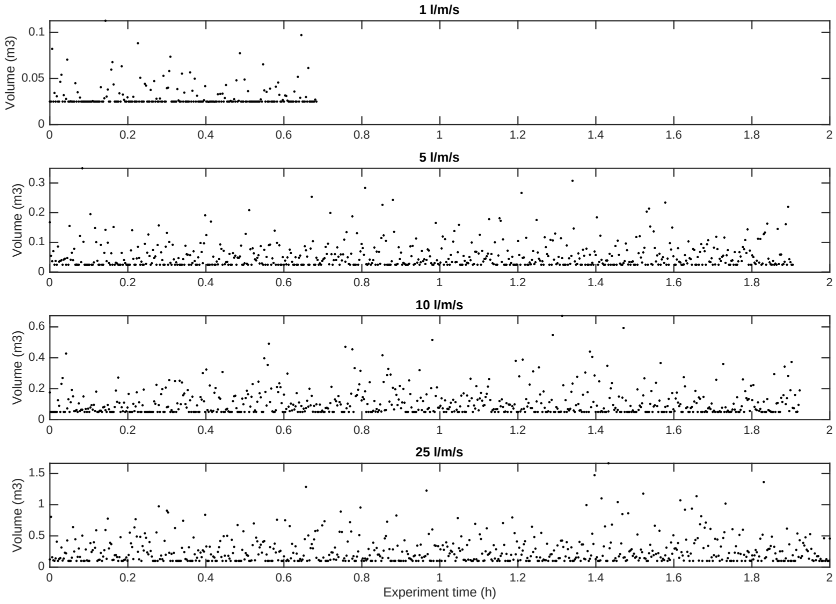

FIGURE 6.6: Scatter plot of the waves as released by the overtopping simulator during the 1, 5, 10 and 25 l/m/s tests.

TABLE 6.5: Input data for the overflow tests

Experiment 1		Experiment 2	
Discharge $[m^3/s]$	Duration [s]	Discharge $[m^3/s]$	Duration [s]
0.010	7200	0.125	3600
0.025	7200	0.170	3600
0.050	7200		
0.085	7200		
0.125	7200		
0.170	7200		

The Wijmeers-II experiments have provided the unique opportunity to compare the impact of overtopping waves and a steady overflow on the same land-side slope of a dike. This means the strength conditions for both overtopping and overflow tests were the same. Therefore uncertainties like animal activity and historic weather conditions, which all affect the friction factor f_F, suddenly become irrelevant since they are the same for both experiments. In previous overflow and overtopping experiments a correction factor had to be added to compensate for these uncertainties. For the application of the Excess volume approximation this means D_E should be the same for both overtopping and overflow when an equal amount of damage appears. This is important as this provides the opportunity to verify the approach as developed by Hughes [17, 18]. The result of the overtopping and overflow experiments clearly show a completely collapsed dike after the overtopping experiment and a more or less intact dike after the overflow experiment, as demonstrated in Figure 6.7a and 6.8a.

According to the Excess volume approximation this would mean D_E calculated from the overtopping experiments should be significantly higher than D_E calculated from the overflow experiments.

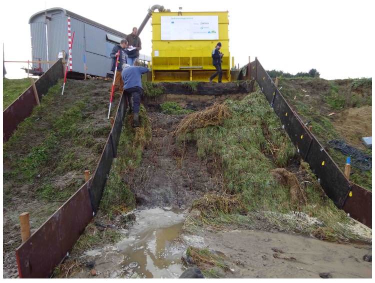

(A) Final result overtopping experiment 1.

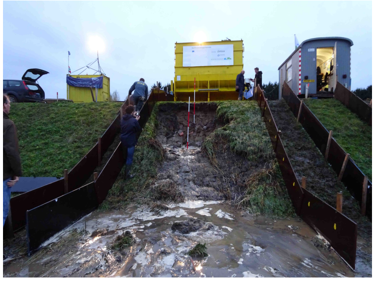

(B) Final result overtopping experiment 2.

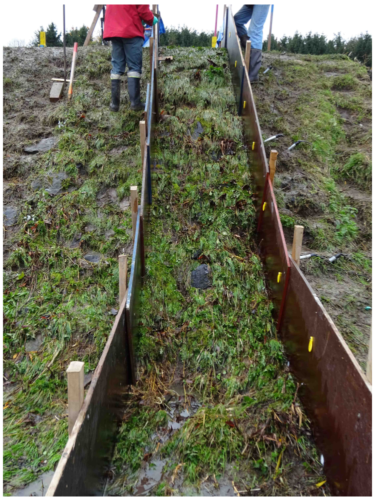

(A) Final result overflow experiment 1.

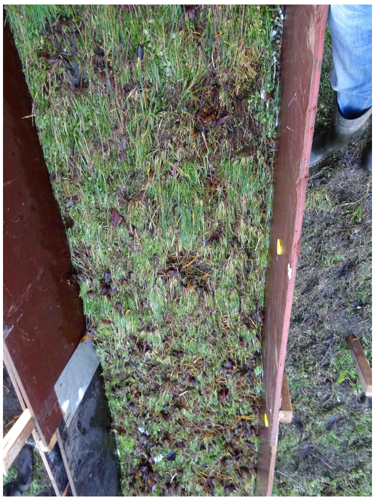

(B) Final result overflow experiment 2.

6.4.1 Result

Using the input data as described earlier a value for the damage factor D_E was calculated for each experiment. The result is presented in Table 6.6.

TABLE 6.6: Result of the Excess wave volume calculations

Experiment	Damage factor D_E				
	$u_c = 0.5$	$u_c = 1.0$	$u_c = 1.5$	$u_c = 2.0$	$u_c = 2.5$
Overtopping 1	2194.1	2187.5	2168.5	2128.5	2056.9
Overflow 1	3337.1	3260.9	3054.0	2651.1	1986.9
Overtopping 2	690.6	687.7	679.3	662.0	631.5
Overflow 2	1060.2	1047.5	1013.0	945.9	835.2

The D_E values as presented in Table 6.6 only show higher D_E values for overtopping compared to overflow when a threshold velocity of $u_c = 2.5$ m/s is applied. Dean et al. [10] found for a grass sod of the classification *plain grass-good cover* a threshold value $u_c = 1.80$. This implies that the grass sod at Wijmeers-II was significantly better than the best grass cover ever tested by Dean et al. This is contradictory to grass cover research on the actual dike, since the grass cover at the Wijmeers-II dike was classified as *very poor* prior to the experiments.

6.5 Conclusion and discussion

Table 6.6 clearly shows results that were not expected at all when looking at Figures 6.7a and 6.8a. Almost all calculated D_E values for overtopping are significantly lower than their corresponding overflow test values while according to the Excess volume theory it should be vice versa. This result indicates that the Excess volume approximation as presented by Hughes [17, 18] needs some improvement in order give a better representation of reality. There are multiple reasons for this statement:

- The Excess volume approach assumes shear stress to be the leading force in the failure of a grass or clay cover during overtopping events. Looking at footage of the Wijmeers-II experiments gives reason to doubt this assumption.
- The theory is based on results from overflow experiments. The flow of an overtopping wave is therefore assumed to be equal to overflow, which is in reality not the case.
- The theory is based on empirical relations rather than pure physics. This makes it hard to apply on other situations than the experiment conditions.

Since the Wijmeers II experiments are the first time both overtopping and overflow experiments have been tested on the same dike section this is also the first time the Excess volume approximation has been validated with realistic data. Now, it appears the approach cannot be verified with the data. Therefore, in the remaining part of this thesis, a new approach has been developed to explain the difference in results.

7 | Wave impact approach

A new approach has been developed for the determination of damage on the land-side slope of a dike. For this new approach the leading failure mechanism is not assumed to be caused by bed shear stress but by the impact stress of the overtopping wave. After extended inspection of footage of overtopping waves, an overtopping wave appeared to be separated from the land-side slope for quite some distance before being reattached with the grass cover. The wave overtopping induced jet load on the slope is not included in any existing wave overtopping erosion model to thus far, therefore an attempt is made to include this in a new modelling approach.

7.1 Failure mechanism

Based on footage of the experiments a failure process of the land-side slope can be distinguished as follows: The first step in the failure process is failure of the grass sod. Once the grass sod is removed the supporting clay layer is exposed. A scour hole develops in the clay layer until the sand core is reached. When the sand core is reached the erosion rates rapidly increase. The scour in the sand core develops due to head-cut erosion. Each of these processes is explained further in Sections C.1.2 to C.1.5. During the Wijmeers-II experiments the moment of initial failure appeared to be crucial for the entire failure process. The erosion process increases rapidly once the clay cover is exposed. Summarizing, the failure process of a land-side slope can be divided into four phases. Since this study focusses on the initial failure process of land-side slope, only phases 1 and 2 will be considered from now on. The four phases are:

1. Initial failure of grass sod
2. Clay cover failure
3. Scour development in sand core
4. Head-cut erosion

7.1.1 Phase 1: Initial failure of grass sod

Initial failure of the grass cover on a land-side slope mostly occurs due to the impact effect of multiple waves in which a so called roll-up process occurs. This process is described in previous studies by Hoffmans [15] and Trung & Verhagen [31]. Direct failure of a grass cover due to a single wave impact happens as well, a piece of grass and clay is then washed away by the impact and flow force of a single wave. However, the required impact stress to achieve this is in most cases so high that this is only exceeded by very little waves. During the roll-up failure process fatigue due to multiple smaller waves plays a more significant role. Direct failure of the grass cover was observed during the hydraulic measurements of the Wijmeers-II experiments. When the simulator was filled to its maximum capacity, the impact stress of the released wave smashed a piece of grass sod out of the grass cover at the impact point. The wave volume at which direct failure occurred was however 1.5 times larger than the biggest wave during the storm simulation experiments. During these experiments direct failure was not documented.

An overtopping wave develops both an impact force induced compressive stress as well as a shear stress on the grass sod causing pieces of grass sod to be pulled out of the cover layer. Interesting enough, as documented during the Wijmeers-II experiments, stems of the grass were all more or less intact when a clump was pulled out. This indicates a failure process due to failure of clusters of roots pulled out of the clay cover and not failure of individual stems of grass. Hoffmans et al. [15] extensively researched this failure process, for details see Sections C.1.2 and 7.4. The documented damage patterns during the Wijmeers-II experiments are in relatively well agreement with the damage patterns described by Hoffmans [15] and Trung and Verhagen [31].

’Roll up’ damage

In their report, Trung and Verhagen [31] describe the failure processes of grass covered slopes due to overtopping as the process of ’roll up’ damage. Trung and Verhagen describe the findings of similar overtopping experiments as Wijmeers-II, only this time in Friesland in The Netherlands. This roll up process, in which the grass cover basically rolls up like a carpet, is a failure process that has been documented multiple times during the Wijmeers-II experiments. The process of roll up is visualized in Figure 7.1. Pieces of the grass sod were turned up side down at the edges of two failed areas. The top layer of about 10 to 15 cm, where usually the highest roots test concentration occurs, was cut underneath and lifted. So the grass cover was cut at a depth where the root density was low. The sod was swept away to expose the soil body underneath. Trung replaced the grass strength factor σ_g, described by Hoffmans [14, 15], by the summation of the individual strength of the roots as measured in a certain area from which a cohesion factor c is derived.

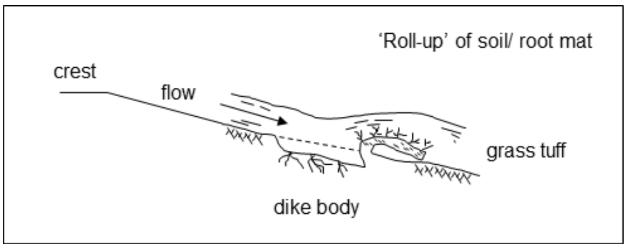

Figure 7.1: Roll up failure process of grass cover as visualized by Trung & Verhagen [31].

7.1.2 Grass cover failure process described from Wijmeers-II observations

A description of the observed erosion processes documented by the author during the Wijmeers-II experiments is given in this section, which is visualized in further detail in Figures 7.3a to 7.3f. The process starts with a small crack in the grass/clay cover (Figure 7.3a). These cracks are the result of natural expansion and shrinkage of the clay cover due to saturation variations and temperature influences. A small crack increases due to wave impact pressure. Wave overtopping induced jet pressure in the crack pushes the walls further aside, which deepens the crack (Figure 7.3b). When the crack reaches the depth of the clay layer below the grass cover a hole starts to form under the grass cover. This is due to the much lower cohesion of pure clay compared to the root/clay mixture. Wave overtopping induced jet pressure pushes the soil under the grass cover aside much easier, leading to widening of the hole beneath the grass cover. The grass cover itself widens much slower (Figure 7.3c). The process of widening of the cracks causes grass aggregates to be pushed out of the grass cover along a shear plane, which leads to increase of the hole formed under the grass cover. This expansion process forms a kind of tunnel under the grass cover. The overtopping induced jet pressure in the freshly formed tunnel causes grass aggregates to be lifted from the cover layer (Figure 7.3d). The flow over the grass cover and the overpressure under the grass cover separates the grass sod from the clay layer and rolls up like a carpet over the downstream grass cover. At a certain moment the overtopping induced pressure under the grass cover becomes too high leading to a piece of grass sod to be ripped from the grass cover and washed away by the flow (Figure 7.3e). After this initial failure of the grass cover the whole process of tunnelling and roll-up of the grass cover repeats itself leading to more pieces of grass sod to be ripped from the cover (Figure 7.3f). Reference pictures for these proposed 6 steps in failure initiation are given in Figures 7.4a to 7.4f.

7.1.3 Phase 2: Clay cover failure

The Wijmeers-II experiments have shown the significant difference in erodability between a constant overflow load on grass cover and constant overflow load on exposed clay. A 125 $lm^{-1}s^{-1}$ followed by a 170 $lm^{-1}s^{-1}$ overflow test, both lasting 1 hour, did not damage the grass cover while a 45 min. lasting 30 $lm^{-1}s^{-1}$ overflow test caused major damage to the exposed clay cover. Since the grass cover was still intact after the 125 and 170 $lm^{-1}s^{-1}$ tests it is hard to determine the actual difference in strength between grass cover and exposed clay cover.

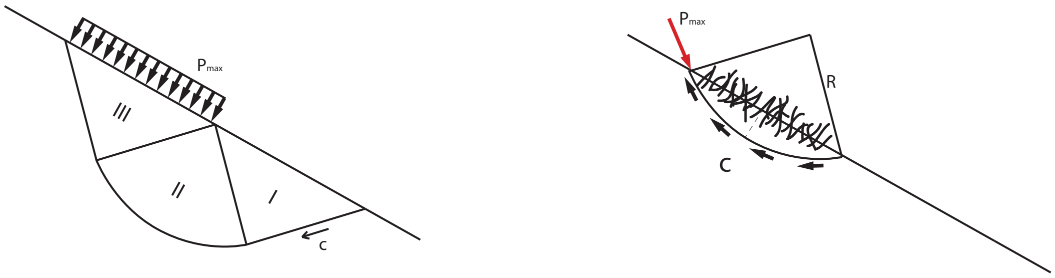

FIGURE 7.2: Direct clay erosion due to a distributed load and a point load.

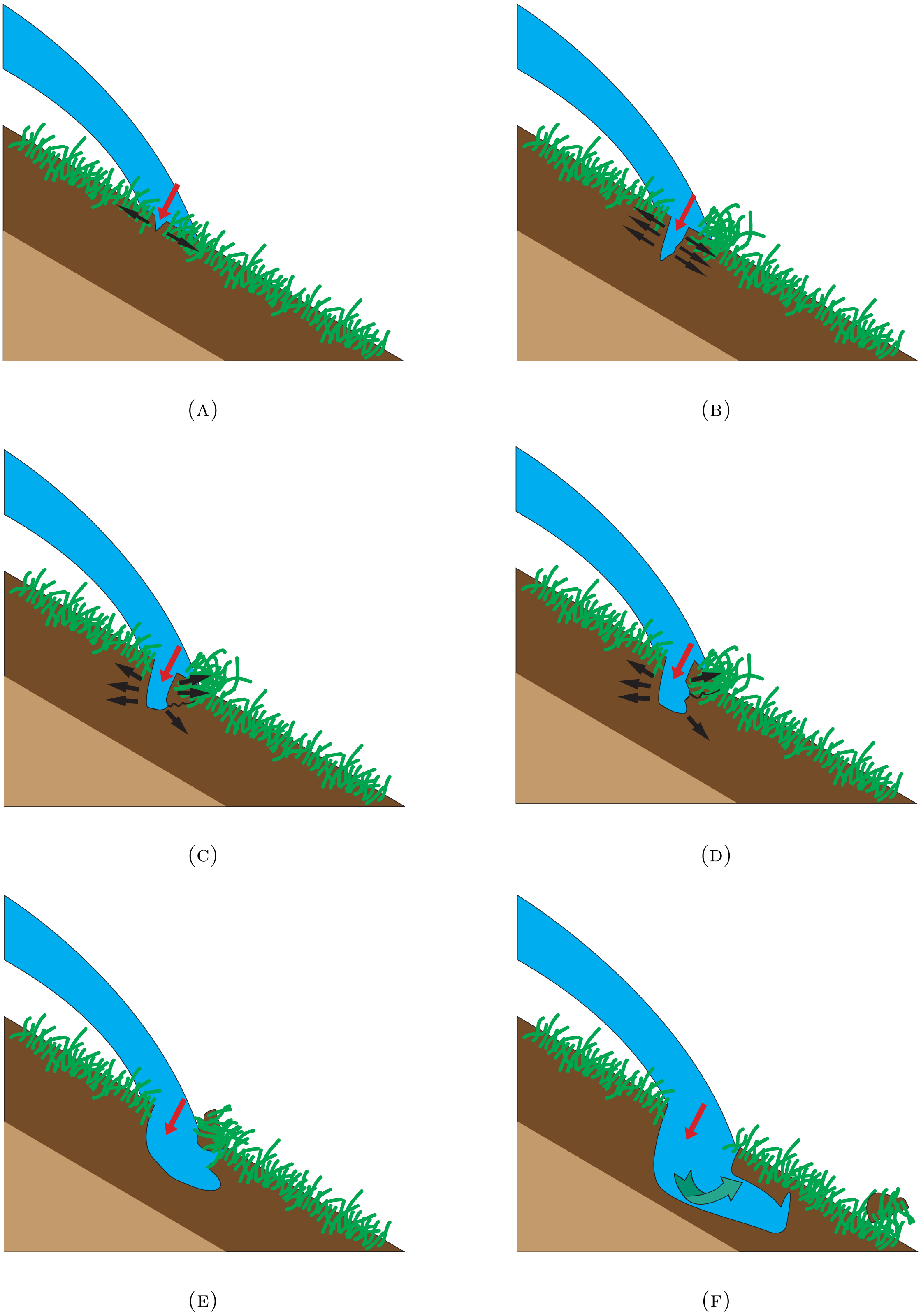
(A) (B) (C) (D) (E) (F)

Figure 7.3: Failure initiation process clarified in 6 steps.

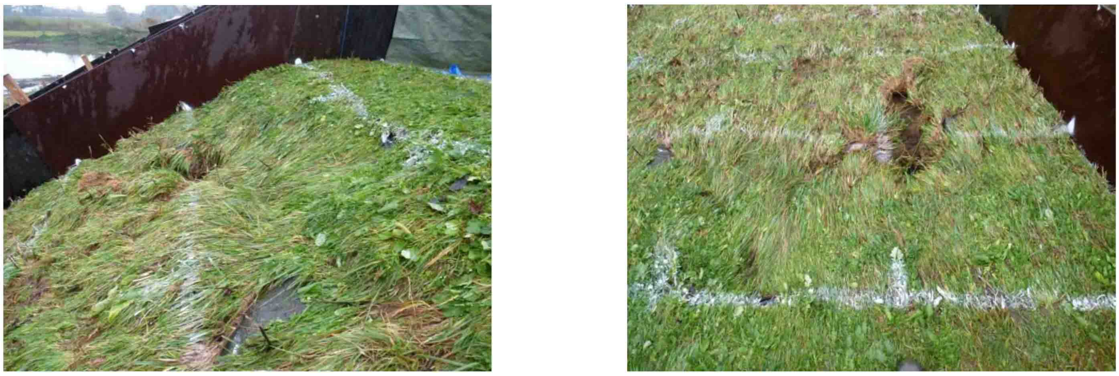

(a) Reference for Figure 7.3a

(b) Reference for Figure 7.3b

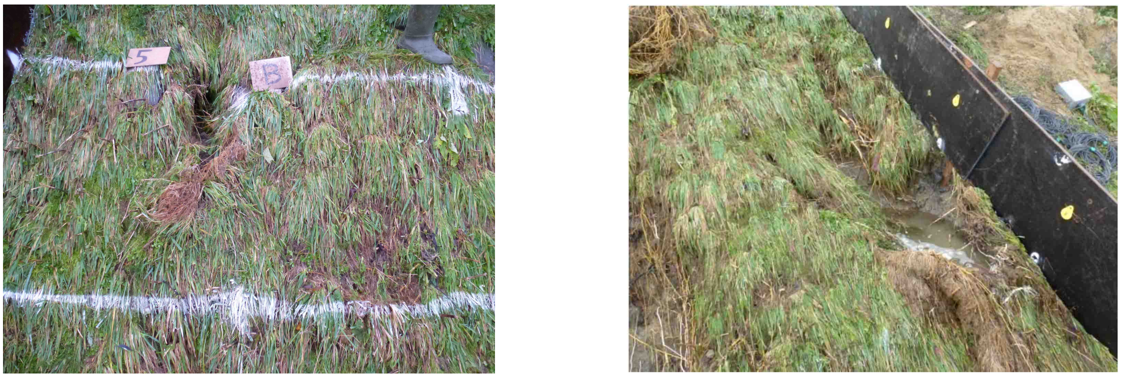

(c) Reference for Figure 7.3c

(d) Reference for Figure 7.3d

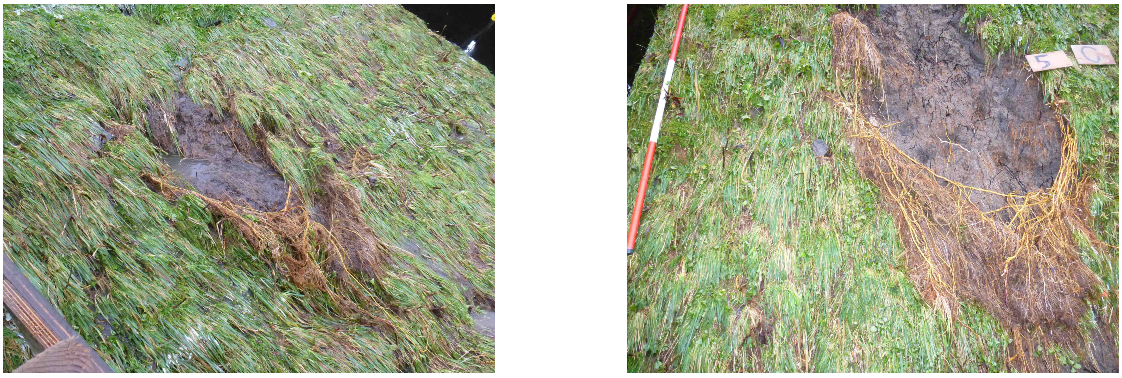

(e) Reference for Figure 7.3e

(f) Reference for Figure 7.3f

Figure 7.4: Reference pictures from the Wijmeers-II experiments for the failure initiation process.

7.2 Wave impact effect

When looking in further detail to the Excess volume approach as suggested by Hughes [17, 18] some (at first view) important factors are not included. In the approach an overtopping wave is assumed to be a flow of duration T_o with decreasing discharge $q(t)$ in which T_o and $q(t)$ can be calculated by the wave volume V. This is not a correct representation of an overtopping wave for two reasons:

- An overtopping wave is separated from the slope for a short period of time before reattached with the land-side slope. This is due to the horizontal wave velocity at the crest. Especially for high volume waves this horizontal velocity can be significant, leading to a distance over which the wave is separated up to 7 m. Therefore only the lower part of the land-side slope is attacked by overtopping waves.
- Due to the separated phase of the overtopping wave there is a certain impact force that could lead to immediate damage on the grass sod, as observed during the 3000 l/m wave during the hydraulic measurements. The wave impact induced force or pressure should be taken into account when determining failure mechanisms of the grass cover.

Figure 7.5 demonstrates a 1000 l. overtopping wave during the hydraulic measurements. The figure shows that the overtopping wave does not make contact with the land-side slope for a significant distance. In Figure 7.5d the first contact with the grass cover is visible, which is in the order of 2.5 to 3 m viewed horizontally from the crest line.

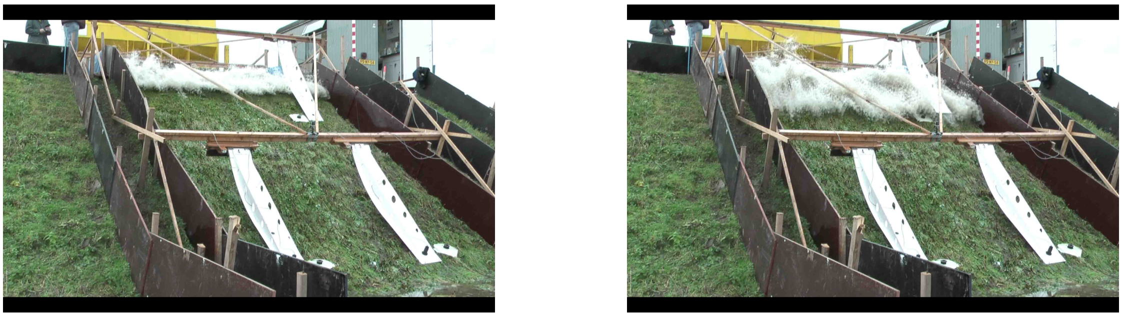

(A) Wave front at the crest (B) Separated from land-side slope

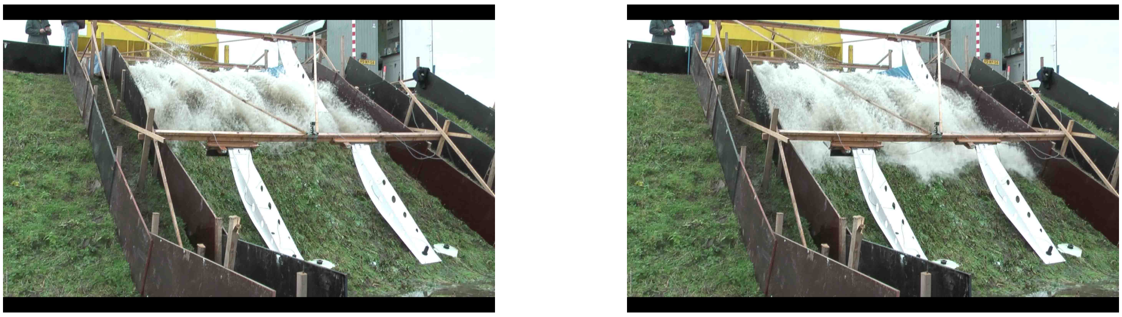

(C) Still separated (D) Moment of impact

FIGURE 7.5: Separation time of an overtopping wave before making contact with the land-side slope. The wave in this case is a 1000l wave during the hydraulic measurements.

In Section 7.3 the impact load of an overtopping wave is determined. In order to determine this impact load, numerous parameters are required which describe wave overtopping processes and how the load of an overtopping wave acts on the land-side slope. The required parameters for the impact load are the separation time of an overtopping wave, the impact location, angle of impact and wave overtopping induced jet stress. These parameters combined eventually lead to an equation that determines wave overtopping induced impact loads.

7.2.1 Separation time

The location of impact of an overtopping wave is determined by following the trajectory of an overtopping wave, which follows from an energy balance in which the air resistance is neglected. This assumption taken into account, the following relations describe the trajectory of an overtopping wave. X-coordinate (horizontal coordinate):

$$X(t) = u_x \cdot t \qquad\qquad t = \frac{x}{u_x} \tag{7.1}$$

With u_x the horizontal velocity component and t the time. The Z-coordinate (vertical coordinate) becomes:

$$Z_{\text{wave}}(t) = -\frac{1}{2} \cdot g \cdot t^2 \tag{7.2}$$

The trajectory of a wave in an x-z system is described by:

$$Z_{\text{wave}}(t) = -\frac{1}{2} \cdot g \left(\frac{X}{u_x}\right)^2 \tag{7.3}$$

7.2.2 Wave impact location

The relations above are to determine the impact location of an overtopping wave. An overtopping wave not only has a velocity but also a certain 'thickness' which is described as the water depth at the crest of the dike. Because of this wave thickness it is more realistic to speak of a wave impact *plane* rather than an impact *point*. An example of the trajectory of an overtopping wave with a certain wave thickness is demonstrated in Figure 7.6.

In this case the slope of the dike is the slope as measured at the Wijmeers-II dike, which is 1:1.7 and is therefore described as (see Figure 7.6)

$$Z_{\text{slope}} = -X \cdot \tan\theta \tag{7.4}$$

In which θ is the angle of the slope, so in this case $\tan(\theta) = \frac{1}{1.7}$

When the flow velocity at the crest during a wave overtopping event is assumed to be uniform over the water depth, the trajectory of an overtopping wave looks exactly like Figure 7.6. To describe

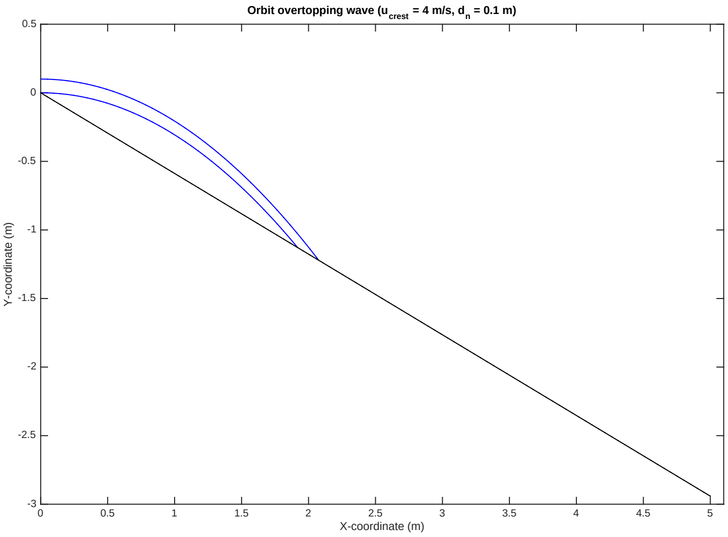

FIGURE 7.6: Orbit of an overtopping wave with horizontal crest flow velocity $u_{\text{crest}} = 4$ m/s and crest water depth $d_{\text{crest}} = 0.1$ m.

this trajectory a water particle at the bottom and a water particle at the water surface of the flow at the crest are considered. These particles represent the respectively minimum and maximum impact point of a wave, described by $X_{\text{wave,min}}$, $X_{\text{wave,max}}$, $Z_{\text{wave,min}}$ and $Z_{\text{wave,max}}$. The impact point of a water particle is the point where Z_{particle} ($= Z_{\text{wave}}$) equals Z_{slope}. The horizontal velocity component u_x is in the case of overtopping defined as the depth averaged flow velocity at the crest u_{crest}, i.e. $u_x = u_{\text{crest}}$. In Figure 7.6 the top blue line represents the orbit of a water particle at the surface of the flow at the crest and the lower blue line represents the orbit of a particle at the bottom of the flow at the crest. The area between these blue lines represents the rest of the water particles in a wave.

Impact locations:

$$Z_{\text{wave,min}} = Z_{\text{slope}} \;\Rightarrow\; -\frac{1}{2} \cdot g \left(\frac{X}{u_x}\right)^2 = -X \cdot \tan\theta \tag{7.5}$$

$$Z_{\text{wave,max}} = Z_{\text{slope}} \;\Rightarrow\; -\frac{1}{2} \cdot g \left(\frac{X}{u_x}\right)^2 + d_{\text{crest}} = -X \cdot \tan\theta \tag{7.6}$$

Since $u_x = u_{\text{crest}}$, this leads to:

$$X_{\text{wave,min}} = \frac{2 \cdot u_{\text{crest}}^2 \tan\theta}{g} \qquad X_{\text{wave,max}} = \frac{u_{\text{crest}}^2 \left(\tan\theta \;+\; \sqrt{\tan^2\theta + \frac{2gd_{\text{crest}}}{u_{\text{crest}}^2}}\right)}{g} \tag{7.7}$$

This leads to an impact plane size:

$$A_{\text{imp}} = \sqrt{(X_{\text{wave,max}} - X_{\text{wave,min}})^2 + (Z_{\text{wave,max}} - Z_{\text{wave,min}})^2} \tag{7.8}$$

NB. This is still under the assumption that flow velocity is uniformly divided over the water depth at the crest.

7.2.3 Wave impact stress

The impact stress of an overtopping wave depends primarily on the impact velocity. The stress of a jet on a surface is basically described as the density times the impact velocity squared. This describes the impact pressure due to a constant jet. The basic relation for constant jet flow induced stress is described by Equation 7.9 and 7.10. In these equations $\tau_{\tilde{z}\tilde{x}}$ is the impact stress component parallel to the slope, $\sigma_{\tilde{z}\tilde{z}}$ is the impact stress component perpendicular to the slope and β the impact angle of an overtopping wave. This is visualized in Figure 7.7.

$$\tau_{\tilde{z}\tilde{x}} = \rho u_{\text{imp}}^2 \ \cos\beta \tag{7.9}$$

$$\sigma_{\tilde{z}\tilde{z}} = \rho u_{\text{imp}}^2 \ \sin\beta \tag{7.10}$$

ρ is the density of the overtopping water. The impact velocity u_{imp} is determined using Pythagoras' equation on the horizontal velocity component u_x and the vertical velocity component u_z.

$$u_{\text{imp}} = \sqrt{u_x^2 + u_z^2} \tag{7.11}$$

The horizontal velocity component is the flow velocity at the crest, the vertical velocity component is determined from an energy balance. As mentioned before the horizontal velocity component u_x is assumed to be constant.

$$mgZ_{\text{wave}} = \frac{1}{2}mu_z^2 \ \Rightarrow \ u_z = \sqrt{2gZ_{\text{wave}}} \tag{7.12}$$

Since $u_x = u_{\text{crest}}$, this leads to:

$$u_{\text{imp}} = \sqrt{u_{\text{crest}}^2 + 2gZ_{\text{wave}}} \tag{7.13}$$

Resulting in impact stress components:

$$\tau_{\tilde{z}\tilde{x}} = \rho \ (u_{\text{crest}}^2 + 2gY_{\text{wave}}) \ \cos\beta \tag{7.14}$$

$$\sigma_{\tilde{z}\tilde{z}} = \rho \ (u_{\text{crest}}^2 + 2gZ_{\text{wave}}) \ \sin\beta \tag{7.15}$$

Substituting Equation 7.5 and 7.7 in Equation 7.14 leads to a new expression for $\sigma_{\tilde{z}\tilde{z}}$ and $\tau_{\tilde{z}\tilde{x}}$:

$$\tau_{\tilde{z}\tilde{x}} = \rho\ (u^2_{\text{crest}} + 2gX\ \ \tan\theta)\ \ \cos\beta \tag{7.16}$$

$$\sigma_{\tilde{z}\tilde{z}} = \rho\ (u^2_{\text{crest}} + 2gX\ \ \tan\theta)\ \ \sin\beta \tag{7.17}$$

Substituting Equation 7.7 for X leads to:

$$\tau_{\tilde{z}\tilde{x}} = \rho\ u^2_{\text{crest}}(1 + 4\ \ \tan^2\theta)\ \ \cos\beta \tag{7.18}$$

$$\sigma_{\tilde{z}\tilde{z}} = \rho\ u^2_{\text{crest}}(1 + 4\ \ \tan^2\theta)\ \ \sin\beta \tag{7.19}$$

The water depth at the crest is not included in Equations 7.18 and 7.19. Therefore these equations only describe the wave bottom induced impact stress. In reality of course an overtopping wave does have a crest water depth which makes Equations 7.18 and 7.19 an incomplete representation for the actual impact stress. Including the overtopping wave crest depth, in this case expressed as the water depth at the crest of the dike, leads to Equations 7.20 and 7.21, describing the wave surface induced stress. Within the impact plane the impact stress decreases from the surface induced stress at X_{max} to the bottom induced stress at X_{min}, which is exaggerated in Figure 7.8.

$$\tau_{\tilde{z}\tilde{x}} = \rho\ u^2_{\text{crest}}\left(1 + 2\tan^2\theta + 2\tan\theta\sqrt{\tan^2\theta + \frac{2gd_{\text{crest}}}{u^2_{\text{crest}}}}\right)\ \cos\varphi \tag{7.20}$$

$$\sigma_{\tilde{z}\tilde{z}} = \rho\ u^2_{\text{crest}}\left(1 + 2\tan^2\theta + 2\tan\theta\sqrt{\tan^2\theta + \frac{2gd_{\text{crest}}}{u^2_{\text{crest}}}}\right)\ \sin\varphi \tag{7.21}$$

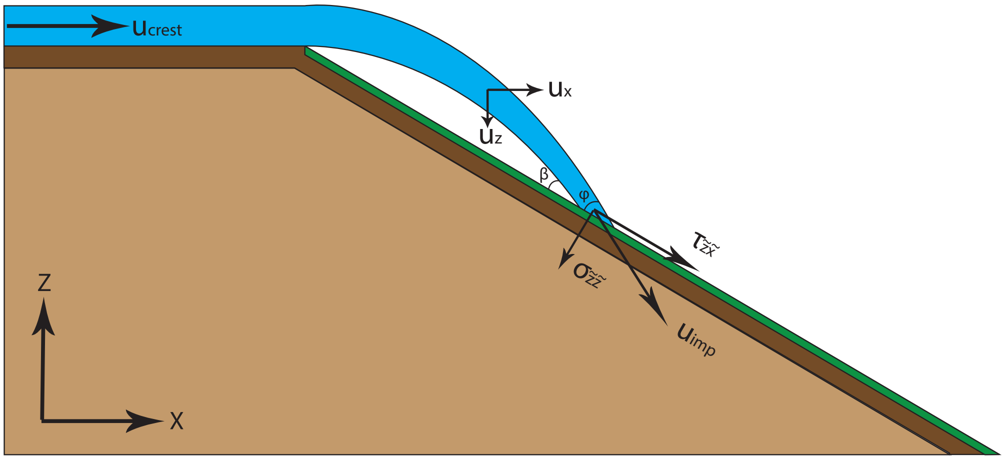

FIGURE 7.7: Wave impact force and impact velocity

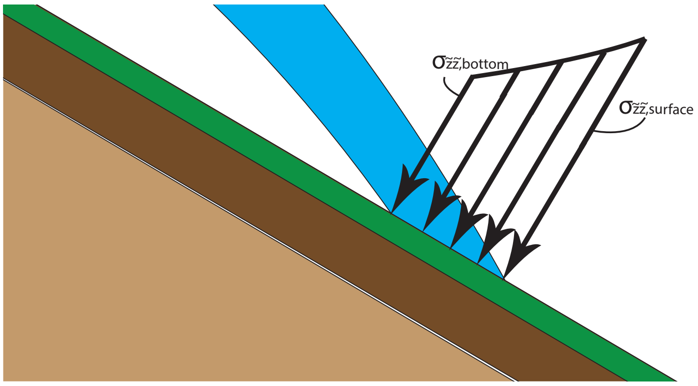
$\sigma_{\tilde{z}\tilde{z},bottom}$
$\sigma_{\tilde{z}\tilde{z},surface}$

FIGURE 7.8: Decrease in overtopping induced jet stress

Equation 7.16 describes the wave overtopping induced jet impact stress perpendicular to the land-side slope at a location X. This impact stress leads to pressure on the grass cover, which causes initial failure of the grass cover as demonstrated in Figures 7.3a and 7.3b. Wave overtopping induced pressure is therefore indicated by the stress component perpendicular to the grass cover i.e. $\sigma_{\tilde{z}\tilde{z}} = P_z$. This pressure term is used in the determination of pressure in crack in the cover layer. When the pressure exceeds a critical pressure threshold, movement of aggregates in the grass and clay cover occurs.

The actual momentum transfer due to impact impulse is not included in this Equation 7.16 since this effect is much harder to describe. In fact a decent relationship to describe the effect of impact of an overtopping wave was not found in literature. Since an overtopping wave is a highly turbulent flow with a high concentration air in the flowing water, the fluid cannot be assumed to be incompressible [28, 29]. This air-water mixture, due to the presence of air bubbles, indicates significantly increased compressibility compared to pure water, which results in higher rate of energy dissipation (pressure damping) and decreased velocity of pressure propagation (50-300 m/s).

In order to test the effect of wave impact on the outer slope of a dike, a wave impact simulator was developed by Deltares [39]. In a large wave flume the effects of wave impact on the outer slope were tested as well [39]. An empirical relation was developed from these experiments. This relation has never been tested to be valid for land-side slopes, which makes it unusable for this research.

Due to the complexity of the actual impact effect of an overtopping wave, a decent approxiamation of this effect cannot be made, therefore this aspect is not considered further.

7.2.4 Wave impact angle

The wave bottom and wave impact angle β and surface wave impact angle φ are calculated using the trajectory of the wave as determined in section 7.2.2. The impact angle is determined by the derivative of the wave trajectory equation at the point of impact (Equation 7.5 to 7.7). The arctangent of this derivative describes the angle of impact.

Impact angle of the bottom of the wave β:

$$\frac{dY_{\text{wave,min}}}{dX_{\text{wave,min}}} = -\frac{g}{u_{\text{crest}}^2} X_{\text{wave,min}} \tag{7.22}$$

Including $X_{\text{wave,min}}$:

$$\frac{dY_{\text{wave,min}}}{dX_{\text{wave,min}}} = -\frac{g}{u_{\text{crest}}^2} \frac{2\ \tan\theta\ u_{\text{crest}}^2}{g} = -2\ \tan\theta$$

The impact angle is the arctangent of the above equation, whith the minus sign is left out of the equation. This is allowed since this has no effect on the magnitude of the angle. The actual impact angle is described when the slope angle θ is distracted from the arctangent of the derivative:

$$\beta = \text{atan}(2\tan\theta) - \theta \tag{7.23}$$

Impact angle of the surface of the wave φ:

$$\frac{dY_{\text{wave,max}}}{dX_{\text{wave,max}}} = -\frac{g}{u_{\text{crest}}^2} X_{\text{wave,max}} \tag{7.24}$$

Including $X_{\text{wave,max}}$:

$$\frac{dY_{\text{wave,max}}}{dX_{\text{wave,max}}} = -\tan\theta + \sqrt{\tan^2\theta + \frac{2gd_{\text{crest}}}{u_{\text{crest}}^2}}$$

Which leads to an expression for the surface impact angle φ:

$$\varphi = \text{atan}\left(\tan\theta + \sqrt{\tan^2\theta + \frac{2gd_{\text{crest}}}{u_{\text{crest}}^2}}\right) - \theta \tag{7.25}$$

7.3 Damage on land-side slope

Damage on the land-side slope is related to the wave overtopping induced load on the slope. In order to determine the damage on the land-side slope after a storm, in which numerous waves overtop the dike, the damage due to an individual wave needs to be determined. Therefore, the load of an overtopping wave is determined first, secondly the load (and therefore also damage) caused by numerous overtopping waves is considered.

7.3.1 Individual wave overtopping load

The Wave overtopping induced load on the land-side slope of a dike is determined by considering an overtopping wave as a water jet. This wave overtopping induced jet flows attacks the land-side slope under an angle leading to stresses as described in Section 7.2.3. Since the crest velocity and crest water depth decrease in time during an overtopping wave, the impact location X also changes within a single overtopping event. Therefore an overtopping wave is much like a a jet moving from the maximum impact point towards the crest of which the flow velocity and thickness decrease during the process. An overtopping wave basically 'pulls back' to the crest once it has made contact with the land-side slope. This phenomenon is demonstrated in Figure 7.9.

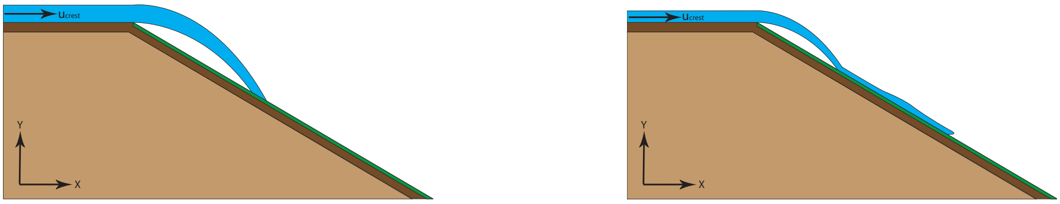

(A) Initial contact moment (B) Impact location moves towards crest

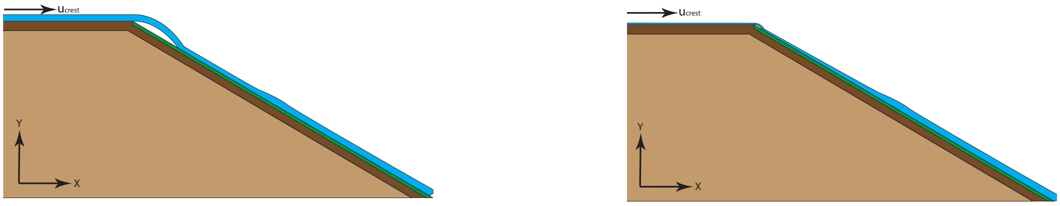

(C) Crest flow velocity decreases (D) Crest flow velocity goes to zero

FIGURE 7.9: An overtopping wave basically 'pulls back' once it has made contact with the land-side slope.

Equation 7.16 shows that the impact location X forms a linear relation with the impact load. The impact location in time, as demonstrated in Figure 7.10, however does not show a linear relation.

Wave overtopping induced stress on the land-side slope $\sigma_{\tilde{z}\tilde{z}}$ can be expressed as a relation with the X-coordinate as derived in Equation 7.16. Since the wave overtopping induced jet is moving, and not constant at one point, it is important to include the time the jet load is applied at a certain location X in order to determine the total load after numerous waves. This time element is important since a small jet load applied for a long time produces the same change in momentum (the same impulse) as a larger jet load applied briefly. Therefore a time element needs to be added to obtain a relation describing the impulse load J_z perpendicular to the land-side slope. This time element is the time

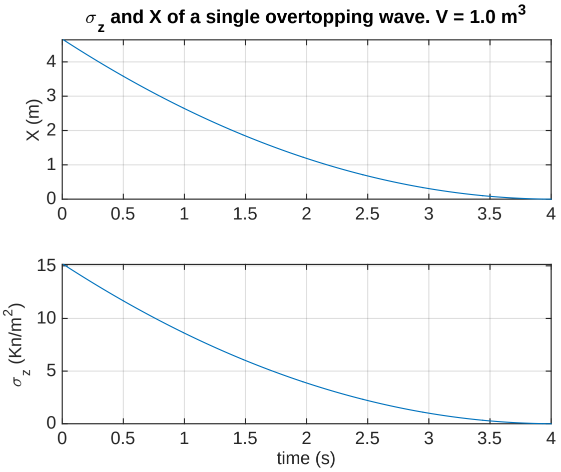

FIGURE 7.10: Example of the impact point and wave load of a single overtopping wave plotted over time. The overtopping volume of this example is 1.0 m^3

a wave load contributes to damage on a certain location on the land-side slope i.e. the time the jet load is applied at location X during a single overtopping wave. For each individual overtopping event this time element at location X is defined as Δt_n. Which leads to the following relation for wave overtopping induced impulse load on the land-side slope:

$$J_z = \rho(u^2_{\text{crest},n} + 2gX_n \ \tan\theta) \cdot \sin\varphi \cdot \Delta t_n \tag{7.26}$$

Δt_n is the time the jet load is applied at location X, which is the time between the moment of impact of the bottom of the wave and the moment of impact of the surface of the wave at location X. This time difference is demonstrated in Figure 7.11. Δt_n could be determined analytically by expressing t in terms of X using the relations published by Hughes [17, 18] (Equations 2.46 and 2.47). This however leads to an unworkable long equation, therefore Δt_n is determined numerically. For an explanation of the numerical determination of Δt_n reference is made to Section 7.6.

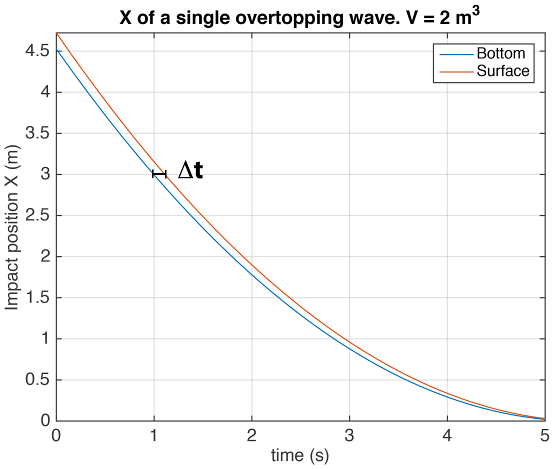

FIGURE 7.11: Example of the impact location a single overtopping wave plotted over time.The overtopping volume of this example is 2.0 m^3

7.3.2 Total load on land-side slope

The total load at location X on the land-side slope during a storm, in which many waves overtop the dike, is determined by the summation of all wave overtopping induced impulse loads applied at location X. This cumulative impulse load is given by:

$$J_{z,\mathrm{tot}} = \sum_{n=1}^{N} \rho(u^2_{\mathrm{crest},n}(t) + 2gX_n(t)\ \tan\theta) \cdot \sin\varphi \cdot \Delta t_n \tag{7.27}$$

7.3.3 Damage threshold

For the determination of damage on the land-side slope, the failure mechanism of the grass and clay cover described in Section 7.1 is observed again. Figures 7.3a and 7.3b show that the walls of a crack in the grass cover are pushed aside due to wave overtopping induced jet pressure. Movement of the walls occurs when the wave overtopping induced jet pressure exceeds a certain threshold, which is called the critical pressure P_c. As mentioned in Section 7.2.3 the wave overtopping induced pressure in a crack is determined by the impact stress (see Figure 7.12), leading to:

$$P_{\mathrm{crack}} = \rho\ (u^2_{\mathrm{crest}} + 2gX\ \tan\theta)\ \sin\beta \tag{7.28}$$

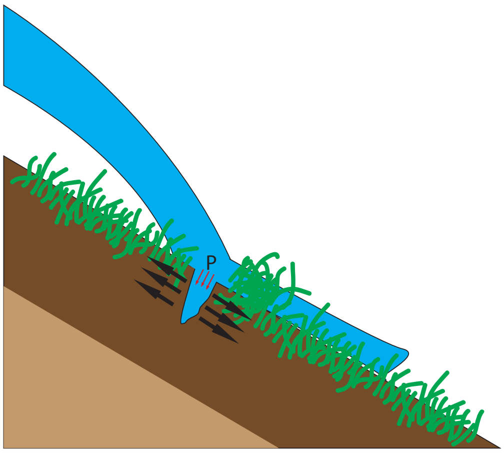

FIGURE 7.12: The pressure in a crack is caused by wave overtopping induced stress on the land-side slope.

If the overtopping induced pressure in the crack exceeds the critical pressure, the crack widens which eventually leads to damage on the grass cover. Therefore an overtopping wave contributes to damage on the land-side slope when its overtopping induced jet pressure exceeds P_c. In other words, damage occurs when:

$$P_{\text{crack}} > P_c \tag{7.29}$$

7.3.4 Maximum damage indication

The process of widening of the crack, erosion under the grass cover and pushing grass aggregates out of the grass layer (Section 7.1) is often not achieved by a single overtopping wave. The overtopping induced impulse is too small to lead to direct removal of aggregates from the grass cover. Numerous waves, of which the overtopping induced jet pressure exceeds the critical pressure, are therefore required to lead to actual removal of aggregates from the grass cover. In other words a certain number of impulses exceeding the critical pressure is required to cause removal of aggregates from the grass and clay layer. This situation is indicated in Equation 7.31. The impact of numerous overtopping waves leads to a fatigue like load on the land-side slope which leads to grass aggregate movement. During the Wijmeers-II experiments the latter was documented to be the leading mechanism for grass aggregate movement. Slow removal of aggregates from the grass cover due to numerous wave impacts was documented many times. Every overtopping wave contributing to aggregate movement pushed aggregates further out of the grass cover. Grass aggregates smashed out of the grass cover due to a the impact of a single overtopping wave was documented once, but this was caused by an unrealistically large wave volume. Damage on the land-side slope, i.e. movement of grass aggregates, therefore is assumed to be caused by the fatigue like load due to multiple overtopping waves and not by the impact of a single overtopping wave. This fatigue like load is indicated by the excess wave overtopping induced impulse of overtopping waves of which the jet pressure exceeds the critical pressure. This excess overtopping induced impulse J_E indicates the excess impulse load on the land-side slope. The maximum damage on the land-side slope during a storm therefore is expected to occur at the location at which the highest cumulative excess impulse load occurs.

$$J_E = (P_{\text{crack}} - P_c)\,\Delta t_n \qquad \text{for } P_{\text{crack}} \geqslant P_c \tag{7.30}$$

The total damage at location X during a storm becomes the summation of the damage caused by each individual wave:

$$J_{E,\text{tot}} = \sum_{n=1}^{N} (P_{\text{crack},n} - P_c) \cdot \Delta t_n \qquad \text{for } P_{\text{crack}} \geqslant P_c \tag{7.31}$$

Or:

$$J_{E,\text{tot}} = \sum_{n=1}^{N} (\rho(u_{\text{crest},n}^2 + 2gX_n \;\tan\theta) \cdot \sin\varphi - P_c) \cdot \Delta t_n \tag{7.32}$$

Figure 7.13 shows the cumulative impulse load at location X caused by the waves as applied during the Wijmeers-II experiments. The figure clearly shows a peak around the X = 0.5 to 1.0 m zone. This however is not the zone at which the first damage on the dike occurred at Wijmeers-II. This is due to the cumulative effect of small waves. Although each individual small wave does not do too much damage to the slope, all the small waves summarized lead to a big cumulative load. This theoretical large cumulative load however is only a measure for damage when each individual wave has indeed contributed to damage on the grass cover i.e. if each individual wave has exceeded the critical impact pressure (P_c) which is a threshold required to cause damage. A wave overtopping induced jet load lower than this initial damage threshold will never cause any damage, no matter how many waves overtop the dike[1]. Only when the impact load exceeds the threshold a contribution to damage occurs.

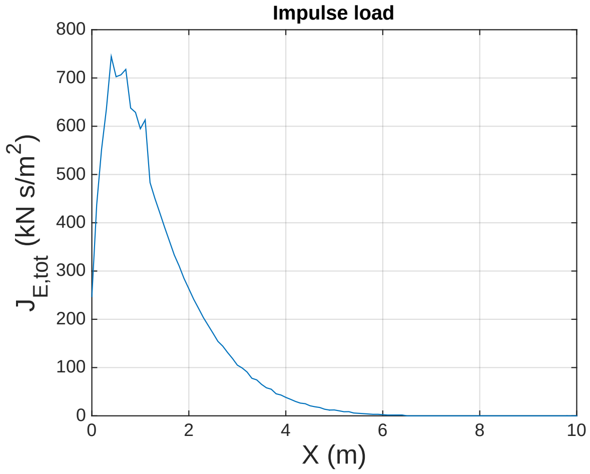

FIGURE 7.13: Cumulative wave load of the waves as applied during the Wijmeers-II experiments.

For the purpose of determination of the location at which the most daage occurs, Equation 7.32 is applied on the wave data from the Wijmeers-II experiments. Plots of the excess impulse load $J_{E,\text{tot}}$ calculated from this data, with varying critical pressures values, are demonstrated in Figure 7.14. The peak in each plot marks the location at which the highest cumulative excess impulse load occurs i.e. where the most damage is expected. The crest water depth of overtopping waves is not included in these plots yet. A numerical approach is required for calculating wave impact induced impulse load with crest water depth taken into account. An analytical solution for including the crest water depth is not possible due to the assumption of a uniform velocity profile at the crest. This is demonstrated later on in Section 7.5. Therefore a numerical approach for the determination of wave overtopping impact including the water depth at the crest is disclosed, which is treated in Section 7.6.

---

[1] When a large amount of waves with a wave load lower than the threshold value overtop the dike damage could still occur. This however includes different failure mechanisms that are not within the scope of this research.

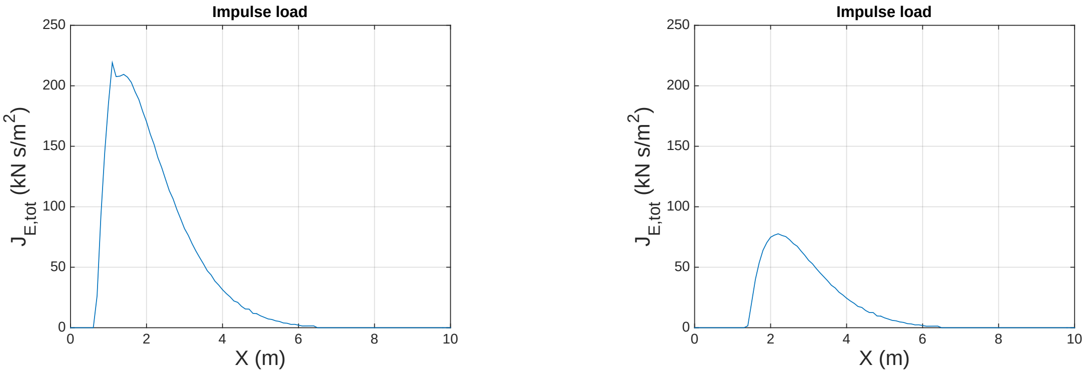

(A) $P_c = 5\ kN/m^2$ (B) $P_c = 10\ kN/m^2$

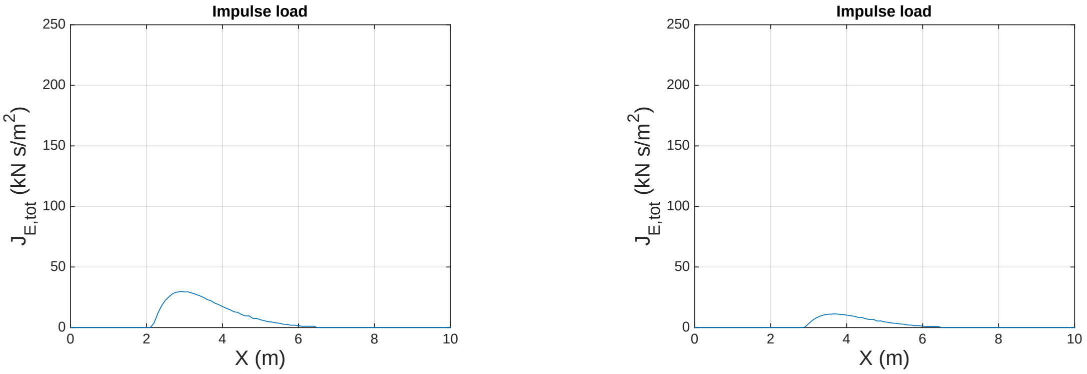

(C) $P_c = 15\ kN/m^2$ (D) $P_c = 20\ kN/m^2$

FIGURE 7.14: Cumulative wave load of the waves as applied during the Wijmeers-II experiments. The overtopping wave thickness is in these plots not taken into account yet.

7.3.5 Residual strength land-side slope

In order to determine whether the amount of erosion on the land-side slope has reached an erosion level in which the land-side slope is classified as *failed* a critical damage parameter D_c is introduced. This parameter determines after how much damage on the land-side slope the cover layer is no longer safe. This parameter has units kNs/m^2, which is the same unit as the outcome of the Wave impact approach model. This threshold parameter is a measure for the time a land-side slope can withstand wave overtopping during a storm. Subsequently D_c indicates the residual strength of a grass cover layer. This is further described in Appendix D.

7.4 Quantification of damage threshold

The failure location on the land-side slope of a dike due to wave overtopping is determined using the earlier developed wave impact calculation method. This method requires a threshold value P_c to determine whether the wave overtopping induced jet pressure of an overtopping wave contributes to damage on the land-side slope. Until now only fictive threshold values were used in the calculation method to demonstrate its potential influence. In this section the threshold value is determined by investigating the physics in the grass and clay cover during an overtopping wave impact event.

Critical pressure

The force required to enlarge cracks in the grass cover is determined by the strength of the clay and grass combined. Figure 7.15 demonstrates how the pressure in a crack causes the walls of the crack to be pushed aside. This only holds for situations in which the pressure in the crack is high enough to initiate motion of grass aggregates i.e. when the pressure in the crack exceeds the critical pressure. The theory developed by Stanczak [28, 29], who based his theory on Führbötter [12], is a physical based theory in which a force balance determines the critical pressure in a crack. Since in clay the cohesion of the soil is the dominant factor as it comes to soil failure forces [20], this is also expected to be the dominant parameter to determine grass aggregate movement. According to the theory of Führbötter aggregate movement occurs when the impact pressure in a crack exceeds two times the cohesion value of clay c, leading to a threshold level:

$$P \geqslant 2 \cdot c \quad \Rightarrow \quad P_c = 2 \cdot c \tag{7.33}$$

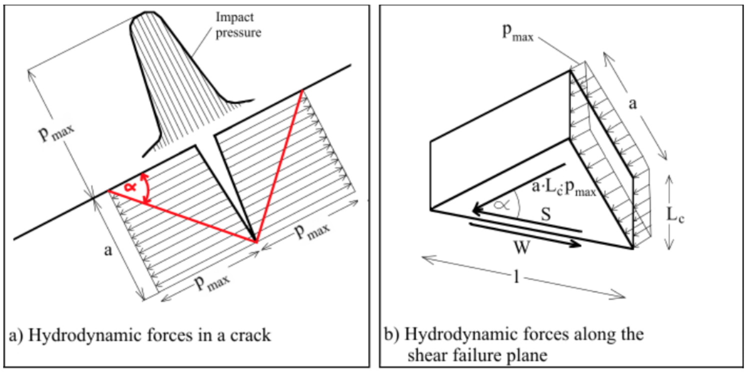
Impact pressure
p_{max}
α
a
p_{max}
p_{max}
p_{max}
a
$a \cdot L_c \cdot p_{max}$
∝
S
W
l
L_c

a) Hydrodynamic forces in a crack

b) Hydrodynamic forces along the shear failure plane

FIGURE 7.15: Forces inside a crack subject to an impact pressure after Führbötter [12]

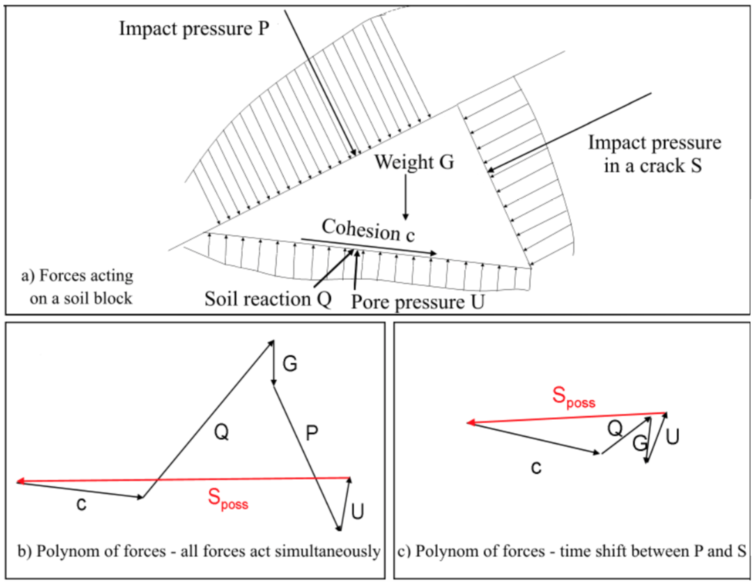
Impact pressure P
Weight G
Impact pressure in a crack S
Cohesion c
Soil reaction Q
Pore pressure U
G
Q
P
c
S_{poss}
U
S_{poss}
Q
G
U
c

a) Forces acting on a soil block

b) Polynom of forces - all forces act simultaneously

c) Polynom of forces - time shift between P and S

FIGURE 7.16: The extended approach introduced by Richwien [24] considers also the forces that were neglected by Führbötter [12]

An extended approach is introduced by Richwien [24] which considers also the forces that were neglected by Führbötter [12], such as the weight of the soil body G, the reaction of the soil Q and the pore water pressure U. This however provides only very rough information on the possibility of failure as it is based on a simplified, graphical analysis of forces. The approach introduced by Richwien is demonstrated in Figure 7.16. Stanczak [28, 29], criticised the theories developed by Führbötter and Richwien [24] as they assume an idealized situation. Stanczak however also admits that application of more advanced models is almost impossible due to several difficulties (as stated by Stanczak [28]):

- All forces except the impact pressure in the crack and the angle of action depend on the shape of the mobilised soil block, that depends explicitly on the searched angle of shear failure α - as a result, only a complex, iterative solution can be applied.
- The time shift between the forces P and S is needed as an input data. In fact, the same problem was solved in the approach of Führbötter [12], assuming that the time shift between forces P and S occurs for every impact event and the shear failure occurs within the short time period, when no impact pressure is no more present on the surface, but is still present within a crack. In the reality, this short time period is in the range of about 3 ms for 1 m deep crack, therefore the inertia of the soil block plays significant role and has to be known.

Due to difficulties in the application of advanced approaches, the simplified approach by Führbötter [12] is applied to the Wave impact approach, despite its shortcomings. The critical pressures is therefore assumed to be the double of cohesion. Assuming this cohesion is the clay cohesion is a rather conservative approach since it does not include the reinforcement of the roots of the grass cover. Therefore two times the clay cohesion is assumed to be the lower limit as it comes to determination of the critical pressure P_c. Typically the strength of roots is modelled by an artificial root cohesion c_r, which takes the reinforcement of the roots into account. The artificial root cohesion could lead to a somewhat over estimation of the grass cover strength as it depends strongly on the depth of the roots and the root density. At local poor root density spots the strength is less, which leads to more rapid failure of the grass cover. Therefore the artificial root cohesion c_r is assumed to be the upper limit as it comes to determination of the critical pressure P_c. This leads to:

$$2 \cdot c \leqslant P_c \leqslant 2 \cdot c_r \tag{7.34}$$

The artificial root cohesion is investigated extensively by Hoffmans et al. [15], which led to quantification of c_r for different types of grass covers in The Netherlands, see Table 7.1. These values are included in the Dutch standards for grass cover design, VTV2006 [21]. The clay cohesion c is unfortunately not included in these standards, therefore the determinations of the c-value depends on local soil investigation.

Table 7.1: Grass cover characteristics as found by Hoffmans et al. [15]

Quality of grass acc. to VTV2006	A_r/A $[mm^2/m^2]$	Number of roots $[number/m^2]$	c_r $[kN/m^2]$
Very poor	200	15100	4.8
Poor	400	30150	9.6
Averaged	600	45200	14.4
Good	800	60300	19.2

7.5 Analytical approach for including crest water depth

An attempt is made to find an analytical expression for the wave overtopping induced stress on the land-side slope of a dike where the water depth at the crest is included. The derivation of this analytical expression is given in Appendix E. The derivation in this appendix eventually leads to an unsolvable equation which is caused by the assumption of a uniform flow velocity profile at the crest. Therefore an analytical expression for wave overtopping induced impact stress cannot be given.

Considering an overtopping wave with uniform flow velocity in stead of a logarithmic distributed flow velocity leads to an overtopping image as demonstrated in Figure E.4. The figure illustrates the moment the bottom of an overtopping wave makes contact with the land-side slope. This very moment in time, named t_{bottom}, differs from the moment the surface of the overtopping wave makes contact with the land-side slope, named t_{surface}. This suddenly divides parameter t in Equation E.15 into multiple t-like parameters (for instance t_{bottom} and t_{surface}), making it not possible to integrate to t. Including all these parameters in an analytical solution requires every t-like parameter to be written in terms of t and substituted in Equation E.15, subsequently integrating this equation to t. This probably leads to an equation of at least one page, presumably more, which is not particularly an elegant solution for the problem. An equation of such length is also close to unusable since it is hard to keep the overview when using it. Besides that would it still be under the assumption of a uniform flow velocity on the crest, which is strictly speaking not correct. Therefore an analytical solution for the impact of overtopping waves on the land-side slope is not further presented in this thesis. The author presumes that an analytical solution should be possible but also admits that this will probably be not easily applicable.

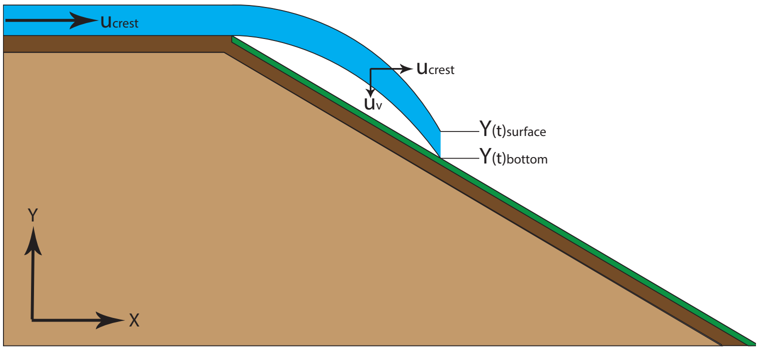

Figure 7.17: An overtopping wave with uniform crest flow velocity considered at the moment of impact of the bottom of the overtopping wave.

7.6 Numerical solution

Since an analytical solution is hard to obtain in the situation of overtopping waves, as demonstrated in Section 7.5, a numerical solution is developed to include the crest water depth in the determination of impact load due to overtopping waves. For the numerical approach initially the water depth at the crest is left out of the approach. This is done to simplify the model, which can serve as the basis for a first validation. When results obtained from this simplified approach shows realistic values, the water depth is included to complete the numerical approach.

7.6.1 Simplified approach

For the simplified approach a wave was considered to have an infinitesimally small water depth at the crest. I.e. the wave was considered concentrated in one point in the water column at the crest. The chosen point in this case was the surface of the overtopping wave, but this could have been any point in the water column. The water depth and flow velocity were assumed to decrease according to the relations as proposed by Hughes [17], see Equations 2.46 and 2.47. The impact location and load on that location on the land-side slope at a certain point in time was then determined by applying Equations 7.7 and 7.16. So basically Equations 7.7 and 7.16 were applied with respectively Equations 2.46 and 2.47 substituted for d_{crest} and u_{crest}. For every time step Δt the water depth and flow velocity according to Hughes' relations were determined and substituted.

Per individual overtopping event n the load and impact location of each time step was calculated using the overtopping discharge $q_{p,n}$ $[m^3s^{-1}]$, Overtopping time $T_{o,n}$ $[s]$, Flow velocity at the crest $u_{\text{crest},n}(t)$ $[ms^{-1}]$ and Water depth at the crest $d_{\text{crest},n}(t)$ $[m]$:

$$q_{p,n} = 0.184\sqrt{g}\, V_n^{3/4} \tag{7.35}$$

$$T_{o,n} = \frac{V_n^{1.16}}{0.43\, q_{p,n}} \tag{7.36}$$

$$u_{\text{crest},n}(t) = u_{p,n}\left(1 - \frac{i \cdot \Delta t}{T_{o,n}}\right)^{a} \tag{7.37}$$

$$d_{\text{crest},n}(t) = d_{p,n}\left(1 - \frac{i \cdot \Delta t}{T_{o,n}}\right)^{b} \tag{7.38}$$

Where the peak water depth $d_{p,n}$ and peak flow velocity at the crest are according to Hughes [17] described by:

$$d_{p,n} = \left(\frac{q_{p,n}^2 n_m^2}{\tan\theta}\right)^{0.3} \qquad u_{p,n} = \frac{q_{p,n}}{d_{p,n}} \tag{7.39}$$

Here V_n is the overtopping volume of an overtopping wave, i is the i^{th} time step and n the n^{th} wave overtopping event. Substituting these equations in Equation 7.7, this leads to an expression for the horizontal coordinate of the impact location X of the overtopping wave:

$$X_{\text{wave},n}(\Delta t) = \frac{\left(u_{p,n}(1-\frac{i\cdot\Delta t}{T_{o,n}})^a\right)^2 \left[\tan\theta \ + \sqrt{\tan^2\theta + \frac{2g\left(d_{p,n}(1-\frac{i\cdot\Delta t}{T_{o,n}})^b\right)}{\left(u_{p,n}(1-\frac{i\cdot\Delta t}{T_{o,n}})^a\right)^2}}\right]}{g} \tag{7.40}$$

In the numerical approach a linear decrease is assumed for the water depth $d(t)$ and flow velocity $u(t)$ at the crest, i.e. parameters a and b are both assumed to be 1. Using Equation 7.16 this leads to a general expression for the wave overtopping induced impulse load J on the dike at time $t = i\cdot\Delta t$:

$$J_{z,n}(\Delta t) = \rho\ \left(u_{p,n}\left(1-\frac{i\cdot\Delta t}{T_{o,n}}\right)^a\right)^2 \left[1+2\tan^2\theta + 2\tan\theta\sqrt{\tan^2\theta + \frac{2g\left(d_{p,n}(1-\frac{i\cdot\Delta t}{T_{o,n}})^b\right)}{\left(u_{p,n}(1-\frac{i\cdot\Delta t}{T_{o,n}})^a\right)^2}}\right]\sin\varphi \tag{7.41}$$

A same kind of relation can be expressed for $J_{x,n}$ by replacing $\sin(\varphi)$ by $\cos(\varphi)$.

At this point, the load and impact location of an overtopping wave at every time step can be determined. But the approach is not completed yet, in fact two more aspects need to be added to the numerical approach in order to provide a realistic outcome. First of all a threshold must be included to indicate whether the calculated load per time step contributes to damage on the land-side slope or not. Secondly the time the overtopping wave contributes to damage is important i.e. the fatigue load of overtopping waves. The first aspect is achieved by simply distracting a threshold value σ_c from the calculated over topping load. When σ - $\sigma_c < 0$ the load is considered too low to contribute to any damage and therefore considered zero. The second aspect is achieved by multiplying the calculated load minus threshold with the time step, so $(\sigma_{z,n} - \sigma_c)\Delta t$. This indicates that for a time period of Δt sec on location $X(i\Delta t)$ a contribution of $(\sigma_{x,n} - \sigma)$ is given to damage on the dike. Later on the summation of these values indicate at which point the land-side slope the heaviest load occurs.

For every time step Δt the wave impact stress $\sigma_{\tilde{z}\tilde{z}}$ and impact location X are saved as digits in two identical sized matrices $M1$ and $M2$ in which every row represents a single overtopping event. An example of such a matrix is given below, where $\sigma_{1,1}$ is the overtopping load of wave event n=1 at time step i=1, $\sigma_{1,2}$ is the overtopping load of wave event n=1 at time step i=2, $\sigma_{2,1}$ is the overtopping load of wave event n=2 at time step i=1, $\sigma_{2,2}$ is the overtopping load of wave event n=2 at time step i=2 and so on. Every row is filled with values for $\sigma(\Delta t)$ until $i\cdot\Delta t = T_{o,n}$, at which the overtopping event is finished and the row is complemented with zeros. This is necessary because due to differences in T_o value for every individual overtopping event the length of the rows differ within the matrix. Therefore the matrix should be as wide a the largest row vector, which is formed by the largest overtopping wave. In order to prevent 'Not a Numbers' in the matrix, each row needs to be complemented with zeros to the size of the maximum row.

$$\mathbf{M1}_{n,i} = \begin{bmatrix} \sigma_{1,1} & \sigma_{1,2} & \cdots & \sigma_{1,i} \\ \sigma_{2,1} & \sigma_{2,2} & \cdots & \sigma_{2,i} \\ \vdots & \vdots & \ddots & \vdots \\ \sigma_{n,1} & \sigma_{n,2} & \cdots & \sigma_{n,i} \end{bmatrix}$$

A same kind of matrix is created for all the impact locations during overtopping events of which an example is given below.

$$\mathbf{M2}_{n,i} = \begin{bmatrix} X_{1,1} & X_{1,2} & \cdots & X_{1,i} \\ X_{2,1} & X_{2,2} & \cdots & X_{2,i} \\ \vdots & \vdots & \ddots & \vdots \\ X_{n,1} & X_{n,2} & \cdots & X_{n,i} \end{bmatrix}$$

If the time step Δt would be infinitesimal, the total load at point X on the land-side slope could be determined by tracing all $X_{n,i}$ in matrix $M2$ and summarize all the corresponding $\sigma_{n,i}$ values from matrix $M1$. This would be valid since for every possible point X on the land-side slope the load per overtopping wave would be calculated. Unfortunately this is not the case because an infinitesimal time step is impossible. Therefore, due to the usage of a finite time step, the load per overtopping wave is only calculated for the finite amount of locations $X(\Delta t)$ on the land-side slope. In order to determine the location where the maximum load on the dike during a storm event occurs the cumulative load on different sections of the land-side slope is determined. Subsequently the X-axis of the land-side slope is divided into d_x m wide strokes. In matrix $M2$ every digit $X_{n,i}$ that lies between the boundaries d_x and d_{x+1} is traced, subsequently its corresponding $\sigma_{n,i}$ value in matrix M is placed in a new formed column vector. This column vector represents all the loads, multiplied by time, that have acted on a d_x m wide piece of land-side slope during all overtopping events. The summation of this column vector indicates the total load that has acted on that specific piece of dike.

$$D_{n,d_x} = \begin{bmatrix} D_{1,1} & D_{1,2} & \cdots & D_{1,d_x} \\ D_{2,1} & D_{2,2} & \cdots & D_{2,d_x} \\ \vdots & \vdots & \ddots & \vdots \\ D_{n,1} & D_{n,2} & \cdots & D_{n,d_x} \end{bmatrix}$$

7.6.2 Including crest water depth in numerical approach

The impact of an overtopping wave is not described by an impact *plane* rather than an impact *point*. The calculation method described in the previous section therefore under estimates the total load on the land-side slope as it only considers the maximum impact *point*. In order to make a decent estimate for the total load the water depth at the crest should be included in the calculation. Therefore, for the numerical solution, an overtopping wave flow at the crest is considered to be an accumulation of multiple d_i m thick flows with flow velocity u_{crest}, this is illustrated in Figure 7.18. For each of these very thin flows the impact *point* is calculated using Equation 7.40 as well as the impact load caused by this thin flow using Equation 7.41. Choosing d_i small enough, in the order of a few millimetres, justifies the assumption of the entire wave impact concentrated in an impact *point*.

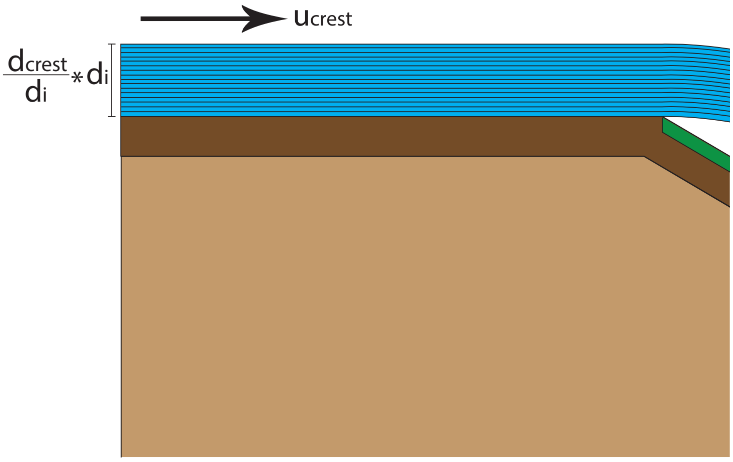

FIGURE 7.18: For the numerical approach the flow at the crest is considered an accumulation of small d_i m thick flows with flow velocity u_{crest}

By adding the crest water depth to the approach matrices $M1$ and $M2$ suddenly obtain an extra dimension and therefore become 3D-matrices. This is not necessarily a problem because the principle of gathering data from these matrices and summarizing this to obtain the total load on a specific dike section remains the same. The amount of gathered data points per selected land-side slope section however increases. An example of the outcome of the numerical approach is given in Figure 7.19.

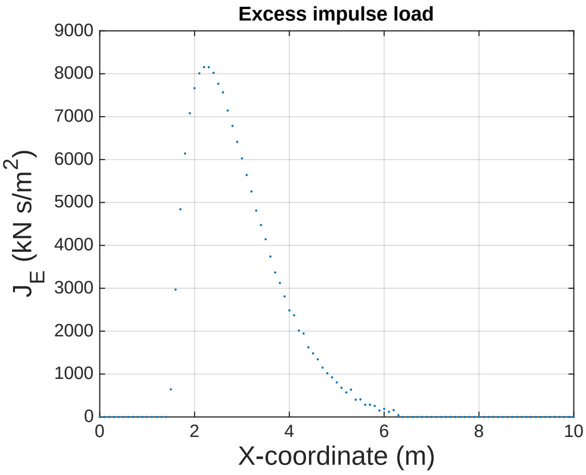

FIGURE 7.19: Load on the land-side slope with a threshold value of $P_c = 10\ kN/m^2$.

Since the only required input variable in this approach is the overtopping wave volume V_n of an overtopping event, which can be distracted from Run-up parameters, it makes the approach very user friendly. This makes it easy to evaluate many different cases in a short period of time. Figure 7.20 for example shows the outcome of the numerical approach including the water depth at the crest for several threshold values. In this case, the input for the simulations is the same as the input used for the wave overtopping simulator during the Wijmeers-II experiments.

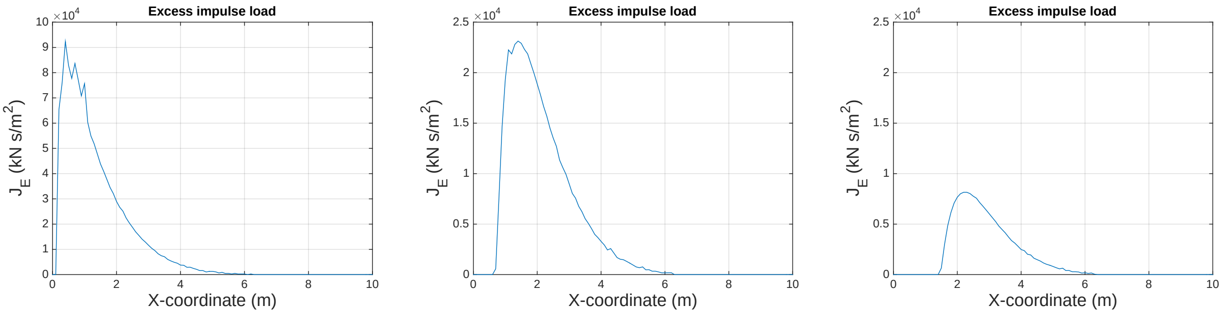

(A) $P_c = 0 \; kN/m^2$ (B) $P_c = 5 \; kN/m^2$ (C) $P_c = 10 \; kN/m^2$

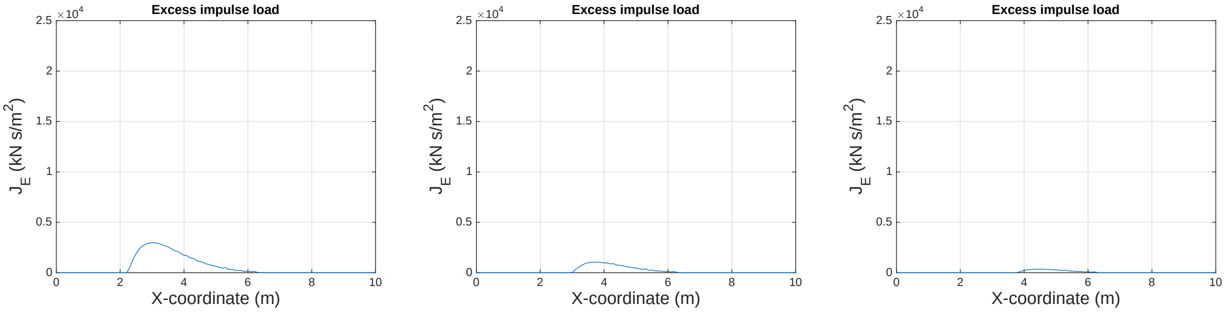

(D) $P_c = 15 \; kN/m^2$ (E) $P_c = 20 \; kN/m^2$ (F) $P_c = 25 \; kN/m^2$

FIGURE 7.20: Cumulative wave overtopping induced impulse load. Data from the Wijmeers-II.

7.7 Sensitivity analysis

The Wave impact approach was developed for the Wijmeers-II situation. Since the Wijmeers-II experiments were executed on a rather steep slope, the model is also tested on flatter land-side slopes with fictive data in which the applicability for the model on steeper slopes is analysed. For the analysis data is generated using a Weibull distributed randomiser. A six hour storm with significant wave height $H_s = 2.0$ m for an average overtopping discharge of 50 l/m/s is simulated. This 'storm' is used as input in the Wave impact approach model for six different slope angles. The results of these simulations are presented in Figure 7.21. Table 7.2 shows the slopes and corresponding slope angles θ that were tested in the sensitivity analysis.

TABLE 7.2: Slopes and slope angles corresponding to different simulations by the Wave impact model.

Simulation	Slope angle θ (rad)	Slope
1	0.53	1:1.7
2	0.46	1:2
3	0.38	1:2.5
4	0.32	1:3
5	0.28	1:3.5
6	0.25	1:4

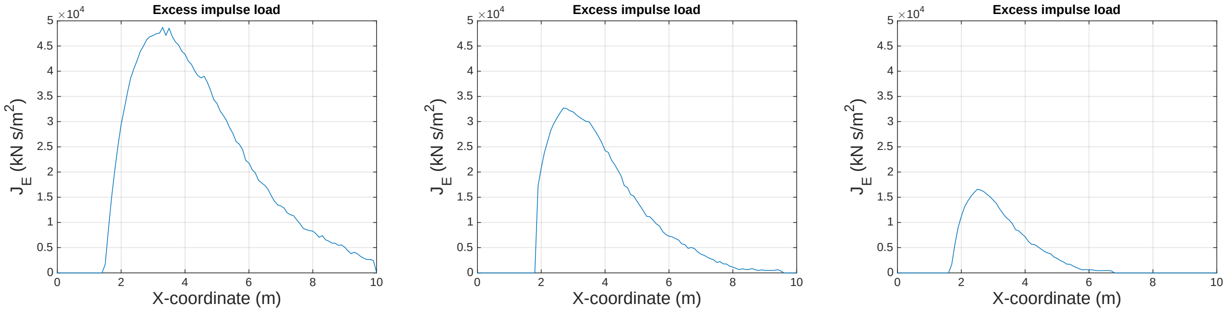

(A) $\theta = 0.53\ rad$ (B) $\theta = 0.46\ rad$ (C) $\theta = 0.38\ rad$

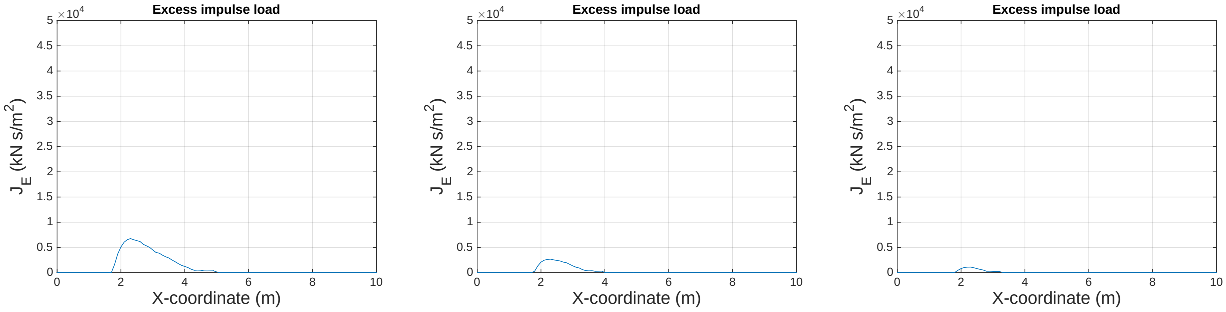

(D) $\theta = 0.32\ rad$ (E) $\theta = 0.28\ rad$ (F) $\theta = 0.25\ rad$

FIGURE 7.21: A six hour Weibull distributed storm of average overtopping discharge were simulated to test the influence of different slope angles on the overtopping wave impact load. The initial damage threshold σ_c was set at 10 kN/m^2.

Figure 7.21 shows that the influence of the slope angle of the land-side slope is significant. The wave impact load on steep slopes ($\theta = 0.53$ - 0.46) is much higher than on milder slopes ($\theta = 0.25$ - 0.28). Because the impact load of each individual wave is lower, the amount of overtopping waves that exceed the threshold value σ_c is lower as well. This eventually leads to a much lower total load on the land-side slope.

Since the overtopping wave induced impact load on mild slopes is quite low, it is possible the wave overtopping induced impact load is not the leading damaging load any more. The impact angle of overtopping waves has become so small that the stress perpendicular to the land-side slope $\sigma_{\tilde{z}\tilde{z}}$ might actually be smaller than the bed shear stress of overflowing water.

7.8 Summary and discussion

Summary

A new approach has been developed for the determination of damage on the land-side slope of a dike. For this new approach the leading failure mechanism is not assumed to be caused by bed shear stress but by the impact stress of the overtopping wave. After extended inspection of footage of overtopping waves, an overtopping wave appeared to be separated from the land-side slope for quite some distance before hitting the grass cover. The wave overtopping induced jet load on the slope is not included in any existing wave overtopping erosion model to thus far, therefore an attempt is made to include this in a new modelling approach. This Wave impact approach accurately determines the location of potential damage on the land-side slope. Therefore an overtopping wave is considered to be a jet moving towards the crest with decreasing flow velocity and jet thickness in time, impacting the land-side slope under an impact angle φ. The stress on the land-side slope caused by this jet is determined using an impulse balance. The location of the impact is determined by the trajectory of the overtopping wave.

The total load on the land-side slope is determined from the cumulative excess impulse load of waves overtopping the dike during a storm event. Therefore the wave overtopping induced jet stress $\sigma_{\bar{z}\bar{z}}$ is determined which is directly related to the impact location X. This overtopping induced jet stress leads to pressure in cracks in the grass cover. When this pressure exceeds a certain threshold, named the critical pressure P_c, the crack widens. How much the crack widens depends on the amount of exceedance and the time period the pressure is applied. The amount of exceedance at location X on the land-side slope, multiplied with the time of exceedance is named the excess impulse load J_E which is determined to be the load leading to damage on the land-side slope. The total excess impulse load at a location X therefore becomes the summation of every single wave overtopping induced excess impulse load at location X. The location X at which the highest cumulative excess impulse load occurs during a storm is the location at which the most damage is expected. This eventually has led to the following equation for the indication of total excess impulse load on the land-side slope:

$$J_{E,\mathrm{tot}} = \sum_{n=1}^{N} (\rho(u_{\mathrm{crest},n}^2 + 2gX_n \ \tan\theta) \cdot \sin\varphi - P_c) \cdot \Delta t_n \qquad (7.42)$$

The threshold value to determine at which overtopping induced jet pressure an overtopping wave contributes to damage on the land-side slope is named the critical pressure P_c. For the determination of the threshold, the critical pressure P_c, the simplified approach by Führböter [12] is assumed to be applicable for the Wave impact approach. The critical pressure is therefore assumed to be somewhere between two times the clay cohesion c and two times the artificial root cohesion c_r:

$$2 \cdot c \leqslant P_c \leqslant 2 \cdot c_r \qquad (7.43)$$

For the determination of the clay cohesion c local soil research is required, the artificial root cohesion c_r is quantified by Hoffmans et al. [15].

Discussion

The flow velocity profile at the crest was for the Wave impact approach assumed to be uniformly. This assumption causes a somewhat overestimation of the total damage on the land-side slope since the bottom flow velocity of the overtopping water layer at the crest is assumed to be equal to the surface flow velocity. In reality the bottom flow velocity is lower than the surface flow velocity causing the impact location to be more towards the crest. Since the impact load is directly dependent on wave impact location, this automatically leads to a lower impact load of the bottom part of an overtopping wave. Therefore the predicted load on the land-side slope is in reality a bit lower. For the purpose of safety a slight overestimation of the occurring load is not so bad because it will lead to a slight overestimation of the probability of failure. In reality the land-side slope of a dike will be slightly safer than the outcome of the Wave impact approach suggests.

The proposed Wave impact approached as described in this chapter seems to generate reasonable outcomes. Whether these outcomes are actually realistic or not is discussed in the next chapter in which the Wave impact approach is validated.

8 | Verification of Wave impact approach

The wave impact approach model is validated using the results of different wave overtopping experiments executed by Infram B.V. The reports are al written in Dutch, therefore a brief summary of the relevant results of each experiment is given in Appendix F. A comment on the contribution of each experiment to the verification of the wave impact approach is given as well. Because not all previous experiment results led to data that can be used for verification, only the relevant experiment results are described in this section. For the full description of all experiment results, reference is made to Appendix F.

For the determination of the wave impact load on the land side slope during overtopping experiments other than the Wijmeers-II experiments the actual files as used for input in the wave overtopping simulator were not present. Therefore these steering files are reproduced using a Weibull distribution randomiser function and the EurOtop manual [23] in which a clear explanation is given on how to calculate overtopping volumes and their probability of exceedance. In the factual reports of the experiments the maximum overtopping volume, number of overtopping waves, and average wave overtopping discharge of a simulated storm is given. These values were used to create a number of samples, depending on how many waves were simulated during a single overtopping experiment, with the Weibull distribution randomiser. This probably does not recreate the exact same input file as used during the actual experiment but it will approach it closely.

8.1 Wijmeers-II experiments

During the Wijmeers-II experiments lots of damage was observed on the land side slope. During the first overtopping experiment initial damage occurred about 2 m below the crest line by the end of the 10 l/m/s overtopping test. This test ran for 2 hours with an average overtopping discharge of 10 l/m/s. A mouse or rabbit hole appeared to be the main reason for damage since the toss and rooting of the animals had weakened the grass and clay cover. One can doubt whether the first overtopping experiment is representative for general situations but the fact is that this experiment was performed on a real dike. Weak spots caused by animal holes can occur at any dike section. The second overtopping experiment was more representative for a fully intact grass cover. Although initial damage had occurred during the hydraulic measurements this did not affect the experiment since this damage spot occurred near the toe. The land side slope was hardly damaged, making the rest of the overtopping experiment still representative.

First Wijmeers-II overtopping experiment

During the first Wijmeers-II overtopping experiment, the first damage on the land side slope occurred around the 2 m line [2]. Since the slope at the land side was 1:1.7, or the angle of the slope was 0.53 rad, this corresponds with a horizontal distance of 1.7 m. So at horizontal coordinate $X = 1.7$ m the first damage was noticed. While the damage spot on top of the land side slope developed into a bigger damage spot (up to 2.5 m wide and 1 m deep) a second initial damage spot was noticed in grid section 7 (see Figure 5.2), which is between the 3 m and 4 m line below the crest line, during the second hour of the experiment. This corresponds with horizontal coordinate $X = 2.6$ to 3.5 m. The initial damage threshold value for these three X coordinates is determined using the wave impact approach as developed. The required threshold values are determined by plotting the load on the land side slope for numerous different threshold values and observing which plot indicates a peak load at the X coordinate where damage was observed. The steering files from the overtopping simulator are used as input for the wave impact approach model. Results of these plots for the first Wijmeers-II overtopping experiment are presented in Figure 8.1. Figure 8.1a shows that $P_c = 5$ kN/m^2 corresponds to a peak damage of the overtopping waves at $X = 1.7$ m. Figures 8.1b and 8.1c show that $P_c = 12$ to 20 kN/m^2 corresponds to a peak damage at $X = 2.6$ to 3.5 m.

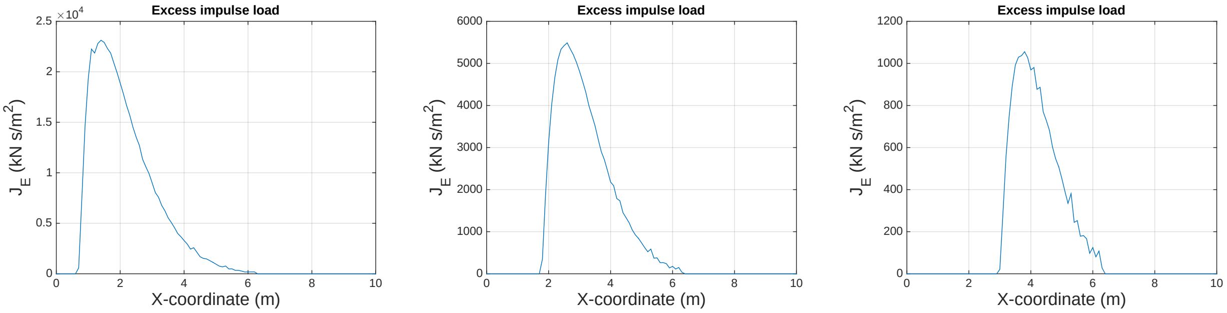

(A) $P_c = 5$ kN/m^2
Peak occurs around $X = 1.7$ m

(B) $P_c = 12$ kN/m^2
Peak occurs around $X = 2.6$ m

(C) $P_c = 20$ kN/m^2
Peak occurs around $X = 3.5$ m

FIGURE 8.1: Peak loads corresponding to the X coordinates at which damage was observed during the first Wijmeers-II overtopping experiment.

Second Wijmeers-II overtopping experiment

For the second Wijmeers-II overtopping experiment the required threshold value is determined using the same method as for the first experiment. During the hydraulic measurements direct damage occurred due to a 3000 l/m wave. Therefore, at the start of the actual overtopping experiment the land side slope was already damaged near the toe. As mentioned this did not affect the overtopping experiment too much. This is the case because observed erosion spots only developed in downwards direction along the land side slope. Since this initial damage spot occurred near the toe, and did not develop in upward direction, the grass sod on the slope was not damaged. During the second Wijmeers-II overtopping experiments damage was observed in the same grid section as during the first overtopping experiments, where the damage occurred in grid section 7. In grid section 5, 1 to 2 m below the crest line, a big crack of about 0.2 m wide was present. Due to this weakened part on the land side slope, damage occurred at that section as well during the overtopping experiment.

Therefore a threshold value is sought for a peak between $X = 0.6$ to 1.2 m (grid section 4) and for a peak between $X = 2.6$ to 3.5 m (grid section 7).

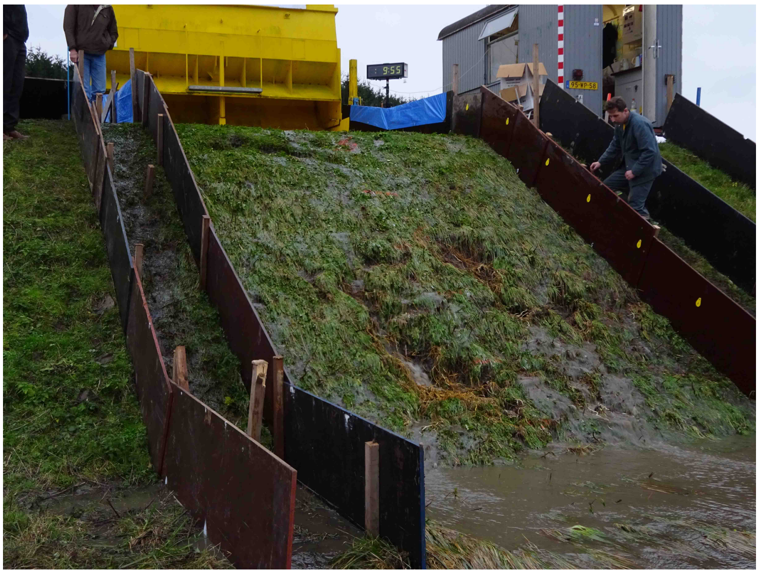

FIGURE 8.2: Initial damage during the second overtopping experiments occurred in grid section 7.

Using the steering files from the overtopping simulator as input for the wave impact approach model, plots are created for the second overtopping experiment, which are shown in Figure 8.3. Figures 8.3a and 8.3b show that $P_c = 0$ to 3 kN/m^2 corresponds to a peak damage of the overtopping waves at respectively $X = 0.6$ to 1.2 m. Figures 8.3c and 8.3d show that $P_c = 12$ to 17 kN/m^2 corresponds to a peak damage at respectively $X = 2.6$ to 3.5 m.

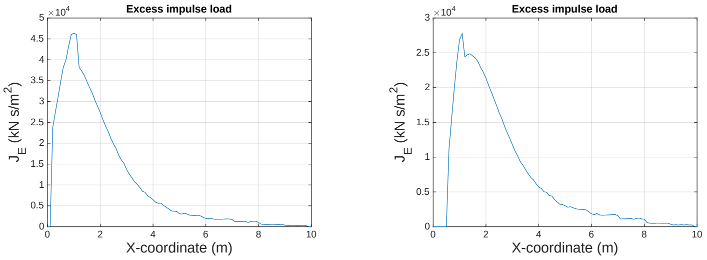

(A) $P_c = 0$ kN/m^2
Peak occurs around $X = 0.6$ m

(B) $P_c = 3$ kN/m^2
Peak occurs around $X = 1.2$ m

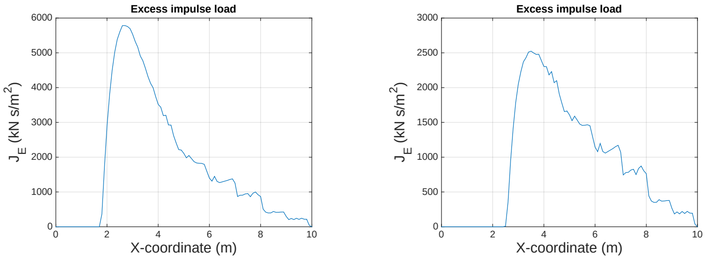

(C) $P_c = 12$ kN/m^2
Peak occurs around $X = 2.6$ m

(D) $P_c = 17$ kN/m^2
Peak occurs around $X = 3.5$ m

FIGURE 8.3: Peak loads corresponding to the X coordinates at which damage was observed during the second Wijmeers-II overtopping experiment.

8.2 Tielrodebroek experiments

Wave overtopping experiments have been executed by Flanders Hydraulics Research in december 2010 near the town of Tielrodebroek. A factual report about these experiments is published by Flanders Hydraulics Research [22]. The wave overtopping simulator developed by Infram B.V. was used to test the erodibility of the land-side slope of a dike located near the river and on the land-side slope of a dike in the middle of the polder. The second dike is a second defence mechanism in case the main defence (the dike located on the riverside) breaches. Both dike conditions were classified as *very poor* to *poor*. The results from overtopping tests on the main dike are not comparable with the Wijmeers-II experiments since preliminary damage was applied on the land-side slope.

On the second dike, two different kind of experiments were executed on 3 test sections. On the first two test sections overtopping waves to be expected during a river flood were simulated. This means many small overtopping wave volumes were released by the wave overtopping simulator. On the third test section overtopping waves to be expected during a storm at sea were simulated, which means the overtopping wave volume of each individual wave was much higher, but the number of overtopping waves was much lower. Therefore on all test sections the same average overtopping volume was used, only he volume and frequency of each individual wave was different on the third test section compared to the first two test sections. The result after overtopping tests on the first two test sections are demonstrated in Figures 8.4 and 8.5.

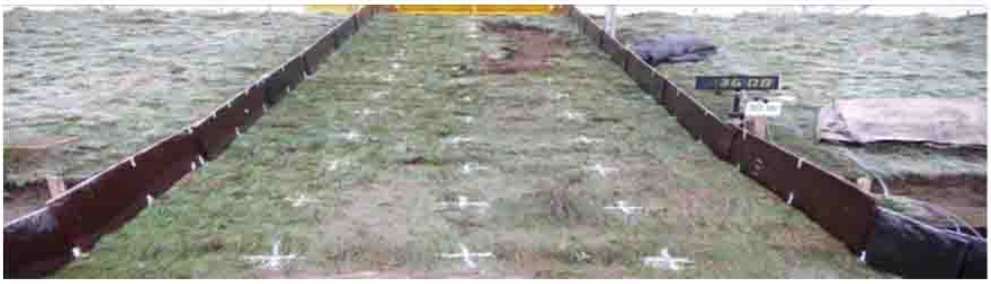

FIGURE 8.4: Tielrode overtopping experiment result test section 1, Picture from the factual report published by Flanders Hydraulics Research [22]

The result after overtopping tests on the first two test sections are demonstrated in Figure 8.6.

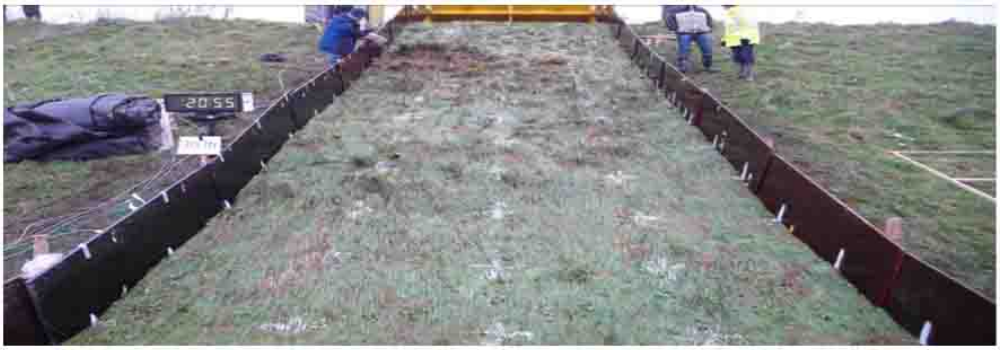

FIGURE 8.5: Tielrode overtopping experiment result test section 2. Picture from the factual report published by Flanders Hydraulics Research [22]

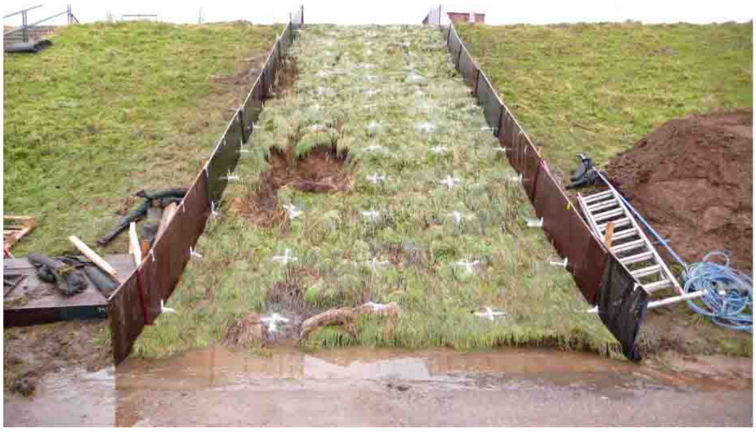

FIGURE 8.6: Tielrode overtopping experiment result test section 3, Picture from the factual report published by Flanders Hydraulics Research [22]

The steering files used during the Tielrode experiments were used in the Wave impact model. On the first two test sections damage occurred on the land-side slope around the 2,0 m. below the crest line. This corresponds with X = 1,9 m. As shown in Figure 8.7a this indicates a critical pressure value of $P_c = 8\ kN/m^2$). On the third test section damage occurred around the 6 m. below the crest line, which corresponds with X = 5.6 m. As shown in Figure 8.7b this indicates a critical pressure value of $P_c = 25\ kN/m^2$). The results from the Wave impact model are demonstrated in Figure 8.7.

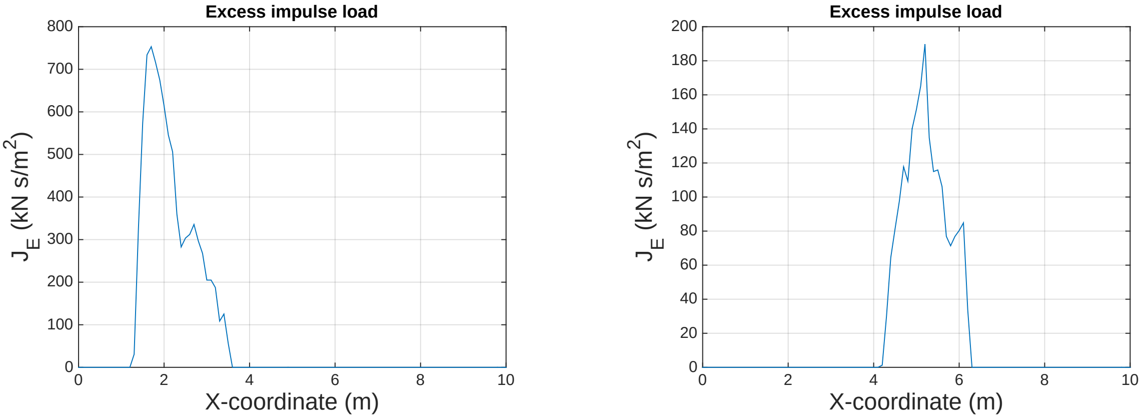

(A) $P_c = 8\ kN/m^2$
Peak occurs around X = 1.9 m

(B) $P_c = 25\ kN/m^2$
Peak occurs around X = 5.5 m

FIGURE 8.7: Peak loads corresponding to the X coordinates at which damage was observed during the Tielrode overtopping experiment.

Although damage further down the land-side slope is expected when higher individual wave volumes overtop the dike, the damage spot documented on the third test section on the second dike tested occurred at a spot quite far down the slope. According to the Wave impact approach this would correspond to a rather high critical pressure value. The results from the first two test sections however indicate a rather low critical pressure value. This makes it hard to either conform or reject the Wave impact approach from he Tielrode experiment result. On the on hand the Wave impact approach is confirmed since higher waves resulted in damage further down the land-side slope, on the other hand the theory is rejected because it leads to different theoretical critical pressure values. Therefore a hard conclusion from the Tielrode experiments cannot be made.

8.3 Afsluitdijk experiments

In February 2009 numerous wave overtopping experiments were executed at the Dutch Afsluitdijk by Infram B.V. [5] using the same overtopping simulator as used during the Wijmeers-II experiments. The Afsluitdijk is a major closure dam that separates lake IJssel and the Waddensea in the North of the Netherlands. This dam is essential in the Dutch water defence system and should therefore be resistant against storms with very high significant wave height. In order to test the actual strength of the Afsluitdijk, Infram B.V. tested the erodibility of the land-side slope. At the Afsluitdijk the 'land' side slope should actually be named 'lake' side slope since the dam does not separate water from land. However, for constancy of this thesis the side that has been tested for wave overtopping resistance is still called 'land-side slope'. In total three different test sections were tested with the overtopping simulator. At a fourth test section a shear stress experiment was executed.

The result of the Afsluitdijk overtopping experiments were in a way quite similar to the result of the Wijmeers-II experiments. Although initial damage occurred much later during the Afsluitdijk experiment, a similar damage pattern was noticed on the land side slope. A big difference between the Afsluitdijk overtopping experiments and the Wijmeers-II overtopping experiments is the damage on the toe of the dike. This first damage spots at the Afsluitdijk were noticed around the toe is the dike while during the Wijmeers-II experiments no damage at the toe was noticed at all. Due to safety regulations the experiments at the Afsluitdijk had to be stopped as soon as significant damage to the grass cover occurred, letting the experiments run until the sand core was reached was in this case too risky. The final damage pattern after each test was still to be classified as 'failed grass cover' [5]. The final result of test section 1 and 2 of the Afsluitdijk overtopping experiments is shown in Figure 8.8.

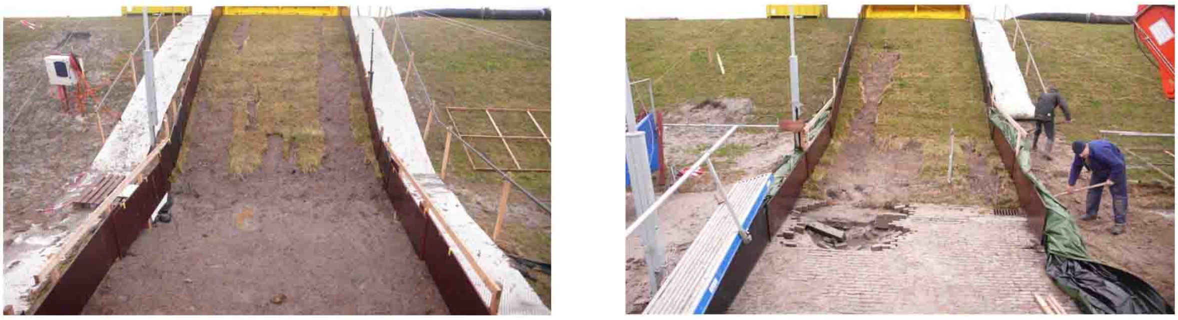

(A) Test section 1

(B) Test section 2

FIGURE 8.8: Final result of the wave overtopping experiments at the Afsluitdijk, February 2009. Photo's taken by Infram B.V. [5]

A third section was tested on wave overtopping as well, this section however contained a 1 m wide stone steps in the center of the section. Therefore test done on this section are performed under such different conditions compared to the Wijmeers-II experiments that they cannot be compared to each other.

First Afsluitdijk overtopping experiment

The land side slope of the entire Afsluitdijk was classified *good* according to the VTV2006 standards [21]. During the overtopping tests on the first test section, the first initial damage spots on the land side slope of the Afsluitdijk were noticed in grid section 5, which in the case of the Afsluitdijk meant between the 4 and 5 m line below the crest [5]. The slope on the land side of the Afsluitdijk was 1:2.6, or a slope angle $\theta = 0.37$ rad. This means the initial damage patterns occurred between respectively horizontal coordinates $X = 3.8$ and 4.7 m. Using the steering files as used during the Afsluitdijk experiments an indication of the required threshold value P_c is obtained. The results are presented in Figure 8.9.

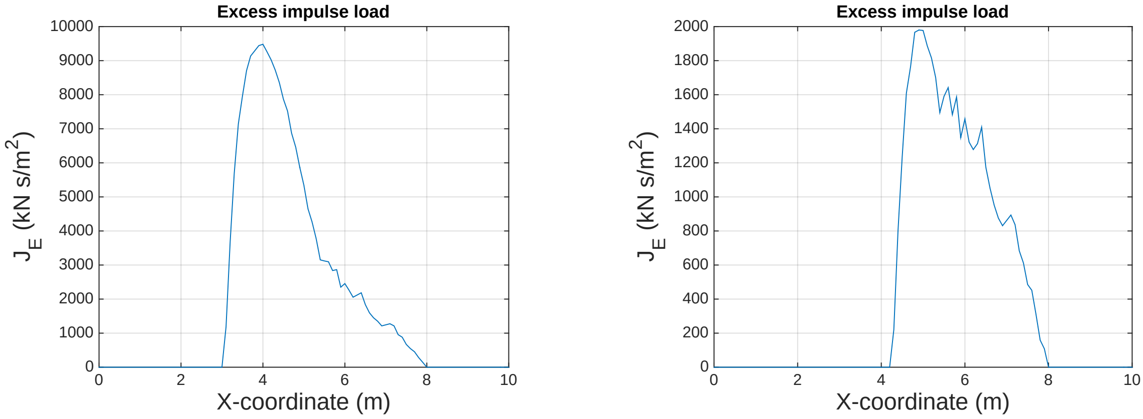

(A) $P_c = 18\ kN/m^2$
Peak occurs around $X = 3.8$ m

(B) $P_c = 25\ kN/m^2$
Peak occurs around $X = 4.7$ m

FIGURE 8.9: Peak loads corresponding to the X coordinates at which damage was observed during the first Afsluitdijk overtopping experiment.

Second Afsluitdijk overtopping experiment

Probably due to a tractor that sank into the soil, a rather deep pit of about 0.13 m had formed on the land side slope of test section 2. This pit had formed around the 3 m line below the crest line which corresponds with horizontal coordinate $X = 2.8$ m. Damage occurred already during the 1 l/m/s test at the spot where the pit had formed. Because the stability of the brick road a few metres below the toe of the land side slope became in jeopardy during the 30 l/m/s test the experiment was stopped. Therefore the total load on the first test section has been much larger than the load on the second test section. This is not really a problem because this only requires different input for the wave impact model. The two experiments are therefore however harder to compare to each other. Results of the second Afsluitdijk overtopping experiment are presented in Figure 8.10.

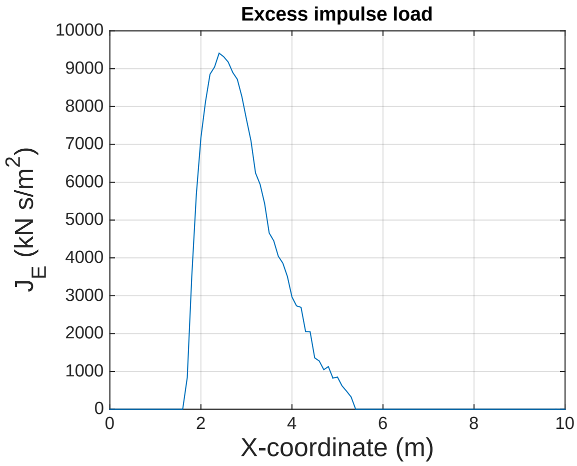

FIGURE 8.10: Peak load corresponding to the X coordinates at which damage was observed during the second Afsluitdijk overtopping experiment. For $P_c = 10\ kN/m^2$ the peak occurs around $X =$ 2.8 m

8.4 Zeeuwse zeedijken experiments

In 2008, in the Dutch province of Zeeland, in the South of The Netherlands, wave overtopping experiments were executed at two locations: St Philipsland and Kattendijke. At St Philipsland one test section was available while at kattendijke four test sections were available. The experiments were set up to gather more knowledge on overtopping resistant dikes. Subsequently different types of land side slope cover were tested at the Kattendijke test sections: two grass cover sections, one Elastocoast cover section and one open asphalt cover section. Elastocoast is a mixture of polyurethane, rocks and granulate which creates an elastic porous cover for the land side slope. Of course the results of the Kattendijke experiments that were not executed on grass cover cannot be used as verification data for the wave impact approach as this theory is developed for grass covered land side slopes.

Like at the Friese Waddenzeedijk overtopping experiment 6 hour storms were simulated using the wave overtopping simulator [4]. Averaged wave overtopping volumes of respectively 0.1, 1, 10, 30, 50 and 75 l/m/s were generated using a Weibull distribution.

St Philipsland overtopping experiment

The tested land side slope at the St Philipsland dike was 13 m long with a 1:2.4 slope, or a slope angle $\theta = 0.38$ rad. The grass cover was in *good* conditions according to the VTV2006 standards. During the overtopping experiments at St Philipsland initial damage spots were noticed around the respectively 4 and 7 m line below the crest line, this is visualized in Figure 8.11. The initial damage spots were probably caused by some minor weak spot in the grass cover. Around the 4 m line, corresponding to a horizontal coordinate $X = 3.7$ m, a minor bold spot was visible in the grass cover and at the 7 m line, corresponding to a horizontal coordinate $X = 6.5$ m, a slight cascade was visible. The initial damage spot around the 7 m line eventually developed into a big eroded area just above the toe in which the head cut erosion stage was reached [4]. This is shown in Figure 8.12.

The results of the wave impact model runs are presented in Figure 8.13.

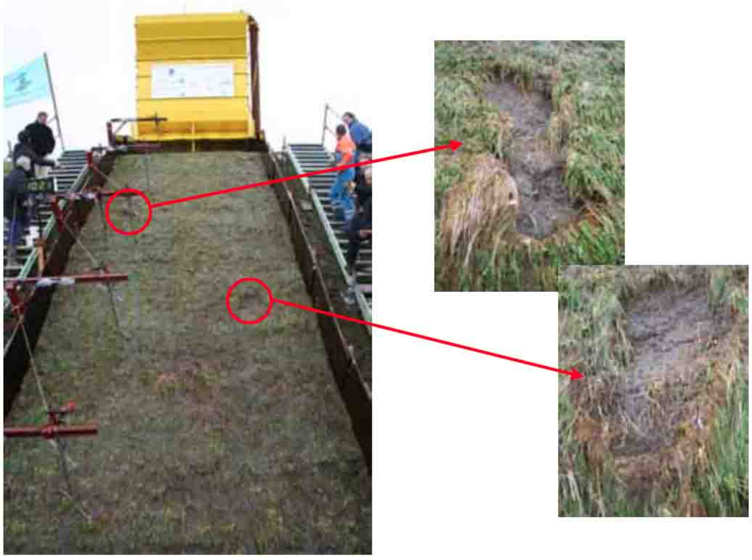

Figure 8.11: Initial damage spots during the St Philipsland overtopping experiments. Photo taken by Infram B.V. [4]

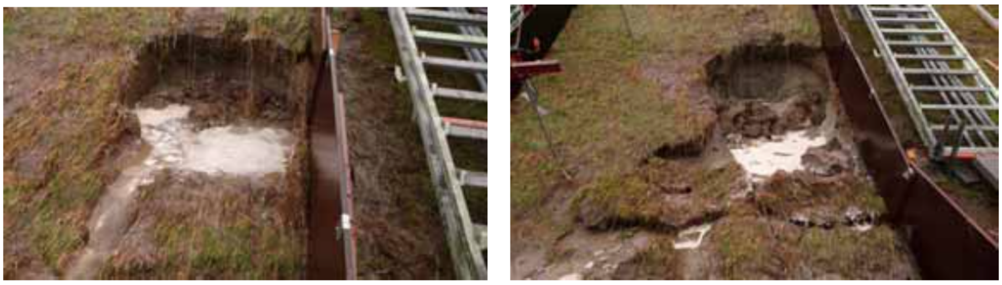

Figure 8.12: Final result of the St Philipsland overtopping experiments. Photo taken by Infram B.V. [4]

Second Kattendijke overtopping experiment

The second Kattendijke overtopping experiment was performed on a 15 m long grass covered land side slope which was in *good* conditions according to the VTV2006 standards. The slope was 1:3 which corresponds with a slope angle $\theta = 0.32$ rad. During the second Kattendijke overtopping experiment damage on the land side slope did occur, due to the removal of a stump from the land side slope a weak spot was created. This removal was necessary because otherwise it would block the flow over the slope. This stump was removed around the 7 m line, corresponding to horizontal coordinate $X = 6.6$ m, below the crest [4]. Mole corridors appeared to be present as well which made the spot even weaker. Unsurprisingly damage to the land side slope occurred first around this spot. Although the initial damage spot occurred rapidly during the experiment, it did not evolve into a major erosion spot. The roots of the grass were apparently so dense that the clay underneath the grass eroded but the grass aggregate itself remained in position. Due to heavily toe erosion during the 50 l/m/s tests of the second Kattendijke overtopping experiment it was decided to stop the tests and not execute the 75 l/m/s tests. The risk of shearing of the land side slope was too high. Therefore the observed damage spot on around the 7 m line on the land side slope did not have the chance to evolve into major damage spots. A picture of the observed damage spots is given in Figure 8.14.

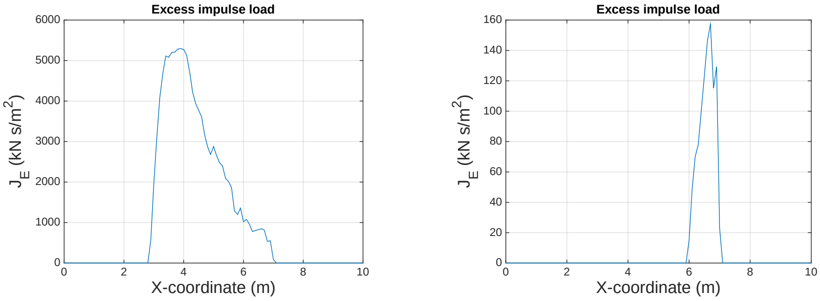

(A) $P_c = 17\ kN/m^2$
Peak occurs around $X = 3.7$ m

(B) $P_c = 35\ kN/m^2$
Peak occurs around $X = 6.5$ m

FIGURE 8.13: Peak loads corresponding to the X coordinates at which damage was observed during the overtopping experiment at St Philipsland.

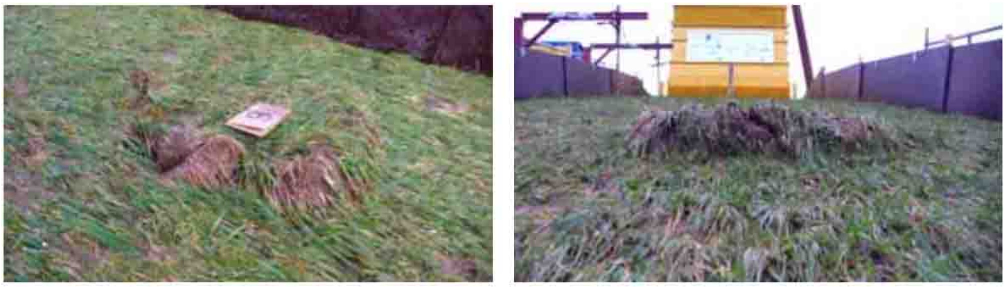

FIGURE 8.14: Initial damage spots noticed during the second Kattendijke overtopping experiments. Photo taken by Infram B.V. [4]

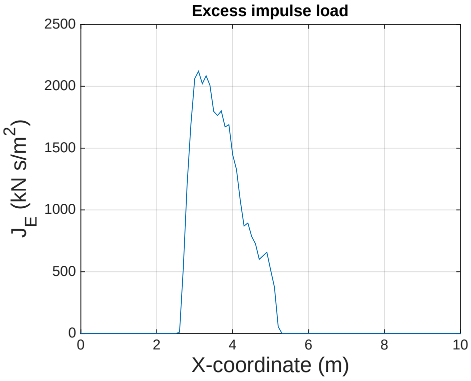

FIGURE 8.15: Peak loads corresponding to the X coordinates at which damage was observed during the overtopping experiment at Kattendijke. $P_c = 15\ kN/m^2$, the maximum wave impact point was $X = 5.5$ m so the damage at $X = 6.6$ m was not caused by wave overtopping.

8.5 Results

Hoffmans et al. [15] did extended research on the characteristics of grass covers in the Netherlands. The research team distinguished four different grass cover qualities of which the typical characteristics were determined. The results as found by Hoffmans et al. are given in Table 8.1. Since only grass cover quality according to VTV2006, and no specific cohesion measurement results, are mentioned in the factual reports [3–6] of the overtopping experiments considered, the cohesion as determined by Hoffmans et al. is used to validate the Wave impact approach.

TABLE 8.1: Grass cover characteristics as found by Hoffmans et al. [15]

Quality of grass acc. to VTV2006	A_r/A $[mm^2/m^2]$	Number of roots $[number/m^2]$	c_r $[kN/m^2]$
Very poor	200	15100	4.8
Poor	400	30150	9.6
Averaged	600	45200	14.4
Good	800	60300	19.2

The results of the verification of the Wave impact approach are presented in Table 8.2. The land side slopes of the Wijmeers-II experiments were not classified according to the VTV2006 standards. Therefore a gamble has to be made of how the the grass cover probably would have been classified. To achieve this a research on the conditions of the grass cover by Bart Vandevoorde of the Belgian INBO (Intstitute for Nature and Forrest research) is used. The grass cover conditions were investigated by counting the amount of vegetation per square meter on several locations on the land side slope. From this research an average vegetation percentage of 66% was measured during the experiments where the rest of the grass cover was mostly mos, open roots and bald spots. 66% vegetation cover is a rather poor number for a grass cover. Therefore the Wijmeers-II land side slope are assumed to be classified *very poor* to *poor* according to the VTV2006 standards. From a description of the land-side slope conditions of the Tielrode experiments the grass cover is also assumed to be classified *very poor* to *poor*. These assumptions taken into account, the Fürbötter theory indicates P_c = 9.6 - 19.2 kN/m^2, which is an upper limit of the threshold since it is based on the artificial root cohesion. Since all land side slopes of the reference experiments were classified *good* an upper limit threshold value of $P_c = 38.4$ according to the theory of Fürbötter is noted. Soil measurements at the Wieringermeerdijk by Infram B.V. [42] were performed in 2008 in order to determine the cohesion of boulder clay, which is the same clay as used for the construction of the afsluitdijk. The cohesion of boulder clay at the afsluitdijk was determined to be $c = 7.7$ kN/m^2, from which the lower limit for the critical pressure threshold at the afsluitdijk is determined ($P_{c,\mathrm{min}} = 2 \cdot c = 15.4$ kN/m^2). During the Friese Waddenzeedijk experiments samples of the clay layer were investigated from which the clay cohesion was determined [3]. The sample provided a minimum clay cohesion $c = 2.4$ kN/m^2, leading to $P_{c,\mathrm{min}} = 2 \cdot c = 4.8$ kN/m^2 as lower limit for both Friese waddenzeedijk experiments. Unfortunately during the rest of the experiments no soil investigations were performed from which the clay cohesion was determined. Therefore the lower critical pressure limit $P_{c,\mathrm{min}}$ for the rest of the experiments was not known. A typical cohesion for structured clay however is 5 kN/m^2 [14]. With lack of a better alternative twice this cohesion value is set as lower critical pressure limit, i.e. $P_{c,\mathrm{min}} = 10$ kN/m^2.

A big side note here is the fact that animal activity in and on the land-side slope as well as weather conditions influence the local soil characteristics in such a matter, that lots of weak spots on the land side slope occur. This causes major deviations in local strength of the grass and clay cover.

Table 8.2: Results verification Wave impact approach.

Experiment	Damage spot	X coordinate $[m]$	P_c from verification $[kN/m^2]$	$P_{c,\min} = 2 \cdot c$ $[kN/m^2]$	$P_{c,\max} = 2 \cdot c_r$ $[kN/m^2]$	Remark
Wijmeers-II section 1	1	1.7 - 2.6	5 - 12	10	9.6 - 19.2	
	2	3.5	20	10	9.6 - 19.2	
Wijmeers-II section 2	1	0.6 - 1.2	0 - 3	10	9.6 - 19.2	
	2	2.6 - 3.5	12 - 17	10	9.6 - 19.2	
Tielrode section 1	1	1.9	8	10	9.6 - 19.2	
Tielrode section 2	1	5.6	25	10	9.6 - 19.2	
Afsluitdijk section 1	1	3.8 - 4.7	18 - 25	15.4	38.4	
Afsluitdijk section 2	1	2.8	10	15.4	38.4	
Friese Waddenzeedijk section 1	1	19.9	-	4.8	38.4	No failure by Wave impact
Friese Waddenzeedijk section 2	1	14.7	-	4.8	38.4	No failure by Wave impact
St Philipsland	1	3.7	17	10	38.4	
	2	6.5	35	10	38.4	
Kattendijke section 1	1	-	-	10	38.4	No observed damage
Kattendijke section 2	1	6.6	-	10	38.4	No failure by Wave impact
Tholen section 1	1	6.5	-	-	-	Downside shearing of levee
Tholen section 2	1	2.0 - 4.0	-	-	-	Total collapse of levee

8.6 Conclusion and discussion

Conclusion critical pressure threshold P_c

Looking at the results of the verification of the Wave impact approach in Table 8.2, the calculated P_c values are quite similar to the theoretical P_c values. Although the difference between the found P_c and theoretical P_c for some of the verification experiments is significant, there is still reason to state that the Wave impact approach gives a rather well representation of occurring damage at the land side slope of a dike. The largest deviation is found for the second Afsluitdijk experiment and one of the damage spots in the first and second Wijmeers-II experiment. The occurred damage during these experiments however was caused by weak spots in the grass cover. For the second Afsluitdijk experiment this initial weak spot was probably caused by a tractor, for the first and second Wijmeers-II experiment the cause of the initial weak spot was unknown. The rest of the verification experiments lead to predicted P_c values which match the found P_c values reasonably well.

The presence of these weak spots make it hard to validate the proposed theories of Führbötter and Hoffmans et al. for the critical pressure threshold P_c. Due to initial weakened or damaged spots in some tested grass covers there are only 5 experimental results left which are actually usable for verification. This of course is not enough to either confirm or reject the theory of the Wave impact approach. More experimental data, both from wave flumes and from in field overtopping experiments, is required to properly verify the Wave impact approach model theory.

Discussion

Notable is that most of the calculated P_c values are slightly lower than the theoretical values. This may be caused by the fact that damage on the land side slope occurs firstly at spots where the grass cover is already weakened. This could be due to animal activity but also due to maintenance equipment such as tractors driving over the land side slope. The theoretical strength of the grass cover is based on a fully grown grass cover without any damage spots. Therefore a slightly higher theoretical value is what could have been expected. Weakened spots however are almost always present at a land side slope. Therefore a kind of correction factor is advised to be added to the theory to include the whether of not presence of weakened spots. This correction factor is to be determined from data from overtopping experiments. Unfortunately lack of sufficient data makes it at this point not possible to determine a reliable correction factor.

9 | Conclusions and Recommendations

In this thesis a method is developed to include the impact of overtopping waves in a land-side slope erosion modelling approach. Land-side slope erosion models are tested based on experimental results from overtopping and overflow experiments at the Wijmeers-II polder in Belgium. Verification of these existing models resulted in criticising the modelling approach, hence a new modelling approach is developed. Subsequently this method is verified using data obtained from multiple reference projects.

9.1 Conclusions existing land side slope erosion models

Several people have worked on land-side slope erosion models which are based on wave overtopping induced bed shear stress. The most advanced version of this modelling approach is published by S. Hughes in 2012. In this model damage on the land side slope is determined by the time period overflowing water exceeds a predetermined threshold flow velocity u_c. An overtopping wave is therefore modelled as a very short but intense overflow event. This assumption leads to a major shortcoming in the model, namely fact that the actual impact stress of overtopping waves is not taken into account. The time overtopping waves are separated from the slope is not included either. The preliminary hypothesis in this thesis states that the consideration of an overtopping wave modelled as a short version of overflow was not valid. From the data obtained from the Wijmeers-II overtopping and overflow experiments this hypothesis was confirmed. The 'Excess volume approach' as developed by Hughes [17, 18] led to predictions of damage to the land side slope that were contrary to observations during the Wijmeers-II experiments. The results of the Wijmeers-II experiments were a total collapsed land side slope during overtopping experiments, while hardly any damage during the overtopping experiments occurred. The Excess volume approach suggested that the damage caused by overflow should have been greater than the damage caused by overtopping waves, which was not the case.

The modelling approach developed by Hughes was criticised by the data obtained from the Wijmeers-II experiments. Therefore, the choice was made to develop a new method for determining damage on the land side slope.

9.2 Conclusions new developed land side slope erosion model

A new approach has been developed for the determination of damage on the land side slope of a dike. This 'Wave impact approach' is capable of accurately determining the location of the highest peak load on the land side slope during a storm event. Due to the usage of a threshold parameter it is possible to predict the location with the most damage. The model approach is verified using the results of different overtopping experiments executed in The Netherlands and Belgium. During this verification, damage locations documented during both the Wijmeers-II experiments and the reference experiments could appropriately be predicted with the Wave impact approach. Confirmation of the Wave impact approach however is rather difficult due to many uncontrollable external effects such as animal activity in and on the land side slope. These side effects cause weak spots in the grass cover. Due to these weak spots it becomes hard to relate the proposed threshold parameters to soil characteristics since the soil becomes very heterogeneous. The proposed threshold parameters in the Wave impact approach provided appropriate results for predicting damage spots on the land side slope of a dike. A more probabilistic method however is required to completely validate the new modelling approach. More research on weak spots in land side slopes is therefore advised in order to find a truly reliable threshold parameter.

9.3 Answering research questions

When starting this thesis the plan was to use the modelling approach as developed by a.o. Hughes and attempt to extend this model with wave impact effects, as well as the cascade effect of the land side slope on overflow. However, since the model was rejected by the data obtained from the Wijmeers-II experiments the choice was made to develop an entirely new method for determining damage on the land side slope. This however means the research questions as proposed in the research proposal of this thesis probably cannot be answered. Therefore other research questions were required, which are presented in Chapter 1. The conclusions on the new developed model approach are presented in the next section.

Main research question

What is the influence of wave impact on the initial failure process of the land side slope of a dike? And what is a physical based method to include this effect in a breach initiation model?

Part 1: *What is the influence of wave impact on the initial failure process of the land side slope of a dike?*
Due to natural processes cracks occur often in grass covers and supporting clay layers. The impact of an overtopping wave leads to increase of the size of these cracks. The impact of several waves leads to growth of the crack until the supporting clay layer is reached. When the supporting clay layer is reached an erosion process occurs under the grass cover which eventually leads to lifting the grass cover.

Part 2: *What is a physical based method to include this effect in a breach initiation model?*
An overtopping wave is described as a crest-wards moving jet with decreasing flow velocity and jet thickness in time. An overtopping wave contributes to damage on the land side slope when a certain initial damage threshold factor P_c is exceeded. This threshold factor is based on either solely the cohesion factor of the soil or a combination of the root strength of the grass combined with the cohesion factor, an artificial root cohesion c_r. Which threshold gives the most accurate representation of real situations is not determined due to lack of data, this aspect is to be determined in future research. The cumulative impact stress of all overtopping waves multiplied with the time each wave impact stress exceeds threshold factor P_c form a fatigue like load on the land-side slope.

Sub-questions

Can existing breach initiation theories of land side slope based failure of a dike be verified with experimental data?
As explained in Section 9.1, the land side slope erosion theory developed by Hughes et al. [17, 18] is criticised using the data obtained from the Wijmeers-II experiment.

What is the leading stress in wave overtopping induced failure?
According to the newly developed Wave impact approach the leading stress is the jet impact induced normal stress in the grass and clay cover. This stress leads to an erosion process which is described in the answer of the next sub-question.

What is the wave overtopping induced failure mechanism of the grass and clay cover of a land side slope?
Since the cohesion of the supporting clay layer is significantly lower than the cohesion of the grass cover layer the impact of multiple waves causes a kind of tunnelling effect. The supporting clay layer erodes under the grass cover creating empty space which is filled with water during a single overtopping event. The jet pressure effect of the overtopping wave eventually pushes grass aggregates out of the grass cover which after some time may lead to failure of the grass cover. The wave impact induced failure process of a grass cover is visualised in 6 steps, demonstrated in Figure 9.1.

How can the impact of overtopping waves be included in a wave overtopping induced land side slope erosion model?
For the proposed new modelling approach the leading failure mechanism is not assumed to be caused by bed shear stress but by the impact normal stress of the overtopping waves. After extended inspection of footage of overtopping waves, an overtopping wave appeared to be separated from the land side slope for 1 to 5 m. before making contact with the grass cover. The effect of the overtopping wave impacting the slope is not included in any existing wave overtopping erosion model to thus far, therefore this is included in a new modelling approach. This Wave impact approach accurately determines the location of potential damage on the land side slope. Therefore an overtopping wave is considered to be a towards the crest moving jet with decreasing flow velocity and jet thickness in time, impacting the land side slope under an impact angle. Normal stresses on the land side slope caused by this jet are determined using an energy balance, the location of the impact is determined by the trajectory of the overtopping wave.

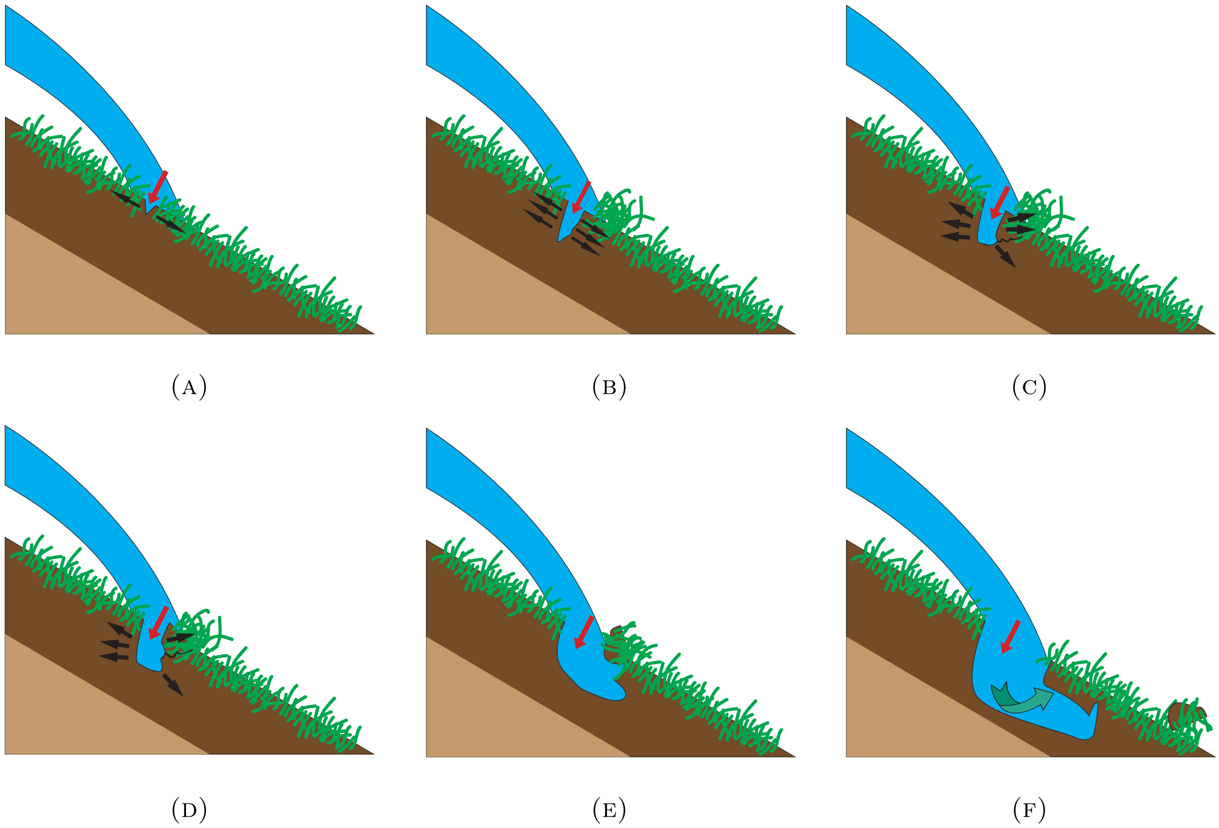

Figure 9.1: Wave overtopping induced failure process clarified in 6 steps.

The total load on the land-side slope is determined from the cumulative impact load of all waves overtopping the dike during a storm event. Since the wave overtopping induced jet stress $\sigma_{\tilde{z}\tilde{z}}$ is directly related to the impact location X. The overtopping induced jet stress leads to pressure in cracks in the grass cover. When this pressure exceeds a certain threshold, named the critical pressure P_c, the crack widens. How much the crack widens depends on the amount of exceedance and the time period the pressure is applied. The amount of exceedance at location X on the land-side slope, multiplied with the time of exceedance is named the excess impulse load J_E which is determined to be the load leading to damage on the land-side slope. The total excess impulse load at a location X therefore becomes the summation of every single wave overtopping induced excess impulse load at location X. The location X at which the highest total excess impulse load occurs during a storm is the location at which the most damage is expected. This eventually has led to the following equation for the indication of total excess impulse load on the land-side slope:

$$J_{E,\text{tot}} = \sum_{n=1}^{N} (\rho(u^2_{\text{crest},n} + 2gX_n \ \tan\theta) \cdot \sin\varphi - P_c) \cdot \Delta t_n \tag{9.1}$$

The threshold value to determine at which overtopping induced jet pressure an overtopping wave contributes to damage on the land-side slope is named the critical pressure P_c. For the determination of the threshold, the critical pressure P_c, the simplified approach by Führbötter [12] is assumed to be valid for the Wave impact approach. The critical pressure is therefore assumed to be somewhere between two times the clay cohesion c and two times the artificial root cohesion c_r:

$$2 \cdot c \leqslant P_c \leqslant 2 \cdot c_r \tag{9.2}$$

For the determination of the clay cohesion c local soil research is required, the artificial root cohesion c_r is quantified by Hoffmans et al. [15].

An attempt is made to estimate the actual probability of exceedance of overtopping induced jet pressure during storm events. The results of these are presented in Appendix A, further research on this subject is however required to make a decent estimation of these probabilities.

9.4 Recommendations

Although a big leap is made in the direction of improving prediction methods for damage on the land side slope of a dike during storm events in this thesis, still lots of research is required to develop an actual usable tool. In the past 7 years the experimental research on initial failure mechanisms of dikes has increased the knowledge about this subject significantly. The difference in outcome of each executed experiment however indicates that many more experiments are required to, for example, validate the proposed Wave impact approach properly. Therefore the major recommendation of this thesis is to keep executing wave overtopping and overflow experiments.

As mentioned before the Wave impact approach method needs more research on several aspects to make the method an actual powerful tool to be used by amongst others governments to test whether their dike can be classified *safe*. Therefore some recommendations are initiated.

Assumption of uniform flow velocity at crest

The assumption of a uniform flow velocity profile at the crest of the dike leads to an overestimation of the load on the dike. In this thesis this effect is assumed to be negligibly small compared to the margin of error of failure of the land side slope. This assumption however is neither confirmed nor rejected and therefore requires more research.

Correction factor threshold parameters

The proposed threshold parameters are purely based on soil characteristics of the grass and clay cover of the land side slope. The effect of weak spots caused by for instance animal activity and weather conditions is not included in these threshold parameters. In order to include these effects probably some kind of correction parameter is required that leads to more realistic threshold values than proposed in this thesis. This correction parameter is most likely probabilistic based and much field research on land side slopes is therefore required. This was out of the scope of this research, therefore it is recommended to include this aspect in further research.

More general expression for failure threshold factor

The failure threshold parameter γ_f as introduced in this thesis is purely experimentally determined. In order to determine this parameter field measurements need to be executed. A more fundamental expression for this parameter is desired, so field measurements are not required.

Probabilistic approach for failure probability

The probability of exceedance equations as presented in Chapter A can be extended towards a failure probability method. To achieve this, a full probabilistic method is required which was not within the scope of this research. It is however highly recommended to include this probabilistic approach in the Wave impact approach because this makes it possible to determine the actual failure probability of a dike. By determining the failure probability of a dike a statement can be made whether the dike is to be classified *safe*.

More robust computer model

A basic Matlab computer model is built for wave overtopping induced impact loads. The model works and provides the right outcome but is rather expensive in computing power. When this computer model is going to be used in the future for the determination of wave impact loads, it is advised to make some internal improvements to reduce the required computing time.

Bibliography

[1] C. André. *High velocity aerated flows on stepped chutes with macro- roughness elements.* PhD thesis, Laboratoire de Constructions Hydrauliques Ecole Polytechnique Federale de Lausanne, 2004.

[2] J. Bakker and R. Mom. Factual report overslagproef wijmeers. Technical report, Infram B.V., 2015.

[3] J. Bakker, R. Mom, and G. Steendam. Factual report golfoverslagproeven friese waddenzeedijk. Technical report, Infram B.V., 2008.

[4] J. Bakker, R. Mom, and G. Steendam. Factual report golfoverslagproeven zeeuwse zeedijken. Technical report, Infram B.V., 2008.

[5] J. Bakker, R. Mom, and G. Steendam. Factual report overslagproeven en afschuifproef afsluitdijk. Technical report, Infram B.V., 2009.

[6] J. Bakker, R. Mom, G. Steendam, and J. Van der Meer. Factual report overslagproeven en oploopproef tholen. Technical report, Infram B.V., 2011.

[7] J. Battjes. Computation of set-up, longshore currents, run-up and overtopping due to wind generated waves. Technical report, Delft University of Technology, 1974.

[8] S. Bonelli, F. Byron, Y. Gremeaux, and G. Nunes. Etude des proprietes des sols constitufs des digues. Technical report, Irstea, unite de recherche ouvrages Hydrauliques et Hydrologie.

[9] S. Canepa and W. Hager. Effect of jet air content on plunge pool scour. *Journal of Hydraulic Engineering*, 2004.

[10] R. Dean, J. Rosati, T. Walton, and B. Edge. Erosional equivalences of levees: Steady and intermittent wave overtopping. *Elsevier*, 2010.

[11] C. D'eliso. *Chapter Breaching of Sea Dikes Initiated by Wave Overtopping: A Tiered and Modular Modelling Approach.* PhD thesis, Faculty of Architecture, Civil Engineering and Environmental Sciences University of Braunschweig – Institute of Technology, 2007.

[12] A. Fuhrbotter. Der druckschlag durch brecher auf deichböschungen. Technical report, Mitteilungen des Franzius-Instituts für Grund- und Wasserbau der Technischen Universität Hannover, 1966.

[13] H. W. M. Hewlett, L. A. Boorman, and M. E. Bramley. Design of reinforced grass waterways. Technical report, CIRIA Report 116 , Construction and Industry Research and Information Association, London, 1987.

[14] G. Hoffmans. Closure problem in jet scour. Technical report, Ministry of Transport, Public Works and Water Management; Road and Hydraulic Engineering Institute Delft, 2008.

[15] G. Hoffmans, G. Akkerman, H. Verheij, A. Van Hoven, and J. Van der Meer. The erodibility of grassed inner dike slopes against wave ovrtopping. Technical report, Deltares, Royal HaskoningDHV, Delft University of Technology, Van der Meer Consulting B.V., 2008.

[16] S. Hughes. Estimation of overtopping flow velocities on earthen levees due to irregular waves. Technical report, U.S. Army Corps of Engineers, 2008.

[17] S. Hughes. Adaptation of the levee erosional equivalence method for the hurricane storm damage risk reduction system (hsdrrs). Technical report, U.S. Army Corps of Engineers, 2011.

[18] S. Hughes, C. Thornton, J. Van der Meer, and B. Scholl. Improvements in descriving wave overtopping processes. Technical report, Coastal Engineering, 2012.

[19] I. Hunt. Design of seawalls and breakwaters. *Journal of Waterways and Harbours Division*, 1959.

[20] S. Miedema. Dredging processes, the cutting of sand, clay and rock. Technical report, Delft University of Technology, 2013.

[21] *Voorschrift Toetsen op Veiligheid Primaire Waterkeringen.* Ministerie van Verkeer en Waterstaat, 2006.

[22] P. Peeters, L. De Vos, B. Vandevoorde, E. Taverniers, and F. Mostaert. Erosiebestendigheid van de grasmat bij golfoverslag. Technical report, Waterbouwkundig laboratorium, Flanders Hydraulics research, 2012.

[23] T. Pullen, N. Allsop, T. Bruce, A. Kortenhaus, H. Sch uttrumpf, and J. Van Der Meer. Eurotop wave overtopping of sea defences and related structures assessment manual. Technical report, HR Wallingford (UK) University Edinburgh (UK) Leichtweiss Institut (DE) Bundesanstalt für Wasserbau (DE) Infram (NL), 2007.

[24] W. Richwien. Die widerstandsfähigkeit von deichen beim wellenüberlauf und die entwicklung von deichbrüchen - eine bestandsaufnahme. Technical report, 2003.

[25] H. Sch uttrumpf and H. Oumeraci. Layer thickness and velocities of wave overtopping flow at seadikes. Technical report, Coastal Engineering, 2005.

[26] H. Sch uttrumpf and M. Van Gent. Wave overtopping at seadikes. Technical report, American society of civil engineers, 2003.

[27] Sommer Messtechnik. *RG-30 Contact-free velocity sensor for open channels and rivers*, 2015.

[28] G. Stanczak. Laboratory tests on the erosion of clay revetment of sea dike with and without a grass cover induced by breaking wave impact. Technical report, Floodsite, 2007.

[29] G. Stanczak, H. Oumeraci, and A. Kortenhaus. Breaching of sead dikes initiated by breaking wave impacts. Technical report, HR Wallingford, 2008.

[30] TAW. Clay for dikes, technical advisory committee on water retaining structures. Technical report, The Netherlands, 1996.

[31] L. Trung and H. Verhagen. Damage to grass covered slopes due to overtopping. Technical report, -, 2014.

[32] A. Valk. Wave overtopping of water jets on grassed inner slope transitions. Master's thesis, Delft University of Technology, 2009.

[33] M. Van Damme. Determining stress conditions on the embankment surface for wave overtopping events. Technical report, Delft University of Technology, 2015.

[34] J. van der Meer. Technisch rapport golfoploop en golfoverslag bij dijken. Technical report, Technische Adviescommissie voor Waterkeringen, 2002.

[35] J. van der Meer. Workpackage 3: Development of alternative overtopping-resistant sea defence. Technical report, Imfram, 2007.

[36] J. Van der Meer, B. Hardeman, G. Steendam, H. Sch uttrumpf, and H. Verheij. Flow depths and belocities at crest and inner slope of a dike, in theory and with the wave overtopping simulator. Technical report, Coastal Engineering, 2010.

[37] J. Van Der Meer, A. Van Hoven, M. Paulissen, G. Steendam, H. Verheij, G. Hoffmans, and G. Kruse. Handreiking toetsen grasbekledingen op dijken t.b.v. het opstellen van het beheerdersoordeel (bo) in de verlengde derde toetsronde. Technical report, Rijkswaterstaat, 2012.

[38] M. Van Gent. Low-exceedance wave overtopping events. measurements of velocities and the thickness of water-layers on the crest and inner slope of dikes. Technical report, Delft Cluster, 2002.

[39] P. Van Steeg, M. Klein Breteler, and A. Labrujere. Use of wave impact generator and wave flume to determine strength of outer slopes of grass dikes under wave loads. Technical report, Deltares, 2015.

[40] A. Verruijt. *Grondmechanica*. VSSD, 1983.

[41] F. Visconti, L. Stefanon, C. Camporeale, F. Susin, L. Ridolfi, and S. Lanzoni. Bed evolution measurement with flowing water in morphodynamics experiments. *Earth Surface Processes And Landforms*, 2011.

[42] J. Wouters. Wieringermeerdijk, samenvattend verslag van de geavanceerde reststerktetoets. Technical report, Infram B.V., 2008.

List of Figures

1 Wave overtopping induced failure process clarified in 6 steps. vi
2 Door golfoverslag geïnitieerde erosie prosessen van de afdeklaag van het binnentalud, verduidelijkt in 6 stappen. viii

1.1 Thesis structure 5

2.1 Breaching of sea dikes initiated by wave overtopping: modelling phases and simulated processes as indicated by D'Eliso [11] 8
2.2 Breaching of sea dikes initiated by wave overtopping: modelling phases and simulated processes as indicated by D'Eliso [11] 8
2.3 Cracks in grass and clay cover layer, picture from TAW 1996 report [30] 9
2.4 Erosion of grass or clay cover described by A. Valk [32]. 10
2.5 Forces acting on a clay aggregate, picture from a paper by Hoffmans et al. [15] . . . 12

3.1 A pump was connected to the overtopping simulator through multiple pipelines. The pump was placed deep into the river water. 26
3.2 Overflow simulator 26
3.3 Interior of the overflow simulator 27
3.4 Outflow of the overflow simulator 27
3.5 Division of the test sections over the dike 28
3.6 Test section for the first overtopping experiment. 28
3.7 Second overflow test section. The section was split in half to create two parts: one to test on the grass layer and one to test directly on the clay layer. 30
3.9 Determination of the discharge of the outflow happened with a weir placed in the current. The water level upstream of the weir is related to the discharge according to equation 3.1 32

4.1 The first 3,5 m of the test section was covered with a plastic sheet to prevent erosion on the crest. Therefore the grass cover was exposed only just in front of the land side slope. 33
4.2 Overview of the damage pattern after the 10, 25, 50 and 85 $\mathrm{lm^{-1}s^{-1}}$ tests. 34
4.3 Overview of the damage pattern after the 125 and 170 $\mathrm{lm^{-1}s^{-1}}$ tests. 35
4.4 Overflow depth during different overflow discharges 36
4.5 Measuring points during overflow simulation 36
4.6 Overflow test at 85 $\mathrm{lm^{-1}s^{-1}}$. Although not clearly visible on the picture, the right part of the test section appeared to be more aerated than the left part. 37
4.7 Velocity measurements as done by the paddle wheels during both the overflow tests . 38
4.8 The warm floater as recorded by the infra-red camera. 39

5.1 Both at the water surface and at the bottom the flow velocity was measured using a paddle wheel. 42
5.2 Positions of the surf boards and paddle wheels on the land side slope of the dike. . . 43
5.3 Wave height for overtopping waves of 500, 1000, 1500 and 2000 l/m. Each wave volume test was repeated 3 times. 44
5.4 Wave height for overtopping waves of 2500, 3000 and 3500 l/m. Each wave volume test was executed once, after executing all three tests the 2500 l/m test was repeated another 2 times. 45
5.5 Surface- and bottom flow velocity for overtopping waves of 500, 1000, 1500 and 2000 l/m. Each wave volume test was repeated 3 times. 46
5.6 Surface- and bottom flow velocity for overtopping waves of 2500, 3000 and 3500 l/m. Each wave volume test was executed once, after executing all three tests the 2500 l/m test was repeated another 2 times. 46
5.7 Peak discharges as obtained from the data from the hydraulic measurements 47

6.1 Theoretical crest flow velocity according to the Van Gent theory [38]. $X = 0$ marks the end of the crest i.e. the start of the land-side slope. 50
6.2 Combinations of (velocities, durations) for acceptable erosion of various coverings due to steady overtopping by Hewlett et al. [13] as reported in Hughes [16] 51
6.3 Discharges as calculated using Equation 2.48 plotted over the measured discharge data at the crest (position I) for a 0.5 m^3 wave 54
6.4 Discharges as calculated using Equation 2.48 plotted over the measured discharge data at the crest (position I) for a 1.0 m^3 wave 54
6.5 Discharges as calculated using Equation 2.48 plotted over the measured discharge data at the crest (position I) for a 1.5 m^3 wave 55
6.6 Scatter plot of the waves as released by the overtopping simulator during the 1, 5, 10 and 25 l/m/s tests. 56

7.1 Roll up failure process of grass cover as visualized by Trung & Verhagen [31]. 60
7.2 Direct clay erosion due to a distributed load and a point load. 61
7.3 Failure initiation process clarified in 6 steps. 62
7.4 Reference pictures from the Wijmeers-II experiments for the failure initiation process. 63
7.5 Separation time of an overtopping wave before making contact with the land-side slope. The wave in this case is a 1000l wave during the hydraulic measurements. . . 64
7.6 Orbit of an overtopping wave with horizontal crest flow velocity $u_{\text{crest}} = 4$ m/s and crest water depth $d_{\text{crest}} = 0.1$ m. 66
7.7 Wave impact force and impact velocity 68
7.8 Decrease in overtopping induced jet stress 69
7.9 An overtopping wave basically 'pulls back' once it has made contact with the land-side slope. 71
7.10 Example of the impact point and wave load of a single overtopping wave plotted over time. The overtopping volume of this example is 1.0 m^3 72
7.11 Example of the impact location a single overtopping wave plotted over time.The overtopping volume of this example is 2.0 m^3 72
7.12 The pressure in a crack is caused by wave overtopping induced stress on the land-side slope. 73
7.13 Cumulative wave load of the waves as applied during the Wijmeers-II experiments. . 75
7.14 Cumulative wave load of the waves as applied during the Wijmeers-II experiments. The overtopping wave thickness is in these plots not taken into account yet. 76

7.15 Forces inside a crack subject to an impact pressure after Führbötter [12] 77
7.16 The extended approach introduced by Richwien [24] considers also the forces that were neglected by Führbötter [12] 77
7.17 An overtopping wave with uniform crest flow velocity considered at the moment of impact of the bottom of the overtopping wave. 79
7.18 For the numerical approach the flow at the crest is considered an accumulation of small d_i m thick flows with flow velocity u_{crest} 83
7.19 Load on the land-side slope with a threshold value of $P_c = 10\ kN/m^2$. 83
7.20 Cumulative wave overtopping induced impulse load. Data from the Wijmeers-II. . . 84
7.21 A six hour Weibull distributed storm of average overtopping discharge were simulated to test the influence of different slope angles on the overtopping wave impact load. The initial damage threshold σ_c was set at $10\ kN/m^2$. 85

8.1 Peak loads corresponding to the X coordinates at which damage was observed during the first Wijmeers-II overtopping experiment. 90
8.2 Initial damage during the second overtopping experiments occurred in grid section 7. 91
8.3 Peak loads corresponding to the X coordinates at which damage was observed during the second Wijmeers-II overtopping experiment. 91
8.4 Tielrode overtopping experiment result test section 1, Picture from the factual report published by Flanders Hydraulics Research [22] 92
8.5 Tielrode overtopping experiment result test section 2. Picture from the factual report published by Flanders Hydraulics Research [22] 92
8.6 Tielrode overtopping experiment result test section 3, Picture from the factual report published by Flanders Hydraulics Research [22] 93
8.7 Peak loads corresponding to the X coordinates at which damage was observed during the Tielrode overtopping experiment. 93
8.8 Final result of the wave overtopping experiments at the Afsluitdijk, February 2009. Photo's taken by Infram B.V. [5] 94
8.9 Peak loads corresponding to the X coordinates at which damage was observed during the first Afsluitdijk overtopping experiment. 95
8.10 Peak load corresponding to the X coordinates at which damage was observed during the second Afsluitdijk overtopping experiment. For $P_c = 10\ kN/m^2$ the peak occurs around $X = 2.8$ m 96
8.11 Initial damage spots during the St Philipsland overtopping experiments. Photo taken by Infram B.V. [4] 97
8.12 Final result of the St Philipsland overtopping experiments. Photo taken by Infram B.V. [4] 97
8.13 Peak loads corresponding to the X coordinates at which damage was observed during the overtopping experiment at St Philipsland. 98
8.14 Initial damage spots noticed during the second Kattendijke overtopping experiments. Photo taken by Infram B.V. [4] 98
8.15 Peak loads corresponding to the X coordinates at which damage was observed during the overtopping experiment at Kattendijke. $P_c = 15\ kN/m^2$, the maximum wave impact point was $X = 5.5$ m so the damage at $X = 6.6$ m was not caused by wave overtopping. 98

9.1 Wave overtopping induced failure process clarified in 6 steps. 106

A.1 Probability of exceedance during a storm event with significant wave height H_s. . . . 125

A.2 Normalized probability of exceedance of horizontal coordinate of wave impact X and wave impact load perpendicular to the land side slope σ_z 127
A.3 Probability of exceedance during a storm of horizontal coordinate of wave impact X and wave impact load perpendicular to the land side slope $\sigma_{\tilde{z}\tilde{z}}$ 128

C.1 Breaching of sea dikes initiated by wave overtopping: modelling phases and simulated processes as indicated by D'Eliso [11] 136
C.2 Breaching of sea dikes initiated by wave overtopping: modelling phases and simulated processes as indicated by D'Eliso [11] 136
C.3 Roll up failure process of grass cover as visualized by Trung [31]. 140
C.4 Erodibility coefficient as a function of clay soil properties, indicated by D'Eliso [11] . 141
C.5 Schematization of forces acting on the soil leading to jet induced scour development. Picture from Msc. Thesis of A. Valk [32] 143
C.6 Scour development as described by Canepa and Hager [9] 144

D.1 Residual strength threshold factor D_c visualized for three different critical pressure values P_c. Figure D.1a indicates failure of the grass cover, Figures D.1b and D.1c indicate a damaged but not failed grass cover. $D_c = 5000$ is purely notional to demonstrate the effect of the threshold. 147

E.1 Example of the impact load of a single overtopping wave plotted against the x-coordinate of the land side slope. The load is plotted for a number of moments in time, the time step in this plot $\Delta t = 0.05$ s. 150
E.2 Example of the impact points of an overtopping wave plotted against time. The colorbar indicates the load on the land side slope. 150
E.3 Example of the impact load of a single overtopping wave plotted against the x-coordinate of the land side slope and time. 151
E.4 An overtopping wave with uniform crest flow velocity considered at the moment of impact of the bottom of the overtopping wave. 154

F.1 Initial damage during the second overtopping experiments occurred in grid section 7. 156
F.2 Final result of the wave overtopping experiments at the Afsluitdijk, February 2009. Photo's taken by Infram B.V. [5] 157
F.3 Final result of the third Friese Waddenzeedijk overtopping experiments. Photo taken by Infram B.V. [3] 159
F.4 Final result of the fourth Friese Waddenzeedijk overtopping experiments. Photo taken by Infram B.V. [3] 160
F.5 Initial damage spots during the St Philipsland overtopping experiments. Photo taken by Infram B.V. [4] 161
F.6 Final result of the St Philipsland overtopping experiments. Photo taken by Infram B.V. [4] 161
F.7 Initial damage spots noticed during the second Kattendijke overtopping experiments. Photo taken by Infram B.V. [4] 162
F.8 Final result of the third wave overtopping test at Tholen, a large part of the land side slope had sheared due to the presence of animal activity. Photo's taken by Infram B.V. [6] 163
F.9 Final result second overtopping experiment Tholen, the land side slope collapsed completely due to the washing away of the sand core by groundwater flow. Photo taken by Infram B.V. [6] 164

G.2 Pump frequency: 20 Hz. 167
G.4 Pump frequency: 25 Hz. 169
G.6 Pump frequency: 30 Hz. 171
G.8 Pump frequency: 35 Hz. 173
G.10 Pump frequency: 40 Hz. 175
G.11 Pump frequency: 45 Hz. 175
G.13 Pump frequency: 50 Hz. 177

H.1 Water depth, bottom velocity, surface velocity and discharge as obtained from position 1 during the 500 l test. 179
H.2 Water depth, bottom velocity, surface velocity and discharge as obtained from position 2 during the 500 l test. 180
H.3 Water depth, bottom velocity, surface velocity and discharge as obtained from position 3 during the 500 l test. 180
H.4 Water depth, bottom velocity, surface velocity and discharge as obtained from position 1 during the 1000 l test. 181
H.5 Water depth, bottom velocity, surface velocity and discharge as obtained from position 2 during the 1000 l test. 182
H.6 Water depth, bottom velocity, surface velocity and discharge as obtained from position 3 during the 1000 l test. 182
H.7 Water depth, bottom velocity, surface velocity and discharge as obtained from position 1 during the 1500 l test. 183
H.8 Water depth, bottom velocity, surface velocity and discharge as obtained from position 2 during the 1500 l test. 184
H.9 Water depth, bottom velocity, surface velocity and discharge as obtained from position 3 during the 1500 l test. 184
H.10 Water depth, bottom velocity, surface velocity and discharge as obtained from position 1 during the 2000 l test. 185
H.11 Water depth, bottom velocity, surface velocity and discharge as obtained from position 2 during the 2000 l test. 186
H.12 Water depth, bottom velocity, surface velocity and discharge as obtained from position 3 during the 2000 l test. 186
H.13 Water depth, bottom velocity, surface velocity and discharge as obtained from position 1 during the first 2500 l test. 187
H.14 Water depth, bottom velocity, surface velocity and discharge as obtained from position 2 during the first 2500 l test. 188
H.15 Water depth, bottom velocity, surface velocity and discharge as obtained from position 3 during the first 2500 l test. 188
H.16 Water depth, bottom velocity, surface velocity and discharge as obtained from position 1 during the second 2500 l test. 189
H.17 Water depth, bottom velocity, surface velocity and discharge as obtained from position 2 during the second 2500 l test. 189
H.18 Water depth, bottom velocity, surface velocity and discharge as obtained from position 3 during the second 2500 l test. 190
H.19 Water depth, bottom velocity, surface velocity and discharge as obtained from position 1 during the 3000 l test. 191
H.20 Water depth, bottom velocity, surface velocity and discharge as obtained from position 2 during the 3000 l test. 192

H.21 Water depth, bottom velocity, surface velocity and discharge as obtained from position 3 during the 3000 l test. 192
H.22 Water depth, bottom velocity, surface velocity and discharge as obtained from position 1 during the 3500 l test. 193
H.23 Water depth, bottom velocity, surface velocity and discharge as obtained from position 2 during the 3500 l test. 194
H.24 Water depth, bottom velocity, surface velocity and discharge as obtained from position 3 during the 3500 l test. 194

I.1 Description of the test section before starting the tests. 196
I.2 Description of the damage after 1 hour of 10 l/m/s test on the first test strip. 197
I.3 Description of the damage after 2 hours of 10 l/m/s test on the first test strip. Immediately after the 10 l/m/s test the 25 l/m/s test started. Therefore this description of damage also holds for the initial damage of the 25 l/m/s test. 198
I.4 Description of the damage after 2 hours of 25 l/m/s test on the first test strip. Immediately after the 25 l/m/s test the 50 l/m/s test started. Therefore this description of damage also holds for the initial damage of the 50 l/m/s test. 199
I.5 Description of the damage after 1 hour of 50 l/m/s test on the first test strip. 200
I.6 Description of the damage after 2 hours of 50 l/m/s test on the first test strip. Immediately after the 50 l/m/s test the 85 l/m/s test started. Therefore this description of damage also holds for the initial damage of the 85 l/m/s test. 201
I.7 Description of the damage after 2 hours of 85 l/m/s test on the first test strip. 202
I.8 Description of the damage after 1 hour of 125 l/m/s test on the first test strip. . . . 203
I.9 Description of the damage after 1 hour of 170 l/m/s test on the first test strip. This is the maximum load that was applied on the test section. 204

List of Tables

2.1 Empirical coefficients as determined by Schüttrumpf and Van Gent. 18

4.1 Estimations of the flow velocity at 125 and 160 $lm^{-1}s^{-1}$. Table shows the stop-watch measurements of the time a floating ball lasted to cover a distance of 6 metres. . . . 37
4.2 Average flow velocities as obtained from the infra-red camera recordings 40

5.1 Position of the surfboards and paddle wheels on the test section during the hydraulic measurements 42
5.2 Peak discharges as determined from the data provided by the paddle wheels. 47
5.3 Volume of each tested wave according to the data obtained from the surfboards and paddle wheels. 48

6.1 The flow depth measurements executed during the overflow tests are used to determine the crest flow velocity. 49
6.2 Average flow velocities as obtained from the infra-red camera recordings 50
6.3 Velocities and durations as obtained from the experiments executed by Hewlett et al. [13] (see also Figure 6.2) 51
6.4 Calculated peak discharges compared to measured peak discharges. 53
6.5 Input data for the overflow tests 56
6.6 Result of the Excess wave volume calculations 57

7.1 Grass cover characteristics as found by Hoffmans et al. [15] 79
7.2 Slopes and slope angles corresponding to different simulations by the Wave impact model. 84

8.1 Grass cover characteristics as found by Hoffmans et al. [15] 99
8.2 Results verification Wave impact approach. 100

A.1 Scaling parameters j for the Rayleigh distribution 123
A.2 Parameters for Rayleigh distribution for the normalized depth of overtopping waves for a 10% crest level 124
A.3 Overtopping variables expressed in each other, these expressions are also worked out in Appendix B 126

Symbols

a	Calibration parameter	-
A	Surface area	m^2
A_r	Root surface area	m^2
b	Calibration parameter	-
c	Cohesion	kNm^{-2}
c_r	Artificial root cohesion	kNm^{-2}
c_s	Soil cohesion	kNm^{-2}
C_z	Chézy constant	$\mathrm{m}^{1/2}\mathrm{s}^{-1}$
d	Water depth	m
d_p	Peak water depth	m
$d_{n\%}$	Water depth exceeded by n% of incoming waves	m
d_{crest}	Crest water depth	m
D_E	Damage factor	-
E_W, K_W, β_W	Soil condition parameters	-
f	Friction factor	-
F_c	Cohesion force	kN
F_g	Grass force	kN
F_p	Overtopping wave impact force	kN
F_s	Shear force	kN
F_g	Weight of overflowing water	kN
g	Gravitational constant	ms^{-2}
H_s	Significant wave height	m
J_z	Impulse load	kNsm^{-2}
J_E	Excess impulse load	kNsm^{-2}
n	Manning coefficient	$\mathrm{sm}^{-1/3}$
P	Probability of exceedance	-
P_{crack}	Pressure in crack	kNm^{-2}
P_{max}	Maximum pressure	kNm^{-2}
$R_{u,2\%}$	Run-up height exceeded by 2% of the incoming waves	m
$R_{u,n\%}$	Run-up height exceeded by n% of the incoming waves	m
T_o	Overtopping time	s
t	Time	s
Δt	Impact time overtopping jet	s

q	Discharge	$m^3s^{-1}m^{-1}$
q_c	Critical discharge	$m^3s^{-1}m^{-1}$
q_p	Peak discharge	$m^3s^{-1}m^{-1}$
$q_{n\%}$	Discharge exceeded by n% of incoming waves	$m^3s^{-1}m^{-1}$
Q	Discharge	m^3s^{-1}
R_C	Freeboard	m
u_p	Peak velocity	ms^{-1}
u_x	Horizontal velocity component	ms^{-1}
u_z	Vertical velocity component	ms^{-1}
u_{crest}	Crest velocity	ms^{-1}
u_{imp}	Impact velocity	ms^{-1}
$u_{n\%}$	Velocity exceeded by n% of incoming waves	ms^{-1}
$u_{A,2\%}$	Run-up velocity at sea-side exceeded by n% of incoming waves	ms^{-1}
$u_{B,2\%}$	Velocity at land-side exceeded by n% of incoming waves	ms^{-1}
$u_{c,2\%}$	Run-up velocity on the crest, exceeded by 2% of the waves	ms^{-1}
u_∞	Terminal velocity	ms^{-1}
u_c	Critical velocity	ms^{-1}
v	Kinematic viscosity	-
V	Volume	m^3
V_W	Wave volume	m^3
V_E	Excess volume	m^3
V_{ET}	Excess volume	m^3
$V_{n\%}$	Volume exceeded by n% of incoming waves	m^3
x_c	Position on dike crest with respect to beginning of dike crest	m
X	Horizontal coordinate on land-side slope	m
z	Height	m
Z	Vertical coordinate on land-side slope	m
α	Water-side slope angle	rad
β	Angle of impact of overtopping wave bottom	rad
ρ	Water density	kgm^{-3}
ρ_s	Soil density	kgm^{-3}
θ	Land-side slope angle	rad
θ_s	Angle of shear deformation	rad
φ	Angle of impact of overtopping wave surface	rad
σ_g	Normal grass strength	kNm^{-2}
$\sigma_{\tilde{z}\tilde{z}}$	Impact stress component perpendicular to land-side slope	kNm^{-2}
τ	Bed shear stress	kNm^{-2}
τ_c	Critical bed shear stress	kNm^{-2}
τ_p	Peak bed shear stress	kNm^{-2}
τ_0	Bed shear stress	kNm^{-2}
$\tau_{\tilde{z}\tilde{x}}$	Impact stress component parallel to land-side slope	kNm^{-2}
$\gamma_b\gamma_f\gamma_\beta$	Correction factors	-
ξ_0	Wave breaker parameter	-

A | Overtopping probability

A.1 Overtopping probability parameters

In a yet unpublished paper Myron van Damme [33] developed a method to describe overtopping wave volumes, shear stess, water depth, discharge and flow velocity in terms of crest height h_c, significant wave height H_s and probability of exceedance P. The method is based on the wave run-up theory as developed by Schüttrumpf and Oumeraci [25] and Van Gent [38]. This probability distribution function describes the probability an overtopping wave during a storm even exceeds a certain value of variable K. K is denoted by overtopping variables: Overtopping peak flow velocity U_p, Overtopping peak shear stress T_p, Overtopping peak flow depth D_p, Overtopping peak discharge Q_p, and Overtopping volume V. Wave run-up is generally assumed to be Rayleigh distributed which leads to a generic equation for a normalized wave overtopping parameter N:

$$N = \left(\frac{R_{n\%} - h_{\text{crest}}}{H_s}\right)^j \tag{A.1}$$

Where j is a scaling factor for different overtopping parameters. For $j = \frac{1}{2}$, N describes the normalized run-up velocity at crest level, for $j = \frac{2}{3}$ the normalized run-up bed shear stress at crest level, for $j = 1$ the normalized run-up depth at crest level, for $j = 1.5$ the normalized run-up discharge at crest level, and for $j = 2$ the normalized unit overtopping volume [33]. These variables are respectively denoted by U_p, T_p, D_p, Q_p, and V. The variables are also presented in Table A.1.

TABLE A.1: Scaling parameters j for the Rayleigh distribution

Paramater	Symbol	j
Overtopping peak velocity	U_p	1/2
Overtopping peak shear stress	T_p	2/3
Overtopping peak water depth	D_p	1
Overtopping peak discharge	Q_p	3/2
Overtopping volume	V	2

The overtopping probability of parameter K for waves with a certain significant wave H_s, crest height h_c and wave breaker parameter ξ is therefore denoted by:

$$P = \exp\left(\frac{h_c^2}{2\varepsilon^2 H_s^2 \epsilon^2}\right) \exp\left(-\frac{[(c_K K)^{\frac{1}{j}} + h_c]^2}{2\varepsilon^2 H_s^2 \epsilon^2}\right) \tag{A.2}$$

Where K is variable for which we want to calculate the probability of overtopping. c_K is a parameter to fit the parameter K in the Rayleigh distribution. Both parameters are further clarified in Table A.2. ε is a scale fit parameter for the Rayleigh distribution and ϵ is a parameter to include the wave breaker parameter ξ_0 in the equation. ϵ is given by:

$$\epsilon = \min\left\{\xi_0\gamma, \frac{\gamma}{1.65}\left(4.0 - \frac{1.5}{\sqrt{\xi_0}}\right)\right\} \tag{A.3}$$

Where γ is a correction factor for the characteristics of a dike. For this case, a normal dike is considered, meaning $\gamma = 1$.

TABLE A.2: Parameters for Rayleigh distribution for the normalized depth of overtopping waves for a 10% crest level

Parameter	Symbol (K)	c_K
Overtopping peak velocity	U_p	$\frac{1}{\sqrt{2g}}$
Overtopping peak shear stress	T_p	$\frac{1}{\rho_w n_m^2 g \tan\alpha^{\frac{1}{3}} c_\tau}$
Overtopping peak depth	D_p	$\frac{\tan\alpha}{c_d}$
Overtopping peak discharge	Q_p	$\frac{\tan\alpha}{c_d\sqrt{g}}$
Overtopping peak volume	V	$\frac{2\sin^2\alpha}{\cos\alpha c_d}$

Here c_d is the run up depth gradient and α is the angle of the water side slope. Using Equation A.2 and Table A.2 a relation is derived that can describe different normalized overtopping parameters in terms of significant wave H_s, crest height h_c and wave breaker parameter ξ. These relations are given below:

$$U_p = \left(\left[-2\varepsilon^2 H_s^2 \epsilon^2 ln\left(P\ \exp\left(-\frac{h_c^2}{\varepsilon^2 H_s^2 \epsilon^2}\right)\right)\right]^{\frac{1}{2}} + h_c\right)^{\frac{1}{2}} \sqrt{g} \tag{A.4}$$

$$T_p = \left(\left[-2\varepsilon^2 H_s^2 \epsilon^2 ln\left(P\ \exp\left(-\frac{h_c^2}{\varepsilon^2 H_s^2 \epsilon^2}\right)\right)\right]^{\frac{1}{2}} + h_c\right)^{\frac{2}{3}} \rho_w n_m^2 g \tan\alpha c_\tau \tag{A.5}$$

$$D_p = \left(\left[-2\varepsilon^2 H_s^2 \epsilon^2 ln\left(P\ \exp\left(-\frac{h_c^2}{\varepsilon^2 H_s^2 \epsilon^2}\right)\right)\right]^{\frac{1}{2}} + h_c\right) \frac{c_d}{\tan\alpha} \tag{A.6}$$

$$Q_p = \left(\left[-2\varepsilon^2 H_s^2 \epsilon^2 ln\left(P\ \exp\left(-\frac{h_c^2}{\varepsilon^2 H_s^2 \epsilon^2}\right)\right)\right]^{\frac{1}{2}} + h_c\right)^{\frac{3}{2}} \frac{c_d\sqrt{g}}{\tan\alpha} \tag{A.7}$$

$$V = \left(\left[-2\varepsilon^2 H_s^2 \epsilon^2 ln\left(P\ \exp\left(-\frac{h_c^2}{\varepsilon^2 H_s^2 \epsilon^2}\right)\right)\right]^{\frac{1}{2}} + h_c\right)^{2} \frac{\cos\alpha c_d}{2\sin^2\alpha} \tag{A.8}$$

In a more general expression this leads to:

$$K = \left(\left[-2\varepsilon^2 H_s^2 \epsilon^2 ln\left(P \text{ exp}\left(-\frac{h_c^2}{\varepsilon^2 H_s^2 \epsilon^2}\right)\right)\right]^{\frac{1}{2}}\right)^j \frac{1}{c_K} \tag{A.9}$$

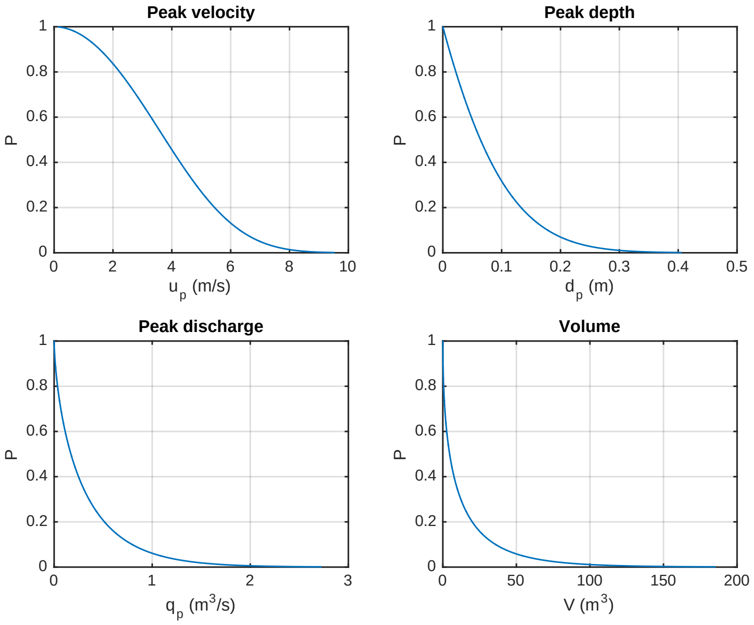

FIGURE A.1: Probability of exceedance during a storm event with significant wave height H_s.

A.2 Overtopping variables expressed in each other

The generic expression given in Equation A.2 also makes it possible to express overtopping parameters in terms of each other. A general expression for that purpose would be:

$$(c_{K,1}K_1)^{\frac{1}{j_1}} = (c_{K,2}K_2)^{\frac{1}{j_2}} \tag{A.10}$$

Comparing the relationship for the peak overtopping volume with the peak overtopping discharge for example gives:

$$\left(\frac{\tan\alpha}{c_d\sqrt{g}}Q_p\right)^{\frac{2}{3}} = \left(\frac{2\sin^2\alpha}{\cos\alpha\ c_d}V\right)^{\frac{1}{2}} \tag{A.11}$$

Which leads to:

$$V = \left(\frac{\tan\alpha\ Q_p}{c_d\sqrt{g}}\right)^{\frac{4}{3}} \frac{\cos\alpha c_d}{2\sin^2\alpha} \tag{A.12}$$

Using Equation B.1, which is a worked out version of Equation A.10, a series of expressions is derived where each overtopping variable is expressed in one other overtopping variable. With 5 different overtopping variables this leads to 20 different equations. All equations are worked out in Appendix B of which the result is presented in Table A.3.

Table A.3: Overtopping variables expressed in each other, these expressions are also worked out in Appendix B

	In terms of U_p	T_p	D_p	Q_p	V
U_p	$\dots$	$\left(\frac{T_p}{\rho_w \tan\alpha^{\frac{1}{3}} n^2 g c_\tau}\right)^{\frac{3}{4}} \sqrt{2g}$	$\left(\frac{D_p \tan\alpha}{c_d}\right)^{\frac{1}{2}} \sqrt{2g}$	$\left(\frac{\tan\alpha}{c_d\sqrt{g}} Q_p\right)^{\frac{1}{3}} \sqrt{2g}$	$\left(\frac{2\sin^2\alpha}{\cos\alpha\ c_d} V\right)^{\frac{1}{4}} \sqrt{2g}$
T_p	$\left(\frac{U_p}{\sqrt{2g}}\right)^{\frac{4}{3}} (\tan\alpha^{\frac{1}{3}} \rho_w n^2 g c_\tau)$	$\dots$	$\left(\frac{D_p\ \tan\alpha}{c_d}\right)^{\frac{2}{3}} \tan\alpha^{\frac{1}{3}} \rho_w n^2 g c_\tau$	$\left(\frac{\tan\alpha\ Q_p}{c_d\sqrt{g}}\right)^{\frac{4}{9}} \rho_w \tan\alpha^{\frac{1}{3}} n^2 g c_\tau$	$\left(\frac{2\sin^2\alpha V}{\cos\alpha c_d}\right)^{\frac{1}{3}} \rho_w \tan\alpha^{\frac{1}{3}} n^2 g c_\tau$
D_p	$\left(\frac{U_p}{\sqrt{2g}}\right)^2 \frac{c_d}{\tan\alpha}$	$\left(\frac{T_p}{\rho_w \tan\alpha n^2 g c_\tau}\right)^{\frac{3}{2}} \frac{c_d}{\tan\alpha}$	$\dots$	$\left(\frac{\tan\alpha}{c_d\sqrt{g}} Q_p\right)^{\frac{2}{3}} \frac{c_d}{\tan\alpha}$	$\left(\frac{2\sin^2\alpha V}{\cos\alpha c_d}\right)^{\frac{1}{2}} \frac{c_d}{\tan\alpha}$
Q_p	$\left(\frac{U_p}{\sqrt{2g}}\right)^3 \frac{c_d\sqrt{g}}{\tan\alpha}$	$\left(\frac{T_p}{\rho_w \tan\alpha^{\frac{1}{3}} n^2 g c_\tau}\right)^{\frac{9}{4}} \frac{c_d\sqrt{2g}}{\tan\alpha}$	$\left(\frac{\tan\alpha\ D_p}{c_d}\right)^{\frac{3}{2}} \frac{c_d\sqrt{g}}{\tan\alpha}$	$\dots$	$\left(\frac{2\sin^2\alpha\ V}{\cos\alpha c_d}\right)^{\frac{3}{4}} \frac{c_d\sqrt{g}}{\tan\alpha}$
V	$\left(\frac{U_p}{\sqrt{2g}}\right)^4 \frac{\cos\alpha\ c_d}{2\sin^2\alpha}$	$\left(\frac{T_p}{\rho_w \tan^{\frac{1}{3}} \alpha n^2 g c_\tau}\right)^3 \frac{\cos\alpha\ c_d}{2\sin^2\alpha}$	$\left(\frac{\tan\alpha\ D_p}{c_d}\right)^2 \frac{\cos\alpha c_d}{2\sin^2\alpha}$	$\left(\frac{\tan\alpha\ Q_p}{c_d\sqrt{g}}\right)^{\frac{4}{3}} \frac{\cos\alpha c_d}{2\sin^2\alpha}$	$\dots$

A.3 Probability of exceedance

Substituting Equations A.4 to A.8 in Equation 7.32 provides the opportunity to express the load on the land side slope in terms of probability of exceedance, significant wave height and crest height. This makes the expression for the land side slope load more workable then the expressions earlier mentioned in this report, where it is expressed in terms of overtopping wave volume. Using this new formed equation it is possible to predict the spot on the land side slope where the heaviest load, and therefore probably the also biggest damage, occurs during a storm event with significant wave height H_s.

First Equation 7.7 is written in terms of u_p only using Table A.3. This is done to get a relation that expresses the maximum impact X-coordinate of an overtopping wave in one single variable, in this case u_p, for which a probability of exceedance relation as shown in Equations A.4 to A.8 is substituted. This eventually leads to a relation that describes the probability of exceedance of maximum impact points of overtopping waves. Equation 7.7 written in terms of u_p becomes:

$$X = \frac{u_p^2}{g}\left(\tan\theta + \sqrt{\tan^2\theta + \frac{c_d}{\tan\alpha}}\right) \tag{A.13}$$

Substituting the probability of exceedance term for u_p in Equation A.13 leads to the following expression:

$$X = \left(\left[-2\varepsilon^2 H_s^2 \epsilon^2 \ln\left(P \exp\left(-\frac{h_c^2}{\varepsilon^2 H_s^2 \epsilon^2}\right)\right)\right]^{\frac{1}{2}} + h_c\right)\left(\tan\theta + \sqrt{\tan^2\theta + \frac{c_d}{\tan\alpha}}\right) \tag{A.14}$$

Since the probability of exceedance of X coordinates of impact is now determined, automatically the probability of impact load is determined. From Equation 7.14 we know that the impact load is linearly related to the point of impact. This gives the following relation:

$$\sigma_{\tilde{z}\tilde{z}} = \left(\left[-2\varepsilon^2 H_s^2 \epsilon^2 \ln \left(P \exp \left(-\frac{h_c^2}{\varepsilon^2 H_s^2 \epsilon^2} \right) \right) \right]^{\frac{1}{2}} + h_c \right) \left(1 + 2\tan^2\theta + 2\tan\theta \sqrt{\tan^2\theta + \frac{c_d}{\tan\alpha}} \right) \sin\varphi \tag{A.15}$$

With this relation the probability of potential damage on the land side slope during a storm event with significant wave height H_s and crest height h_c can be predicted. With 'probability of potential damage' in this case is meant the probability that the impact load of overtopping waves contributes to damage on the land side slope. This is the case when the impact load of overtopping waves exceeds the threshold level $\P_c$. A visual impression impression of an example of the probability of exceedance of the maximum horizontal impact coordinate X and the corresponding wave impact load perpendicular to the land side slope σ_z is given in Figure A.2. In this case a significant wave height $H_s = 1.5\ m$ and crest height $h_c = 3.75\ m$ is used, this however is only an example to demonstrate the distribution of the probability of exceedance.

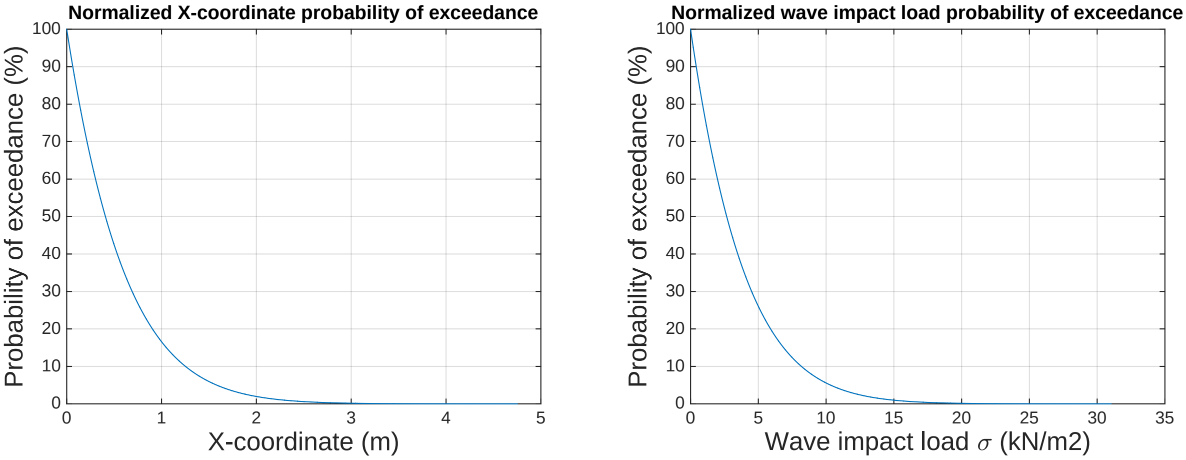

(A) $H_s = 1.5\ m$, $h_c = 3.75\ m$ (B) $H_s = 1.5\ m$, $h_c = 3.75\ m$

FIGURE A.2: Normalized probability of exceedance of horizontal coordinate of wave impact X and wave impact load perpendicular to the land side slope σ_z

Figure A.2 shows the wave impact probability of exceedance of all the waves that overtop the dike during a storm event. Since not all incoming waves actually overtop the dike during a storm event it makes more sense to write Equation A.15 in such a way that all incoming waves during a storm event are considered. Normally dikes are designed for a so called 2% run-up level [23] which means that during a design storm with a certain significant wave height H_s the crest level should be at such a level h_c, that 2% of the waves are allowed to overtop. Assumed that a dike is designed well, Equation A.15 calculates the wave impact load probability of exceedance of those 2% overtopping waves. Therefore, to calculate the actual probability of exceedance Equation A.15 should be multiplied by the overtopping percentage of the waves during a storm event. In the case of a well designed dike this means multiplying Equation A.15 by 0.02.

Equation A.2 is a normalized equation for the determination of overtopping probability of exceedance. In order to arrive at an expression for the overtopping probability of exceedance that includes all waves during a storm event, Equation A.2 needs to be denormalized. This is achieved by removing the first exponent, $\exp\left(\frac{h_c^2}{2\sigma^2 H_s^2 \epsilon^2}\right)$, from the equation. Which leads to the following relation:

$$X = \left(\left[-2\varepsilon^2 H_s^2 \epsilon^2 \ln\left(P\right)\right]^{\frac{1}{2}} + h_c\right)\left(\tan\theta + \sqrt{\tan^2\theta + \frac{c_d}{\tan\alpha}}\right) \tag{A.16}$$

$$\sigma_{\tilde{z}\tilde{z}} = \left(\left[-2\varepsilon^2 H_s^2 \epsilon^2 \ln\left(P\right)\right]^{\frac{1}{2}} + h_c\right)\left(1 + 2\tan^2\theta + 2\tan\theta\sqrt{\tan^2\theta + \frac{c_d}{\tan\alpha}}\right)\sin\varphi \tag{A.17}$$

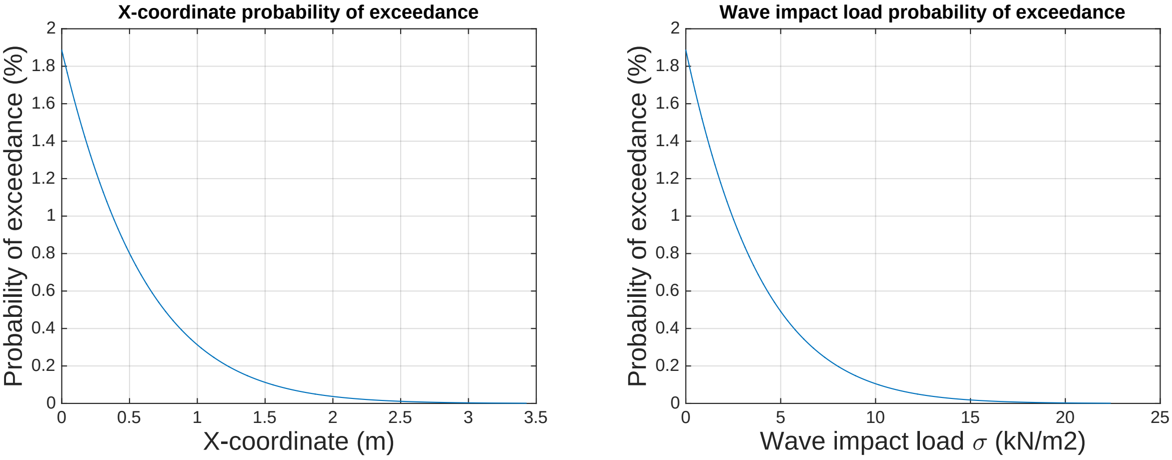

(A) $H_s = 1.5\ m$, $h_c = 3.75\ m$ (B) $H_s = 1.5\ m$, $h_c = 3.75\ m$

FIGURE A.3: Probability of exceedance during a storm of horizontal coordinate of wave impact X and wave impact load perpendicular to the land side slope $\sigma_{\tilde{z}\tilde{z}}$

In fact Equations A.17 and A.16 still do not tell anything about the actual failure probability of the land side slope of a dike. The equation indicates the probability of exceedance of a certain wave impact load given a storm of significant wave height H_s occurs. Equation A.17 and A.16 need to be multiplied by the probability of exceedance P_{storm} of a storm with significant wave height H_s in order to come to the actual failure probability of a specific land side slope:

$$X = \left(\left[-2\varepsilon^2 H_s^2 \epsilon^2 \ln\left(P\right)\right]^{\frac{1}{2}} + h_c\right)\left(\tan\theta + \sqrt{\tan^2\theta + \frac{c_d}{\tan\alpha}}\right) \cdot P_{\text{storm}} \tag{A.18}$$

$$\sigma_{\tilde{z}\tilde{z}} = \left(\left[-2\varepsilon^2 H_s^2 \epsilon^2 \ln\left(P\right)\right]^{\frac{1}{2}} + h_c\right)\left(1 + 2\tan^2\theta + 2\tan\theta\sqrt{\tan^2\theta + \frac{c_d}{\tan\alpha}}\right)\sin\varphi \cdot P_{\text{storm}} \tag{A.19}$$

The probability of exceedance of storm events in The Netherlands and Belgium is out of scope of this research, therefore Equations A.18 and A.19 are not further considered.

A.4 Conclusion

With Equations A.16 and A.17 a powerful tool is developed to calculate the safety of the land side slope of a dike. Given the design storm significant wave height H_s, design crest height h_c, breaker parameter ξ and soil characteristics c_s and $sigma_g$, the probability of exceedance of the threshold $sigma_c$ can be determined. This probability of exceedance is a very conservative measure for the actual failure probability of the land side slope since the residual strength of the dike is not yet considered in this tool. Therefore the actual failure probability of the land side slope will be much lower than the calculated probability of exceedance.

For future studies, it is advised to apply a probabilistic method to determine the probability of exceedance of a storm in Equations A.18 and A.19. The probability of exceedance of storms is out of the scope of this research but is important to include when the Wave impact approach is used to determine the failure probability of a dike.

B Overtopping terms expressed in each other

As mentioned in Section A.2 the Rayleigh distribution of the overtopping variables makes it possible to express overtopping terms in each other. Using Equation B.1 a series of expressions is derived where each overtopping variable is expressed in one other overtopping variable. With 5 different overtopping variables this leads to 20 different equations. All equations are presented below.

$$\left(\frac{U_p}{\sqrt{2g}}\right)^2 = \left(\frac{T_p}{\rho_w \tan\alpha^{\frac{1}{3}} n^2 g c_\tau}\right)^{\frac{3}{2}} = D_p \frac{\tan\alpha}{c_d} = \left(\frac{\tan\alpha}{c_d\sqrt{g}} Q_p\right)^{\frac{2}{3}} = \left(\frac{2\sin^2\alpha}{\cos\alpha\ c_d} V\right)^{\frac{1}{2}} \tag{B.1}$$

Peak overtopping flow velocity

$$U_p = \left(\frac{T_p}{\rho_w \tan\alpha^{\frac{1}{3}} n^2 g c_\tau}\right)^{\frac{3}{4}} \sqrt{2g} \tag{B.2}$$

$$U_p = \left(\frac{D_p \tan\alpha}{c_d}\right)^{\frac{1}{2}} \sqrt{2g} \tag{B.3}$$

$$U_p = \left(\frac{\tan\alpha}{c_d\sqrt{g}} Q_p\right)^{\frac{1}{3}} \sqrt{2g} \tag{B.4}$$

$$U_p = \left(\frac{2\sin^2\alpha}{\cos\alpha\ c_d} V\right)^{\frac{1}{4}} \sqrt{2g} \tag{B.5}$$

Peak overtopping shear stress

$$T_p = \left(\frac{(U_p}{\sqrt{2g}}\right)^{\frac{4}{3}} \tan\alpha^{\frac{1}{3}} \rho_w n^2 g c_\tau \tag{B.6}$$

$$T_p = \left(\frac{D_p \ \tan\alpha}{c_d}\right)^{\frac{2}{3}} \tan\alpha^{\frac{1}{3}} \rho_w n^2 g c_\tau \tag{B.7}$$

$$T_p = \left(\frac{\tan\alpha \ Q_p}{c_d\sqrt{g}}\right)^{\frac{4}{9}} \rho_w \tan\alpha^{\frac{1}{3}} n^2 g c_\tau \tag{B.8}$$

$$T_p = \left(\frac{2\sin^2\alpha V}{\cos\alpha c_d}\right)^{\frac{1}{3}} \rho_w \tan\alpha^{\frac{1}{3}} n^2 g c_\tau \tag{B.9}$$

Peak overtopping water depth

$$D_p = \left(\frac{U_p^2}{\sqrt{2g}}\right)^{\frac{1}{2}} \frac{c_d}{\tan\alpha} \tag{B.10}$$

$$D_p = \left(\frac{T_p}{\rho_w \tan\alpha^{\frac{1}{3}} n^2 g c_\tau}\right)^{\frac{3}{2}} \frac{c_d}{\tan\alpha} \tag{B.11}$$

$$D_p = \left(\frac{\tan\alpha}{c_d\sqrt{g}} Q_p\right)^{\frac{2}{3}} \frac{c_d}{\tan\alpha} \tag{B.12}$$

$$D_p = \left(\frac{2\sin^2\alpha V}{\cos\alpha c_d}\right)^{\frac{1}{2}} \frac{c_d}{\tan\alpha} \tag{B.13}$$

Peak overtopping discharge

$$Q_p = \left(\frac{U_p}{\sqrt{2g}}\right)^{3} \frac{c_d\sqrt{g}}{\tan\alpha} \tag{B.14}$$

$$Q_p = \left(\frac{T_p}{\rho_w \tan\alpha^{\frac{1}{3}} n^2 g c_\tau}\right)^{\frac{9}{4}} \frac{c_d\sqrt{2g}}{\tan\alpha} \tag{B.15}$$

$$Q_p = \left(\frac{\tan\alpha \ D_p}{c_d}\right)^{\frac{3}{2}} \frac{c_d\sqrt{g}}{\tan\alpha} \tag{B.16}$$

$$Q_p = \left(\frac{2\sin^2\alpha \ V}{\cos\alpha c_d}\right)^{\frac{3}{4}} \frac{c_d\sqrt{g}}{\tan\alpha} \tag{B.17}$$

Overtopping volume

$$V = \left(\frac{U_p}{\sqrt{2g}}\right)^4 \frac{\cos\alpha c_d}{2\sin^2\alpha} \tag{B.18}$$

$$V = \left(\frac{T_p}{\rho_w \tan^{\frac{1}{3}}\alpha n^2 g c_\tau}\right)^3 \frac{\cos\alpha c_d}{2\sin^2\alpha} \tag{B.19}$$

$$V = \left(\frac{\tan\alpha\ D_p}{c_d}\right)^2 \frac{\cos\alpha c_d}{2\sin^2\alpha} \tag{B.20}$$

$$V = \left(\frac{\tan\alpha\ Q_p}{c_d\sqrt{g}}\right)^{\frac{4}{3}} \frac{\cos\alpha c_d}{2\sin^2\alpha} \tag{B.21}$$

C | Breaching process of a dike

C.1 Breaching processes of dikes

C.1.1 6 phases in dike breaching

D'Eliso [11] described in his Phd. thesis the process of dike breaching in six phases. His model reproduces the whole breaching process in the following six phases:

1. Failure of the grass due to gradual erosion.
2. Local erosion of the clay cover.
3.
    - 3a. Scour erosion and headcut advance in the clay cover up to sand core exposure to flow action
    - 3b. Instantaneous sliding of the clay cover, initial breaching channel at the inner slope with bed of sand and slopes of clay.
4. Dike crest shortening due to scour erosion in sand, progressive failure of the clay cover at the crest.
5.
    - 5a. Dike crest lowering and breach widening due to scour erosion in sand and breach slopes instability, progressive failure of clay cover at the outer slope, driven by wave overtopping.
    - 5b. Dike crest lowering and breach widening due to scour erosion in sand and breach slopes instability, progressive failure of clay cover at the outer slope, driven by combined flow
6.
    - 6a. Full breach, breach widening due to scour erosion in sand and breach slopes instability driven by super-critical flow in the breach (transitional flow)
    - 6b. Breach widening due to scour erosion in sand and breach slopes instability up to equilibrium final breach driven by sub-critical flow in the breach (non-transitional flow)

The six phases as described by D'Eliso are demonstrated in figure C.1 and C.2.

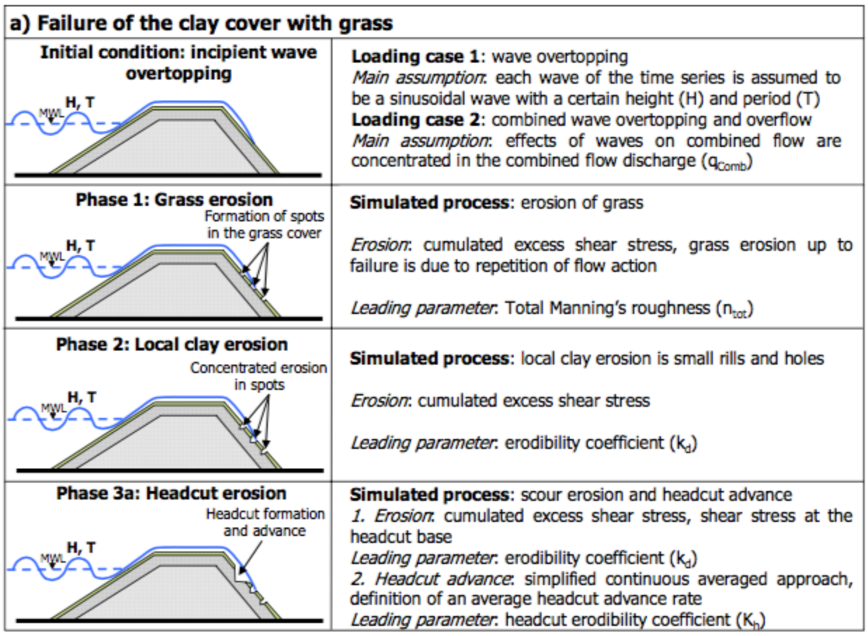

a) Failure of the clay cover with grass

Initial condition: incipient wave overtopping	**Loading case 1**: wave overtopping *Main assumption*: each wave of the time series is assumed to be a sinusoidal wave with a certain height (H) and period (T) **Loading case 2**: combined wave overtopping and overflow *Main assumption*: effects of waves on combined flow are concentrated in the combined flow discharge (q_{Comb})
Phase 1: Grass erosion Formation of spots in the grass cover	**Simulated process**: erosion of grass *Erosion*: cumulated excess shear stress, grass erosion up to failure is due to repetition of flow action *Leading parameter*: Total Manning's roughness (n_{tot})
Phase 2: Local clay erosion Concentrated erosion in spots	**Simulated process**: local clay erosion is small rills and holes *Erosion*: cumulated excess shear stress *Leading parameter*: erodibility coefficient (k_d)
Phase 3a: Headcut erosion Headcut formation and advance	**Simulated process**: scour erosion and headcut advance *1. Erosion*: cumulated excess shear stress, shear stress at the headcut base *Leading parameter*: erodibility coefficient (k_d) *2. Headcut advance*: simplified continuous averaged approach, definition of an average headcut advance rate *Leading parameter*: headcut erodibility coefficient (K_h)

FIGURE C.1: Breaching of sea dikes initiated by wave overtopping: modelling phases and simulated processes as indicated by D'Eliso [11]

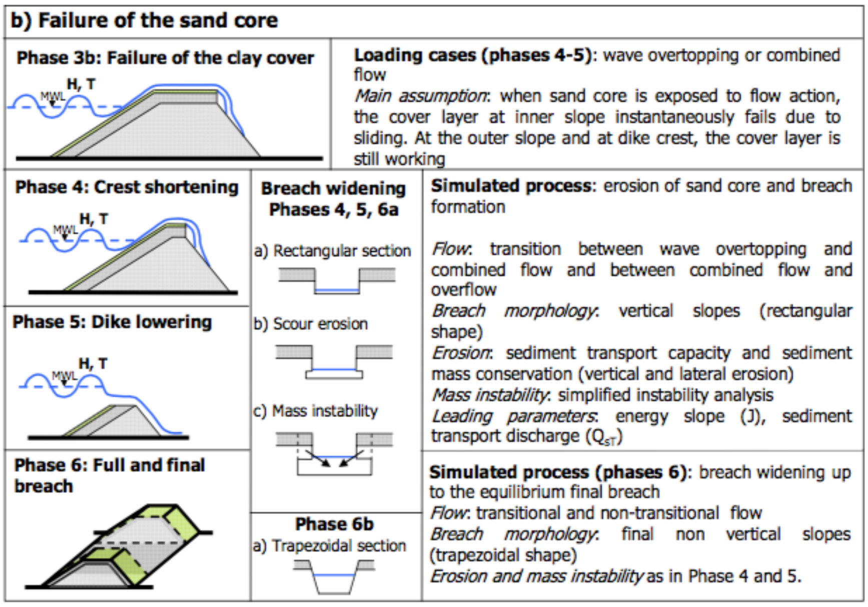

b) Failure of the sand core

Phase 3b: Failure of the clay cover		**Loading cases (phases 4-5)**: wave overtopping or combined flow *Main assumption*: when sand core is exposed to flow action, the cover layer at inner slope instantaneously fails due to sliding. At the outer slope and at dike crest, the cover layer is still working
Phase 4: Crest shortening	**Breach widening Phases 4, 5, 6a** a) Rectangular section b) Scour erosion c) Mass instability	**Simulated process**: erosion of sand core and breach formation *Flow*: transition between wave overtopping and combined flow and between combined flow and overflow *Breach morphology*: vertical slopes (rectangular shape) *Erosion*: sediment transport capacity and sediment mass conservation (vertical and lateral erosion) *Mass instability*: simplified instability analysis *Leading parameters*: energy slope (J), sediment transport discharge (Q_{ST})
Phase 5: Dike lowering		
Phase 6: Full and final breach	**Phase 6b** a) Trapezoidal section	**Simulated process (phases 6)**: breach widening up to the equilibrium final breach *Flow*: transitional and non-transitional flow *Breach morphology*: final non vertical slopes (trapezoidal shape) *Erosion and mass instability* as in Phase 4 and 5.

FIGURE C.2: Breaching of sea dikes initiated by wave overtopping: modelling phases and simulated processes as indicated by D'Eliso [11]

C.1.2 Phase 1: Initial failure of grass sod

The initial failure process of the grass cover layer on a land side slope is described in many researched. Almost every research on initial grass cover failure describes the process slightly different. Roughly three different failure mechanisms are distinguished from the literature which are, according to the writer, best described by D'Eliso [11], Hoffmans [14, 15] and Trung [31].

D'Eliso description

The instability of grass and clay cover are of two types (TAW, 2000):

- *Grass set-off cover sliding*: As a result of infiltration due to wave overtopping and overflow the weight of the soil increases and the shear stress equals the shear strength.
- *Cover up-lift and cover push-off*: As a result of infiltration due to wave overtopping and overflow and seepage, water infiltrated in the core cannot be easily expelled. The resulting water pressure at sand-clay interface tends to up-lift or push-off the cover.

According to D'Eliso [11] the grass cover layer fails due to gradual erosion, mostly as a particle detachment due to flow-induced shear stress on clay soil. This is described in phase 1 in section C.1.1. In his models D'Eliso assumed that breach initiation is detected along the land side slope assuming weak sections. Failure starts at a randomly located section at the inner slope. Field tests have shown that the erosion at the dike crest is much lower than at the inner slope and therefore assumed negligible [11]. D'Eliso recommends to use a permissible tractive force based model for the effective shear stress on the grass cover layer since this is the only approach that directly includes the effects of wave overtopping flow. In this approach the effective bottom shear stress ($\tau_{0,e}$) is described by:

$$\tau_{0,e} = \tau_0(1 - C_f)\left(\frac{n_c}{n_{tot}}\right)^2 \tag{C.1}$$

With

$$\tau_0 = \rho_w g h J \tag{C.2}$$

in which:
τ_0 = Bottom shear stress
h = Flow depth $[m]$
J = Energy slope
C_f = Grass cover factor
n_c = Manning roughness of clay
n_{tot} = Total Manning roughness

In case of wave overtopping the *energy slope (J)* is directly taken as the gradient of the total flow energy described by Bernoulli:

$$H = z + h + \frac{v^2}{2g} \tag{C.3}$$

$$\frac{dH}{dx} = -J \tag{C.4}$$

The Manning roughness includes the effects of both clay and soil particles and grass. Available formula's strictly apply to sub-critical flows. Application of these formulae to super critical small flow depths often yield unrealistic values. D'Eliso [11] recommends to use the Diáz formula's. They can tentatively be applied in case of overtopping. The reason for this recommendation lies in the fact that the Diáz formula's are derived for small flow depths, don't include grass parameters that are affected by strong uncertainties and the flow action is included in the local Froude number.

The *grass cover factor (C_f)* has experimentally been tested as a function of the type of grass by Temple et al. (1987) [11]. In his model D'Eliso [11] located the location of incipient grass failure and breach initiation based on the definition of sections along the inner slope that are mostly exposed to erosion. To do so, the grass cover factor (C_f) was normally distributed and randomly assigned at the inner slope by extractions from its probability distribution. Dike breaching then starts where the model assumes the lowest value for C_f. This approach is not really process orientated but based on the evidence that the initial breach is located at a weak section along the inner slope.

The time it takes until grass cover layer failure depends on the cumulated flow action, which is in the model used by D'Eliso the integral over time of the effective bottom shear stress. The integral is defined in such a way that it is valid for a value higher than a certain threshold, which is the plastic index of clay (I_P).

$$\int_0^{t_{gf}} \tau_{0,e} dt = 3600(9I_P + 50) \tag{C.5}$$

Two types of initial failure of the grass sod are distinguished: Direct failure and Roll up failure. Direct failure means a clump of grass and clay is washed away by the impact and flow force of a single wave. During the roll up failure process fatigue due to multiple smaller waves plays a more significant role.

Hoffmans description

An overtopping wave develops both an impact force induced compressive stress as well as a shear stress on the grass sod causing clumps of grass sod to be pulled out of the cover layer. Interesting to notice is that the stems of the grass were all more or less intact when a clump was pulled out. This indicates a failure process due to failure of clusters of roots pulled out of the clay cover and not failure of individual stems of grass. Hoffmans et al. [15] extensively researched this failure process and defined the failure of a grass-clay aggregate as:

$$F_p \geqslant F_w + \Sigma F_s + \Sigma F_c + F_g \tag{C.6}$$

In which F_p is the load of an overtopping wave, F_w the weight of the overflowing water, ΣF_s the sum of the shear forces, ΣF_c the sum of cohesion forces and F_g the grass force. A relation for the minimum required pressure for soil failure is derived from Equation C.6:

$$p \geqslant (1+2f)(\rho_s-\rho)gd+5c_s+\sigma_g \tag{C.7}$$

Here p is the pressure fluctuation caused by an overtopping wave or overflow, f a friction factor, ρ_s the density of soil, ρ the density of overtopping water, d the representative aggregate diameter, c_s an artificial cohesion factor of the soil and σ_g is the normal grass strength, given as:

$$\sigma_g = t_r\frac{A_r}{A}cos\ \theta_s \tag{C.8}$$

Here t_r is the root tensile stress, A_r/A the root area ratio (RAR) and θ_s is defined as the angle of shear deformation. The critical condition for lifting the grass-clay aggregate is reached if $p = P_{max}$ and if the mean bed shear stress τ_0 equals the critical bed shear stress τ_c. Since pressure peaks can reach up to $p_{max} = 18\tau_0$, this leads to:

$$\tau_c = \alpha_\tau((\rho_s-\rho)gd+c_s+\sigma_g) \qquad \alpha_\tau = \frac{1}{18} \tag{C.9}$$

This equation however only work for a steady (turbulent) flow and does not take the effect of wave impact into account. Later on in this rapport this effect is added to the steady flow load leading to a new expression for the maximum allowable overtopping waves.

Trung description

Le Hai Trung [31] described in a paper about the failure processes of grass covered slopes due to overtopping the process of 'roll up' damage. Trung describes the findings of similar overtopping experiments as Wijmeers-II, only this time in Friesland in The Netherlands. This roll up process, in which the grass cover basically rolls up like a carpet, is a failure process that has been documented multiple times during the Wijmeers-II experiments. The process of roll up is visualized in Figure C.3. Pieces of the grass sod were turned up side down at the edges of these two failed areas. The top layer of about 10 to 15 cm, where most roots concentrated, was cut underneath and lifted up. The sod was swept away to expose the soil body underneath. Trung replaced the grass strength factor σ_g by the summation of the individual strength of the roots as measured in a certain area. Leading to the cohesion factor:

$$c = c_s + a_2\Sigma\tau_r \tag{C.10}$$

With the factor a_2 depending very much on the root properties and τ_r, the roots induced tensile strength at a certain depth d, defined as:

$$\Sigma\tau_r = n_r \cdot F_p \cdot \frac{1}{a_s} \qquad a_s = \pi r_s^2 \tag{C.11}$$

Where n_r is the number of roots at depth d and r_s the sample area radius where roots are counted. This equation however is only valid under the assumption that all roots resist the same breaking force and work simultaneously.

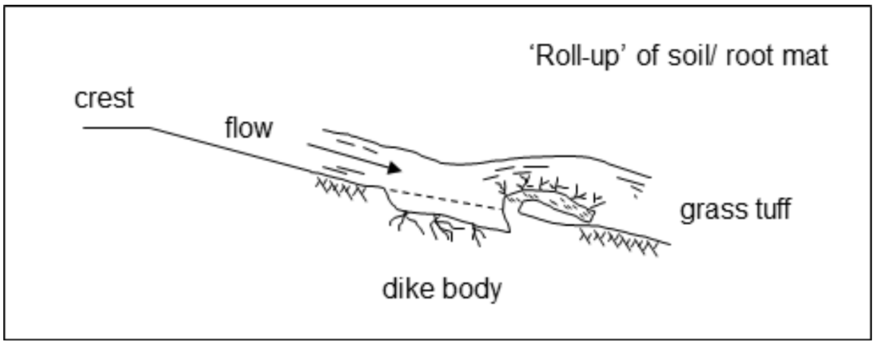

FIGURE C.3: Roll up failure process of grass cover as visualized by Trung [31].

C.1.3 Phase 2: Clay cover failure

Once a grass-clay aggregate is removed by the overtopping waves the supporting clay cover is exposed. Important in the failure process of the exposed clay cover is the fact that reinforcement of the roots is no longer present. Since the cohesion factor of roots can be up to a factor 6 larger than the cohesion factor for clay this means the erosion process will be much faster. For example, experiments done by Stanczak [29] showed $c_{roots} = 41$ kPa and $c_{clay} = 7$ kPa making the total mean shear strength of that specific grass cover $\tau_{total} = 48$ kPa. For a clay cover without roots this strength reduces to $c_{clay} = 7$ kPa.

Erosion of the clay layer occurs as soon as the grass layer has failed. Clay cover erosion can roughly be divided into two phases [11]

- a. *Local clay erosion*, phase 2 of figure C.1 and C.2. Key parameters of the selected model to calculate the vertical erosion depth (dz) are the erodibility coefficient (k_d) and the critical shear stress ($\tau_{0,cr}$).
- b1. *Headcut erosion*, phase 3a of figure C.1 and C.2. Calculation of the vertical depth (dz) and the headcut advance (dZ). Important parameters are the initial headcut height ($H_{H,0}$) and the erodibility coefficient (K_h).
- b2. *Clay cover failure*, phase 3b of figure C.1 and C.2, initial breach channel height ($H_{b,0}$) and width ($B_{b,0}$)

Local clay erosion

In his model, D'Eliso defined the vertical erosion depth proportional to the excess effective bottom shear stress ($\tau_{0,e} - \tau_{0,cr}$) using Duboy's sediment transport equation, modified for rill erosion.

$$\frac{dz}{dt} = k_d(\tau_{0,e} - \tau_{0,cr})^a \tag{C.12}$$

The parameter a is an erosion rate parameter that should be estimated from laboratory tests. In the past the value for a differed between 1 and 1.15 but it is normally assumed to be 1.

The effective bottom shear stress is in this case a function of the flow depth (h) and the erosion depth at the previous time step ($dz_{(t-dt)}$)

$$\tau_{0,e} = \rho_w g(h + dz_{(t-dt)})J \tag{C.13}$$

The erodibility parameter (k_d) and critical shear stress ($\tau_{0,cr}$) are defined by D'Eliso [11] to be, respectively:

$$k_d = 10^{-6}\frac{10\rho_w}{\rho_{c,d}} exp\left(-0.121 c_{\%}^{0.406}\left(\frac{\rho_{c,d}}{\rho_w}\right)^{3.10}\right) \tag{C.14}$$

and

$$\tau_{0,cr} = 5.43 * 10^{-6}\left(\rho_{c,d} * \frac{\rho_{cw} - \rho_w}{\rho_{c,d} - \rho_w}\right)^{2.28} \tag{C.15}$$

in which:
ρ_w = Density water
$\rho_{c,d}$ = Density of the dry clay soil
ρ_{cw} = Density of the water-clay mixture $\approx 1100[kg/m^3]$
$c_{\%}$ = Weight percentage of the clay in the cohesive soil

The weight percentage of the clay in the cohesive soil $c_{\%}$ can be determined by using figure C.4.

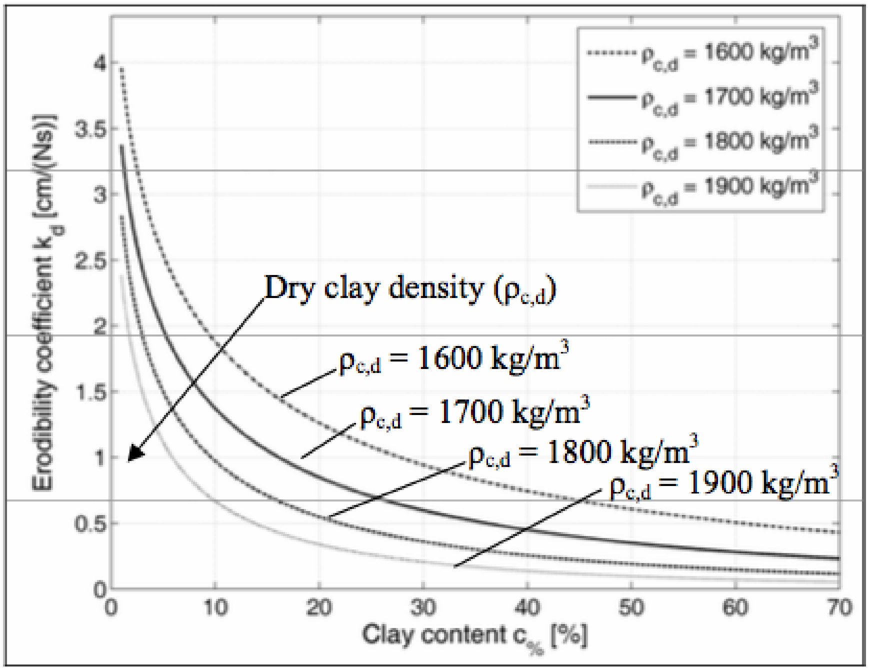

FIGURE C.4: Erodibility coefficient as a function of clay soil properties, indicated by D'Eliso [11]

Headcut erosion and clay cover

Headcut initiation takes place when a vertical headcut starts migrating seaward. The time of headcut initiation (t_H) is conventionally defined as the time corresponding to a vertical erosion depth (dz) in the clay cover greater than a threshold value, which is the initial headcut height ($H_{H,0}$) in the headcut erosion model. There are two possibilities in the model to specify the initial headcut height ($H_{H,0}$)

- As an input parameter, depending on the flow discharge (q), inner slope ($1 : n$) and material properties.
- Equal to the critical flow depth ($h_c r$)

The second approach is preferred but is not always applicable due to the presence of waves. A representative value of the flow discharge is not defined. The flow over a dike caused by a wave was defined by D'Eliso [11] as:

$$q_m = \frac{a}{N_w} \sum_{i=s}^{N_w} q_i \tag{C.16}$$

On page 45-48 of the Phd Thesis of D'Eliso the modelling of headcut calculation is explained.

C.1.4 Phase 3: Scour development in sand core

Once the sand core is reached the erosion process becomes clearly visible by the naked eye. As the overflowing water changes color from white-light brownish into darker brown due to the transported sand. After reaching the sand core a scour hole starts to develop. Hoffmans [14] derived a scour relation according to the momentum equation. The relation describes the scour depth in the equilibrium phase. The forces acting on this element of the fluid are demonstrated in Figure C.5.

in which: M_1 = Momentum flux in the jet in section 1
M_2 = Momentum flux of the jet in section 2
F_1, F_2 = Hydrostatic forces
G = Weight of water
P = Resultant or dynamic force exerted by the jet on the bed

Using the basic parameters: mean velocity in the jet U_1, and at the outlet U_2, angle between R and the horizontal δ, air-water ratio ε, angle of impingement χ, application of Newtons law (per unit width) gives:

Horizontal direction:

$$F_1 - F_2 - R\ cos\ \delta - \rho q U_2 + (1+\varepsilon)\rho q U_1\ cos\ \chi = 0 \tag{C.17}$$

Vertical direction:

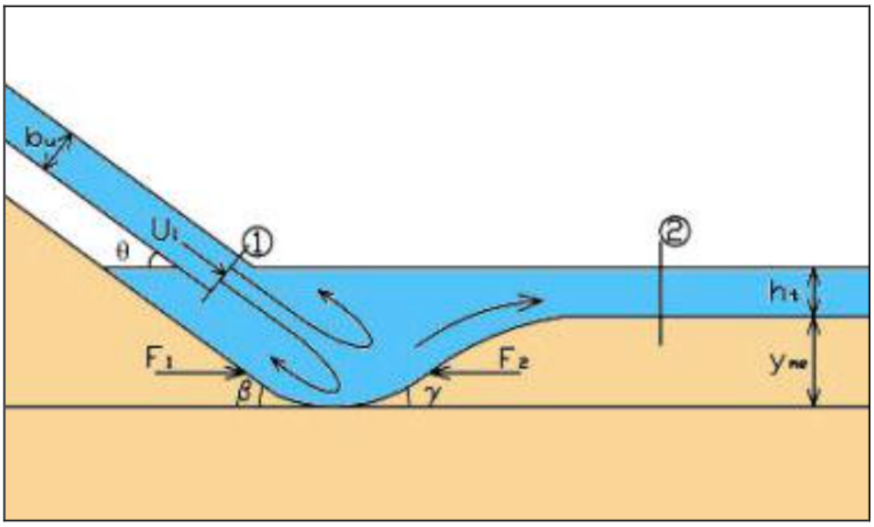

FIGURE C.5: Schematization of forces acting on the soil leading to jet induced scour development. Picture from Msc. Thesis of A. Valk [32]

$$-G + R\ sin\ \delta - (1+\varepsilon)\rho q U_1\ sin\ \chi = 0 \tag{C.18}$$

Which eventually leads to a formula for the scour depth;

$$\gamma_{m,e} + h_t = \frac{load}{strength} = \frac{\sqrt{\frac{qU_1\ sin\ \chi}{g}}}{\frac{1}{c_{2v}}} \tag{C.19}$$

In which:

$$c_{2v} = \sqrt{\frac{\alpha a_b^2}{\Psi_c \Delta D_{90*}^{2/3}} - (1-\varepsilon)\ tan\ \phi} \approx \frac{20}{D_{90*}^{1/3}} \tag{C.20}$$

And

$$D_{90*} = d_{90}\left(\frac{\Delta g^{1/3}}{\upsilon}\right) \tag{C.21}$$

Here Ψ_c is the critical Shields parameter, Δ the relative density, υ the kinematic viscosity and d_{90} is the particle diameter for which 90% of the sediment grains is finer than d_{90}

Equation C.17 and C.18 describe the scour development of a jet impact in a horizontal surface. Of course the surface at the land side slope of a dike is not horizontal. Therefore, if Equation C.17 and C.18 are used to describe scour development on a slope some modifications of the relations are required.

C.1.5 Phase 4: Headcut erosion

An interesting aspect as observed during the Wijmeers-II experiments is the development of a vertical wall at the river side of the scour hole. This vertical wall develops due to turbulent flows in the scour hole. This effect is demonstrated in Figure C.6. Through a test set up Canepa researched the impact of a jet running from a spillway which led to a relation to describe the scour depth due to this effect. The impact of this jet looks very much like the impact of an overtopping wave. Figure C.6 can be pictured under an angle, which explains the vertical wall leading to headcut erosion.

The exact depth where headcut erosion starts is unknown, therefore in different model approaches the assumption is made that this critical depth is equal to the initial thickness of the clay layer (0.3 - 0.5 m). After the scour hole reaches this depth the sand core material erodes. If the core starts to erode, the clay layer on the slope is undermined and the soil becomes instable leading to headcut erosion.

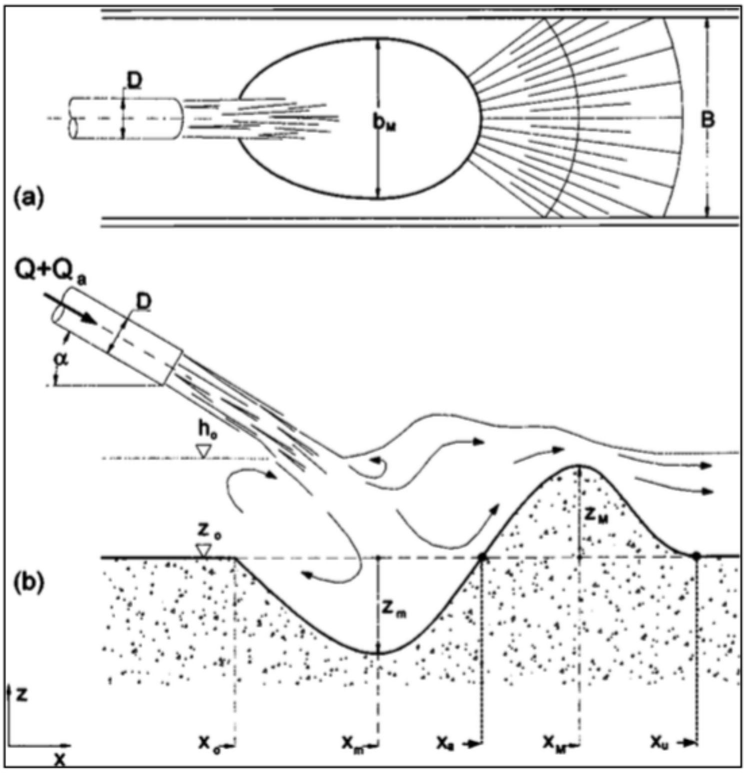

FIGURE C.6: Scour development as described by Canepa and Hager [9]

In the rest of the report the focus will be on the first two phases of cover failure. In order to predict how long a dike can withstand certain overtopping wave attack and/or overflow more knowledge about the actual failure process of these cover layers is required. Since the erosion process rapidly increases once the sand core is reached the moment the clay cover fails is crucial for the failure moment of the dike.

C.1.6 Phase 5 and 6: Development into full breach

As soon as head cut erosion on the land side slope occurs the breaching process is increased rapidly. The lowering of the crest eventually causes the dike to be fully breached. This process however is not part of this thesis, therefore phase 5 and 6 are no longer considered.

D | Residual strength land-side slope

In order to determine whether the amount of erosion on the land-side slope has reached an erosion level in which the land-side slope is classified as *failed* a critical damage parameter D_c is introduced. This parameter determines after how much damage on the land-side slope the cover layer is no longer safe. This parameter has units kNs/m^2, which is the same unit as the outcome of the Wave impact approach model. This threshold parameter is a measure for the time a land-side slope can withstand wave overtopping during a storm. Subsequently D_c indicates the residual strength of a grass cover layer.

$$D_{\text{tot}} = \left(\sum_{n=1}^{N} (P_n - P_c) \cdot \Delta t_n \right) - D_c \tag{D.1}$$

If $D_{\text{tot}} > 0$, the land-side slope cover is classified as *failed*. The influence of the residual strength threshold factor D_c is demonstrated in Figure D.1. A notional threshold value of D_c is picked to demonstrate the effect of the threshold. The figure demonstrates that both a high P_c and high D_c value lead to a damaged, but not failed grass cover while a rather low P_c value and high D_c value will eventually lead to a failed grass cover.

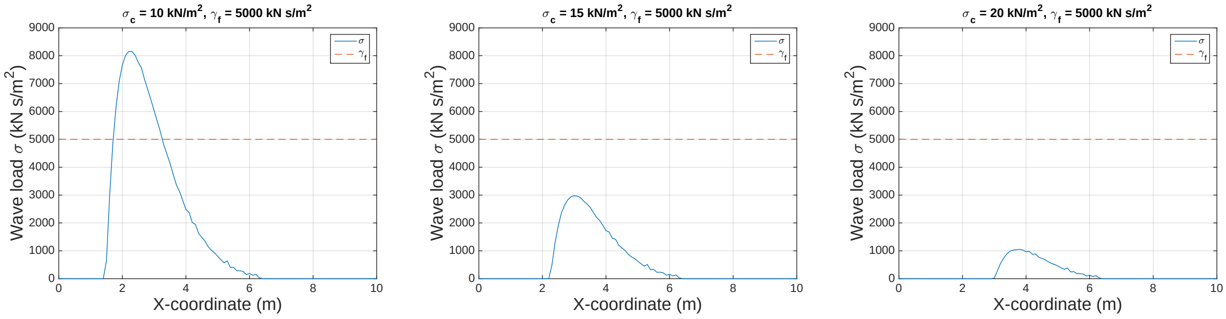

(A) $P_c = 10\ kN/m^2$
$D_c = 5 \cdot 10^3\ kNs/m^2$

(B) $P_c = 15\ kN/m^2$
$D_c = 5 \cdot 10^3\ kNs/m^2$

(C) $P_c = 20\ kN/m^2$
$D_c = 5 \cdot 10^3\ kNs/m^2$

FIGURE D.1: Residual strength threshold factor D_c visualized for three different critical pressure values P_c. Figure D.1a indicates failure of the grass cover, Figures D.1b and D.1c indicate a damaged but not failed grass cover. $D_c = 5000$ is purely notional to demonstrate the effect of the threshold.

E | Analytical approach for Wave impact model

In previous equations an overtopping wave is assumed to have an infinitesimal water depth at the crest. In order to determine the maximum impact point of a wave with a certain water depth d_{crest} this assumption is legit. In Figure **??** is shown that the impact force on the land side slope is linearly related to the distance X on the slope. A plot of an overtopping wave with an infinitesimal wave thickness looks similar to Figure **??** where only its size differs for each individual wave since the maximum impact point differs, the slope of the line is exactly the same. The line is formed from the maximum impact point X_{max} to zero as the wave retreats over the slope. Of course an overtopping wave does not have an infinitesimal thickness in reality, therefore this element needs to be added to Equation 7.32. Since including the water depth into the analytical equation is rather complex, a visualization of the process of an overtopping wave is presented in Figures E.1 and E.2. Figure E.1 shows the load of an overtopping event at numerous moments in time, plotted against the X-coordinate of the land-side slope. Starting at the first moment of impact ($t = 0$) the load on the dike is plotted for every time step ($\Delta t = 0.05$ s.) until the wave has retreated towards the crest, at which both σ and X are zero. Figure E.2 shows the course of impact area in time, where the time step goes towards zero, the load is indicated with a colorbar. To clarify both figures, a 3d plot is made of Figure E.1 and E.2 combined in which time is plotted over de z-axis, which is shown in Figure E.3.

Figure E.1 shows that at a certain point in time during the overtopping, the load of the overtopping wave acts on the land side slope from the minimum to the maximum impact point (X_{min} to X_{max}). These impact points are both related to the water depth at the crest, see Equation 7.7.

$$X_{min} = X(d = 0) \qquad\qquad X_{max} = X(d = d_{surface}) \tag{E.1}$$

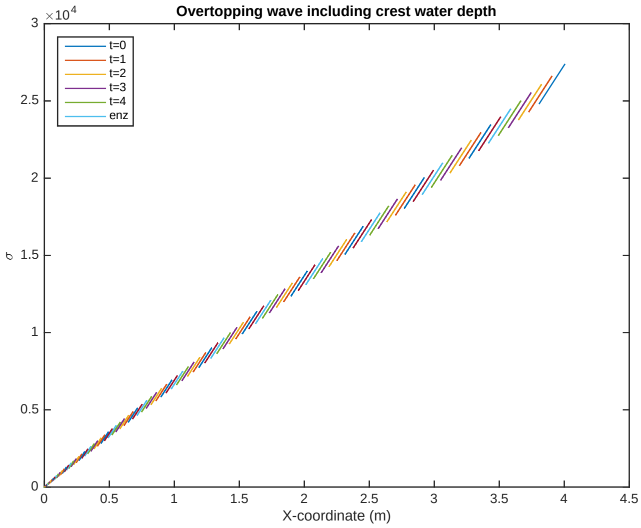

FIGURE E.1: Example of the impact load of a single overtopping wave plotted against the x-coordinate of the land side slope. The load is plotted for a number of moments in time, the time step in this plot $\Delta t = 0.05$ s.

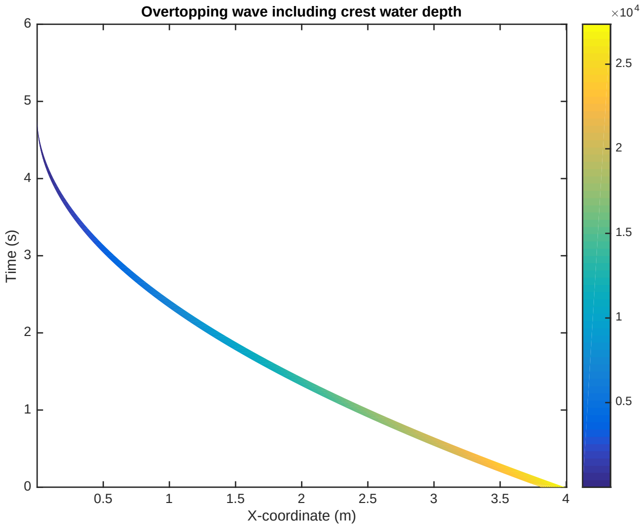

FIGURE E.2: Example of the impact points of an overtopping wave plotted against time. The colorbar indicates the load on the land side slope.

Now the overtopping process is clarified the process is to be described analytically. To achieve this, the integral of Equation 7.27 is taken with variable X, dependent on water depth d. The water depth d varies from $d = 0$ to $d = d_{crest}$. First a single overtopping wave is considered.

The impact load σ of an infinitesimal thick wave:

$$\sigma = \rho(u_{crest}^2(t) + 2gX(d)\ tan\ \theta) - \sigma_c \tag{E.2}$$

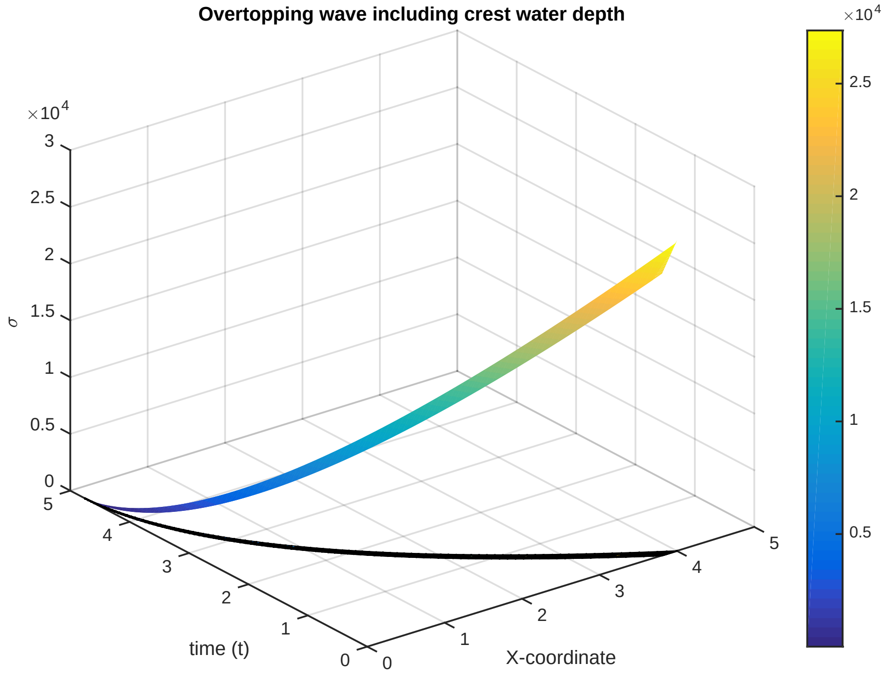

FIGURE E.3: Example of the impact load of a single overtopping wave plotted against the x-coordinate of the land side slope and time.

In order to include the water depth at the crest the integral of Equation E.2 from $d = 0$ to $d = d_{crest}$ is taken. This leads to the impact force F:

$$F = \int_0^{d_{crest}} \left(\rho(u_{crest}^2(t) + 2gX(d)\ tan\ \theta) - \sigma_c\right)\ \mathrm{d}d \tag{E.3}$$

For the purpose of readability of the derivation, $u_{crest}(t)$ is written as u.

$$F = \int_0^{d_{crest}} \left(\rho u^2 + \rho 2g\ tan\theta\ X(d) - \sigma_c\right)\ \mathrm{d}d \tag{E.4}$$

$$F = [prim(\sigma(d))]_0^{d_{crest}} = prim(\sigma(d_{crest})) - prim(\sigma(0)) \tag{E.5}$$

Where $prim(\sigma(d))$ is the primitive of $\sigma(d)$. The primitive of Equation E.4 therefore becomes:

$$prim(\sigma(d)) = \rho u^2 d + 2\rho\ tan^2\theta u^2 d + \frac{2\rho\ tan\theta\ u^2}{3g}\left(tan^2\theta + \frac{2gd}{u^2}\right)^{1\frac{1}{2}} \frac{u^2}{2g} - \sigma_c d$$

Which can be rewritten into:

$$prim(\sigma(d)) = \rho u^2 d(1 + 2tan^2\theta) + \frac{\rho\ tan\theta\ u^4}{3g}\left(tan^2\theta + \frac{2gd}{u^2}\right)^{1\frac{1}{2}} - \sigma_c d + c$$

Here c is a constant required to determine the primitive of Equation E.4. This leads to the determination of F from the integral:

$$F = \left[\rho u^2 d(1 + 2tan^2\theta) + \frac{\rho\ tan\theta\ u^4}{3g}\left(tan^2\theta + \frac{2gd}{u^2}\right)^{1\frac{1}{2}} - \sigma_c d + c\right]_0^{d_{crest}} \tag{E.6}$$

With the parameters $d = 0$ and $d = d_{crest}$ implemented in Equation E.5 this leads to:

$$F = \rho u^2 d(1 + 2tan^2\theta) + \frac{\rho\ tan\theta\ u^4}{3g}\left(tan^2\theta + \frac{2gd}{u^2}\right)^{1\frac{1}{2}} - \sigma_c d + c - \frac{\rho\ tan\theta\ u_n^4}{3g}tan^3\theta - c \tag{E.7}$$

Which eventually leads to the equation:

$$F = \rho u^2 d(1 + 2tan^2\theta) + \frac{\rho\ tan\theta\ u^4}{3g}\left(tan^2\theta + \frac{2gd}{u^2}\right)^{1\frac{1}{2}} - \sigma_c d - \frac{\rho\ tan\theta\ u_n^4}{3g}tan^3\theta \tag{E.8}$$

Or:

$$F = \rho u^2 d(1 + 2tan^2\theta) + \frac{\rho\ tan\theta\ u^4}{3g}\left(\left(tan^2\theta + \frac{2gd}{u^2}\right)^{1\frac{1}{2}} - tan^3\theta\right) - \sigma_c d \tag{E.9}$$

d can be written in terms of X as follows:

$$d = \frac{gX^2}{2u^2} - \frac{1}{2}Xtan\ \theta + \frac{u^2}{g}tan^2\theta \tag{E.10}$$

From Equation 2.47 we learned that water depth in time $d(t)$ decreases according to:

$$d(t) = d_p(1 - \frac{t}{T_o})^b \tag{E.11}$$

Where the water depth $d(t)$ at zero point of time is the peak depth d_p. This leads to a relation that expresses d in terms of horizontal coordinate X and time t:

$$d(X,t) = \left(\frac{gX^2}{2u^2} - \frac{1}{2}Xtan\ \theta + \frac{u^2}{g}tan^2\theta\right)(1 - \frac{t}{T_o})^b \tag{E.12}$$

Earlier on a linear decrease of the water depth in time was assumed, which makes the power $b = 1$. However, this is only an assumption. Therefore, for completeness of the expression the term b is left in the equation. When Equation E.12 is implemented in Equation E.9 this leads to:

$$\begin{aligned} F = {} & \rho u^2 \left(\frac{gX^2}{2u^2} - \frac{1}{2}Xtan\ \theta + \frac{u^2}{g}tan^2\theta\right)(1 - \frac{t}{T_o})^b(1 + 2tan^2\theta) \\ & + \frac{\rho\ tan\theta\ u^4}{3g}\left(\left(tan^2\theta + \frac{2g\left(\frac{gX^2}{2u^2} - \frac{1}{2}Xtan\ \theta + \frac{u^2}{g}tan^2\theta\right)(1 - \frac{t}{T_o})^b}{u^2}\right)^{1\frac{1}{2}} - tan^3\theta\right) \\ & - \sigma_c\left(\frac{gX^2}{2u^2} - \frac{1}{2}Xtan\ \theta + \frac{u^2}{g}tan^2\theta\right)(1 - \frac{t}{T_o})^b \end{aligned} \tag{E.13}$$

Which is rewritten into:

$$\begin{aligned} F = {} & \left(\frac{1}{2}\rho gX^2 - \frac{1}{2}\rho u^2 Xtan\theta + \frac{\rho u^4}{g}tan^2\theta\right)\left(1 - \frac{t}{T_o}\right)^b(1 + 2tan^2\theta) \\ & + \frac{\rho u^4 tan\theta}{3g}\left(\left(tan^2\theta + \left(\frac{g^2X^2}{u^4} - \frac{X}{u^2}Xtan\theta + 2tan^2\theta\right)\left(1 - \frac{t}{T_o}\right)^b\right)^{1\frac{1}{2}} - tan^3\theta\right) \\ & - \sigma_c\left(\frac{gX^2}{2u^2} - \frac{1}{2}Xtan\ \theta + \frac{u^2}{g}tan^2\theta\right)\left(1 - \frac{t}{T_o}\right)^b \end{aligned} \tag{E.14}$$

Unfortunately this relation only becomes longer when the expression for u over time is implemented in the equation. u decreases over time like d does ($u(t) = u_p(1 - \frac{t}{T_o})^a$) with a also assumed to be 1, see also Equation 2.46. This leads to:

$$\begin{aligned} F = {} & \left(\frac{1}{2}\rho gX^2 - \frac{1}{2}\rho\left(u_p(1 - \frac{t}{T_o})^a\right)^2 Xtan\theta + \frac{\rho\left(u_p(1 - \frac{t}{T_o})^a\right)^4}{g}tan^2\theta\right)\left(1 - \frac{t}{T_o}\right)^b(1 + 2tan^2\theta) \\ & + \frac{\rho\left(u_p(1 - \frac{t}{T_o})^a\right)^4 tan\theta}{3g}\left(\left(tan^2\theta + \left(\frac{g^2X^2}{\left(u_p(1 - \frac{t}{T_o})^a\right)^4} - \frac{X}{\left(u_p(1 - \frac{t}{T_o})^a\right)^2}Xtan\theta + 2tan^2\theta\right)\left(1 - \frac{t}{T_o}\right)^b\right)^{1\frac{1}{2}}\right) \\ & - \frac{\rho\left(u_p(1 - \frac{t}{T_o})^a\right)^4 tan\theta}{3g}tan^3\theta \\ & - \sigma_c\left(\frac{gX^2}{2\left(u_p(1 - \frac{t}{T_o})^a\right)^2} - \frac{1}{2}Xtan\ \theta + \frac{\left(u_p(1 - \frac{t}{T_o})^a\right)^2}{g}tan^2\theta\right)\left(1 - \frac{t}{T_o}\right)^b \end{aligned} \tag{E.15}$$

In order to get a decent analytical solution for the load of an overtopping wave on the land side slope of a dike Equation E.15 needs to be integrated to t. This integral is hard to solve by hand, therefore math computer programme Maple was used to solve this integral. Maple however kept giving an error although all the input parameters were correct. To find the reason for this constant error the previous equations have been checked for correctness. This led to the conclusion that the assumption of a uniform flow velocity at the dike crest was the cause of the unsolvable integral. The reason for this statement is explained in the next subsection.

Uniform crest flow velocity assumption

Considering an overtopping wave with a uniform flow velocity in stead of a logarithmic distributed flow velocity leads to an overtopping image as demonstrated in Figure E.4. The figure illustrates the moment the bottom of an overtopping wave makes contact with the land side slope. This very moment in time, named t_{bottom}, differs from the moment the surface of the overtopping wave makes contact with the land side slope, named $t_{surface}$. This suddenly divides parameter t in Equation E.15 into multiple t-like parameters (for instance t_{bottom} and $t_{surface}$), making it not possible to integrate to t. Including all these parameters in an analytical solution requires every t-like parameter to be written in terms of t and substituted in Equation E.15, subsequently integrating this equation to t. This probably leads to an equation of at least one page, presumably more, which is not particularly an elegant solution for the problem. An equation of such length is also close to unusable since it is hard to keep the overview when using it. Besides that would it still be under the assumption of a uniform flow velocity on the crest, which is strictly speaking not correct. Therefore an analytical solution for the impact of overtopping waves on the land side slope is not further presented in this thesis. The writer presumes that an analytical solution should be possible but also admits that this will probably leads to a hard to use equation.

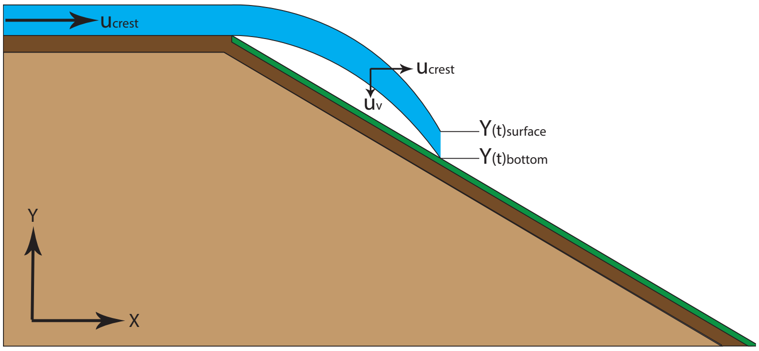

Figure E.4: An overtopping wave with uniform crest flow velocity considered at the moment of impact of the bottom of the overtopping wave.

F | Verification of Wave impact approach

The wave impact approach model is verified using the results of different wave overtopping experiments executed by Infram B.V. The reports are al written in Dutch, therefore a brief summary of the relevant results of each experiment is given below. A comment on the contribution of each experiment to the validation of the wave impact approach is given as well.

For the determination of the wave impact load on the land side slope during overtopping experiments other than the Wijmeers-II experiments the actual files as used for input in the wave overtopping simulator were not present. Therefore these steering files are reproduced using a Weibull distribution randomiser function and the EurOtop manual [23] in which a clear explanation is given on how to calculate overtopping volumes and their probability of exceedance. In the factual reports of the experiments the maximum overtopping volume, number of overtopping waves, and average wave overtopping discharge of a simulated storm is given. These values were used to create a number of samples, depending on how many waves were simulated during a single overtopping experiment, with the Weibull distribution randomiser. This probably does not recreate the exact same input file as used during the actual experiment but it will approach it closely.

F.1 Wijmeers-II experiments

During the Wijmeers-II experiments lots of damage was observed on the land side slope. During the first overtopping experiment initial damage occurred about 2 m below the crest line by the end of the 10 l/m/s overtopping test. This test ran for 2 hours with an average overtopping discharge of 10 l/m/s. A mouse or rabbit hole appeared to be the main source of damage since the toss and rooting of the animals had weakened the grass and clay cover. One can doubt whether the first overtopping experiment is representative for general situations but the fact is that this experiment was performed on a real dike. Weak spots caused by animal holes can occur at any dike section. The second overtopping experiment was more representative for a fully intact grass cover. Although initial damage had occurred during the hydraulic measurements this did not affect the experiment since this damage spot occurred near the toe. The land side slope was hardly damaged, making the rest of the overtopping experiment still representative.

First Wijmeers-II overtopping experiment

During the first Wijmeers-II overtopping experiment, the first damage on the land side slope occurred around the 2 m line [2]. Since the slope at the land side was 1:1.7, or the angle of the slope was 0.53 rad, this corresponds with a horizontal distance of 1.7 m. So at horizontal coordinate $X = 1.7$ m the first damage was noticed. While the damage spot on top of the land side slope developed into a bigger damage spot (up to 2.5 m wide and 1 m deep) a second initial damage spot was noticed in grid section 7 (see Figure 5.2), which is between the 3 m and 4 m line below the crest line, during the second hour of the experiment. This corresponds with horizontal coordinate $X = 2.6$ to 3.5 m.

Second Wijmeers-II overtopping experiment

For the second Wijmeers-II overtopping experiment the required threshold value is determined using the same method as for the first experiment. During the hydraulic measurements direct damage occurred due to a 3000 l/m wave. Therefore, at the start of the actual overtopping experiment the land side slope was already damaged near the toe. As mentioned this did not affect the overtopping experiment too much. This is the case because observed erosion spots only developed in downwards direction along the land side slope. Since this initial damage spot occurred near the toe, and did not develop in upward direction, the grass sod on the slope was not damaged. During the second Wijmeers-II overtopping experiments damage was observed in the same grid section as during the first overtopping experiments, where the damage occurred in grid section 7. In grid section 5, 1 to 2 m below the crest line, a big crack of about 0.2 m wide was present. Due to this weakened part on the land side slope, damage occurred at that section as well during the overtopping experiment. Therefore a threshold value is sought for a peak between $X = 0.6$ to 1.2 m (grid section 4) and for a peak between $X = 2.6$ to 3.5 m (grid section 7).

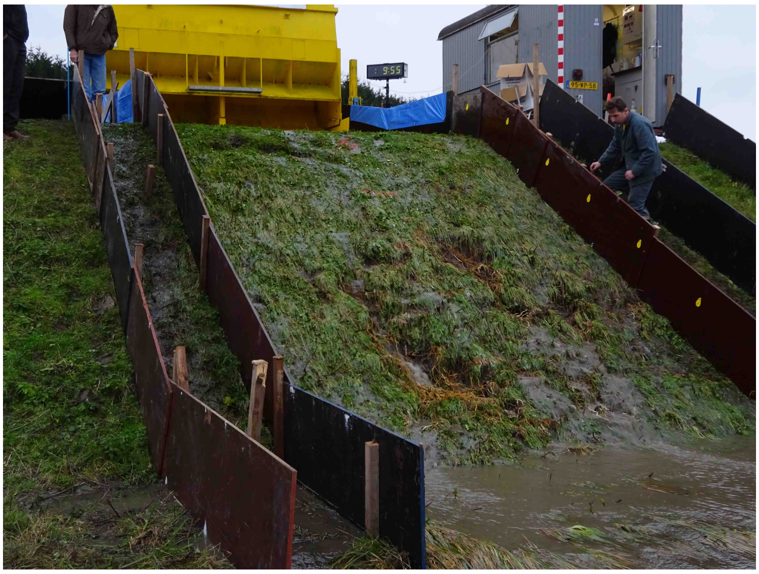

FIGURE F.1: Initial damage during the second overtopping experiments occurred in grid section 7.

F.2 Afsluitdijk experiments

In February 2009 numerous wave overtopping experiments were executed at the Dutch Afsluitdijk by Infram B.V. [5] using the same overtopping simulator as used during the Wijmeers-II experiments. The Afsluitdijk is a major closure dam that separates lake IJssel and the Waddensea in the North of the Netherlands. This dam is essential in the Dutch water defence system and should therefore be resistant against storms with very high significant wave height. In order to test the actual strength of the Afsluitdijk, Infram B.V. tested the erodibility of the land side slope. At the Afsluitdijk the 'land' side slope should actually name 'lake' side slope since the dam does not separate water from land. However, for constancy of this thesis the side that has been tested for wave overtopping resistance is still called 'land side slope'. In total three different test sections were tested with the overtopping simulator. At a fourth test section a shear stress experiment was executed.

The result of the Afsluitdijk overtopping experiments were in a way quite similar to the result of the Wijmeers-II experiments. Although initial damage occurred much later during the Afsluitdijk experiment, a similar damage pattern was noticed on the land side slope. A big difference between the Afsluitdijk overtopping experiments and the Wijmeers-II overtopping experiments is the damage on the toe of the dike. This first damage spots at the Afsluitdijk were noticed around the toe is the dike while during the Wijmeers-II experiments no damage at the toe was noticed at all. Due to safety regulations the experiments at the Afsluitdijk had to be stopped as soon as significant damage to the grass cover occurred, letting the experiments run until the sand core was reached was in this case too risky. The final damage pattern after each test was still to be classified as 'failed grass cover' [5]. The final result of test section 1 and 2 of the Afsluitdijk overtopping experiments is shown in Figure **??**.

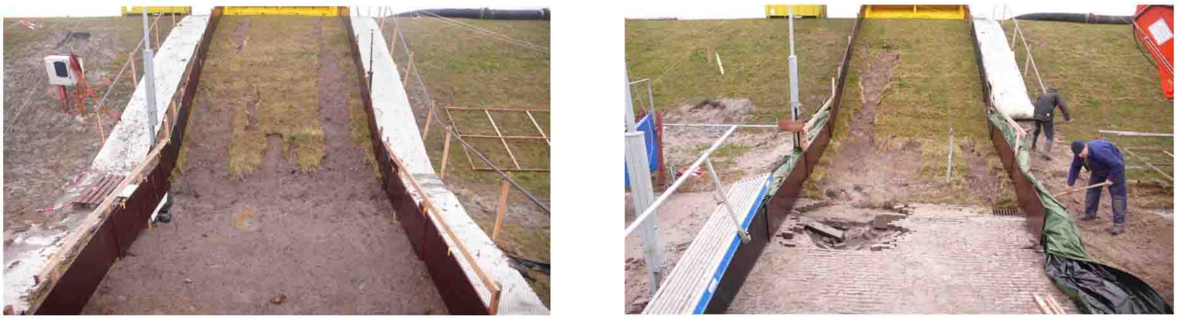

(A) Test section 1

(B) Test section 2

FIGURE F.2: Final result of the wave overtopping experiments at the Afsluitdijk, February 2009. Photo's taken by Infram B.V. [5]

A third section was tested on wave overtopping as well, this section however contained a 1 m wide stone steps in the center of the section. Therefore test done on this section are performed under such different conditions compared to the Wijmeers-II experiments that they cannot be compared to each other.

First Afsluitdijk overtopping experiment

The land side slope of the entire Afsluitdijk was classified *good* according to the VTV2006 standards [21]. During the overtopping tests on the first test section, the first initial damage spots on the land side slope of the Afsluitdijk were noticed in grid section 5, which in the case of the Afsluitdijk meant between the 4 and 5 m line below the crest [5]. The slope on the land side of the Afsluitdijk was 1:2.6, or a slope angle $\theta = 0.37$ rad. This means the initial damage patterns occurred between respectively horizontal coordinates $X = 3.8$ and 4.7 m.

Second Afsluitdijk overtopping experiment

Probably due to a tractor that sank into the soil, a rather deep pit of about 0.13 m had formed on the land side slope of test section 2. This pit had formed around the 3 m line below the crest line which corresponds with horizontal coordinate $X = 2.8$ m. Damage occurred already during the 1 l/m/s test at the spot where the pit had formed. Because the stability of the brick road a few metres below the toe of the land side slope became in jeopardy during the 30 l/m/s test the experiment was stopped. Therefore the total load on the first test section has been much larger than the load on the second test section. This is not really a problem because this only requires different input for the wave impact model. The two experiments are therefore however harder to compare to each other.

F.3 Friese Waddenzeedijk experiments

In Fabruary 2008, close to the village of St Jacobiparochie in the province of Friesland in the North of the Netherlands, wave overtopping experiments have been executed on four different test sections. Each test section had had a different maintenance policy for the past 15 years which provided the unique opportunity to test influence of different kinds of maintenance policies on the grass cover of a dike. Again the wave overtopping simulator, designed by Van der Meer consultancy and Van der Meer Innovation, as used during the Wijmeers-II experiments was used to simulate wave overtopping on the dike [3]. The erodibility was tested by simulating a 6 hour storm that generated averaged wave overtopping volumes of respectively 0.1, 1, 10, 30, 50 and 75 l/m/s. For each of these average overtopping volumes a Weibull distribution provided the input values for the wave overtopping simulator.

The first two overtopping experiments did not lead to any damage on the land side slope. The land side toe however was damaged quite heavily after the experiments. Since no damage on the land side slope of the dike occurred during the first two overtopping experiments these will not be considered in the comparison with the Wijmeers-II experiments. There is no comparable data obtained from these tests. The third and fourth Friese Waddenzeedijk experiments did provide usable data which is considered in the next sections.

Third Friese Waddenzeedijk overtopping experiment

The grass cover of the land side slope during the third overtopping experiment was classified *good* according to the VTV2006 standards. During the overtopping tests damage occurred in the 21 m grid section. With a land side slope of 1:2.9, or a slope angle $\theta = 0.33$ rad, this means the damage was noticed between horizontal coordinates $X = 19.9$ and 20.8 m. Using Equation 7.7 this would mean a crest flow velocity of at least 16.9 m/s is required for overtopping waves to even reach this point on the land side slope. If the grass cover would have failed due to wave impact, many waves would have to exceed this flow velocity, which is an absurd assumption. In similar experiments, using the same simulator, the crest velocities at maximum capacity of the simulator were not even half this velocity [6] [5] [4] [2]. Unfortunately crest flow velocities were not measured at the Friese Waddenzeedijk. However, based on observation from similar experiments, it is stated that failure on the grass cover was in this case not caused by the impact of overtopping waves but by a different process.

The failure mechanism however as described in the report [3] was very similar to the failure mechanism as visualized in Figures 7.3a to 7.3f. The failure process is described as a grass aggregate that is pushed out of its position by water under the grass sod. The clay under the grass was eroded by the flowing water which eventually led to lifting a big clump of grass out of the grass cover. As described in the report the creep of water under the grass cover was probably initiated by the presence of mice holes. The mice holes had led to a weak spot in the clay underneath the grass cover which had eventually developed into creep of water under the grass cover. The creep under the grass cover was probably caused by pressure gradients in the overflowing water. The final result of the third overtopping experiment of the Friese Waddenzeedijk experiments is shown in Figure F.3. Although this picture seems quite similar to other overtopping damage pictures it is actually different because the length of the land side slope is nearly 27 m, much longer than the land side slope of other dike sections tested.

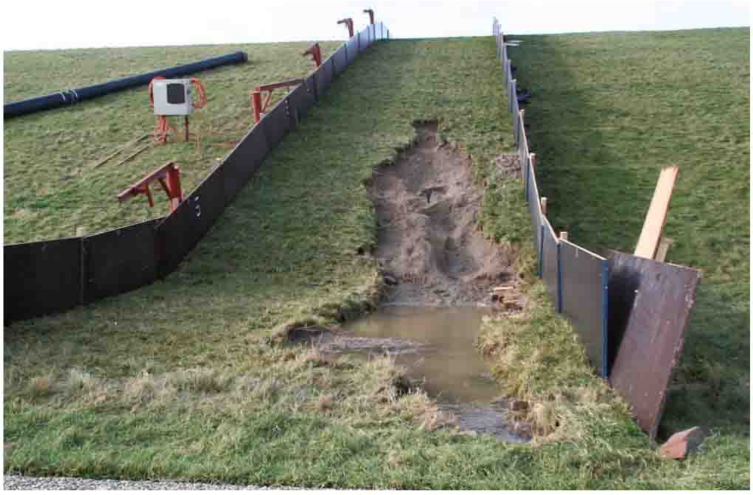

FIGURE F.3: Final result of the third Friese Waddenzeedijk overtopping experiments. Photo taken by Infram B.V. [3]

Fourth Friese Waddenzeedijk overtopping experiment

During the fourth overtopping experiment at the Friese Waddenzeedijk experiments a same kind of failure mechanism occurred as during the third experiment. Except for the fact that the location of this damage spot was around the 16 m line in stead of the 21 m line. However, in order to reach this impact point a crest velocity of 14.7 m/s is required, still way higher than any observed flow velocity. Therefore also for this test section it is concluded that wave impact is not the leading force in the failure process of this land side slope. A picture of the final result of the fourth overtopping experiment is given in Figure F.4.

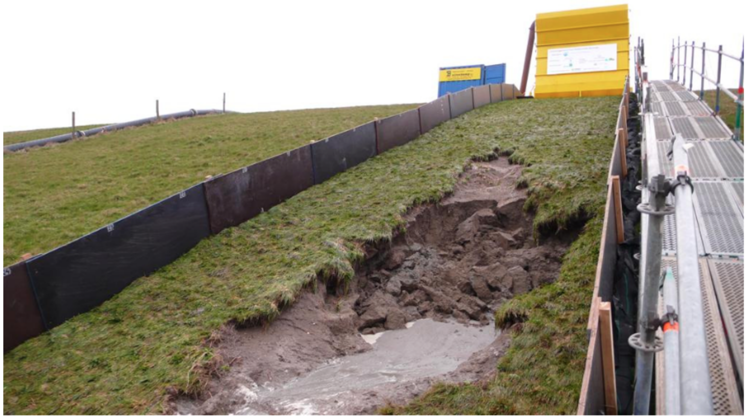

FIGURE F.4: Final result of the fourth Friese Waddenzeedijk overtopping experiments. Photo taken by Infram B.V. [3]

Although the potential reason the grass cover failed during the third and fourth overtopping experiments is very interesting, and investigating this process could help a lot in the understanding of dike failure, it is not within the scope of this research.

F.4 Zeeuwse zeedijken experiments

In 2008, in the Dutch province of Zeeland, in the South of The Netherlands, wave overtopping experiments were executed at two locations: St Philipsland and Kattendijke. At St Philipsland one test section was available while at kattendijke four test sections were available. The experiments were set up to gather more knowledge on overtopping resistant dikes. Subsequently different types of land side slope cover were tested at the Kattendijke test sections: two grass cover sections, one Elastocoast cover section and one open asphalt cover section. Elastocoast is a mixture of polyurethane, rocks and granulate which creates an elastic porous cover for the land side slope. Of course the results of the Kattendijke experiments that were not executed on grass cover cannot be used as validation data for the wave impact approach as this theory is developed for grass covered land side slopes.

Like at the Friese Waddenzeedijk overtopping experiment 6 hour storms were simulated using the wave overtopping simulator [4]. Averaged wave overtopping volumes of respectively 0.1, 1, 10, 30, 50 and 75 l/m/s were generated using a Weibull distribution.

St Philipsland overtopping experiment

The tested land side slope at the St Philipsland dike was 13 m long with a 1:2.4 slope, or a slope angle $\theta = 0.38$ rad. The grass cover was in *good* conditions according to the VTV2006 standards.

During the overtopping experiments at St Philipsland initial damage spots were noticed around the respectively 4 and 7 m line below the crest line, this is visualized in Figure F.5. The initial damage spots were probably caused by some minor weak spot in the grass cover. Around the 4 m line, corresponding to a horizontal coordinate $X = 3.7$ m, a minor bold spot was visible in the grass cover and at the 7 m line, corresponding to a horizontal coordinate $X = 6.5$ m, a slight cascade was visible. The initial damage spot around the 7 m line eventually developed into a big eroded area just above the toe in which the head cut erosion stage was reached [4]. This is shown in Figure F.6.

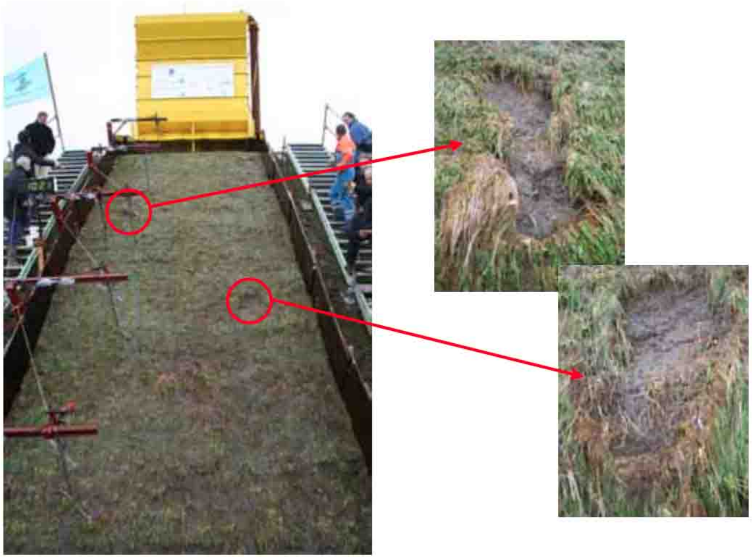

Figure F.5: Initial damage spots during the St Philipsland overtopping experiments. Photo taken by Infram B.V. [4]

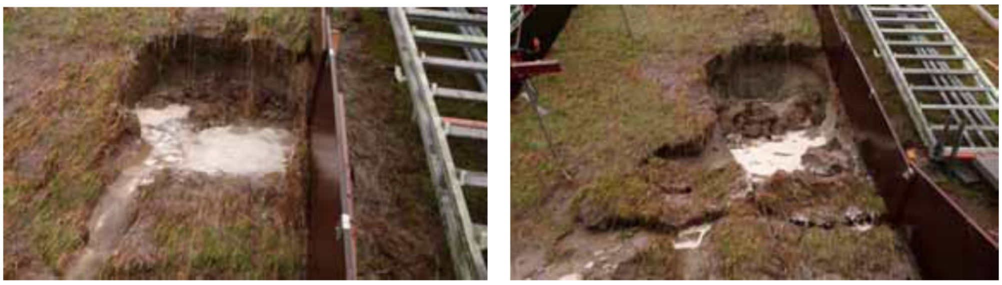

Figure F.6: Final result of the St Philipsland overtopping experiments. Photo taken by Infram B.V. [4]

First Kattendijke overtopping experiment

The first Kattendijke overtopping test did not form any significant damage to the land side slope. The toe however was heavily damaged, head cut erosion had damaged the area landwards of the toe so heavily that a vertical wall of at least 0.5 m occurred down the land side slope [4]. Since no damage occurred on the land side slope the experiment results of the first Kattendijke overtopping experiment are not directly usable for validation.

Second Kattendijke overtopping experiment

The second Kattendijke overtopping experiment was performed on a 15 m long grass covered land side slope which was in *good* conditions according to the VTV2006 standards. The slope was 1:3 which corresponds with a slope angle $\theta = 0.32$ rad. During the second Kattendijke overtopping experiment damage on the land side slope did occur, due to the removal of a stump from the land side slope a weak spot was created. This removal was necessary because otherwise it would block the flow over the slope. This stump was removed around the 7 m line, corresponding to horizontal coordinate $X = 6.6$ m, below the crest [4]. Mole corridors appeared to be present as well which made the spot even weaker. Unsurprisingly damage to the land side slope occurred first around this spot. Although the initial damage spot occurred rapidly during the experiment, it did not evolve into a major erosion spot. The roots of the grass were apparently so dense that the clay underneath the grass eroded but the grass aggregate itself remained in position. Due to heavily toe erosion during the 50 l/m/s tests of the second Kattendijke overtopping experiment it was decided to stop the tests and not execute the 75 l/m/s tests. The risk of shearing of the land side slope was too high. Therefore the observed damage spot on around the 7 m line on the land side slope did not have the chance to evolve into major damage spots. A picture of the observed damage spots is given in Figure F.7.

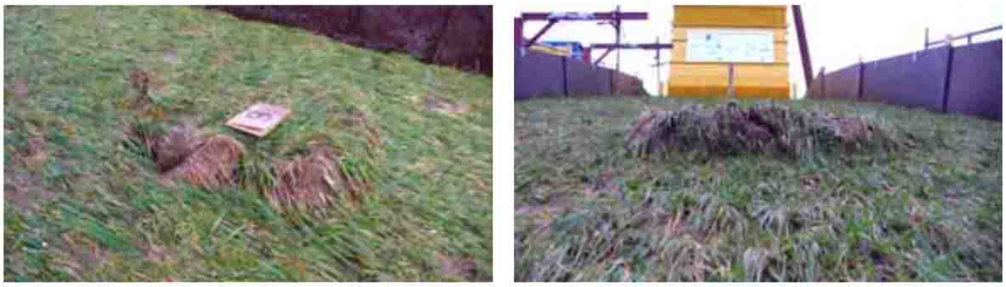

FIGURE F.7: Initial damage spots noticed during the second Kattendijke overtopping experiments. Photo taken by Infram B.V. [4]

F.5 Tholen experiments

On the island of Tholen in the Dutch province of Zeeland wave overtopping experiments were executed on a sea dike. Three different kinds of land side slope cover were tested on 4 different test sections. Like with the previous mentioned reference experiments, only the overtopping experiments executed on grass covered test sections are considered. In the case of the Tholen experiments this means test section 3 and 4, the other test sections are not representative. Test section 1 was orientated on the water side slope in stead of the land side slope and test section 2 contained stone steps in the center line of the test section. The slope of both grass covered test sections was in the order of 1:2.5, or a slope angle $\theta = 0.38$ rad. Both land side slope test sections were classified y Infram as 'very bad condition' [6].

Third Tholen overtopping experiment.

During the overtopping experiments on the third test section of the sea dike at Tholen already during the first 5 l/m/s overtopping test a hole in the land side slope was noticed. This hole appeared to be caused by intesive mole activities under the grass cover. This intensive mole activity had weakened the test section in such a way that during the 5 l/m/s test a 6 m^2 piece of grass sod had sheared. The mole activity had formed a system of tunnels just underneath the grass cover. Overflowing water also flowed through this system of tunnels leading to erosion from inside out on the clay an grass cover layer. The initial hole in the land side slope was noticed around the 9 m line on the land side slope below the crest line. This corresponds to a horizontal coordinate $X = 8.2$ m.

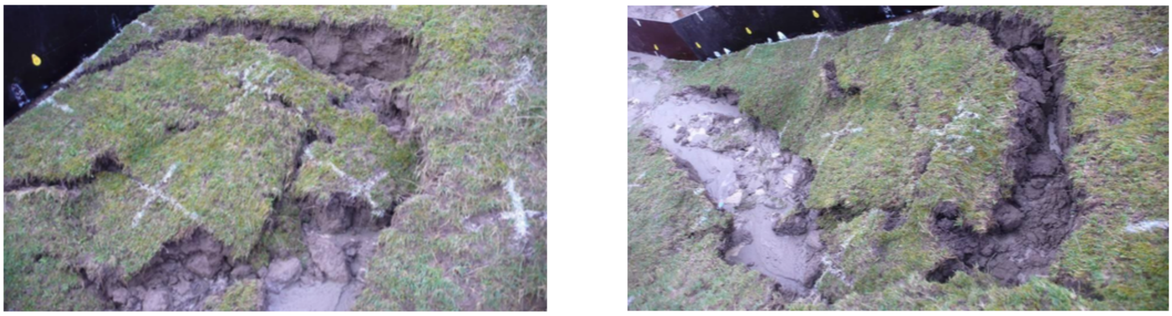

(A) Test section 1 (B) Test section 1

FIGURE F.8: Final result of the third wave overtopping test at Tholen, a large part of the land side slope had sheared due to the presence of animal activity. Photo's taken by Infram B.V. [6]

Fourth Tholen overtopping experiment.

After some time during the third Tholen wave overtopping experiments the toe of the land side slope was damaged in such a way that the sand core was reached. Due to groundwater flow inside the dike the sand core was basically flushed away through the hole under the toe. This caused a total collapse of the land side slope which is visible in Figure F.9. Due the total collapse of the land side slope the result of the fourth overtopping experiment at Tholen is not really representative for general failure of a land side slope. The collapse was caused by other processes than described earlier. Therefore unfortunately also this experiment is not usable for validation of the wave impact approach method.

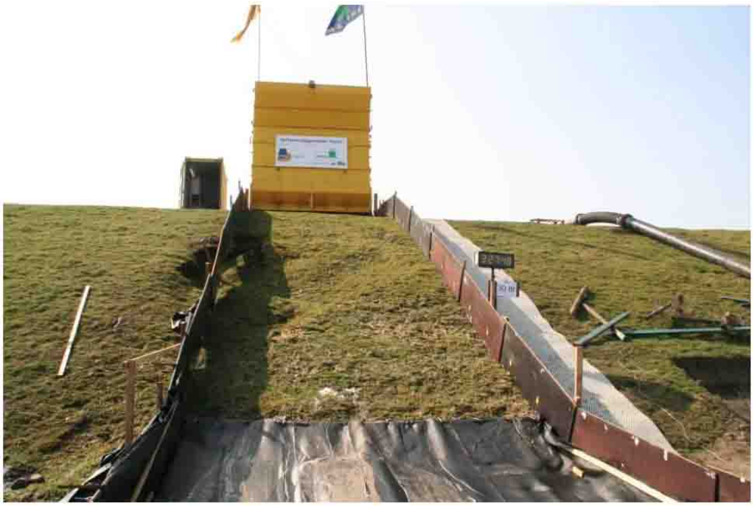

FIGURE F.9: Final result second overtopping experiment Tholen, the land side slope collapsed completely due to the washing away of the sand core by groundwater flow. Photo taken by Infram B.V. [6]

G | Tracking plots Infrared camera

G.1 Track and velocity components of the floater

Floater track at pump frequency of 20 Hz

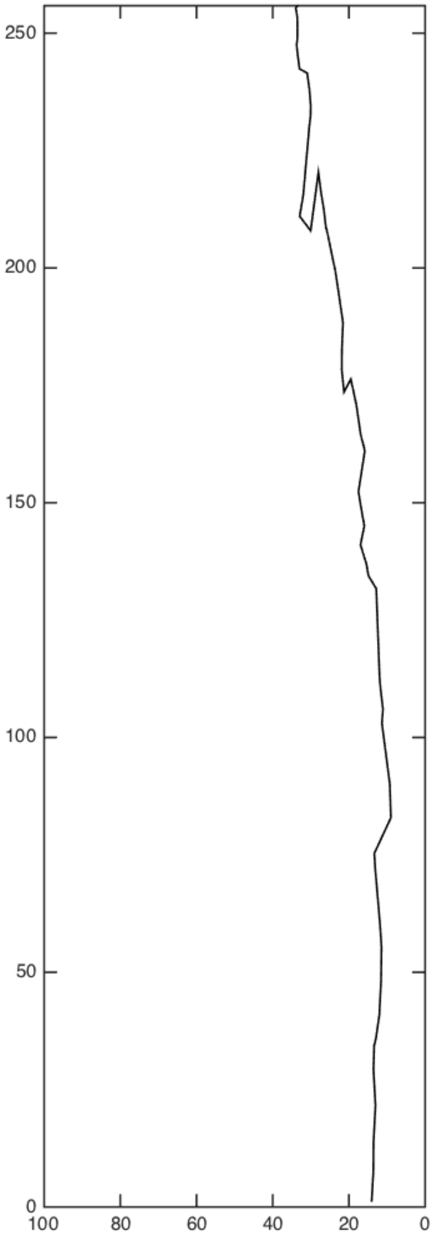

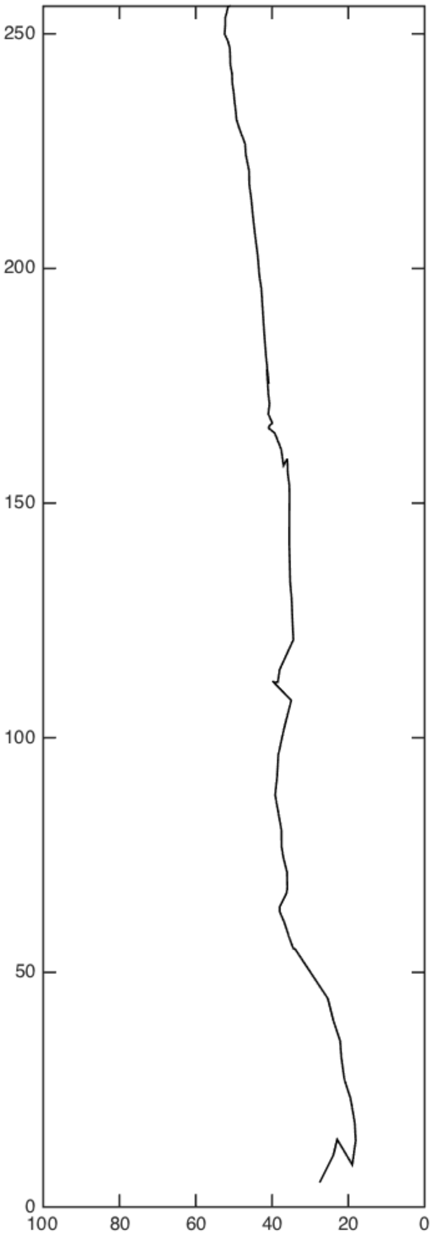

(A) Track of the hot ball through the flow during the first measurements at a pump frequency of 20Hz.

(B) Track of the hot ball through the flow during the hydraulic calibration at a pump frequency of 20Hz.

Velocity components at pump frequency of 20 Hz

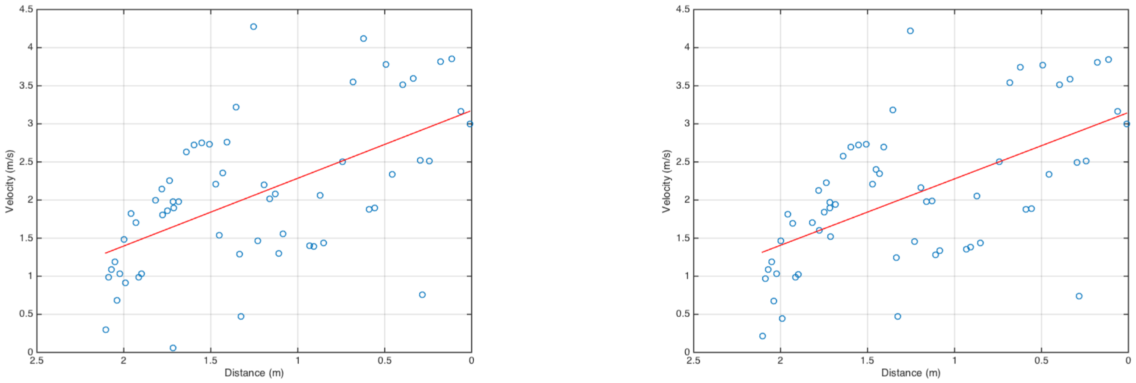

(A) Velocity component in the flow direction of the tracked hot ball during the first measurements.

(B) Width averaged velocity component in the flow direction of the test section during the first measurements.

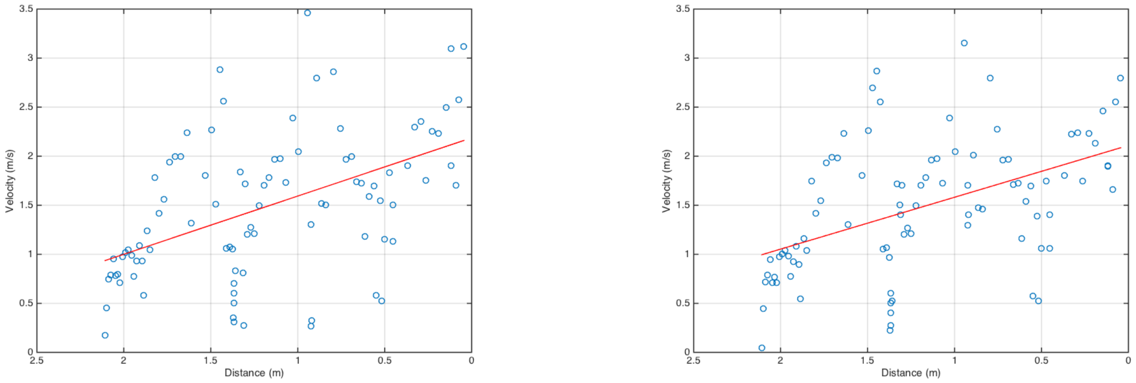

(C) Width averaged velocity component in the flow direction of the test section during the hydraulic calibration.

(D) Width averaged velocity component in the flow direction of the test section during the hydraulic calibration.

Figure G.2: Pump frequency: 20 Hz.

Floater track at pump frequency of 25 Hz

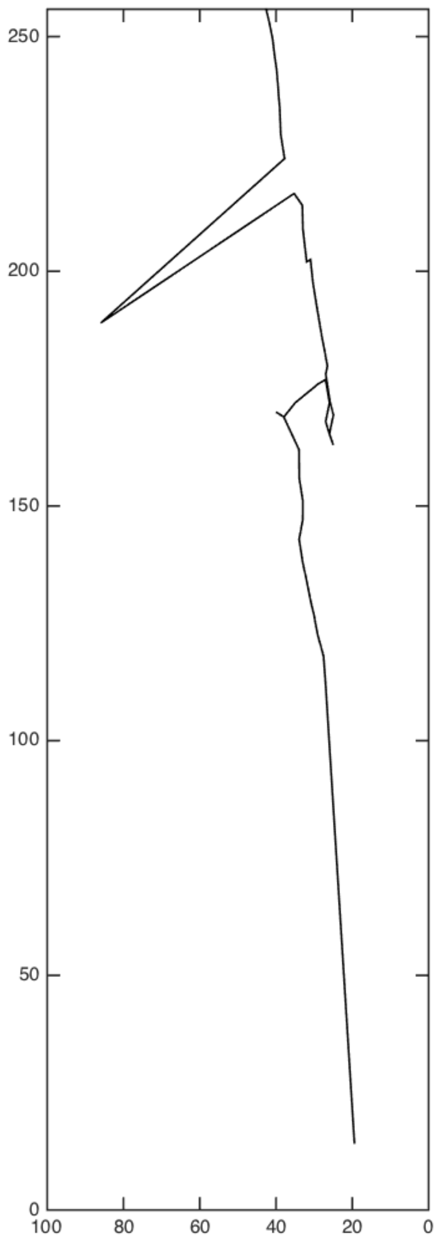

(A) Track of the hot ball through the flow during the first measurements at a pump frequency of 25Hz.

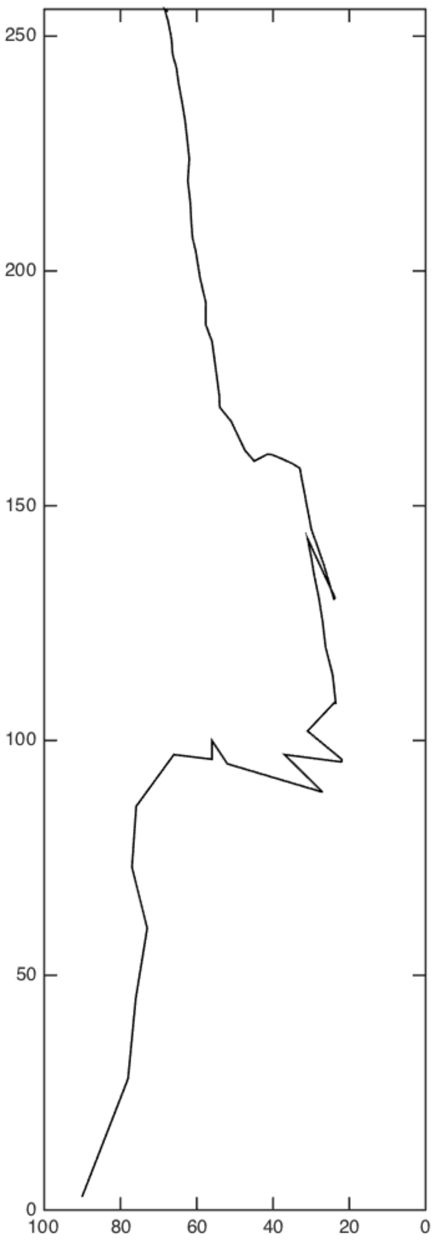

(B) Track of the hot ball through the flow during the hydraulic calibration at a pump frequency of 25Hz.

Velocity components at pump frequency of 25 Hz

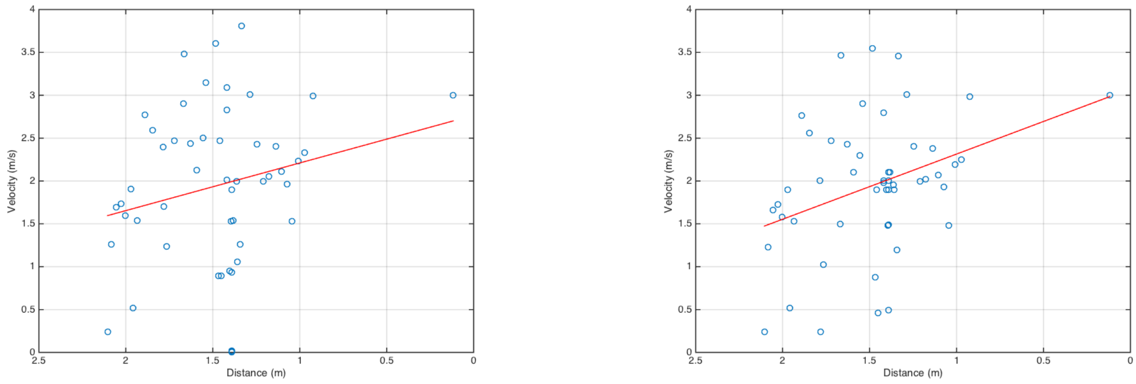

(A) Velocity component in the flow direction of the tracked hot ball during the first measurements.

(B) Width averaged velocity component in the flow direction of the test section during the first measurements.

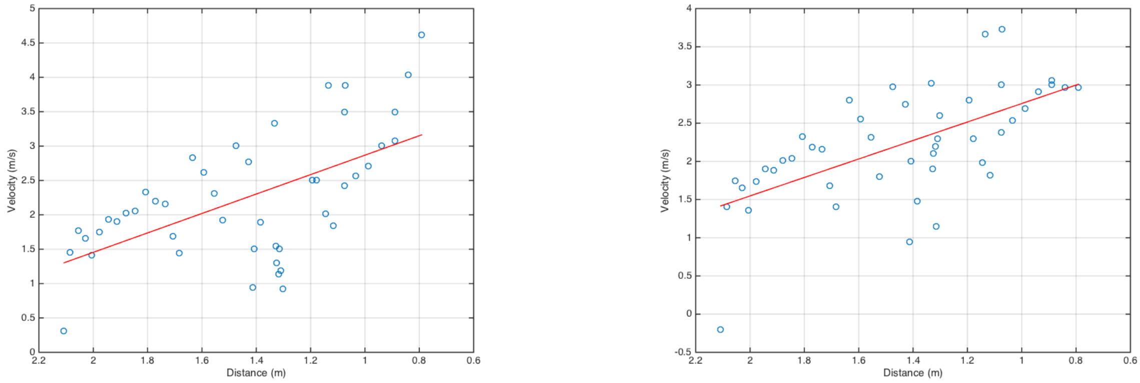

(C) Width averaged velocity component in the flow direction of the test section during the hydraulic calibration.

(D) Width averaged velocity component in the flow direction of the test section during the hydraulic calibration.

Figure G.4: Pump frequency: 25 Hz.

Floater track at pump frequency of 30 Hz

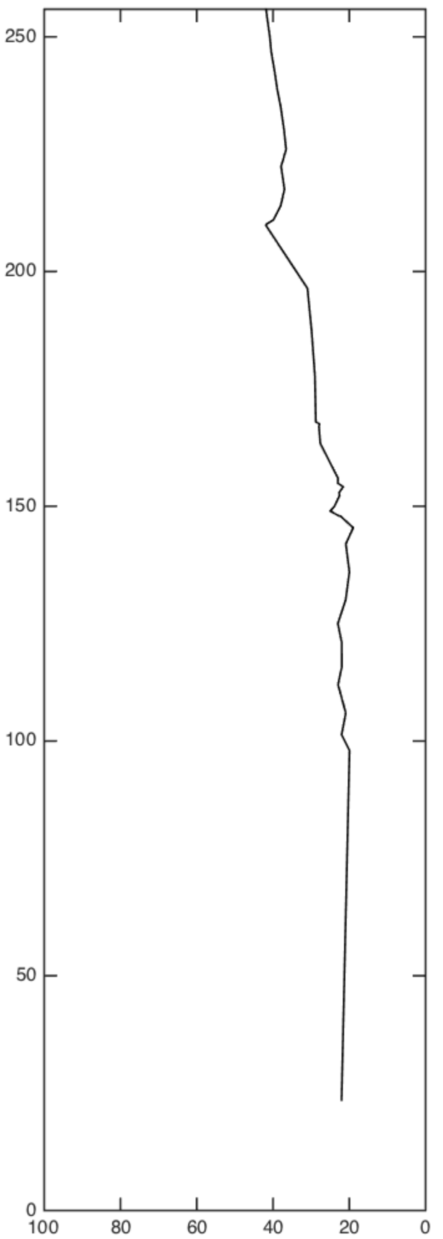

(A) Track of the hot ball through the flow during the first measurements at a pump frequency of 30Hz.

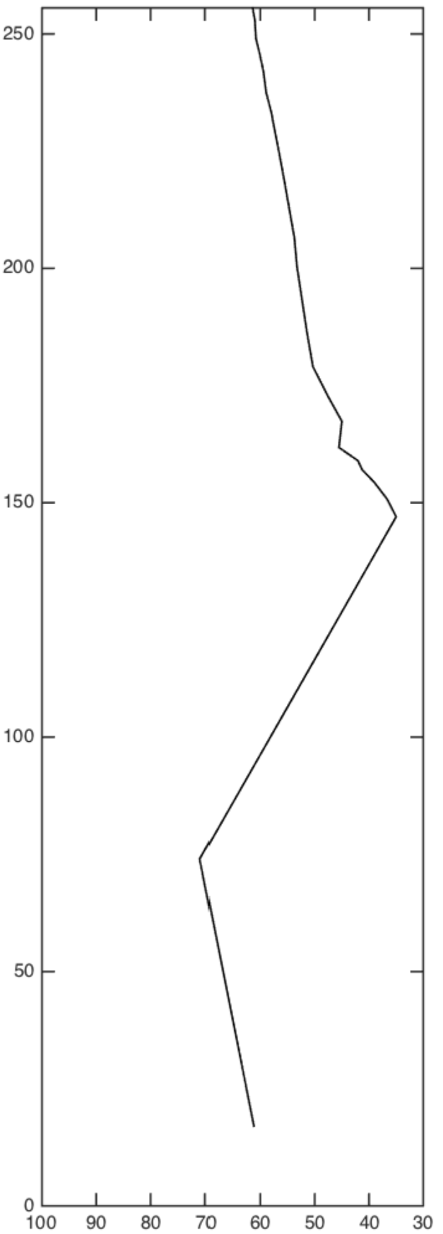

(B) Track of the hot ball through the flow during the hydraulic calibration at a pump frequency of 30Hz.

Velocity components at pump frequency of 30 Hz

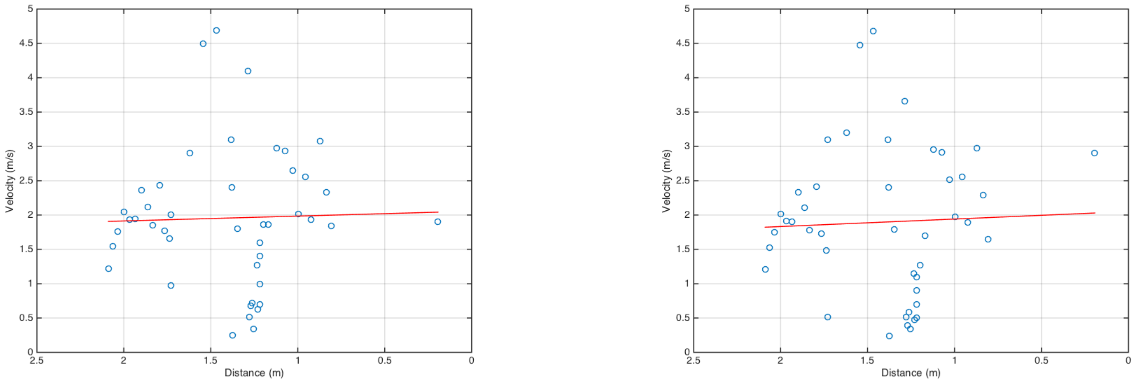

(A) Velocity component in the flow direction of the tracked hot ball during the first measurements.

(B) Width averaged velocity component in the flow direction of the test section during the first measurements.

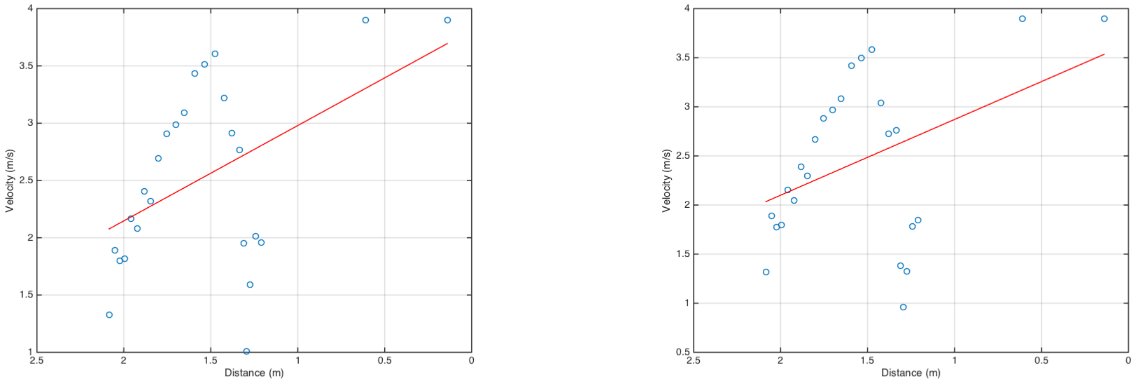

(C) Width averaged velocity component in the flow direction of the test section during the hydraulic calibration.

(D) Width averaged velocity component in the flow direction of the test section during the hydraulic calibration.

FIGURE G.6: Pump frequency: 30 Hz.

Floater track at pump frequency of 35 Hz

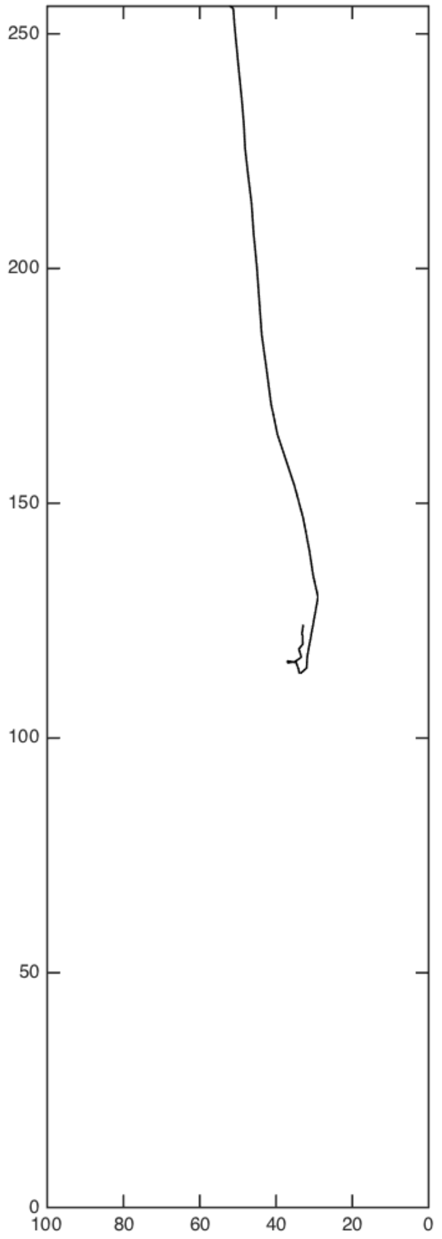

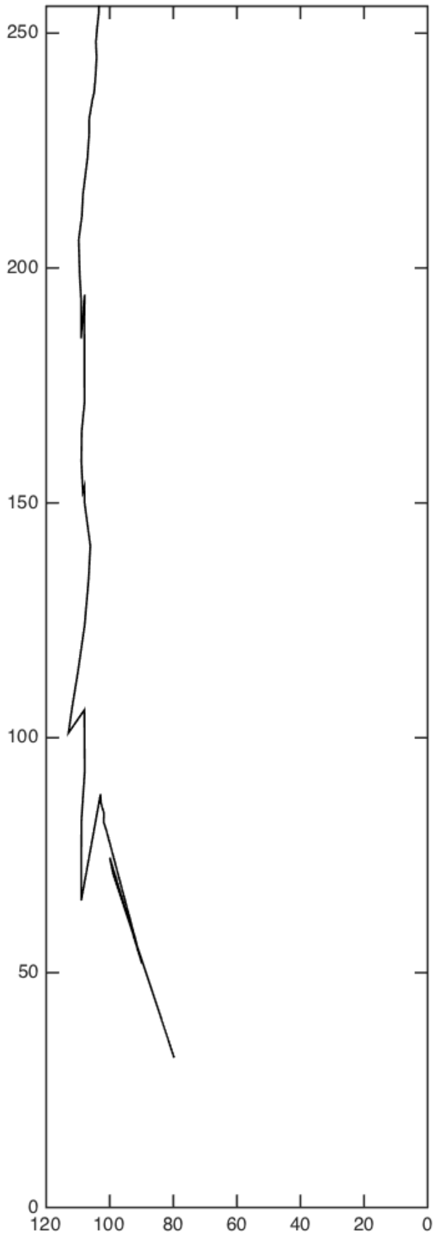

(A) Track of the hot ball through the flow during the first measurements at a pump frequency of 35Hz.

(B) Track of the hot ball through the flow during the hydraulic calibration at a pump frequency of 35Hz.

Velocity components at pump frequency of 35 Hz

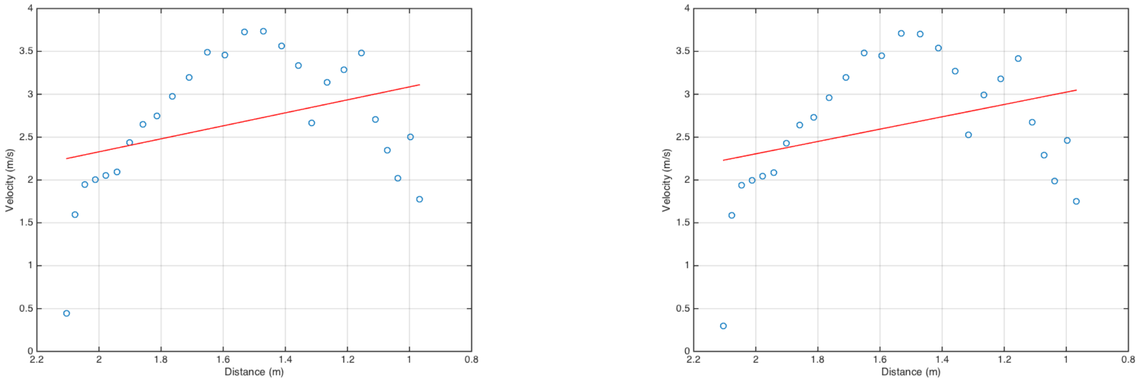

(A) Velocity component in the flow direction of the tracked hot ball during the first measurements.

(B) Width averaged velocity component in the flow direction of the test section during the first measurements.

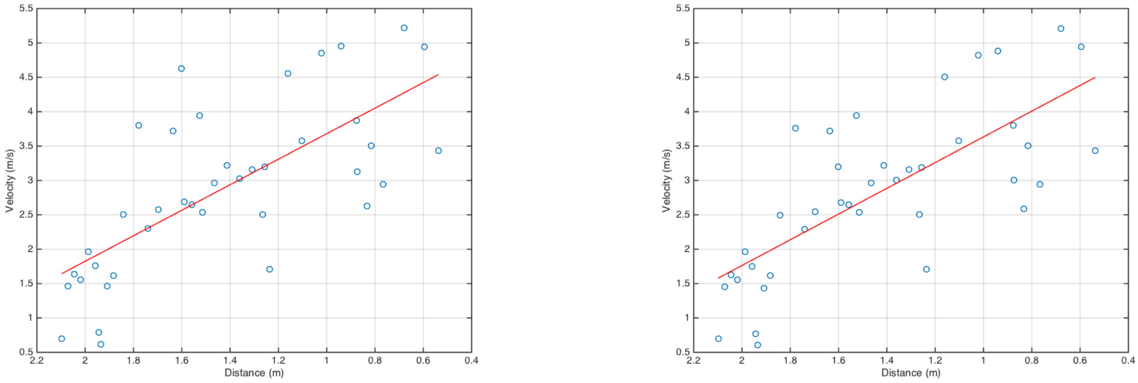

(C) Width averaged velocity component in the flow direction of the test section during the hydraulic calibration.

(D) Width averaged velocity component in the flow direction of the test section during the hydraulic calibration.

FIGURE G.8: Pump frequency: 35 Hz.

Floater track at pump frequency of 40 and 45 Hz

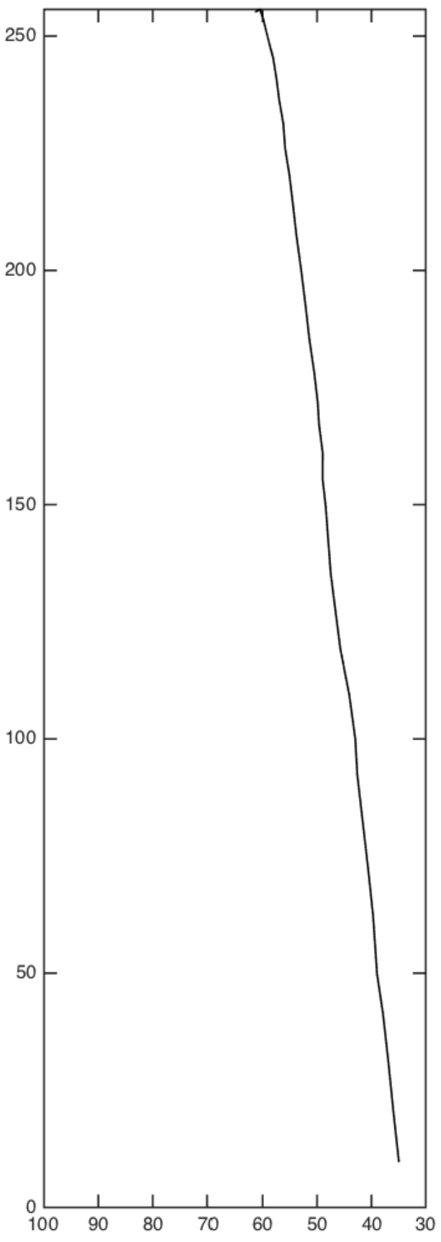

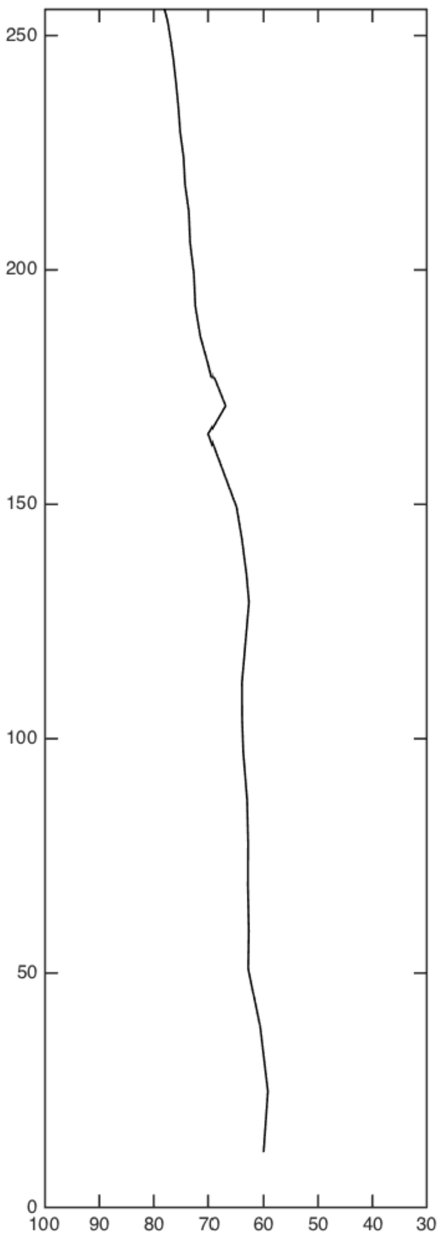

(A) Track of the hot ball through the flow during the first measurements at a pump frequency of 40Hz.

(B) Track of the hot ball through the flow during the hydraulic calibration at a pump frequency of 45Hz.

Velocity components at pump frequency of 40 and 45 Hz

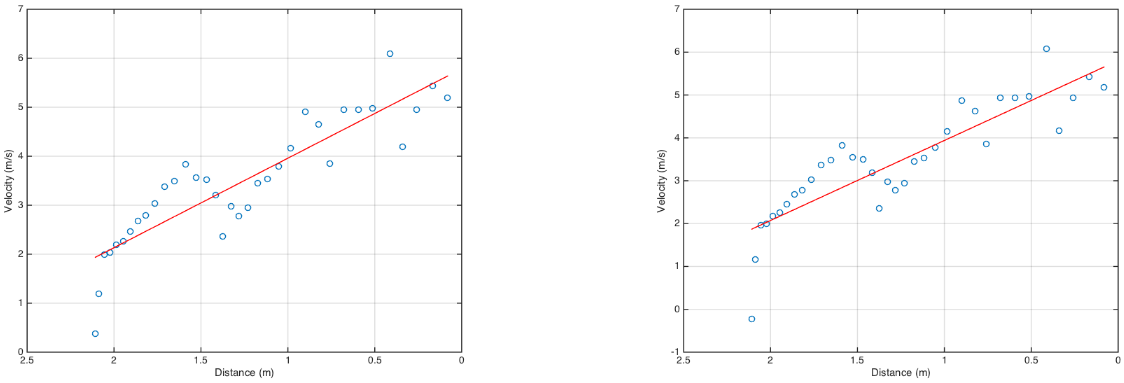

(A) Velocity component in the flow direction of the tracked hot ball during the first measurements.

(B) Width averaged velocity component in the flow direction of the test section during the first measurements.

Figure G.10: Pump frequency: 40 Hz.

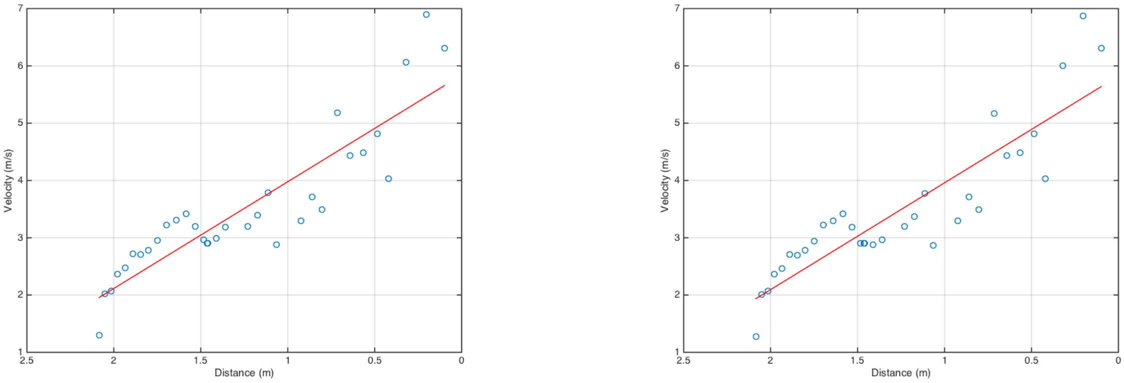

(A) Width averaged velocity component in the flow direction of the test section during the hydraulic calibration.

(B) Width averaged velocity component in the flow direction of the test section during the hydraulic calibration.

Figure G.11: Pump frequency: 45 Hz.

Floater track at pump frequency of 50 Hz

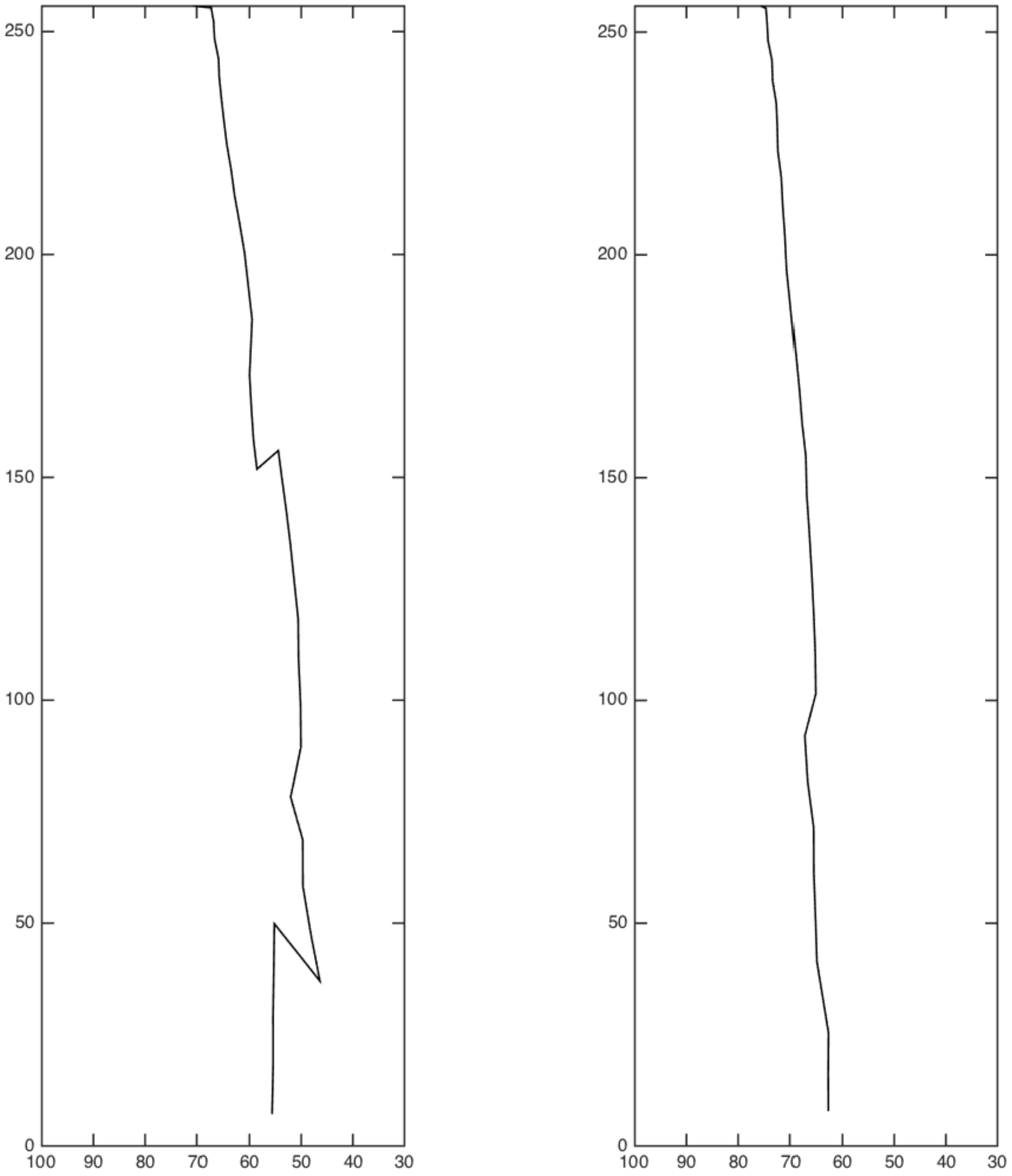

(A) Track of the hot ball through the flow during the first measurements at a pump frequency of 50Hz.

(B) Track of the hot ball through the flow during the hydraulic calibration at a pump frequency of 50Hz.

Velocity components at pump frequency of 50 Hz

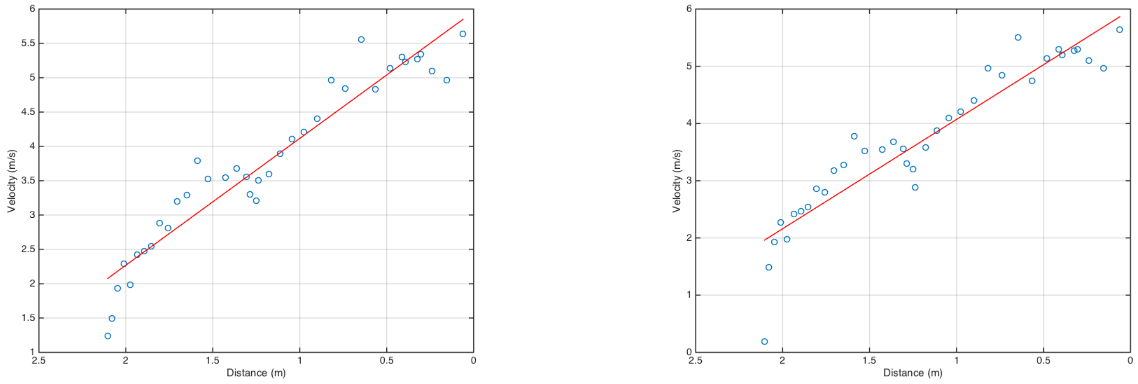

(A) Velocity component in the flow direction of the tracked hot ball during the first measurements.

(B) Velocity component in the flow direction of the tracked hot ball during the first measurements.

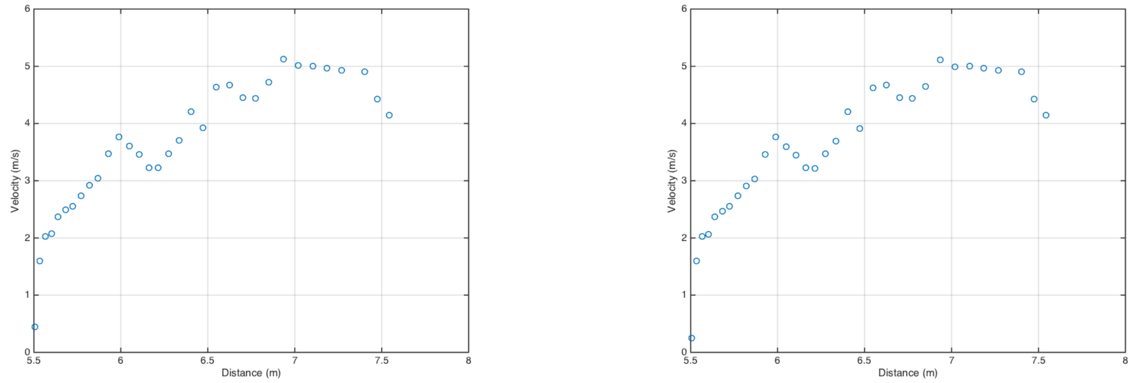

(C) Width averaged velocity component in the flow direction of the test section during the hydraulic calibration.

(D) Width averaged velocity component in the flow direction of the test section during the hydraulic calibration.

FIGURE G.13: Pump frequency: 50 Hz.

H | Peddle wheel and surf board data

In this appendix the data as obtained from the paddle wheels and surfboards during the hydraulic measurements of the overtopping tests are presented. During the hydraulic measurement waves of predetermined volumes were released over the land side slope of the dike. Every wave volume was repeated 3 times, so 3 times 500 l followed by 3 times 1000 l and so on up to 3500 l. The 3000 and 3500 l waves were done only once since a 3000 l wave already caused minor damage to the dike. After a 3500 l wave the damage was significant which made it unadvised to repeat these waves.

For every measurement point the water depth and flow velocity at the bottom and water surface are presented into clusters of identical wave volume. For every measurement position the measured water depth, surface velocity and bottom velocity are plotted. From this data the discharge over the dike is calculated and plotted in the same figure.

Data as obtained from the 500 l test waves.

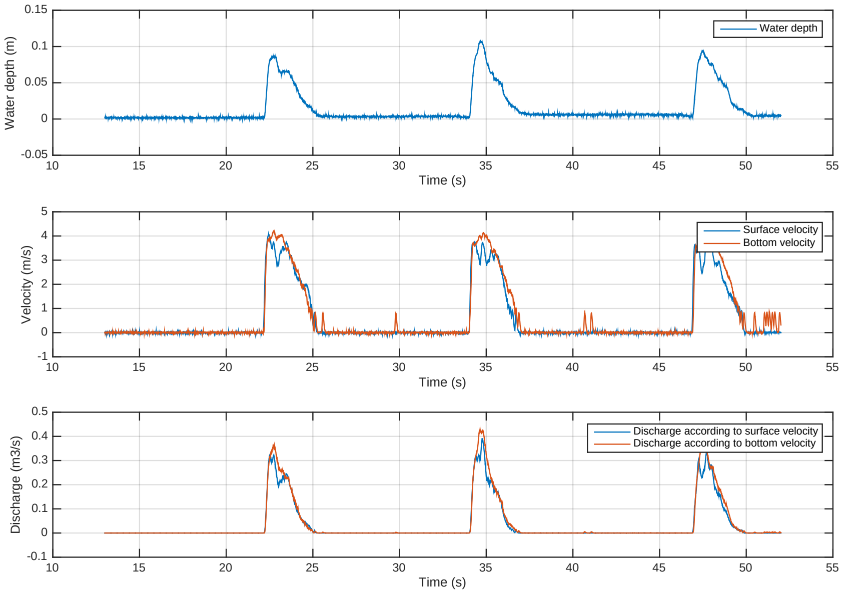

FIGURE H.1: Water depth, bottom velocity, surface velocity and discharge as obtained from position 1 during the 500 l test.

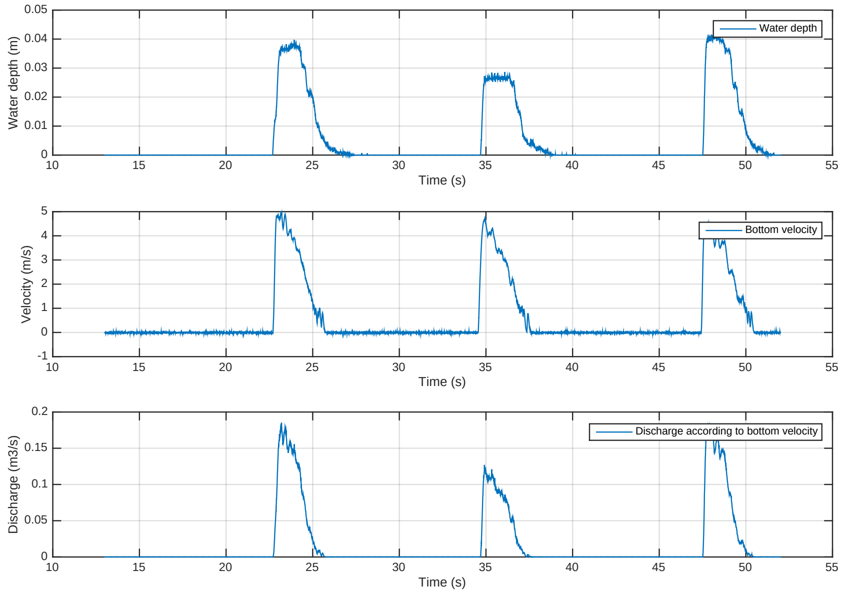

FIGURE H.2: Water depth, bottom velocity, surface velocity and discharge as obtained from position 2 during the 500 l test.

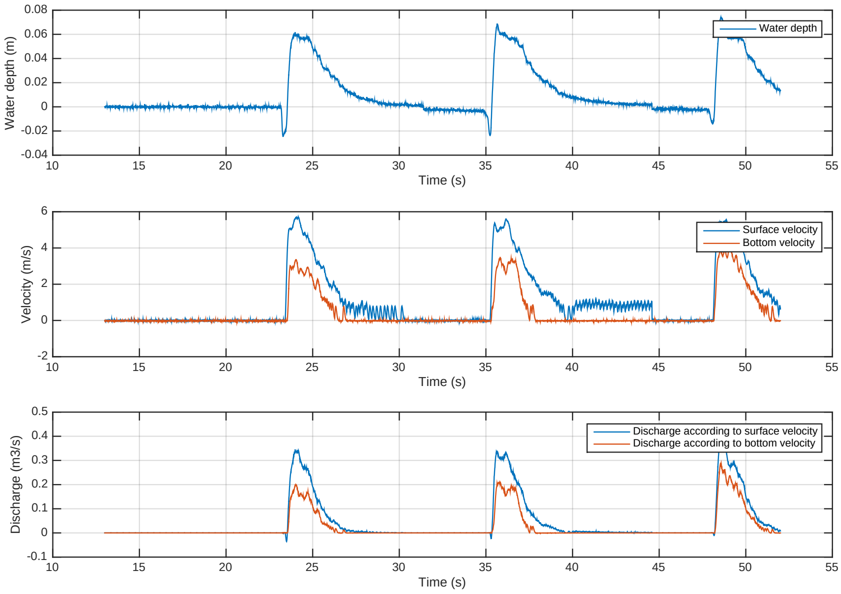

FIGURE H.3: Water depth, bottom velocity, surface velocity and discharge as obtained from position 3 during the 500 l test.

Data as obtained from the 1000 l test waves.

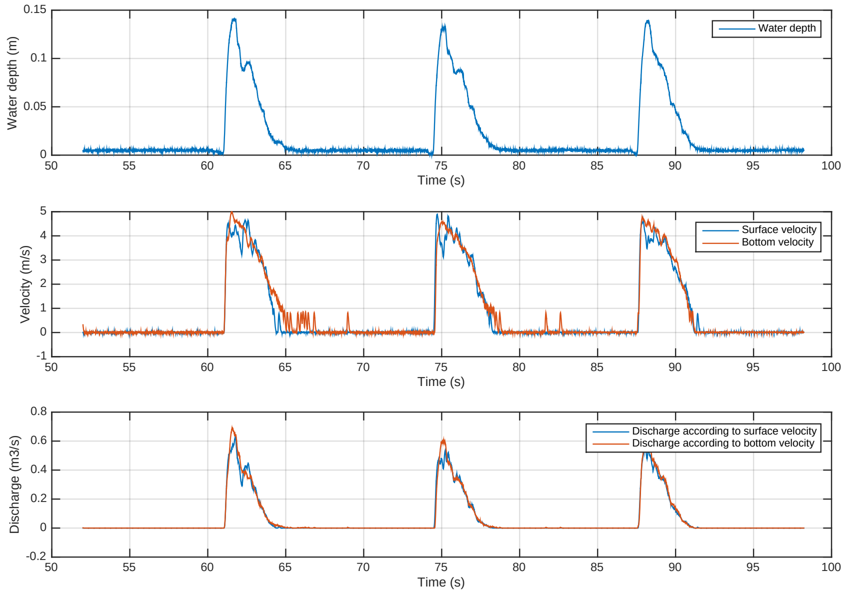

Figure H.4: Water depth, bottom velocity, surface velocity and discharge as obtained from position 1 during the 1000 l test.

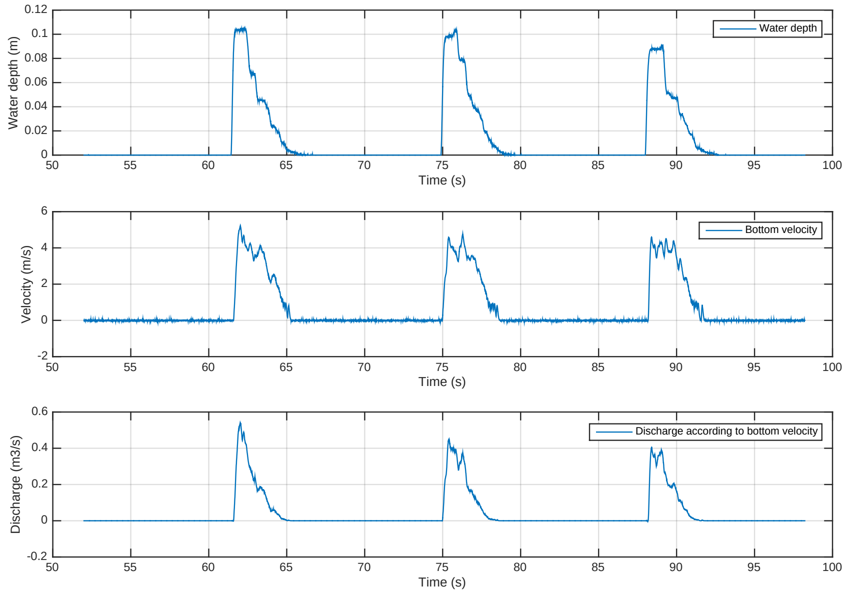

FIGURE H.5: Water depth, bottom velocity, surface velocity and discharge as obtained from position 2 during the 1000 l test.

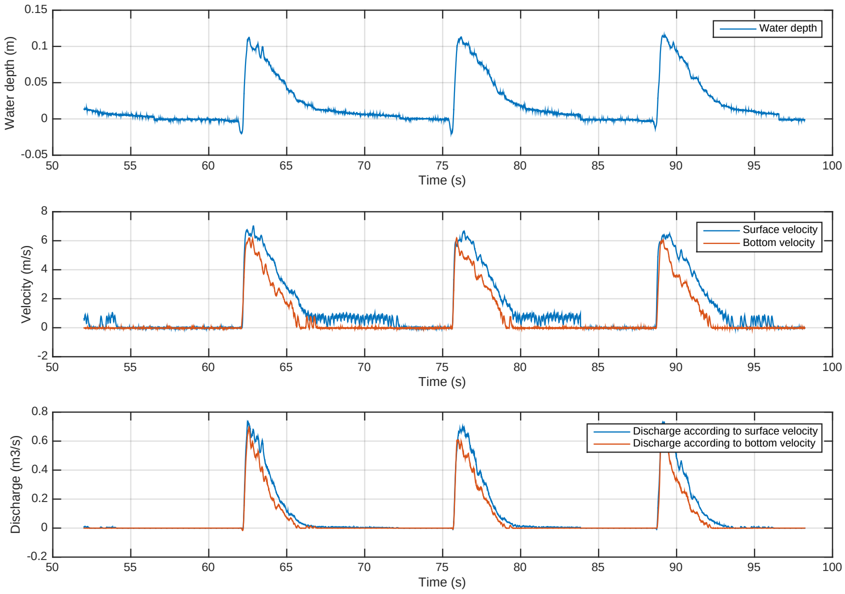

FIGURE H.6: Water depth, bottom velocity, surface velocity and discharge as obtained from position 3 during the 1000 l test.

Data as obtained from the 1500 l test waves.

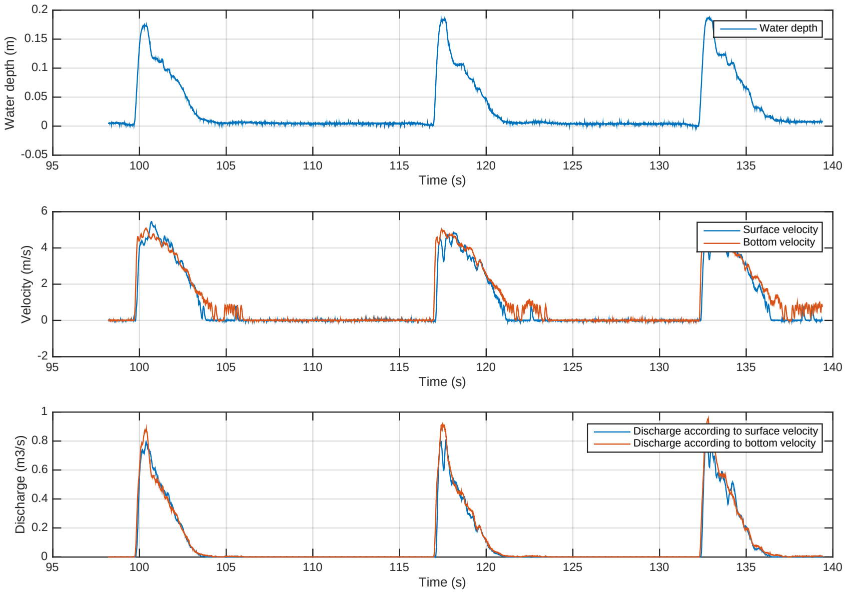

Figure H.7: Water depth, bottom velocity, surface velocity and discharge as obtained from position 1 during the 1500 l test.

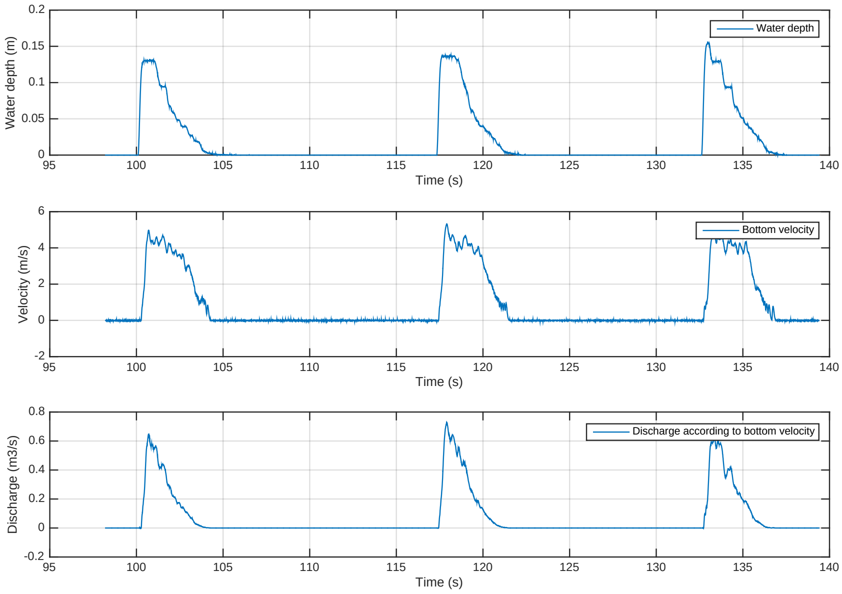

Figure H.8: Water depth, bottom velocity, surface velocity and discharge as obtained from position 2 during the 1500 l test.

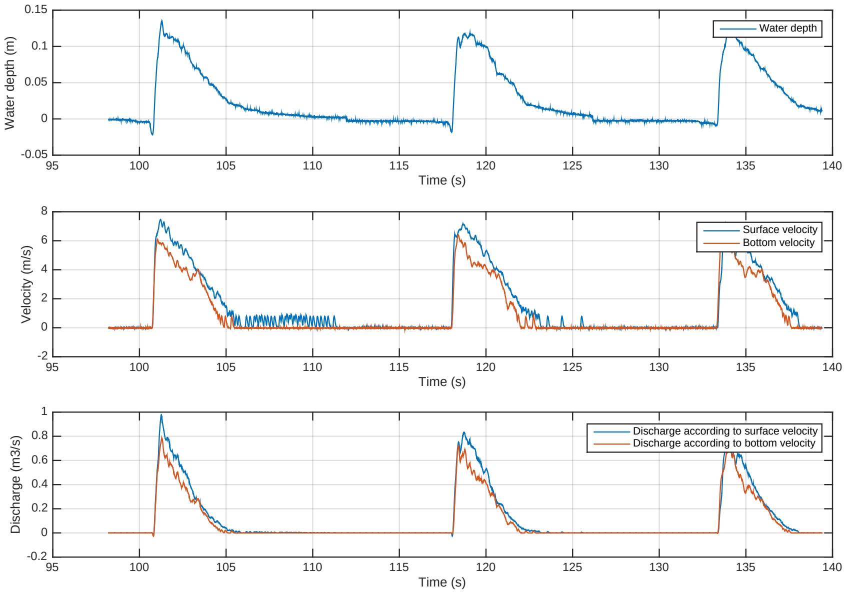

Figure H.9: Water depth, bottom velocity, surface velocity and discharge as obtained from position 3 during the 1500 l test.

Data as obtained from the 2000 l test waves.

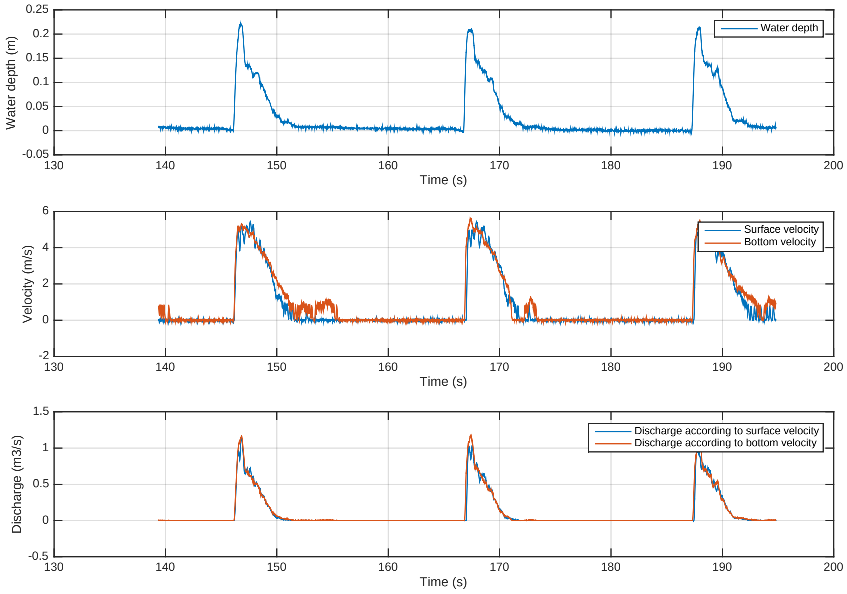

Figure H.10: Water depth, bottom velocity, surface velocity and discharge as obtained from position 1 during the 2000 l test.

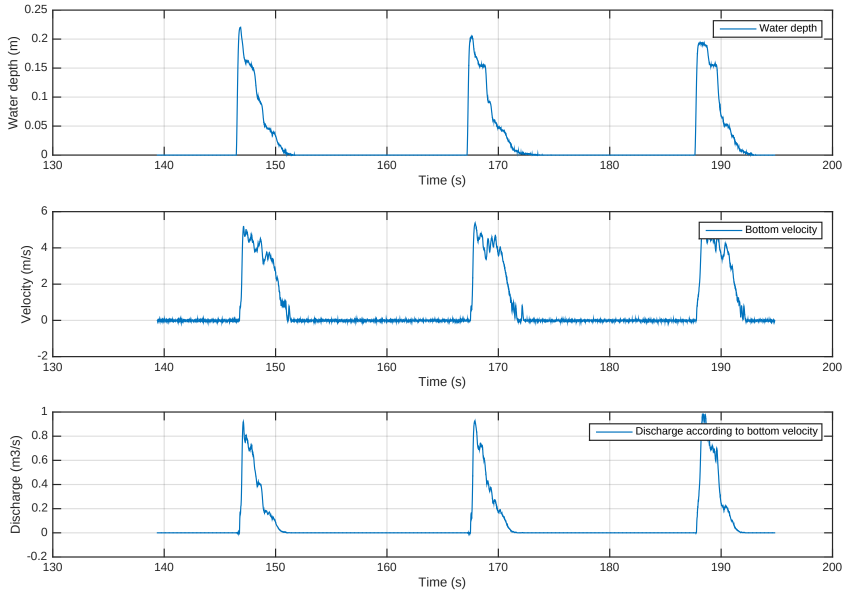

FIGURE H.11: Water depth, bottom velocity, surface velocity and discharge as obtained from position 2 during the 2000 l test.

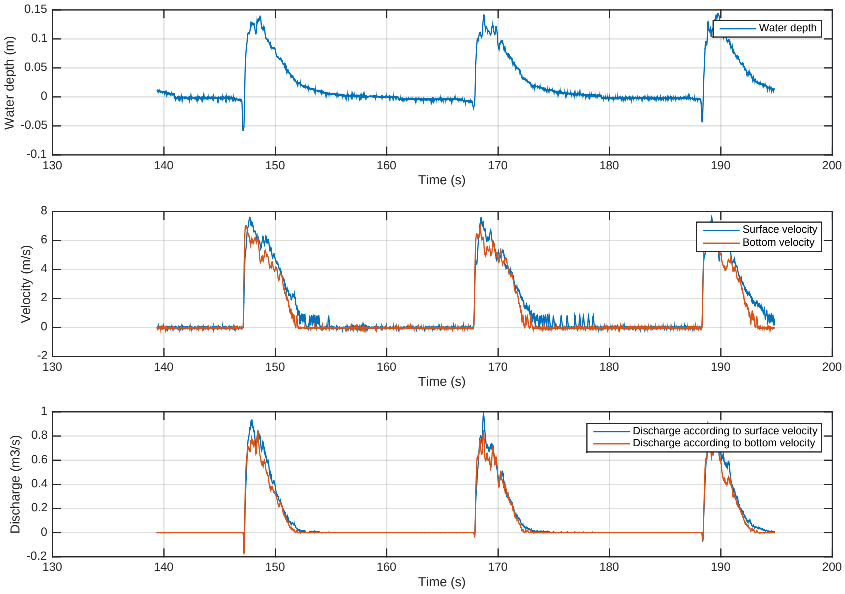

FIGURE H.12: Water depth, bottom velocity, surface velocity and discharge as obtained from position 3 during the 2000 l test.

Data as obtained from the 2500 l test waves.

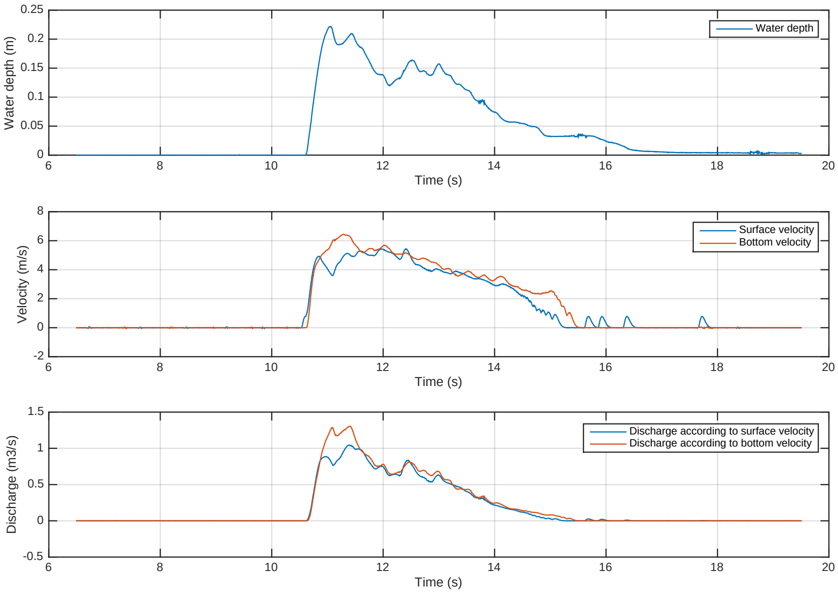

Figure H.13: Water depth, bottom velocity, surface velocity and discharge as obtained from position 1 during the first 2500 l test.

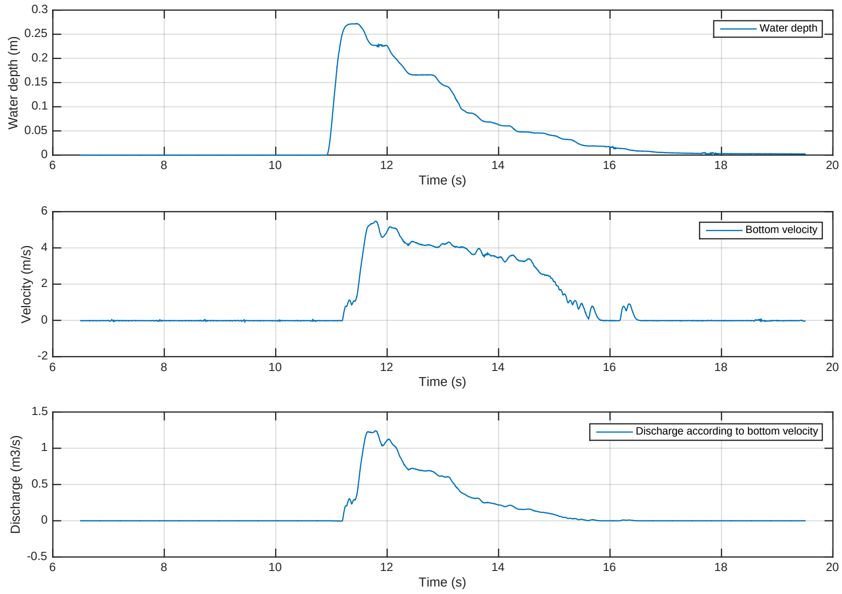

Figure H.14: Water depth, bottom velocity, surface velocity and discharge as obtained from position 2 during the first 2500 l test.

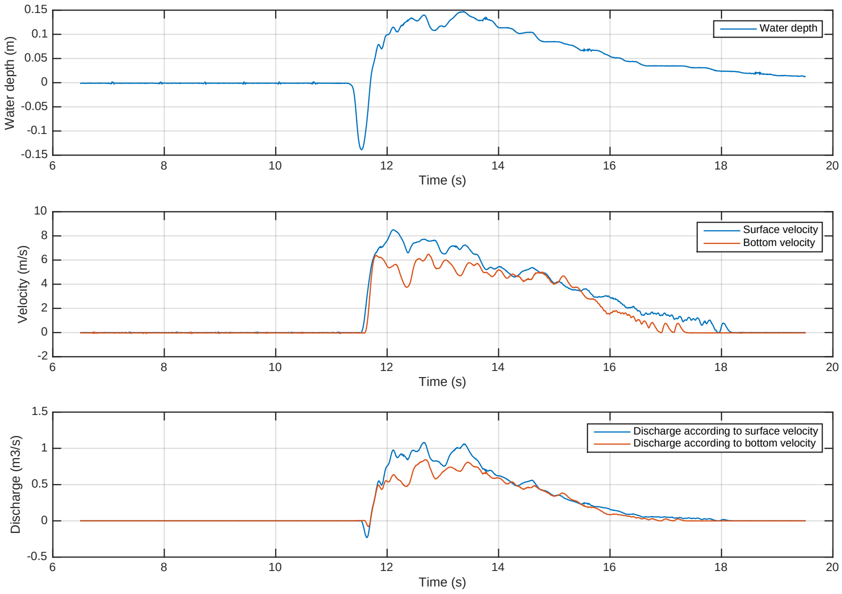

Figure H.15: Water depth, bottom velocity, surface velocity and discharge as obtained from position 3 during the first 2500 l test.

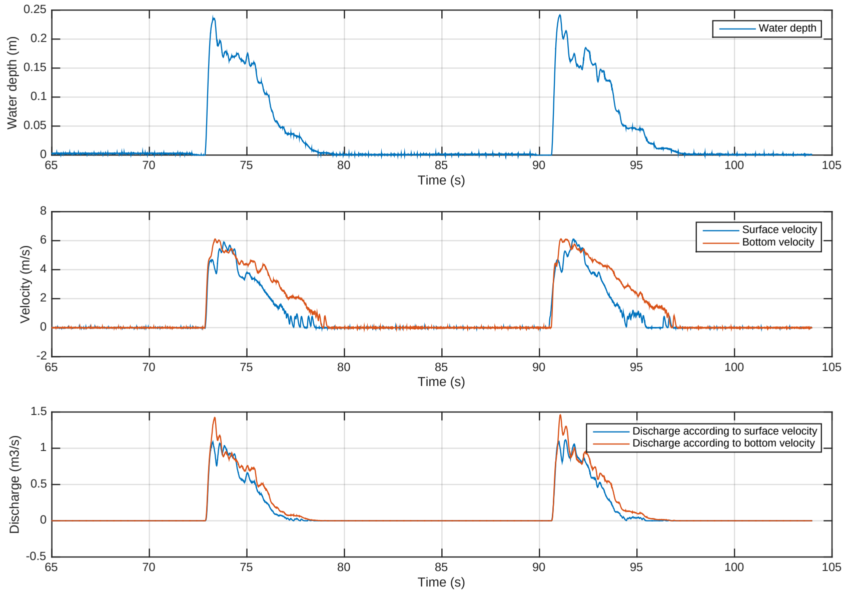

Figure H.16: Water depth, bottom velocity, surface velocity and discharge as obtained from position 1 during the second 2500 l test.

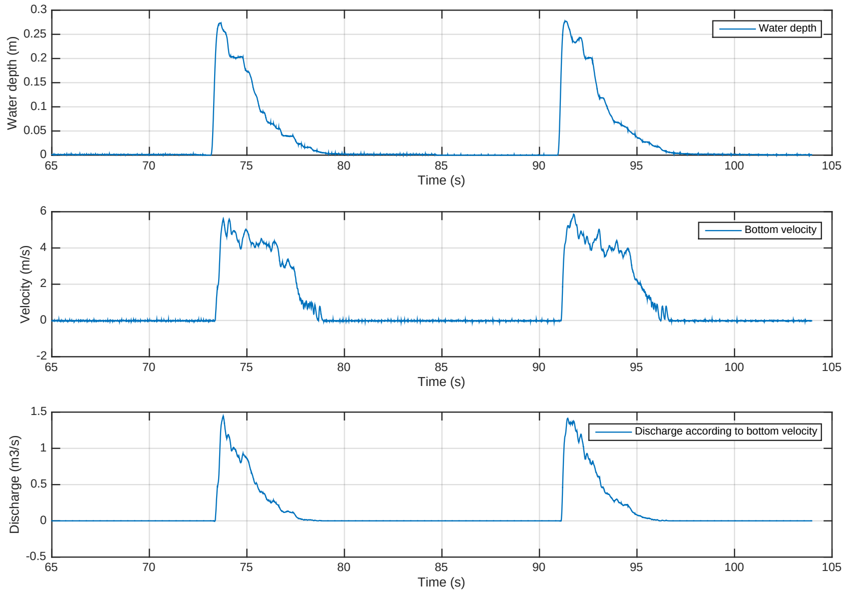

Figure H.17: Water depth, bottom velocity, surface velocity and discharge as obtained from position 2 during the second 2500 l test.

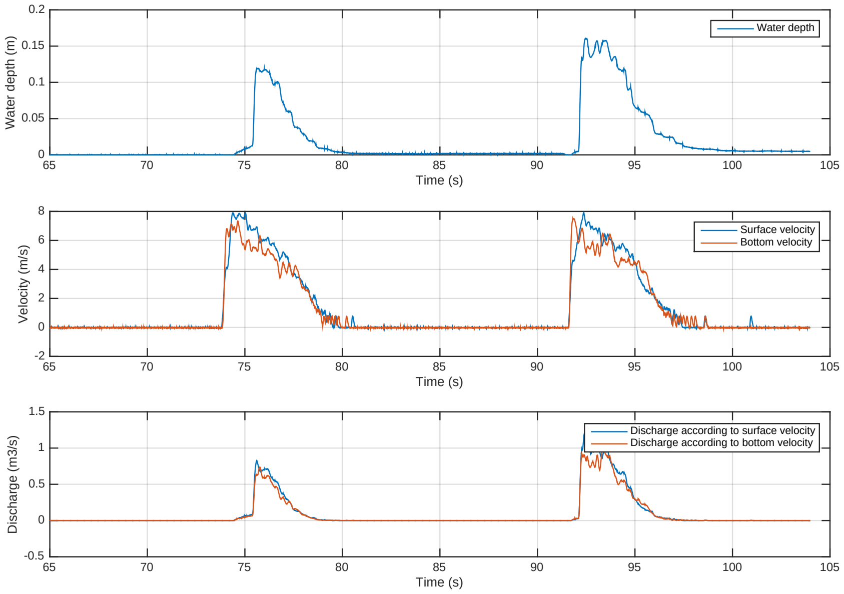

Figure H.18: Water depth, bottom velocity, surface velocity and discharge as obtained from position 3 during the second 2500 l test.

Data as obtained from the 3000 l test waves.

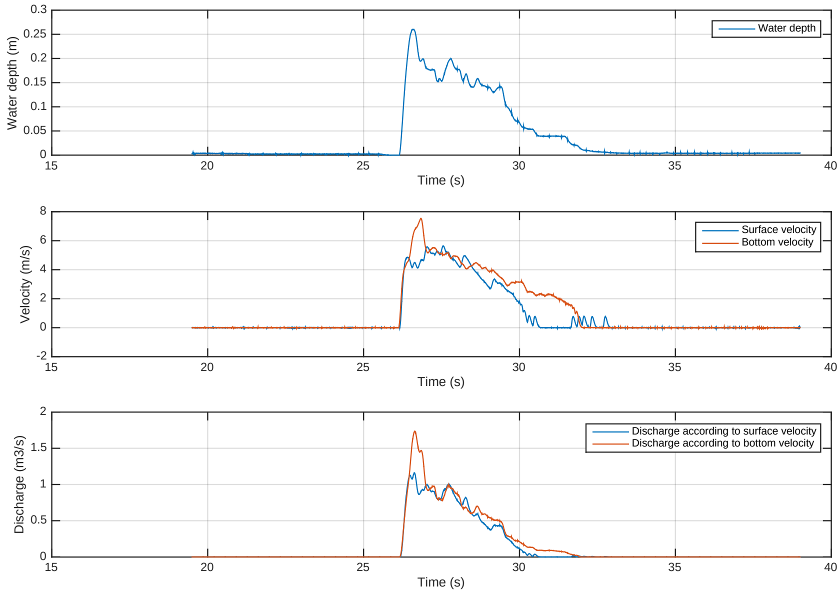

Figure H.19: Water depth, bottom velocity, surface velocity and discharge as obtained from position 1 during the 3000 l test.

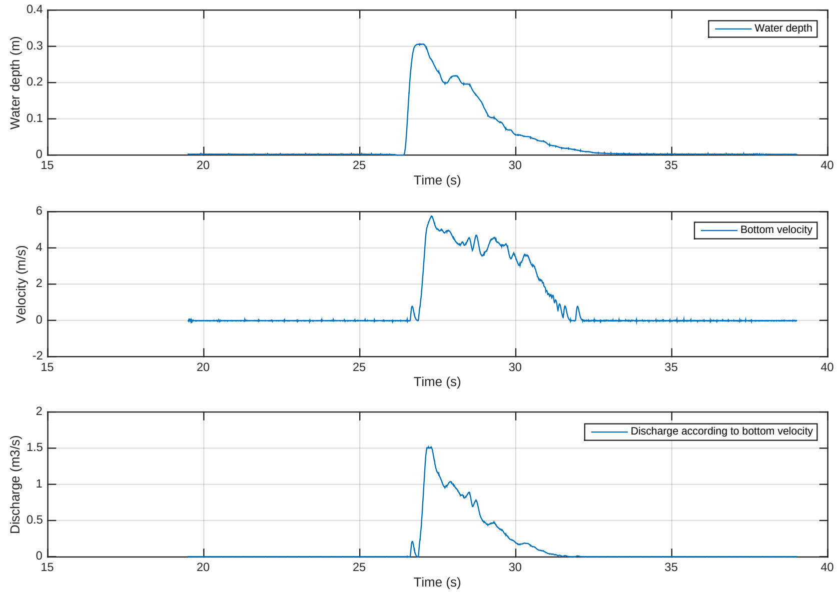

FIGURE H.20: Water depth, bottom velocity, surface velocity and discharge as obtained from position 2 during the 3000 l test.

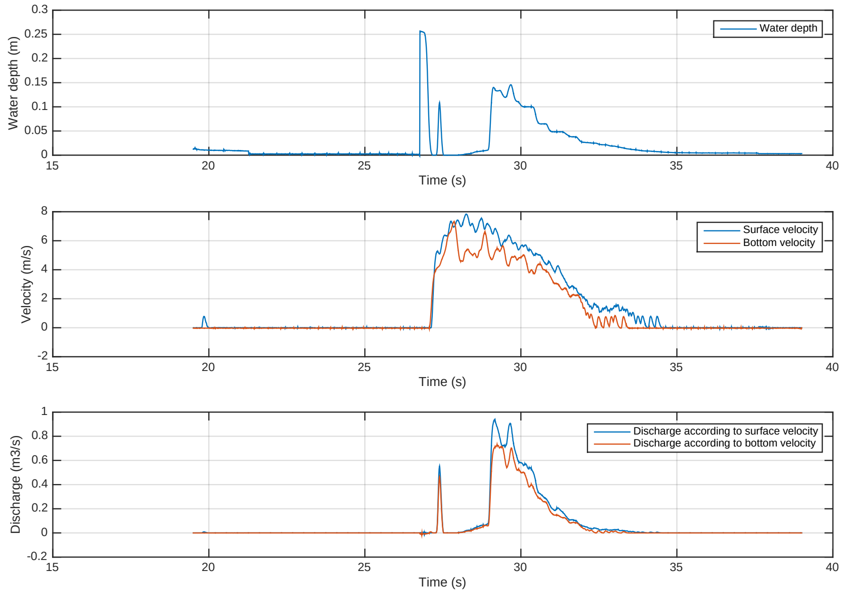

FIGURE H.21: Water depth, bottom velocity, surface velocity and discharge as obtained from position 3 during the 3000 l test.

Data as obtained from the 3500 l test waves.

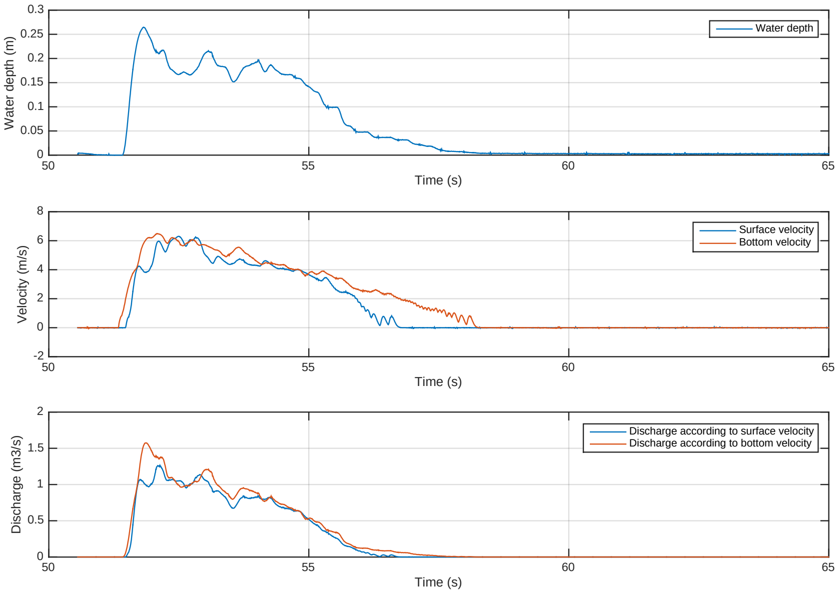

Figure H.22: Water depth, bottom velocity, surface velocity and discharge as obtained from position 1 during the 3500 l test.

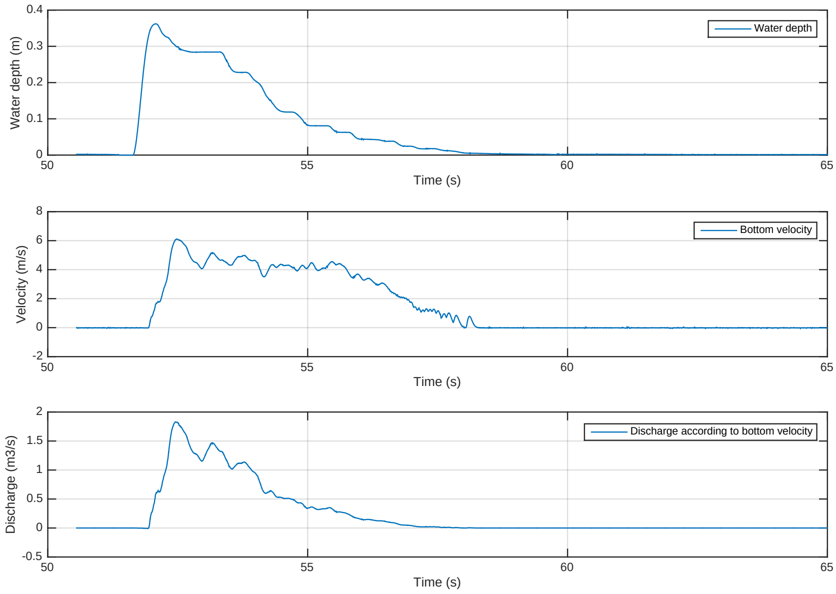

FIGURE H.23: Water depth, bottom velocity, surface velocity and discharge as obtained from position 2 during the 3500 l test.

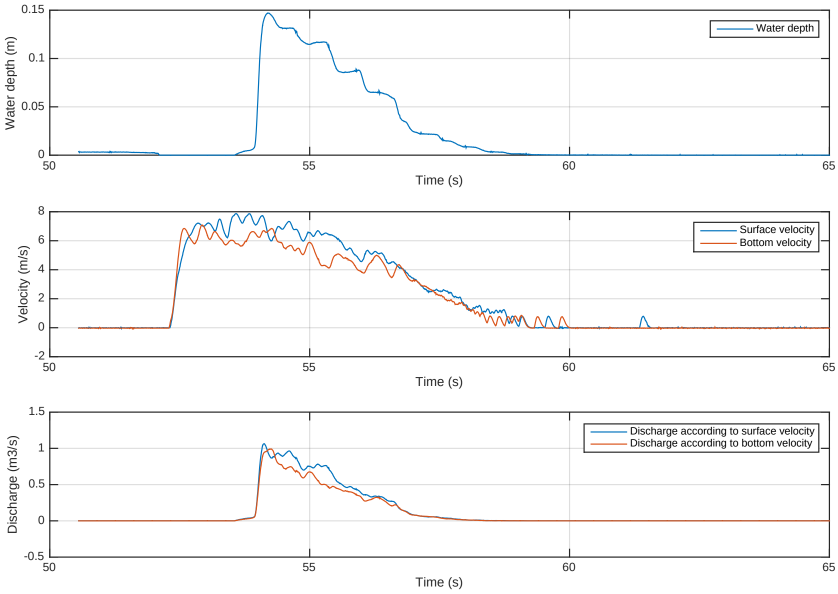

FIGURE H.24: Water depth, bottom velocity, surface velocity and discharge as obtained from position 3 during the 3500 l test.

I Description of damage during overflow tests

In this appendix the description of damage at the test sections during the overflow tests is given. Damage was visually observed and noted by Myron van Damme. The test started at 10 l/m/s. 10, 25, 50 and 85 l/m/s tests were performed for 2 hours each. After the 85 l/m/s test still no significant damage had occurred. This however was the maximum capacity of the pump. Therefore the test section was decreased to 1 m wide in order to get a higher discharge over the test section. Starting at 125 l/m/s, the discharge was further increased when no significant damage had occured. Finally, also a 150 and 170 l/m/s test were performed. After the 170 l/m/s test the test section finally started to show signs of significant damage.

In the descriptions sheets as presented in Figure I.1 to I.9 the red figures indicate the presence of rocks and stones and the blue figures indicate (signs of) damage to the dike.

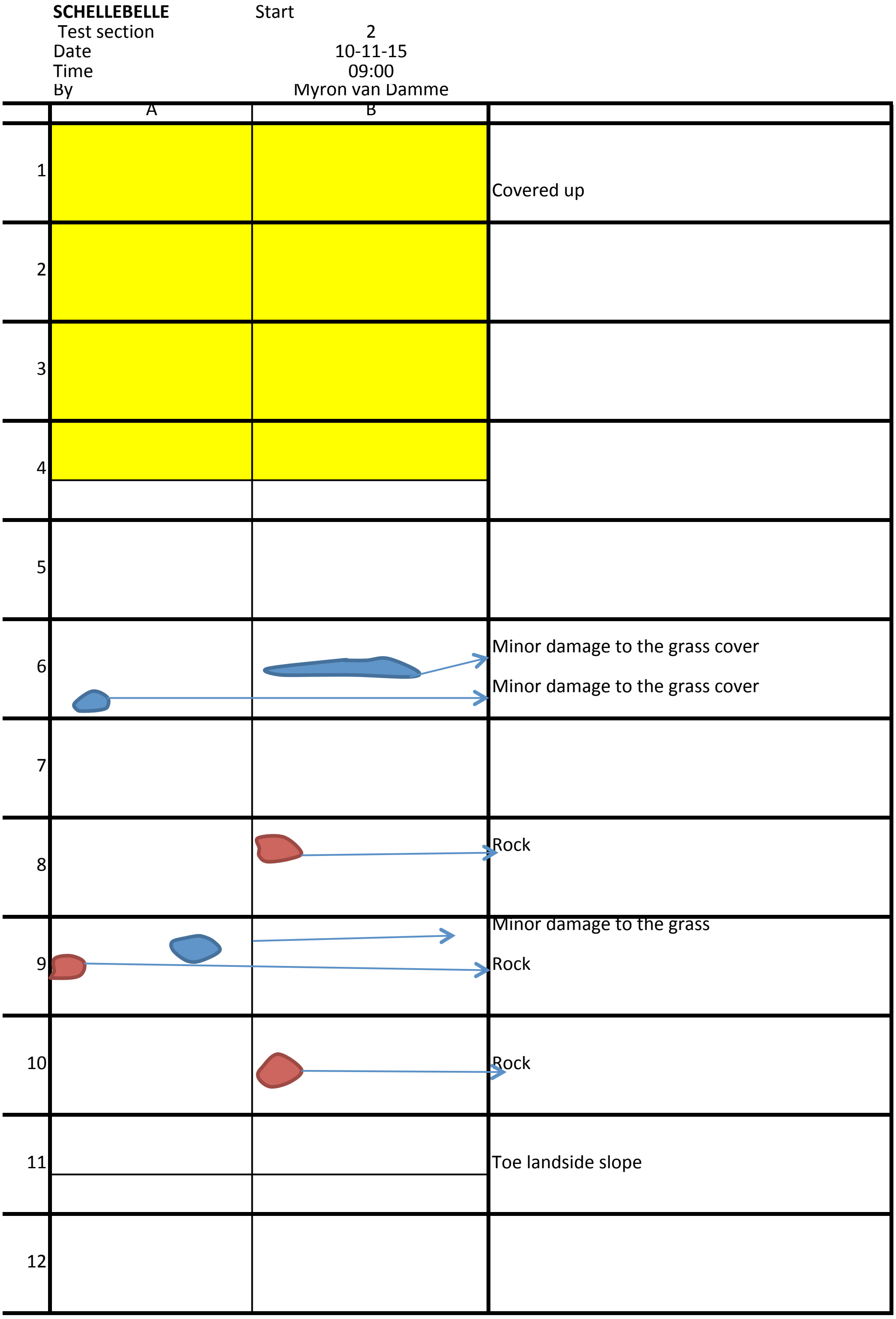

SCHELLEBELLE Start
Test section 2
Date 10-11-15
Time 09:00
By Myron van Damme

	A	B	
1			Covered up
2			
3			
4			
5			
6			Minor damage to the grass cover Minor damage to the grass cover
7			
8			Rock
9			Minor damage to the grass Rock
10			Rock
11			Toe landside slope
12			

FIGURE I.1: Description of the test section before starting the tests.

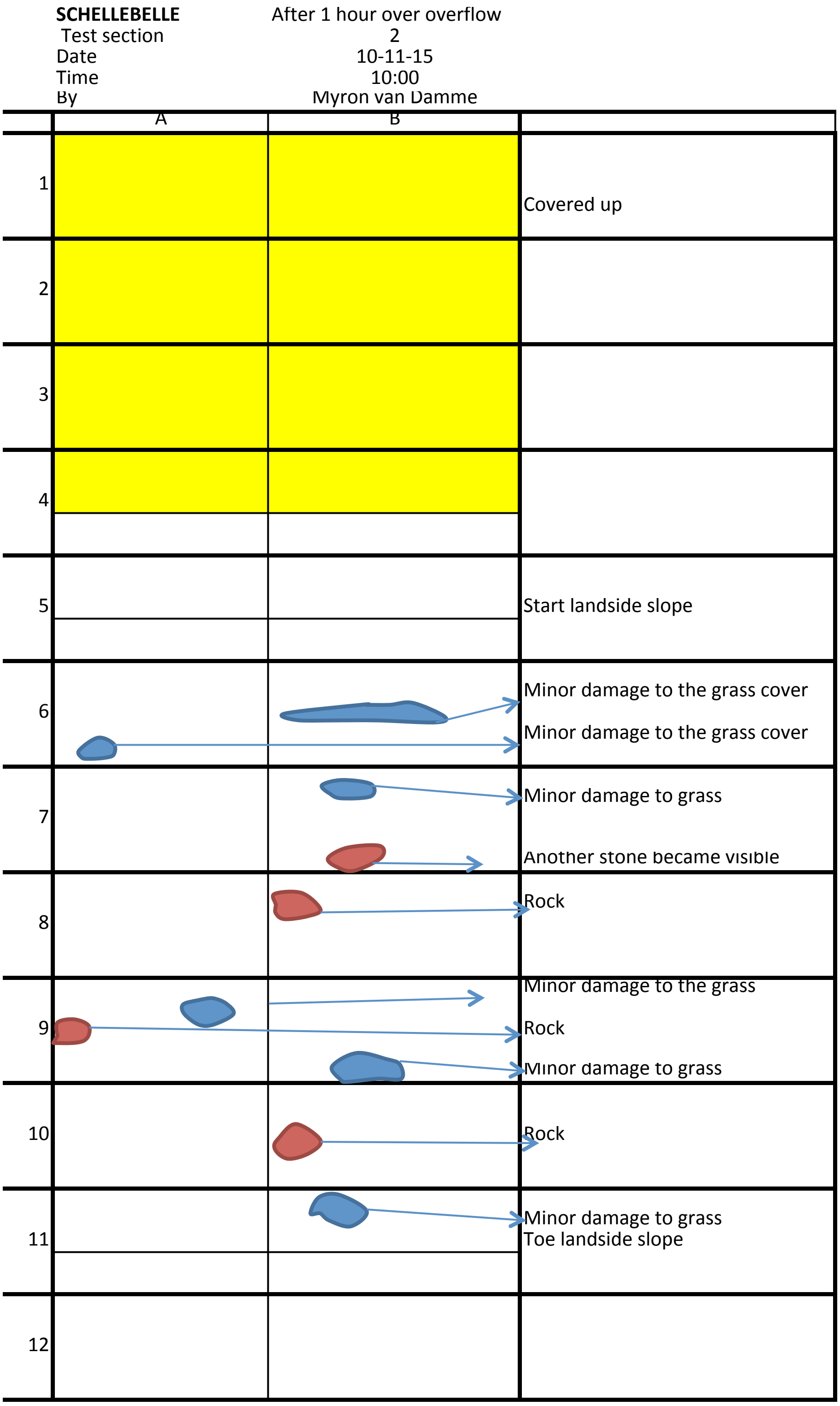

SCHELLEBELLE	After 1 hour over overflow
Test section	2
Date	10-11-15
Time	10:00
By	Myron van Damme

Covered up

Start landside slope

Minor damage to the grass cover

Minor damage to the grass cover

Minor damage to grass

Another stone became visible

Rock

Minor damage to the grass

Rock

Minor damage to grass

Rock

Minor damage to grass

Toe landside slope

Figure I.2: Description of the damage after 1 hour of 10 l/m/s test on the first test strip.

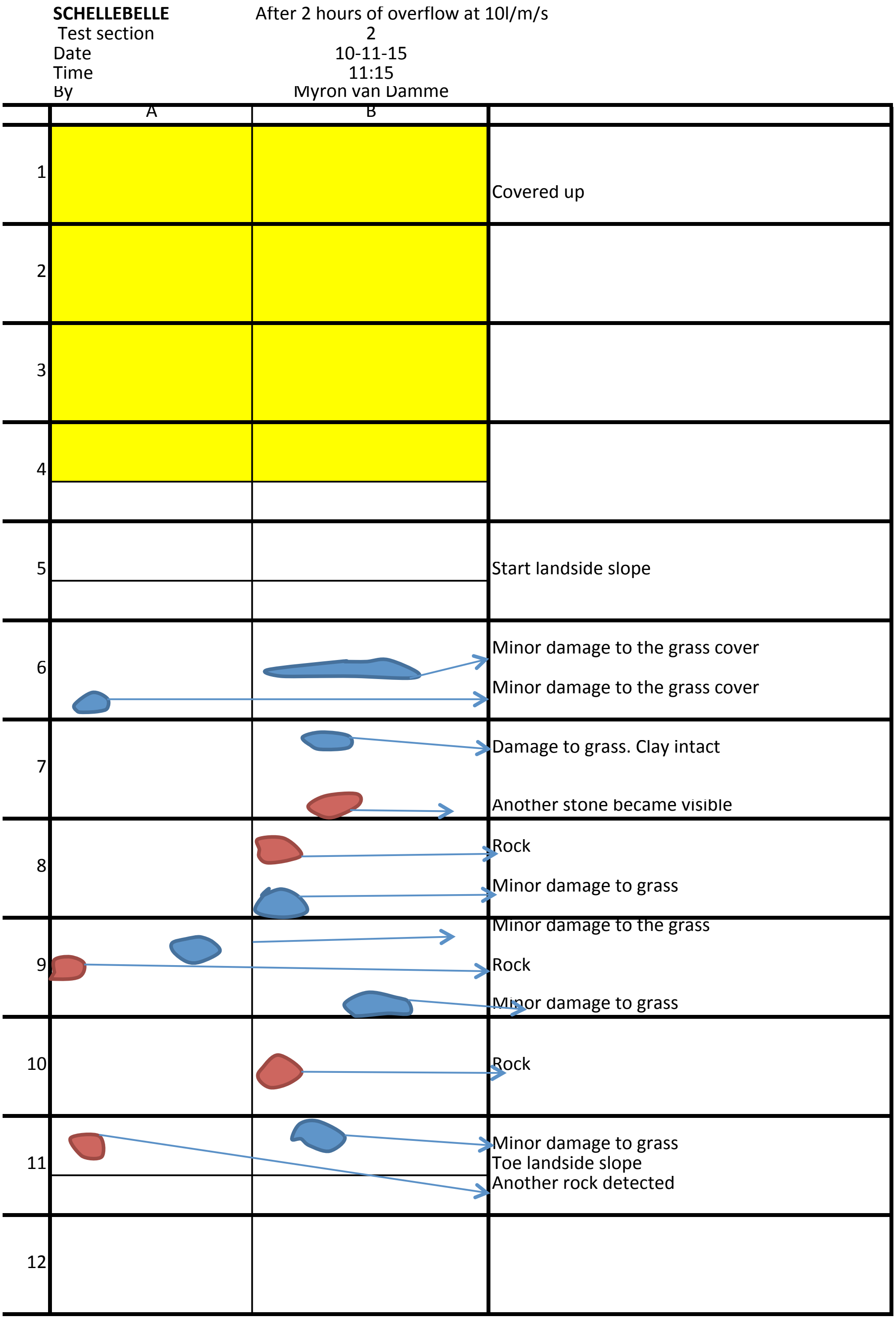

SCHELLEBELLE After 2 hours of overflow at 10l/m/s
Test section 2
Date 10-11-15
Time 11:15
By Myron van Damme

	A	B	
1			Covered up
2			
3			
4			
5			Start landside slope
6			Minor damage to the grass cover Minor damage to the grass cover
7			Damage to grass. Clay intact Another stone became visible
8			Rock Minor damage to grass
9			Minor damage to the grass Rock Minor damage to grass
10			Rock
11			Minor damage to grass Toe landside slope Another rock detected
12			

FIGURE I.3: Description of the damage after 2 hours of 10 l/m/s test on the first test strip. Immediately after the 10 l/m/s test the 25 l/m/s test started. Therefore this description of damage also holds for the initial damage of the 25 l/m/s test.

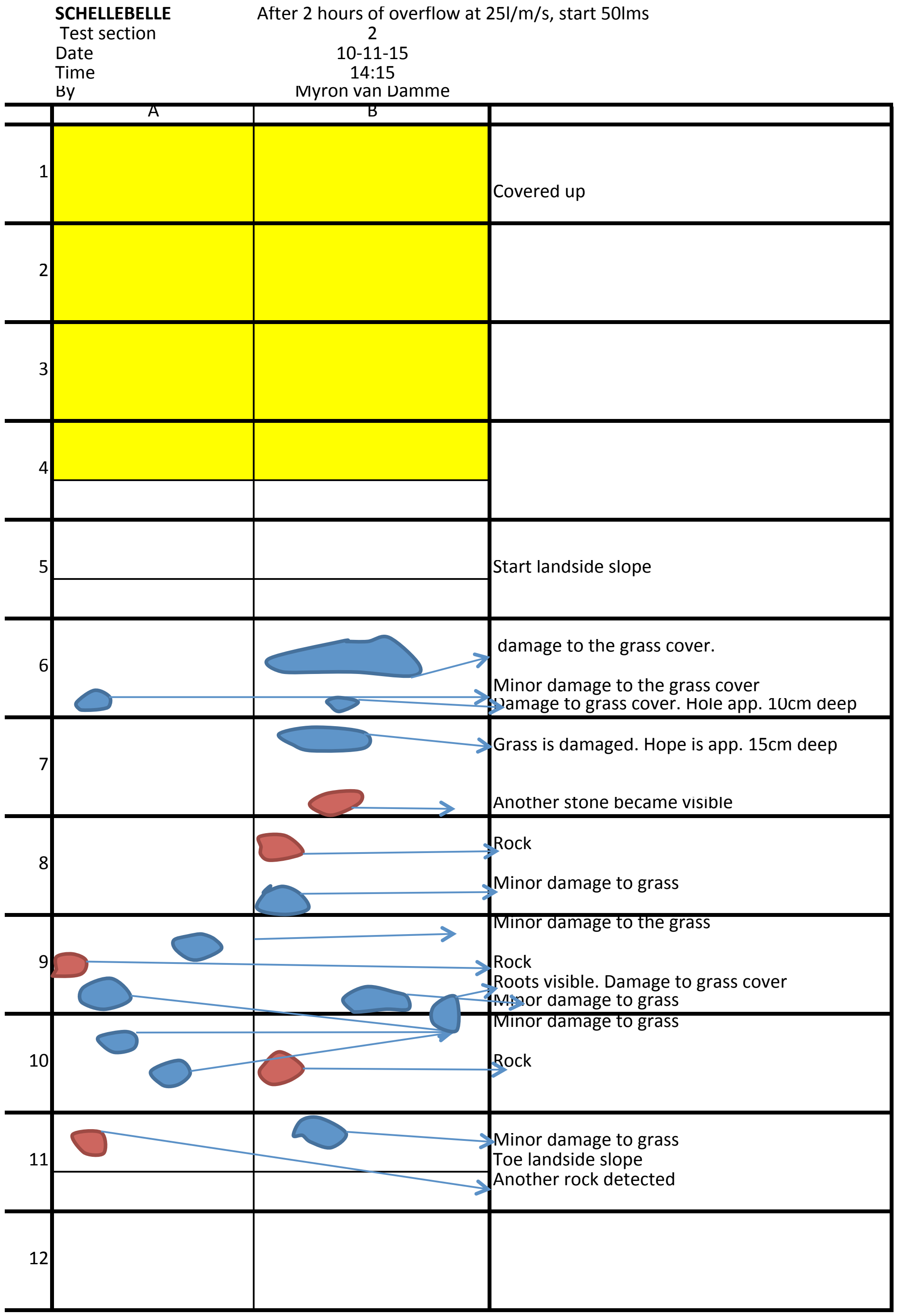
SCHELLEBELLE
After 2 hours of overflow at 25l/m/s, start 50lms
Test section
2
Date
10-11-15
Time
14:15
By
Myron van Damme
A
B
1
2
3
4
5
6
7
8
9
10
11
12
Covered up
Start landside slope
damage to the grass cover.
Minor damage to the grass cover
Damage to grass cover. Hole app. 10cm deep
Grass is damaged. Hope is app. 15cm deep
Another stone became visible
Rock
Minor damage to grass
Minor damage to the grass
Rock
Roots visible. Damage to grass cover
Minor damage to grass
Minor damage to grass
Rock
Minor damage to grass
Toe landside slope
Another rock detected

FIGURE I.4: Description of the damage after 2 hours of 25 l/m/s test on the first test strip. Immediately after the 25 l/m/s test the 50 l/m/s test started. Therefore this description of damage also holds for the initial damage of the 50 l/m/s test.

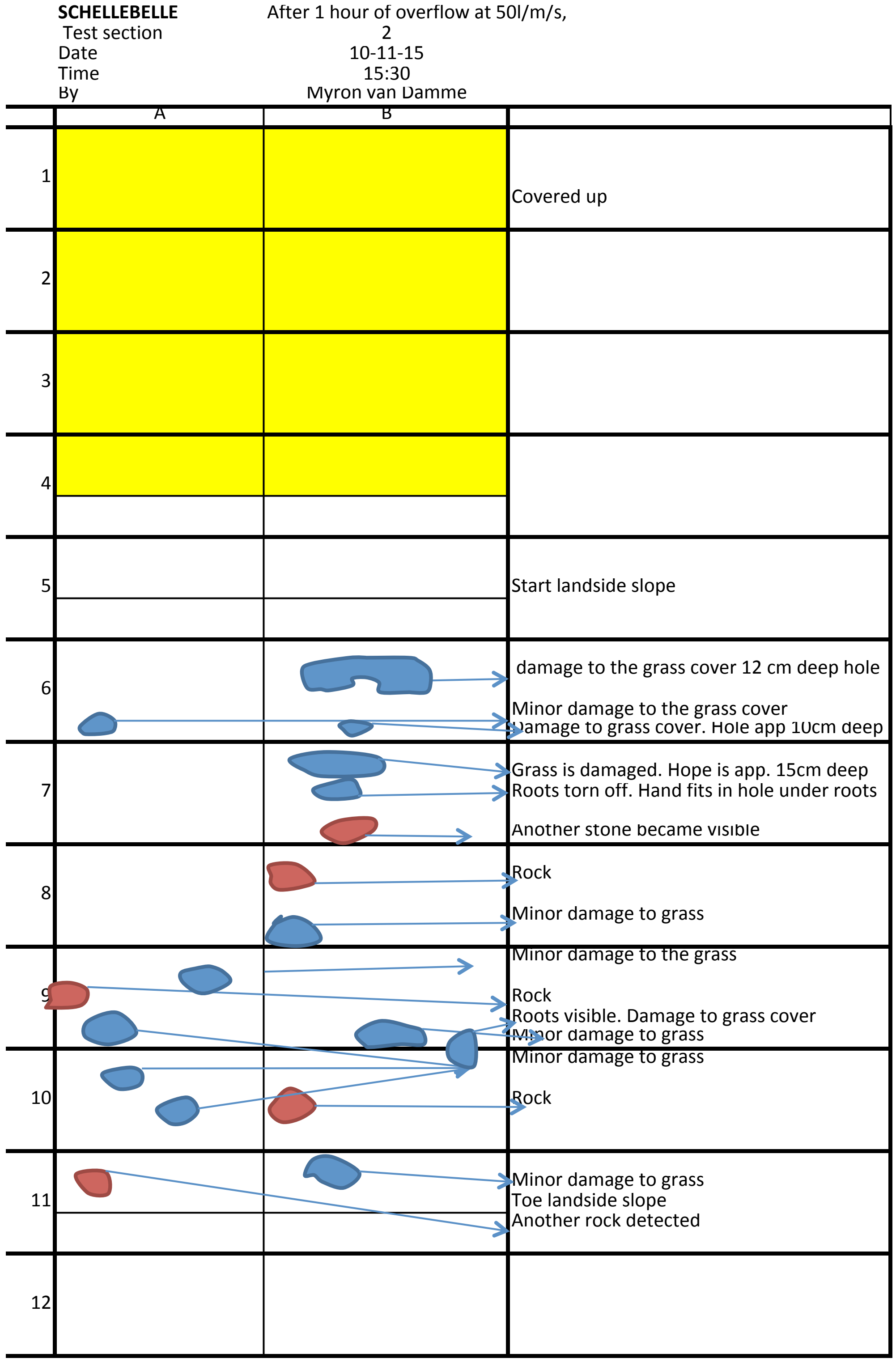

SCHELLEBELLE After 1 hour of overflow at 50l/m/s,
Test section 2
Date 10-11-15
Time 15:30
By Myron van Damme

Covered up

Start landside slope

damage to the grass cover 12 cm deep hole
Minor damage to the grass cover
Damage to grass cover. Hole app 10cm deep

Grass is damaged. Hope is app. 15cm deep
Roots torn off. Hand fits in hole under roots
Another stone became visible

Rock
Minor damage to grass

Minor damage to the grass
Rock
Roots visible. Damage to grass cover
Minor damage to grass

Minor damage to grass
Rock

Minor damage to grass
Toe landside slope
Another rock detected

FIGURE I.5: Description of the damage after 1 hour of 50 l/m/s test on the first test strip.

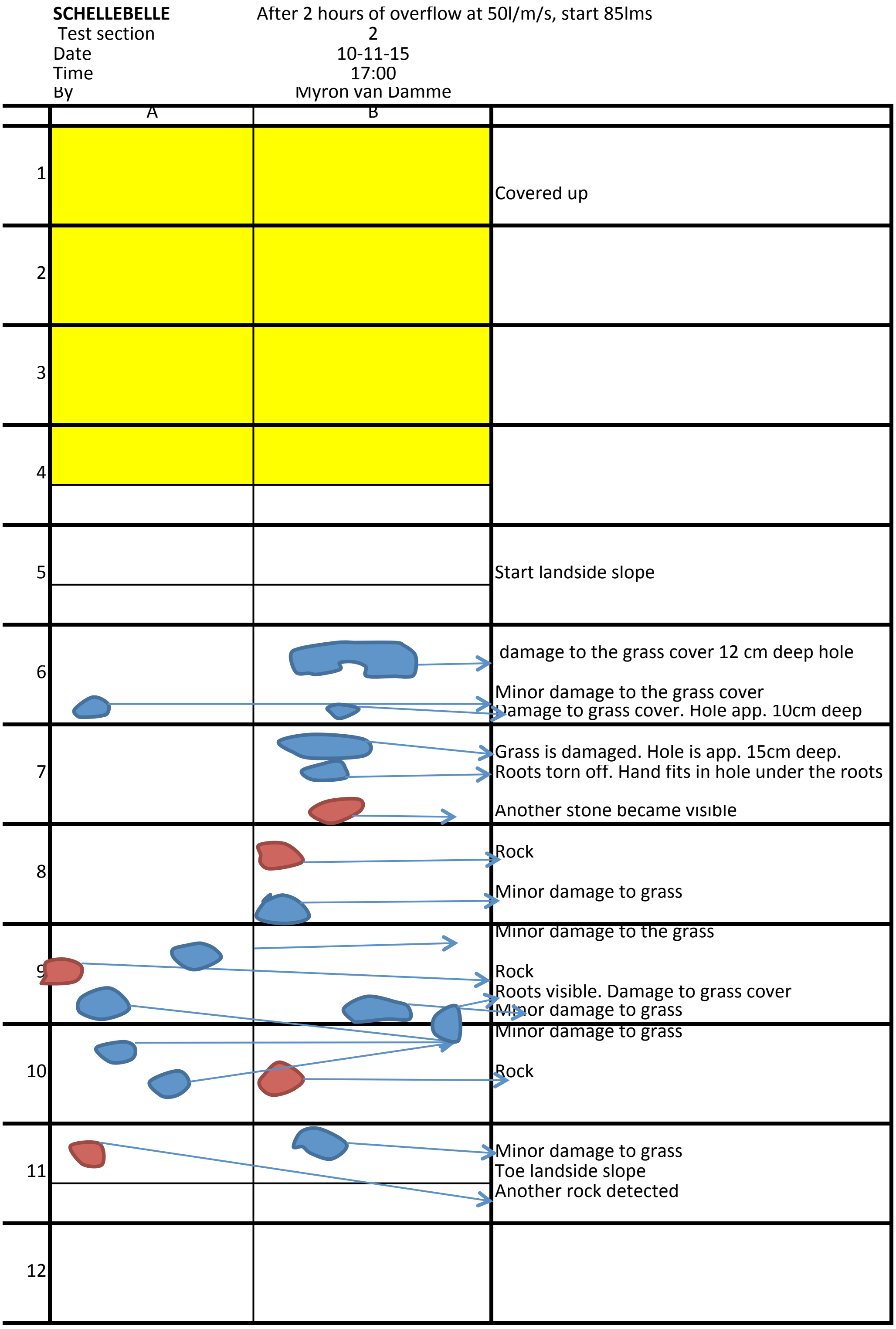

SCHELLEBELLE After 2 hours of overflow at 50l/m/s, start 85lms
Test section 2
Date 10-11-15
Time 17:00
By Myron van Damme

Covered up

Start landside slope

damage to the grass cover 12 cm deep hole

Minor damage to the grass cover

Damage to grass cover. Hole app. 10cm deep

Grass is damaged. Hole is app. 15cm deep.

Roots torn off. Hand fits in hole under the roots

Another stone became visible

Rock

Minor damage to grass

Minor damage to the grass

Rock

Roots visible. Damage to grass cover

Minor damage to grass

Minor damage to grass

Rock

Minor damage to grass

Toe landside slope

Another rock detected

Figure I.6: Description of the damage after 2 hours of 50 l/m/s test on the first test strip. Immediately after the 50 l/m/s test the 85 l/m/s test started. Therefore this description of damage also holds for the initial damage of the 85 l/m/s test.

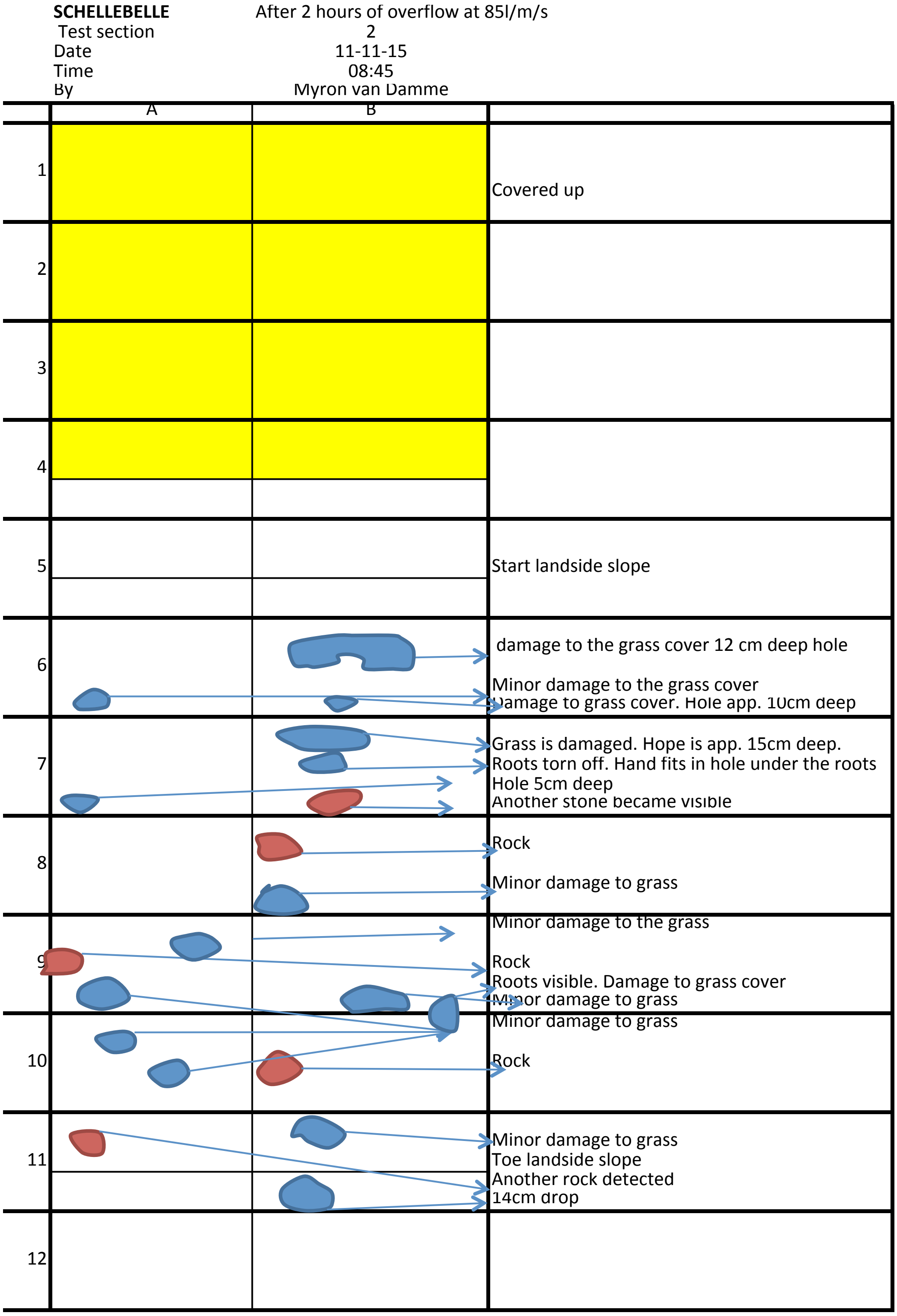

SCHELLEBELLE	After 2 hours of overflow at 85l/m/s
Test section	2
Date	11-11-15
Time	08:45
By	Myron van Damme

	A	B	
1			Covered up
2			
3			
4			
5			Start landside slope
6			damage to the grass cover 12 cm deep hole Minor damage to the grass cover Damage to grass cover. Hole app. 10cm deep
7			Grass is damaged. Hope is app. 15cm deep. Roots torn off. Hand fits in hole under the roots Hole 5cm deep Another stone became visible
8			Rock Minor damage to grass
9			Minor damage to the grass Rock Roots visible. Damage to grass cover Minor damage to grass
10			Minor damage to grass Rock
11			Minor damage to grass Toe landside slope Another rock detected 14cm drop
12			

FIGURE I.7: Description of the damage after 2 hours of 85 l/m/s test on the first test strip.

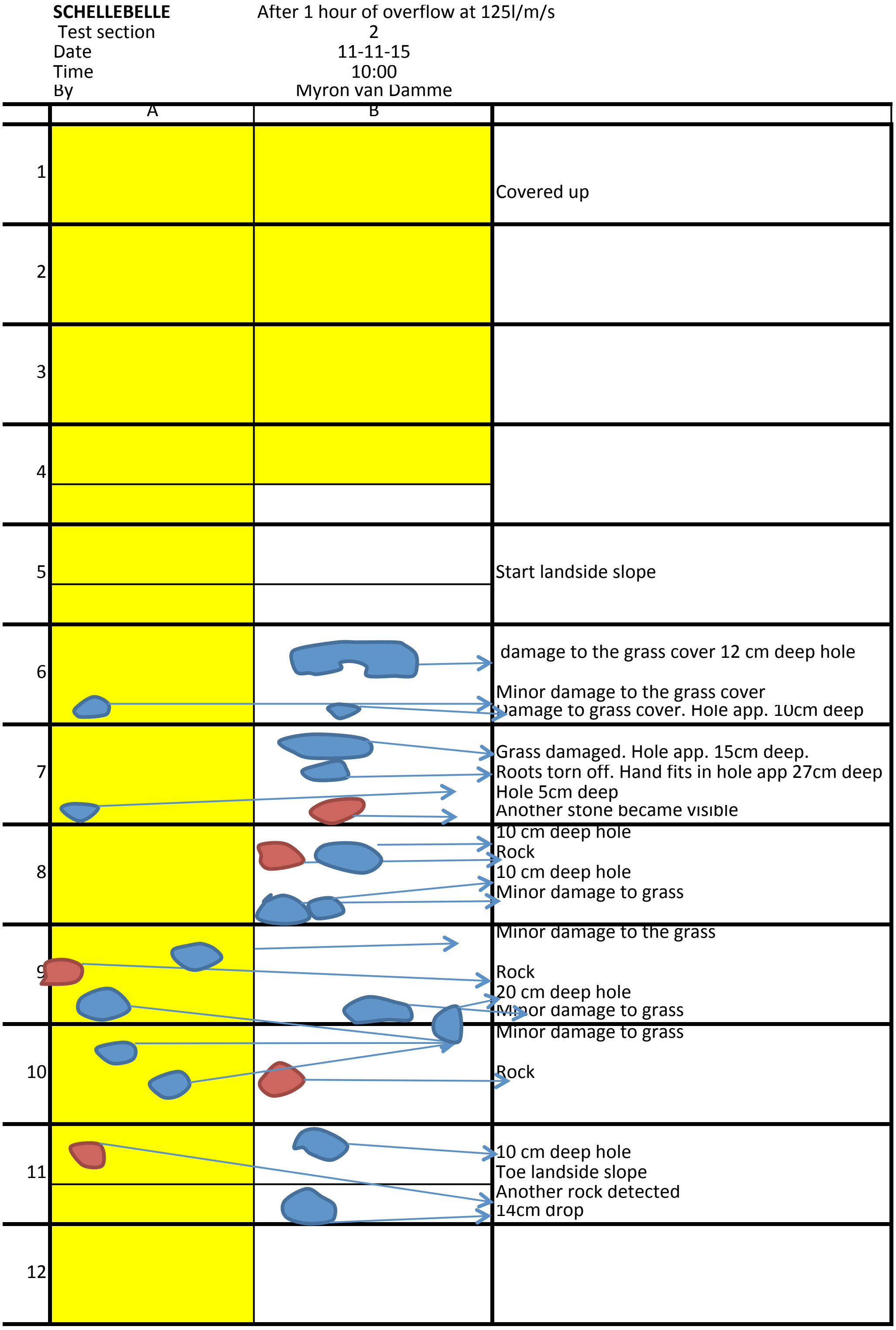

SCHELLEBELLE	After 1 hour of overflow at 125l/m/s
Test section	2
Date	11-11-15
Time	10:00
By	Myron van Damme

	A	B	
1			Covered up
2			
3			
4			
5			Start landside slope
6			damage to the grass cover 12 cm deep hole Minor damage to the grass cover damage to grass cover. Hole app. 10cm deep
7			Grass damaged. Hole app. 15cm deep. Roots torn off. Hand fits in hole app 27cm deep Hole 5cm deep Another stone became visible
8			10 cm deep hole Rock 10 cm deep hole Minor damage to grass
9			Minor damage to the grass Rock 20 cm deep hole Minor damage to grass
10			Minor damage to grass Rock
11			10 cm deep hole Toe landside slope Another rock detected 14cm drop
12			

FIGURE I.8: Description of the damage after 1 hour of 125 l/m/s test on the first test strip.

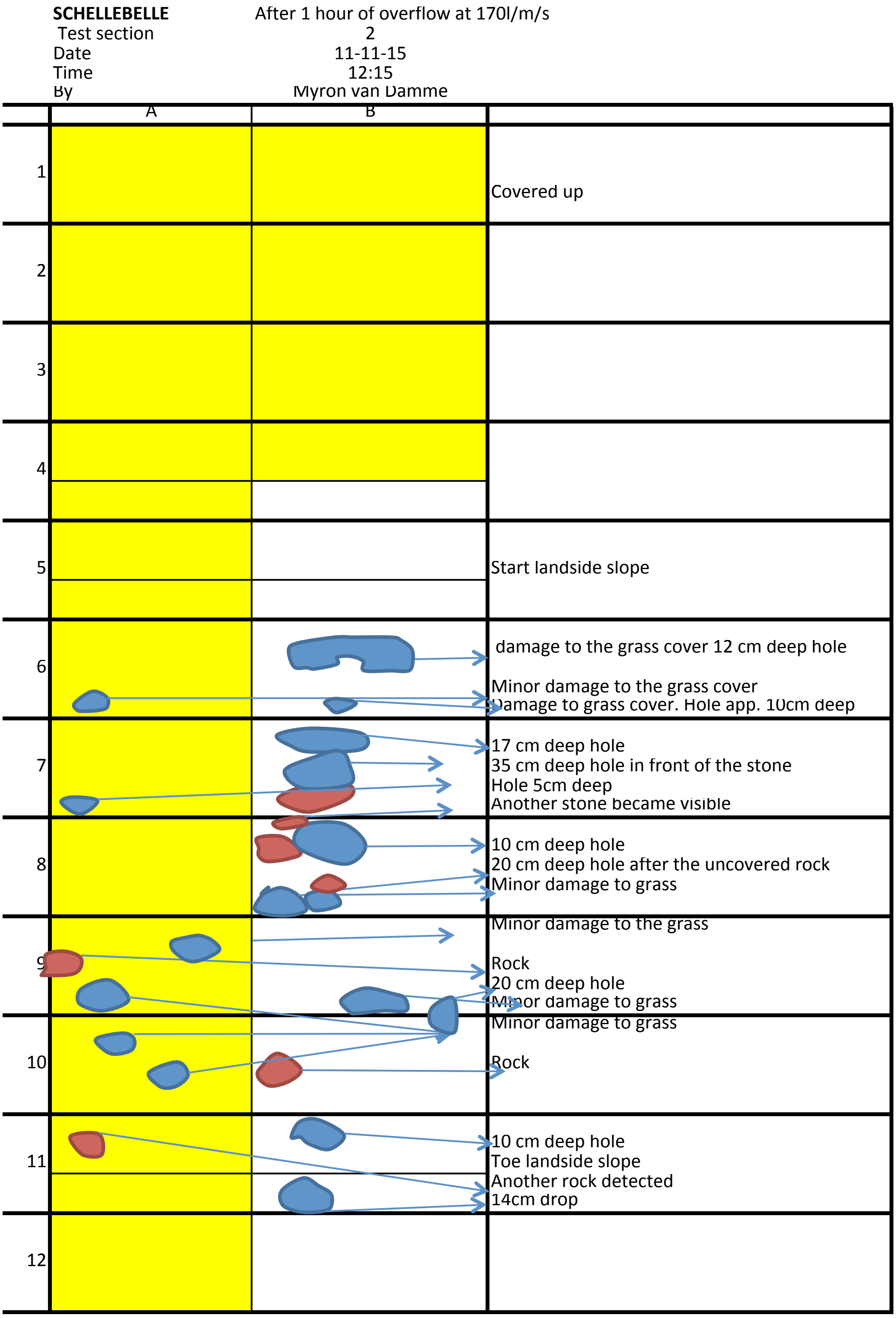

SCHELLEBELLE After 1 hour of overflow at 170l/m/s

Test section	2
Date	11-11-15
Time	12:15
By	Myron van Damme

	A	B	
1			Covered up
2			
3			
4			
5			Start landside slope
6			damage to the grass cover 12 cm deep hole Minor damage to the grass cover Damage to grass cover. Hole app. 10cm deep
7			17 cm deep hole 35 cm deep hole in front of the stone Hole 5cm deep Another stone became visible
8			10 cm deep hole 20 cm deep hole after the uncovered rock Minor damage to grass
9			Minor damage to the grass Rock 20 cm deep hole Minor damage to grass
10			Minor damage to grass Rock
11			10 cm deep hole Toe landside slope Another rock detected 14cm drop
12			

Figure I.9: Description of the damage after 1 hour of 170 l/m/s test on the first test strip. This is the maximum load that was applied on the test section.